

## PDF hosted at the Radboud Repository of the Radboud University Nijmegen

The following full text is a publisher's version.

For additional information about this publication click this link.

<http://hdl.handle.net/2066/77577>

Please be advised that this information was generated on 2017-12-06 and may be subject to change.

**Force spectroscopy to understand  
cell surface receptor interactions  
in the immune system**

The research in this thesis was performed at the Department of Scanning Probe Microscopy of the Institute for Molecules and Materials (IMM), Radboud University Nijmegen and the Department of Tumor Immunology, Nijmegen Centre for Molecular Life Sciences (NCMLS), Radboud University Nijmegen Medical Centre, The Netherlands, and was supported by a grant from NanoNed, the Dutch nanotechnology programme of the Ministry of Economic Affairs.

Printing of this thesis was financially supported by the following companies and foundations: NT-MDT Europe BV, Veeco Instruments, SmartTip BV and the J.E. Jurriaanse Stichting.

© 2010 by Joost te Riet (Radboud University Nijmegen)

All rights reserved. No part of this book may be reproduced or transmitted in any form or by any means without written permission of the author and the publisher holding the copyright of the published articles.

Cover design: Joost te Riet & Tim Smit

Page design: Joost te Riet

Printed by: Ipskamp Drukkers BV, Enschede, The Netherlands

# **Force spectroscopy to understand cell surface receptor interactions in the immune system**

Een wetenschappelijke proeve op het gebied van de

Natuurwetenschappen, Wiskunde en Informatica  
&  
Medische Wetenschappen

## **Proefschrift**

ter verkrijging van de graad van doctor  
aan de Radboud Universiteit Nijmegen  
op gezag van de rector magnificus prof. mr. S.C.J.J. Kortmann,  
volgens besluit van het college van decanen  
in het openbaar te verdedigen op maandag 21 juni 2010  
om 15.30 uur precies

door

**Joost te Riet**

geboren op 7 juli 1980  
te Lossier

---

**Promotores:**

Prof. dr. S. Speller

Prof. dr. C.G. Figdor

**Copromotor:**

Dr. A. Cambi

**Manuscriptcommissie:**

Prof. dr. A.E. Rowan (voorzitter)

Prof. dr. P. Hinterdorfer (Johannes Kepler Universiteit, Linz)

Prof. dr. V. Subramaniam (Universiteit Twente)

---

*Equipped with his five senses,  
man explores the universe  
around him and calls the  
adventure Science.*

*Edwin Powell Hubble*

Voor mijn ouders

---

---

## Contents

<b>Chapter 1</b>	General Introduction	9
<b>Chapter 2</b>	The threshold at which substrate nanogroove dimensions may influence fibroblast alignment and adhesion <i>Biomaterials (2007) 28: 3944-51</i>	35
<b>Chapter 3</b>	Interlaboratory round robin on cantilever calibration for AFM force spectroscopy <i>Submitted for publication</i>	45
<b>Chapter 4</b>	Distinct kinetic and mechanical properties govern homo- and heterotypic ALCAM mediated cell adhesion as shown by single-molecule force spectroscopy <i>Journal of Cell Science (2007) 120: 3965-3976</i>	67
<b>Chapter 5</b>	Mapping single interactions between DC-SIGN and <i>Candida albicans</i> -associated molecular patterns by AFM force spectroscopy <i>Manuscript in preparation</i>	87
<b>Chapter 6</b>	Measuring nanopatterns of His-tagged proteins by AFM <i>Manuscript in preparation</i>	103
<b>Chapter 7</b>	Molecular friction as a tool to identify functionalized alkanethiols <i>Langmuir (2010) 26: 6357-6366</i>	119
<b>Chapter 8</b>	AFM topography and friction studies of hydrogen-bonded bilayers of functionalized alkanethiols <i>Submitted for publication</i>	137
<b>Chapter 9</b>	General Discussion	151
<b>Summary</b>		166
<b>Samenvatting</b>		168
<b>Dankwoord</b>		172
<b>Curriculum Vitae &amp; List of publications</b>		175



---

The following companies provided financial support for the publication of this thesis, which is gratefully acknowledged:



# CHAPTER 1

---

## General Introduction

*Te weten wat men weet en  
te weten wat men niet weet,  
dat is kennis.*

*Confucius*

## Microscopy

In 1590, two Dutch spectacle makers, Zaccharias Jansen and his father Hans, while experimenting with several lenses in a tube, discovered that nearby objects appeared greatly enlarged. Some decennia later, Antoni van Leeuwenhoek used this knowledge to construct the first microscope to perform his first studies. With the microscopes he built, he was a pioneer in cell biology and microbiology. These early microscopes made use of lenses to bundle light and with that magnify the samples. Since then, a lot of improvements, especially made in the 20<sup>th</sup> century, ensured that nowadays light microscopy is widely applied to study cells, tissues and materials. However, conventional light microscopy is limited by the diffraction limit of light; details smaller than the wavelength of visible light can not be distinguished. In 1931, Ernst Ruska built another type of microscope based on the use of electrons which have a much smaller wavelength than visible light. With this electron microscope it was possible to 'see' details up to the size of single atoms. There are two types of electron microscopy: transmission electron microscopy (TEM), in which the electrons that pass *through* a sample are detected, and scanning electron microscopy (SEM), in which the electrons that are scattered *from* a sample are detected. Another family of microscopes that was developed exploits a 'needle' to probe a sample, and also achieves atomic resolution. This is the family of scanning probe microscopes (SPM), of which the best known examples are scanning tunneling microscopy (STM), atomic force microscopy (AFM), and near-field scanning optical microscopy (NSOM).

## Atomic Force Microscopy

The STM was invented in 1981 by Gerd Binnig and Heinrich Rohrer.<sup>1</sup> In 1986, Gerd Binnig, Calvin Quate and Christoph Gerber adjusted the STM to become the first AFM.<sup>2</sup> The AFM can acquire topographic images of a substrate by raster scanning the specimen using a piezoelectric scanner. Piezoelectric material shrinks or expands depending on the electric charge that is applied on it. This scanner moves the sample in the x-, y- and z-direction with respect to a sharp tip at the end of a flexible cantilever that bends according to the contours of the surface (Fig. 1A). Resolution up to the atomic level is obtained by translating the deflection of the cantilever into an image map of the surface topography, which is measured by a laser spot reflecting from the end of the cantilever onto a four-quadrant detector. The essential components of the AFM are further discussed in Fig. 1.

### Imaging modes

There are basically two different modes of operation for the AFM, which differ depending on whether the cantilever is driven to oscillate in proximity of its resonant frequency or not.

(i) In **Contact mode** (also known as *static mode*) the static tip deflection is used to keep the deflection – actually the applied force – constant by moving either the sample or cantilever via a feedback mechanism. The surface topography is then reconstructed from this vertical movement of the sample or the cantilever (Fig. 1B). In parallel to the topography, other properties of the sample can be mapped. Information on these properties are visualized in additional acquisition channels of the AFM, such as the *deflection error* and the *lateral force* or *friction*. The *deflection error* information acquired during scanning the sample is interesting for its high contrast images. Namely, at ridges

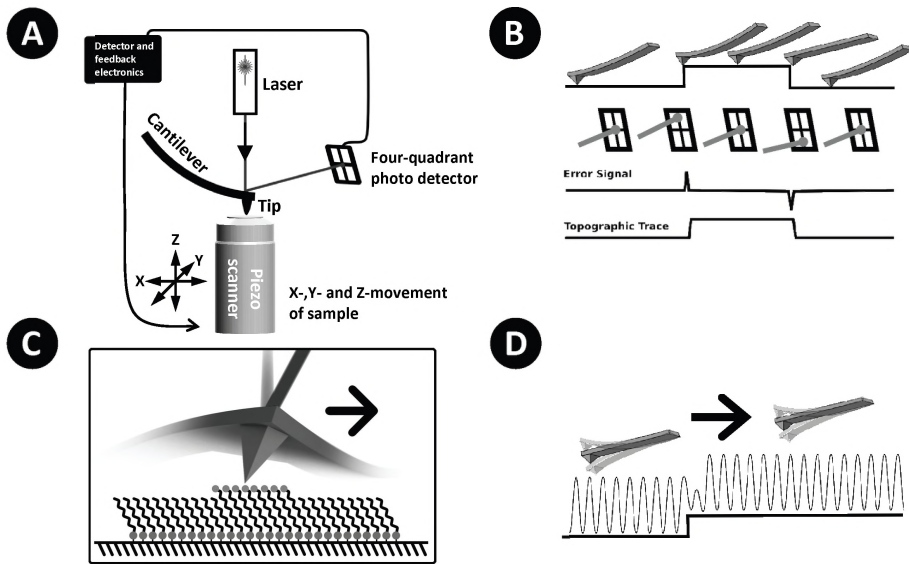


**Figure 1: Atomic force microscopy**

(A) With a piezo scanner a sample can be scanned by moving the sample in the x-, y- and z-direction. The topography of the sample can be probed by a sharp tip at the end of a flexible cantilever. A laser reflected from the end of the cantilever is used to detect the deflection of the cantilever by a four-quadrant photo detector. (B) In contact mode the height differences are measured by the change in deflection. The reflected laser beam shifts vertically up or down on the photo detector. To compensate for this shift, the piezo scanner moves in the z-direction. Because of that, the laser spot gets re-centered and the cantilever has the same deflection as before. The real laser position on the detector is interpreted as the error signal (2<sup>nd</sup> trace from below) and the movement of the scanner as the topography (lower trace). (C) In contact mode the variation in frictional behavior of a sample is measured as the lateral or torsional change in deflection. The reflected laser beam varies in the horizontal direction of the four-quadrant photo detector, so perpendicular to the (height) deflection. (D) In tapping mode the cantilever is brought into oscillation. Upon scanning a step in the topography of a sample the amplitude is dampened (smaller). By moving the sample in the z-direction the amplitude recovers and the topography of the sample is probed.

or other sharp changes in the topography the cantilever deflection has to be corrected to keep it constant, so actually the 'error' information is used to obtain a 'derivative' image (Fig. 1B).<sup>3</sup> The *friction mode* uses the information acquired by the torsional deformation of the cantilever while scanning the sample in the lateral direction. This deformation of the cantilever is converted into friction images by measuring the shift of the laser signal on the four-quadrant detector in the horizontal direction. Note that the topography information is measured as the vertical shift of the reflected laser on the detector (Fig. 1C).

In general, *contact mode* is applied on samples that are relatively hard by nature and are not easily affected by the probing tip. However, with soft cantilevers and low forces, high resolution imaging of e.g. membrane proteins is possible.<sup>4</sup>

(ii) In **Tapping mode** (also known as *dynamic mode* and *resonant mode*) the AFM tip is oscillated near its resonant frequency while it scans over the surface, to avoid being continuously in contact with the sample (Fig. 1D). In *tapping mode* the cantilever is brought in oscillation with a piezoelectric element (acoustic mode), embedded in the holder of the cantilever. An alternative, applied by some commercial AFMs, is driving magnetically coated probes with an external magnetic coil (magnetic mode). In both the

acoustic and the magnetic mode, the amplitude of the tip is kept constant by a feedback loop and the topography is reconstructed in a similar way as in *contact mode*.

The most commonly used mode in AFM is *intermittent contact mode*. This name originates from the way of scanning a sample; the cantilever shortly comes into contact with the substrate every oscillation cycle (Fig. 1D). In this mode the cantilever's oscillation amplitude is kept constant. Any variations in amplitude are corrected by moving the sample in the z-direction, via a feedback loop, which results in a topography map of the surface.

In the *noncontact mode*, the sample is scanned by keeping the cantilever in close proximity to the substrate. Close to the surface the cantilever senses the van der Waals forces, which causes a phase shift in the resonant frequency of the cantilever. This shift is used as a feedback signal in this mode to scan the substrate's topography. However, due to contaminations and/or a water layer on the sample the cantilever is pulled onto the sample and the scanning is disrupted, because the phase shift is too large for feedback. In general, this implies that the *noncontact mode* is more sensitive to capillary forces than the *intermittent contact mode*. Therefore, this mode is rarely used outside vacuum conditions.

To conclude, *tapping mode* AFM can be used to study almost any sample, but due to the reduced contact and minimal lateral forces it can be used to scan soft samples without damaging it. Furthermore, samples requiring a liquid environment, such as biological ones, can be scanned in *intermittent contact mode*. There are many advantages for working in liquid, such as having near physiological conditions. Nevertheless, scanning is slow due to a slow feedback caused by the dampening of the cantilever's oscillation by the surrounding solvent and the resulting lowered resonant frequency. Performing *liquid tapping mode* AFM is therefore more complicated and slower compared to *contact mode*; however, with the latter mode soft samples are more easily damaged.<sup>5</sup>

So, the AFM's ability to work in almost any environment, its versatility, its high resolution, and many different imaging modes (see also Box 1), makes this instrument

#### Box 1: Different imaging modes

Except for the classical topography imaging modes, there are other modes that can map different material properties. A commonly used acquisition mode is the *phase imaging mode*. In this mode the phase lag between excitation and resulting oscillation of the cantilever is recorded in a second acquisition channel and is used to discriminate between different sample characteristics, such as packing density, hardness, or other chemo-physical properties of the sample.<sup>6-8</sup> Besides, specialized modes can acquire one specific material property, such as, *force mapping mode* (or *force modulation mode*) in which the elasticity of a sample is mapped by probing the stiffness of the material with a cantilever by measuring force-distance curves.<sup>5</sup> A faster method to quantify the elasticity of a sample is the so-called *Harmonix mode*, which was developed by Sahin et al.<sup>9</sup> in cooperation with Veeco. In this mode a substrate is scanned in ordinary *tapping mode*, however a special tip is used that torsionally deforms every oscillation cycle the cantilever comes into contact with the surface and in this way probes its elasticity. Further examples of specialized imaging modes are *magnetic force microscopy* (MFM),<sup>10</sup> with which a magnetic map of a sample can be made, and *topography and recognition imaging* (TREC) in which a functionalized tip is used to probe its interaction with the sample mapping interaction spots.<sup>11</sup>

very useful for a wide range of applications and indispensable for performing research at the nanoscale.

## AFM force spectroscopy

### Force measurements

The versatility of the AFM is further demonstrated by its ability to precisely measure the interaction forces between a substrate and a flexible cantilever. These forces are measured as the deflection of the cantilever. The attractive and repulsive regions are mapped by moving the cantilever vertically – in the z-direction – to the sample with piezo electric elements (Fig. 1A). At retraction of the cantilever, an attractive interaction will cause the cantilever to deflect downward (negative force). According to Hooke's law ( $F = k \times d$ ), the deflection  $d$  will be proportional to the force  $F$  acting on the cantilever – with  $k$  the spring constant of the cantilever. The piezoelectric z-position plotted versus the force results in a so-called *force-distance curve* (Fig. 2).

### Single molecule force spectroscopy (SMFS)

Force is a natural measure for how strong molecules interact with each other. In the *force scan mode* the AFM's ultra sensitivity can be used to measure interactions between two individual molecules with a force resolution of single picoNewtons ( $10^{-12}$  Newton). Therefore, the tip of the cantilever is 'functionalized', which implies that molecules (e.g. proteins) are immobilized onto it. Subsequently, this tip is used to study ligand-receptor interactions and quantify bond strengths. An important step to be able to quantify these forces is the calibration of the system. In Box 2 the most important steps are described.

The AFM was used for the first time in measuring forces of biological ligand-receptor interactions in 1994 by Lee et al. <sup>12, 13</sup> They succeeded in measuring the unbinding force

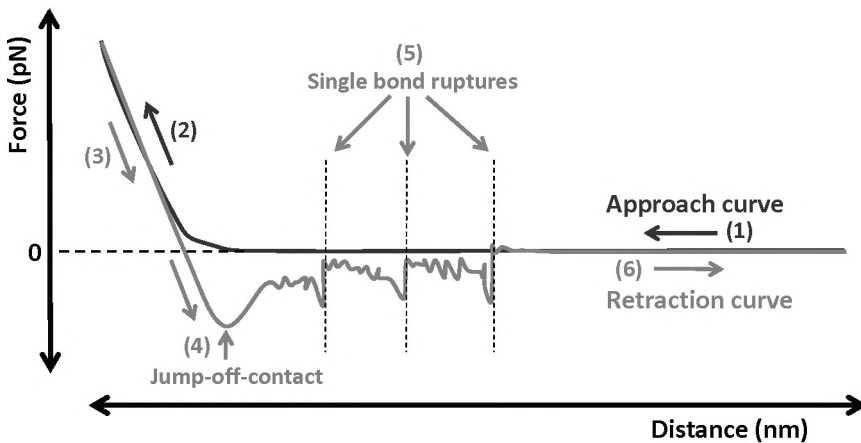


**Figure 2: A force-distance curve showing single bond ruptures**

(1) In the approach curve the substrate is moved to the cantilever by the piezoelectric scanner until contact is made (2). Then the force between substrate and cantilevers builds up until a specified force limit is reached. During a preset period of time (interaction time) the functionalized cantilever and substrate are allowed to interact (3). Upon retraction the cantilever sticks to the substrate and causes the cantilever to bend in the other direction (4), until the force acting on the molecular bonds are large enough for bond rupture to occur (5). After a first jump-off contact, which is mostly non-specific, single specific ruptures occur. Finally, after the last rupture the cantilever returns to its resting position (6).

**Box 2: Calibration of the system**

To measure the precise dimensions of a sample and the forces involved at probing, the calibration of the piezo scanner of the AFM and the cantilever spring constant is essential. The x-, y- and z-directions of the piezo scanner are calibrated with a calibration-grid from which the dimensions are given with an accuracy of 1-5%. This calibration is checked half-yearly to adjust for aging effects of the piezo-electronic devices.

To measure and quantify forces, the deflection light path of the laser reflected from the tip of the cantilever on the four-quadrant photo detector must be calibrated. Two steps are needed for conversion of the cantilever deflection measured in Volts into Newtons. The first step is to convert the deflection of the cantilever into nanometers. Therefore, the deflection sensitivity (m/V; also called InvOLS,<sup>30</sup> Inverse Optical Lever Sensitivity) has to be determined,

which can be done by bringing the cantilever into contact with a hard substrate and measure its deflection. Hereby, the calibrated piezo is used to gauge the deflection in the z-direction (Fig. B1). An alternative method is the calculation of the InvOLS which will be described in Chapter 3. The second step is to determine the cantilever's spring constant and then convert the deflection from nanometers into Newtons using Hooke's law ( $Force [N] = spring\ constant [N/m] \times deflection [m]$ ). This spring constant can be determined by different methods e.g. the thermal noise method<sup>31</sup> and the Sader method,<sup>32</sup> which will be detailed in Chapter 3. Finally, after both steps the actual forces encountered by the cantilever are known.

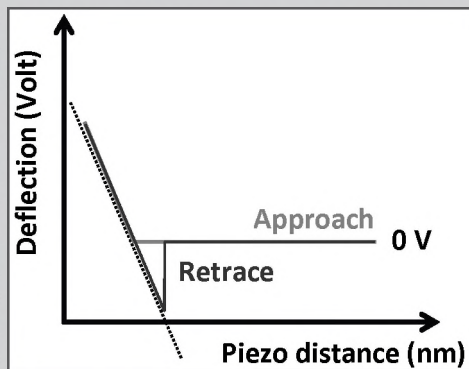


**Figure B1: Deflection gauging.** The deflection in (nm) is determined from a force curve obtained by bringing a cantilever into contact with a hard (glass) substrate. The contact region of the approach curve is linear and by fitting it the deflection in Volt is gauged into nm. In other words, a displacement of 100 nm by the piezo scanner translates by definition into a deflection of 100 nm for the cantilever.

of single streptavidin-biotin interactions, by immobilizing the ligand (streptavidin) on the surface of the AFM cantilever, while the receptor (biotin) was attached to a glass substrate.<sup>12</sup> Subsequently, they measured forces between complementary strands of DNA.<sup>13</sup> This paved the way to use the AFM as an ultra-sensitive force transducer for probing biomolecular interactions. This nonimaging AFM technique – often referred to as AFM (Single Molecule) Force Spectroscopy<sup>14, 15</sup> – was subsequently adopted by Gaub, Florin and Moy to study the unbinding of ligand/receptor complexes of actin monomers and biotin to avidin-analogs.<sup>16, 17</sup> Later, in 1996, Hinterdorfer et al. succeeded in measuring antibody (Ab)-ligand interactions.<sup>18</sup> The *rupture forces* detected upon separating single ligand-receptor pairs (Fig. 2) provides new insights into the binding strength, binding kinetics, (un)binding energy landscape, and the localization of receptors on the cell surface.<sup>19, 20</sup> In these experiments, however, unspecific interactions can easily superimpose with specific ones. To separate unspecific from specific interactions, the ligand may be attached via a molecular crosslinker (spacer) to the AFM tip.<sup>18</sup> Continuous improvement

of the SMFS methodology (tip modification, data acquisition and interpretation) has enabled researchers to determine the interaction forces and the dynamics of a variety of cell surface proteins, including cadherins,<sup>21</sup> integrins,<sup>22</sup> selectins,<sup>23</sup> growth factor receptors,<sup>24</sup> heat shock proteins,<sup>25</sup> and bacterial adhesins.<sup>26</sup> Furthermore, interaction forces were measured between polysaccharides,<sup>27</sup> polymers,<sup>28</sup> and rupture of covalent bonds.<sup>29</sup>

### Single cell force spectroscopy (SCFS)

A novel development by Benoit et al. in 2000, was to use force spectroscopy in adhesion studies involving whole cells, which later became known as SCFS.<sup>33</sup> In SCFS, ligand-receptor interactions are measured between a cell attached to the cantilever and expressing a receptor of interest and a ligand immobilized on a substrate, or another cell expressing the ligand.<sup>15, 34</sup> A major advantage of this method is that cellular affinity (the single-molecular adhesive capacity of a receptor to a ligand) modulation can be analyzed directly by monitoring single-bond rupture forces. Related to this is the possibility to discriminate between affinity and avidity (the cooperativity of the receptors) by studying the overall cell adhesion from the perspective of the individual bonds in response to physiologically relevant stimuli. Importantly, SCFS further provides insight into what extent receptor-ligand complexes can withstand external forces in their native state on the cell membrane. This leads to a better insight of the overall dynamic capacity of the cell to withstand external forces.

### *Evaluation of force spectroscopy data*

In the following paragraph, I will describe a couple of important steps required to interpret force spectroscopy data. The basis of force spectroscopy is the *force-distance curves* acquired by probing ligand-receptor interactions. The molecular bond ruptures observed in the retraction part of these force curves ruptures are visible as discrete steps (Fig. 2). The magnitude of this step is used as a measure of (de)adhesion: the *rupture force*. However, to get insight into the binding dynamics of a receptor-ligand pair commonly the influence of the speed at which the force builds up is investigated, this speed is the so-called *loading rate* (see Box 3).

The dependence of the *rupture forces* on the *loading rate* was first described by Bell in 1978<sup>36</sup> and revisited by Evans<sup>37</sup> in 1997. Their Bell-Evans model, or in short Bell model, is based on the transition state theory of a binding potential in which the free energy available varies with the separation of the receptor and ligand.<sup>38-40</sup> Later, this binding potential was described as the sum of a complex of hydrogen, van der Waals, and chemical bonds.<sup>41</sup> When a ligand-receptor bond is loaded by retracting the AFM cantilever, work is done on the bond. The total energy, which is the sum of the bond energy and the work added by pulling on the bond, results in lowered energy barriers (Fig. 3A, C) and an increase of the dissociation rate constant. At the same time, bonds appear to strengthen with increased load, resulting in higher rupture forces. In this model, a pulling force  $F$  distorts the energy landscape of the ligand-receptor complex which results in lowered activation barrier(s). As a consequence the dissociation rate constant  $k_{off}(F)$  increases:<sup>35</sup>

$$k_{off} = k_{off}^0 \exp\left[\frac{Fx_{\beta}}{k_B T}\right] \quad (\text{Eq. 1})$$



Here,  $k_{off}^0$  is the dissociation rate constant in the absence of the pulling force;  $x_\beta$  is the reactive compliance, which is the separation distance between the receptor and ligand needed to overcome the energy barrier resulting in unbinding;  $T$  the absolute temperature, and  $k_B$  is the Boltzmann's constant.<sup>37,42</sup> Assuming that the bond dissociation is a random process, the probability density function for failure of a single bond at time  $t$  and external loading force  $F$  is given by:<sup>43</sup>

$$P(t, F) = k_{off}(F) \exp\left[-\int_0^t k_{off}(F(\tau)) d\tau\right] \quad (\text{Eq. 2})$$

Under conditions of a constant loading rate  $r_f$  ( $F = r_f \cdot t$ ) and combining Eq. 1 and Eq. 2, the probability density function for the failure of a single bond in a complex at force  $F$  is given by:

$$P(F_{rup}) = k_{off}^0 \exp\left(\frac{F_{rup} x_\beta}{k_B T}\right) \exp\left\{\frac{k_{off}^0 k_B T}{x_\beta r_f} \left[1 - \exp\left(\frac{F_{rup} x_\beta}{k_B T}\right)\right]\right\} \quad (\text{Eq. 3})$$

By setting  $\frac{\partial P(F)}{\partial F} = 0$ , one can determine the maximum of the density function. The corresponding force of the maximum is given by the rupture force  $F_{rup}$ :

$$F_{rup} = \frac{k_B T}{x_\beta} \ln\left(\frac{x_\beta}{k_{off}^0 k_B T}\right) + \frac{k_B T}{x_\beta} \ln(r_f) \quad (\text{Eq. 4})$$

So, according to the Bell model, the mean rupture force is a function of the loading rate  $r_f$  and the Bell parameters  $x_\beta$  and  $k_{off}^0$ . Equation 4 implies that the relation between the rupture force  $F_{rup}$  and the natural logarithm of the loading rate  $r_f$  is linear. The

### Box 3: Loading rate

The loading rate during an experiment is dependent on both the elasticity of the system and the speed at which the cantilever is retracted.<sup>35</sup> The loading rate  $r_f$  (rate of force building up in time) is varied by pulling the molecules apart at different cantilever retraction speeds. These speeds are adjusted by varying the scan rate of the AFM, but leaving the traveled distance of the cantilever constant. The retraction speed  $v_c$  is then the scan frequency multiplied by the traveled distance  $x_{cant}$ . To convert the retraction speed to loading rate, we must determine the effective force constant (the elasticity) of the system. This effective force constant consists of the following elastic parts: the cantilever, the bead or cell (actually the filament to which the investigated molecule is coupled) and the bond examined (Fig. B2). The force constants of these elements are different but at the moment the probed bond is fully stretched, rupture of the bond takes place at the weakest link, which in general is the investigated interaction. The effective spring constant is determined by measuring the slope just before a single rupture event in the retract trace. Finally, this slope relates the effective spring constant to the cantilever's spring constant and the loading rate is then defined by the product of the effective spring constant and the retraction speed:  $r_f = k_{eff} \times v_c$ .

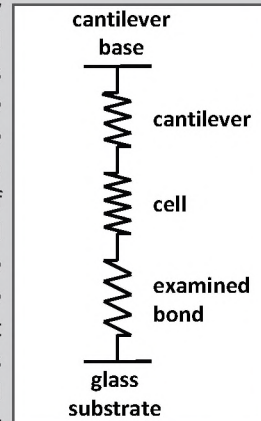
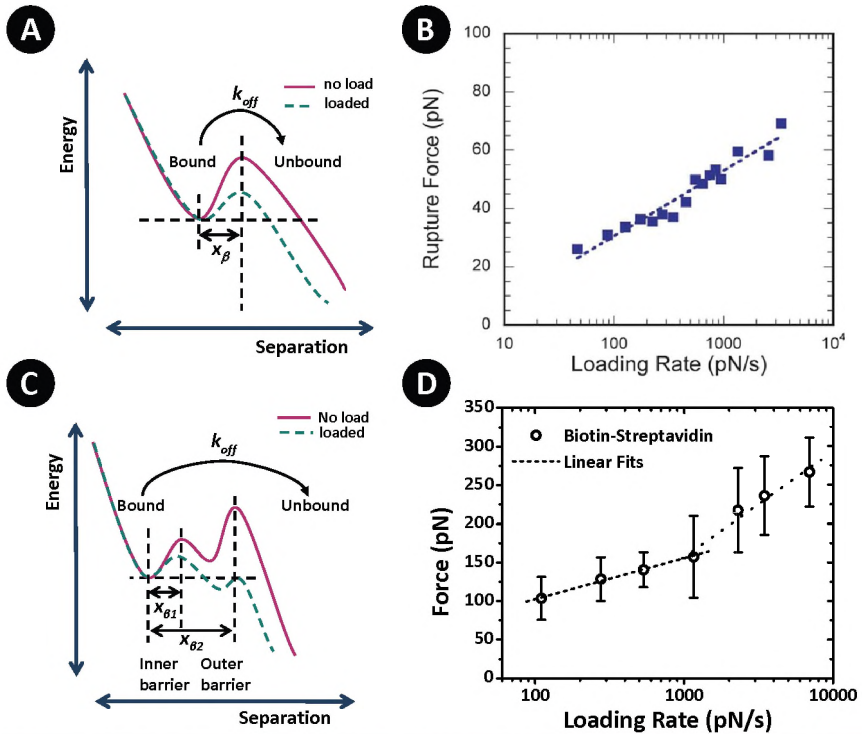


Figure B2: Spring model of the probing system. The effective spring constant of the system  $k_{eff}$  is the result of a series of springs: the examined bond, the cell, and the cantilever.



**Figure 3: The Bell parameters define both the energy diagram and force spectrum**

(A) Energy diagram representing the Bell parameters  $k_{off}$  and  $x_{\beta}$  in terms of the energy barrier between the bound and unbound state. The height of the energy well is the energy needed to unbind and is defined by  $k_{off}$ . Subsequently,  $x_{\beta}$  describes the width of the potential well. By applying external forces on the bond the energy well lowers, shown by the solid and dotted lines. (B) An example of a single barrier force spectrum. The mean rupture forces are dependent on the loading rate. The data points in the semilogarithmic plot are linearly fitted by the Bell model, in which the linear slope determines  $x_{\beta}$  and the intercept with the y-axis  $k_{off}^0$ . (C) Energy diagram of a double barrier. The widths of the inner- and outer barrier of the potential well are described by  $x_{\beta 1}$  and  $x_{\beta 2}$ , respectively. Upon applying an external load the energy wells are lowered, shown by the solid and dotted lines. At some load the inner barrier becomes higher than the outer barrier and will describe the  $k_{off}$  of the system. (D) In the force spectrum this results in two different regimes of which the lower loading rate regime describes the outer barrier and the higher loading rate regime the inner barrier. These type of force spectrum is a double barrier one. (Example depicts the force spectrum of a biotin-streptavidin interaction).

mean rupture force is found by plotting rupture forces of many force measurements in a histogram. The observed statistical distribution of the data depicts the distribution described by Eq. 3. The determination of the mean rupture forces as function of the loading rate (pN/s) provides the main data for force spectroscopy measurements. A graph plotting the mean rupture force versus the loading rate is known as the *force spectrum* (Fig. 3B, D).

In these force spectra, rupture forces obtained at high loading rates are corrected for drag, as the cantilever response is dampened by the liquid (see Box 4). Fitting these data with Eq. 4 yields the Bell parameters  $x_{\beta}$  and  $k_{off}^0$ . These parameters are characteristic for each type of interaction. Therefore, the Bell parameters can be used to compare the different dynamical properties of biological ligand-receptor complexes, as will be demonstrated in Chapters 4 and 5.

### Box 4: Hydrodynamic drag

When a cantilever passes through a medium, especially in liquid, it will experience a certain hydrodynamic force when displacing the medium. This force is called drag. At fast cantilever retraction speeds in an aqueous solution ( $>1 \mu\text{m/s}$ ), the hydrodynamic drag on the cantilever becomes substantial. The rupture forces obtained appear smaller than the actual unbinding forces of the ligand-receptor complexes. Thus, for AFM force spectroscopy these rupture forces should be corrected.<sup>44</sup>

To correct for the drag exerted on the cantilever, the damping coefficient of the cantilever  $\xi$  has to be determined.<sup>†</sup> This coefficient is measured by moving the cantilever through a medium with a constant velocity. Generally, these measurements should be performed at conditions that the cantilever moves through the medium under laminar flow (Reynolds number  $\ll 1$ ). Then, Stokes' law provides a measure of the distributed load due to fluid flow acting on the cantilever:<sup>45</sup>

$$F_{\text{drag}} = s\eta va = \xi \cdot v \quad (\text{Eq. 5})$$

where  $F_{\text{drag}}$  is the uniformly distributed drag force,  $s$  is a shape-related factor and  $a$  the length of the cantilever,  $\eta$  is the viscosity of the fluid, and  $v$  the flow speed. As  $s$ ,  $a$  and  $\eta$  are constant at these conditions, drag is proportional to the speed of the cantilever moving through the fluid. However,  $s$  depends on the distance from the surface. Therefore, the hydrodynamic drag is determined by moving the cantilever freely in medium, very close to the surface, at different speeds, and finally measuring the difference between trace and retrace (Fig. B3A).<sup>45</sup> The observed difference in deflection is a measure for the hydrodynamic force on the cantilever that acts in the opposite direction of the cantilever's movement and has a magnitude that is proportional to the cantilever's speed. The damping coefficient  $\xi$  is found by linearly fitting the plot of hydrodynamic force versus speed, where  $\xi$  is the slope. In Fig. B3B, I show the determination of this coefficient for the B-, C- and D-type cantilevers of

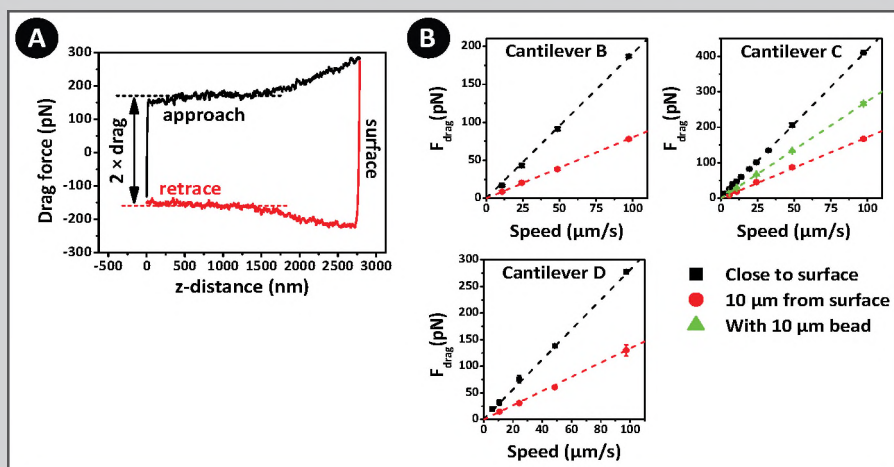


**Figure B3: Drag force determination.** (A) Drag force versus the z-distance of the piezo which traveled over  $2.8 \mu\text{m}$ . The drag force encountered is half of the difference between the approach and retrace curves in the hysteresis loop. (B) The found drag force is dependent on the speed, the distance from the substrate, and the type of cantilever. Drag forces were measured for different cantilevers (B-, C- and D-type) at different distances from the surface. The drag depends linearly on the speed. The drag coefficient  $\xi$  is the slope in these curves.

Cantilever and condition	$\xi$ (pN·s/ $\mu$ m)	Shape factor (m <sup>2</sup> )
B (close to surface)	1.82	10.3
C (close to surface)	4.05	14.5
D (close to surface)	2.72	14.4
B (10 $\mu$ m distance)	0.80	4.5
C (10 $\mu$ m distance)	1.74	6.2
D (10 $\mu$ m distance)	1.31	6.9
C (10 $\mu$ m bead)	2.76	9.8

**Table B1: Drag factors of B-, C-, and D-type cantilevers.** The drag factor  $\xi$  and shape factor  $s$  as obtained by fitting the data of Fig. B3B with Eq. 5. ‘Close to surface’ means that the drag is measured by moving the cantilever over a range of 0-2.8  $\mu$ m from the surface; ‘10  $\mu$ m distance’ moving the cantilever over a range of 10-12.8  $\mu$ m; and ‘10  $\mu$ m bead’ a C-type cantilever with a 10  $\mu$ m latex bead glued underneath the end of the cantilever, that is moved over a range of 0-2.8  $\mu$ m. If all ranges are corrected for the distance from the cantilevers lower surface (excluding the tip’s length of 3  $\mu$ m) they are 3-5.8  $\mu$ m, 13-15.8  $\mu$ m and 10-12.8  $\mu$ m, respectively, for the cases described above.

an MLCT/MSCT-chip (Veeco), which are the type of cantilevers used throughout the studies described in this thesis. It should be noted that the Reynolds number is always lower than 1 ( $Re < 0.04$  at 100  $\mu$ m/s), implying that measurements are performed in a laminar flow. In the Table B1 below, the measured  $\xi$  and  $s$  are given. The  $\xi$  decreases upon moving the cantilever further away from the surface. In addition, the  $\xi$ ’s are cantilever size dependent and reflect the differences in plan view areas of the cantilevers ( $C > D > B$ ;  $Area[B] \approx \frac{1}{2} \times Area[D] \approx \frac{1}{3} \times Area[C]$ ). The shape factors of the rectangular cantilever B compared to the V-shaped cantilevers C & D display a 1:1.4 relation.

Finally, the damping coefficients  $\xi$  measured by us are nearly the same as the only factor described in literature of  $\sim 2$  pN·s/ $\mu$ m, which is the  $\xi$  of a C-type cantilever bearing a cell.<sup>46, 47</sup> In summary, the unbinding forces plotted in a force spectrum are corrected for the drag by taking the sum of the measured force and the hydrodynamic force calculated by  $\xi \times v$ .

<sup>†</sup> Note that the quality factor  $Q$  of a cantilever in fluid, which describes the state of damping, is related to the damping coefficient via  $\xi = k/(2\pi f_R Q)$  (with  $k$  spring constant and  $f_R$  resonance frequency). However, it is only valid under laminar flow conditions ( $Re < 1$ ), whereas during the  $Q$  factor determination the flow is turbulent ( $Re > 1$ ).

## Micro- and nanopatterns for biological applications

Micro- and nanofabrication techniques have revolutionized the development of diagnostic devices, which are applied in the pharmaceutical and medical fields, including novel drug delivery systems, microelectronics and biosensors.<sup>48</sup> These techniques were initially developed for applications in the semiconductor industry; later it also became interesting to study chemical, biological, and physical processes at the molecular and cellular scale.<sup>48</sup>

Important micro- and nanofabrication techniques are photolithography, soft lithography film deposition, electron beam lithography (EBL), and SPM based lithography (SPL).<sup>48, 49</sup> Photolithography is used to transfer a user-generated shape onto a material through the selective exposure of a light sensitive polymer. Soft lithography encompasses three different techniques that are all based on the generation and utilization of the mold of a microstructure made of polydimethylsiloxane (PDMS). Film deposition, as the name suggests, is the formation of micron-thick films on the surface of a substrate subsequent etching selectively removes material from the surface of the microdevice by either chemical or physical processes. Electron beam lithography has many similarities to photolithography only instead of light, electrons are used to transfer patterns, with this technique nanopatterns can be created. In Chapter 2, I will discuss a study exploiting nanopatterns created with EBL.

SPLs offer both ultrahigh resolution and *in situ* imaging capabilities, and as such, these techniques are actively used as nanofabrication tools.<sup>50</sup> Most SPL techniques rely on the elimination or modification (through oxidation, etching, shaving, or grafting) of a passivating layer and subsequent adsorption of the patterning material from solution.<sup>50</sup> In Chapters 6-8, I will demonstrate the use of nanografting in creating nanopatterns. Another technique called dip-pen nanolithography (DPN) uses the opposite approach: an 'ink'-coated AFM tip is used to write a pattern on a surface of which the 'background' layer is passivated afterwards.<sup>49</sup>

Finally, micro- and nanopatterns give cell biologists new opportunities to investigate, for example, the spatial regulation of cellular processes. Modification of these patterns chemically, e.g. stamping adhesive materials, as well as physically, e.g. making 3D patterns, makes it possible to study how the cell responds (Fig. 4).<sup>51, 52</sup> Subsequently, by

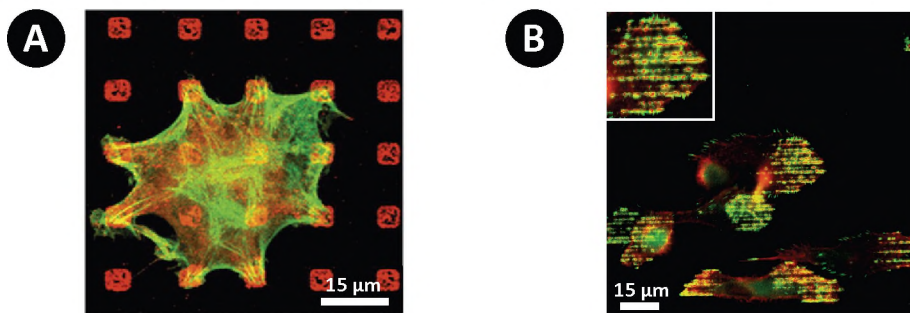


**Figure 4: Examples of micropatterned substrate for adhesion studies**

(A) A B16 cell spreads on a  $9 \mu\text{m}^2$  dotted fibronectin pattern. On  $15 \mu\text{m}$  distant dots the actin cytoskeleton forms stress fibres between adjacent dots. Cells are labeled for fibronectin (red) and actin (green). Adapted from Lehnert et al., *J. Cell Sci.*, 2004. (B) Dendritic cells adhered on  $2 \mu\text{m}$  sized micropatterns align their podosomes, a type of cell adhesion structure, along the lines of the structure. The podosomes consist of an actin core (red) and a vinculin ring (green). Adapted from Van den Dries, et al., in prep.

providing biocompatible surfaces cell-cell and cell-extracellular matrix (ECM) interactions can be controlled on the micron and submicron scale.<sup>52-54</sup> Combined with fluorescence microscopy and other cell biological approaches, an ever expanding toolbox is becoming available.<sup>55</sup>

## The role of forces in cell adhesion

### The immune system

The main function of the immune system is to protect the human body against harmful pathogens i.e. bacteria, parasites, fungi, and viruses, but also to protect us from uncontrolled cellular processes like cancer. The immune system can respond to these potential dangers in two distinct ways. First, by an innate immune response which forms a non-specific line of defense against invading pathogens by for example anti-viral interferon responses or phagocytosis. The second more specific line of defense is formed by the adaptive immune response, which is orchestrated by professional antigen presenting cells as dendritic cells (DCs) (Fig. 5). DCs have the unique ability to recognize, take up and process pathogens into antigenic peptides. Pattern recognition receptors (PRRs) are expressed by DCs to recognize 'danger' via specific pathogen-associated molecular patterns (PAMPs). These PRRs have a preference for a given set of PAMPs. Important players are Toll-like receptors (TLRs) and C-type lectins (CLRs), which bind to e.g. specific lipids, proteins and carbohydrates of pathogens.<sup>56, 57</sup> After binding and recognition, these pathogens are taken up by the DC and subsequently processed into small pieces. Peptides derived from this process are presented on the outside of the cell as so-called antigens. Simultaneously, these DCs undergo maturation and migrate

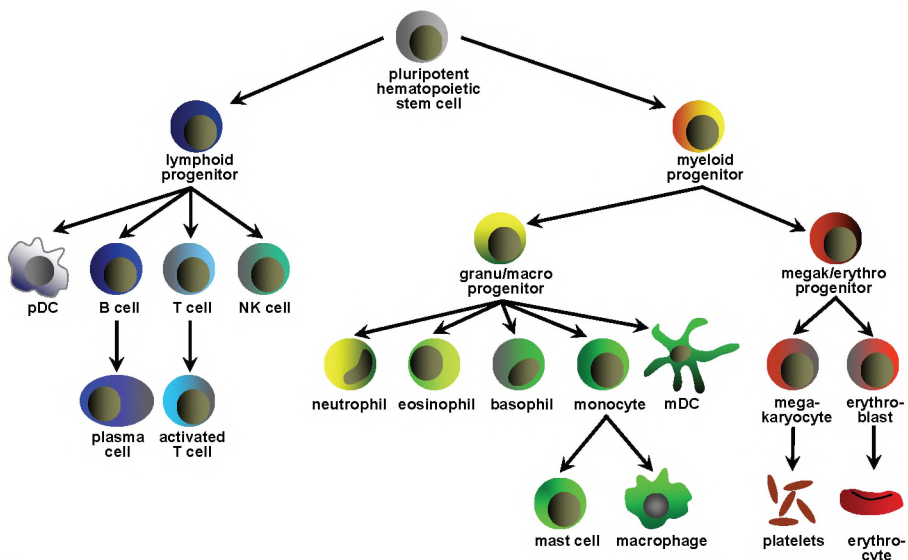


**Figure 5: Hematopoietic cell lineage**

The pluripotent hematopoietic stem cell gives rise to the progenitor cells of the lymphoid and myeloid cell lineage. The first gives rise to the plasmacytoid dendritic cell (pDC), B-, T-, and natural killer (NK) cells. The second progenitor gives rise to the neutro-, eosino-, and basophils, myeloid dendritic cells (mDC), mast cells and macrophages on the one side, on the other side the platelets and erythrocytes (red blood cells). The cells from the lymphoid cell lineage as well as the cells originated from the granulocyto/macrophage progenitor form together the leukocytes (white blood cells). The lymphocyte subset includes the B-, T- and NK cells.

to lymph nodes, where they present the antigens to resting T and B cells. During these cell-cell contacts in the lymph nodes, information is transferred between the cells, and a specific set of T cells are instructed by the DCs to remove the invaders. At the same time, DCs instruct B cells to start producing pathogen-specific antibodies (Abs). These Abs are newly produced within approximately 10 days; however, upon a second encounter with the same pathogen, memory B cells are present and antibody production occurs much faster (within  $\pm 3$  days). This activation of Ab production and the proliferation of activated killer T cells upon DC-T cell interaction both belong to the pathogen-specific adaptive immune response. All these immunological cell-cell contacts are very dynamical and involve the binding and breakage of many ligand-receptor bonds to communicate and migrate. Therefore, cells express proteins that regulate those processes.

## Cell adhesion molecules

The ability of cells to form stable contacts with one another, and with the extracellular matrix, is of vital importance for the proper functioning of a multicellular organism. Examples include the organization of tissues and organs, but also in the nervous- and immune system, cell-cell contacts are essential for proper transfer of information. Cell adhesion plays a crucial role in the formation of these cell-cell contacts, and cell adhesive properties are regulated via specific cell adhesion molecules (CAMs). CAMs are typically transmembrane molecules present at the plasma membrane and they can be divided into four major families: (se)lectins, integrins, the immunoglobulin superfamily of cell adhesion molecules (Ig-CAMs), and cadherins. CAMs bind homotypically or heterotypically to other CAMs or ligands, as proteins and sugars (Fig. 6). Besides, cell adhesion mediated by (se)lectins, integrins, and cadherins can be  $\text{Ca}^{2+}$ - or  $\text{Mg}^{2+}$ -dependent.

### Selectins and lectins

The first family of CAMs consists of lectins and the closely related selectins all binding specifically to carbohydrate moieties. They typically play a role in biological recognition phenomena, such as the specific binding of microorganisms onto the host cell. This is especially true for the afore-mentioned C-type lectins. The selectins, on the other hand, are important to help leukocytes that are attracted to a site of infection to pass through the wall of blood vessels. This process is known as trans-endothelial migration (Fig. 7). Stimuli, such as histamine, released at the infection site induce upregulation of selectins at the cell membrane of endothelial cells in surrounding blood vessels. When leukocytes flow along the wall of these blood vessels, the selectins expressed by endothelial cells bind to certain carbohydrate moieties presented at the cell surface of these leukocytes. This causes the leukocytes to slow down and start rolling along the endothelial cell surface. This phenomenon involves high shear forces applied on single molecules. By AFM force spectroscopy, the binding of the three main members of the selectin family, L-selectin, E-selectin and P-selectin was investigated by studying their binding to the specific ligands PSGL-1<sup>58, 59</sup> and sialyl-LewisX (sLeX).<sup>23</sup> They revealed that L-selectin-PSGL-1 bonds were weaker than either E- or P-selectin bonds, which explains the faster L-selectin-mediated rolling.<sup>58</sup> Besides, it was found that the binding of selectin/sLeX is governed by two distinct sLeX-carbohydrate binding epitopes. One is attributed to the inner barrier and one to the outer barrier of the energy diagram (Fig. 3C).<sup>23</sup>

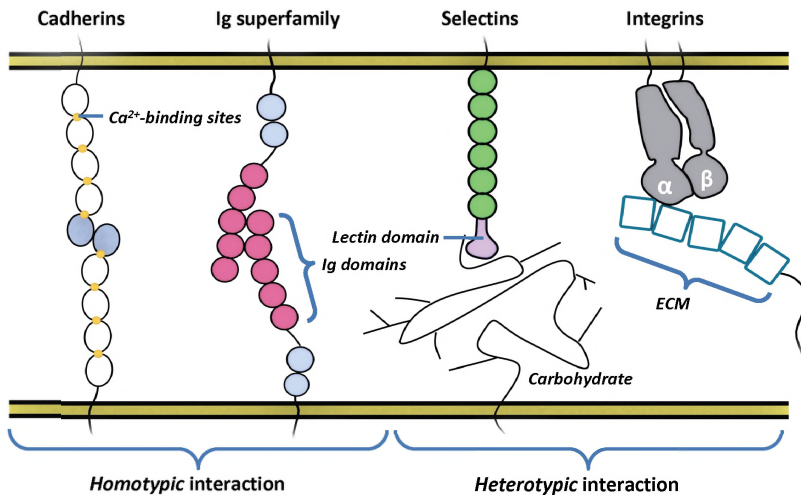


**Figure 6: The four families of cell adhesion molecules (CAMs)**

Model interactions of the cadherins, the immunoglobulin (Ig) superfamily having diverse binding partners, the (se)lectins binding to carbohydrate domains, and the heterodimeric ( $\alpha$  and  $\beta$ ) integrins.

### Integrins

The second family of CAMs is represented by the integrins, which mediate the adhesion of cells to the extracellular matrix (ECM) and to one another. They are important for the mechanics of cell adhesion and migration, and for the propagation of various cell signals.<sup>60</sup> The integrin molecule is a heterodimer of an  $\alpha$  and  $\beta$  transmembrane glycoprotein subunit. Specific  $\alpha_n\beta_m$  subunit combinations define ligand binding activities and various signaling functions. An example of a thoroughly studied integrin is the lymphocyte function associated antigen-1 (LFA-1 or  $\alpha_L\beta_2$ ), expressed by all leukocytes.<sup>61</sup> LFA-1 gets activated by chemokines during the rolling process of a leukocyte on the endothelial cells (Fig. 7). After the initial capture by the selectins, LFA-1 forms more stable adhesions by binding to intercellular adhesion molecule-1 (ICAM-1) on endothelial cells. The stable adhesion implies that LFA-1 molecules have to endure strong forces to keep the cell attached to the endothelium. Force spectroscopy has also been used to study the LFA-1/ICAM-1 bond,<sup>22, 62</sup> but also other integrin ligand-receptor interactions were studied, like the  $\alpha_5\beta_1$ /fibronectin bond, involved in binding to the ECM,<sup>63</sup> and the  $\alpha_4\beta_1$ /vascular cell adhesion molecule-1 (VCAM-1) bond, also playing a crucial role in both the rolling and firm attachment of leukocytes onto the endothelium.<sup>64</sup> Amongst other things, it was found in those studies that after activation of the integrins the affinity changes reflected by biophysical changes in the force spectrum. Also in some cases, the energy diagram can be described with a single-barrier (Fig. 3A) before activation of the integrin and after activation by a double-barrier energy potential (Fig. 3C).

### Immunoglobulin superfamily

The third family of CAMs consists of molecules bearing an Ig domain and therefore belonging to the immunoglobulin superfamily (IgSF). The above-mentioned molecules ICAM and VCAM as well as more than 100 other CAMs belong to this large IgSF. They function as cell adhesion and signaling receptors that transduce extracellular signals from other cells or the ECM to the intracellular signaling machinery.<sup>65</sup> In contrast to other



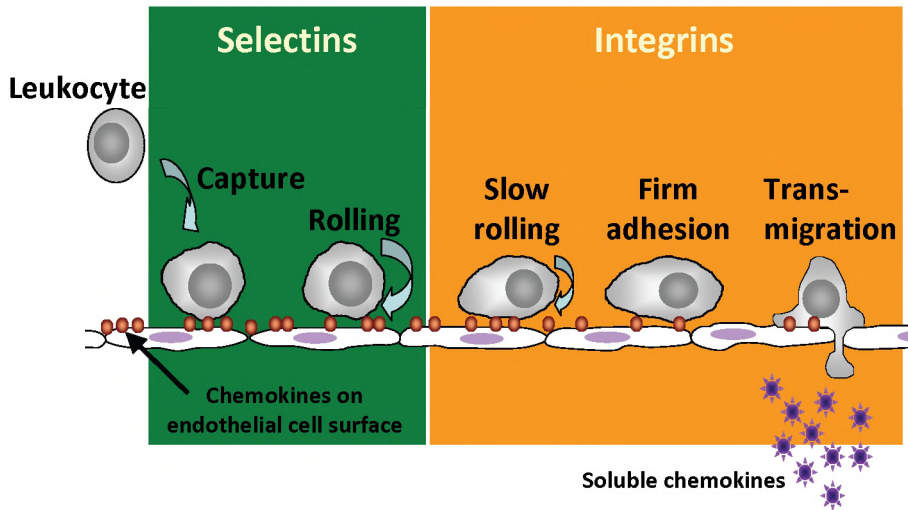


**Figure 7: Trans-endothelial migration**

When leukocytes enter a site of infection from the blood, they get attracted by chemokines bound to the endothelial cell surface. The cells get captured by binding of selectins on the leukocyte to carbohydrates expressed by the endothelial cells. They start rolling and the chemokines activate the leukocyte to slow down and start to adhere firmly by the binding of integrins to other CAMs expressed by the endothelial cells. Finally, the activated leukocyte starts to transmigrate across the endothelium to further migrate to the site of infection by sensing soluble chemokines.

CAMs, members of the IgSF do not require  $\text{Ca}^{2+}$  for cell-cell adhesion interactions. Besides, they can form homotypic bonds as well as heterotypic bonds. Examples of IgSF members studied with force spectroscopy are the earlier described heterotypic interactions of ICAM-1/LFA-1<sup>22, 62</sup> and VCAM-1/ $\alpha_v\beta_1$ .<sup>64</sup> An example of a homotypic interaction is that of ALCAM-ALCAM (activated leukocyte cell adhesion molecule) which will be discussed in Chapter 4.

### Cadherins

Finally, the family of cadherins are all  $\text{Ca}^{2+}$ -dependent cell adhesion molecules. Cadherins play an important role in tissue architecture and form stable junctions between cells in various tissues, and due to their homotypic binding mediate cell sorting of similar cells into specific tissue structures.<sup>66</sup> The stability of cell contacts formed was investigated by force spectroscopy in the case of many cadherins, for example the classical cadherins E- and N-cadherin which are involved in epithelial and neural tissue architecture.<sup>67</sup> In this study, it was found that E- and N-cadherin have significantly different kinetic and micromechanical properties which are reflected by a single- versus a double-barrier energy potential (Fig. 3).

### Adhesion regulation: affinity versus avidity

Cell adhesion is the result of many different interactions between CAMs and must be tightly regulated. For example, leukocytes have a dual function in the immune system that requires them to circulate throughout the body as non-adherent cells and become adherent whenever they transmigrate across the vascular endothelium at sites of inflammation, encounter other leukocytes in the lymph nodes, or act as pathogen eliminating cells. This 'on-off' adhesion behavior of leukocytes is controlled by the

activity of CAM receptors on the cell surface. There are in general three ways in which cells regulate their adhesive properties (Fig. 8A):

- Enhanced or decreased expression levels of the CAMs (density variation on cell surface)
- Activation of the CAMs (changes in molecular conformation, also known as affinity)
- Clustering of the CAMs (cooperation/valency change, also known as avidity)

The actual molecular mechanisms regulating cell adhesion are incredibly complex and involve an ever growing list of adaptor and regulatory molecules.<sup>68</sup> However, often the actin cytoskeleton plays an important role in these processes.<sup>69-71</sup> The actin cytoskeleton is a biopolymer framework of actin that provides rigidity to the cell and serves as binding-backbone for biomolecules and organelles of the cell. Coupling to the cytoskeleton makes it also possible for the cell to influence CAM density and mobility at the plasma membrane.

CAM density and mobility are thought to play a role in the regulation of adhesion through the mechanism of avidity. While affinity generally refers to the binding-potential of an individual receptor-ligand complex and involves basic molecular properties, avidity refers to the overall strength of cellular adhesive interactions resulting from a combination of both the affinity of individual bonds and the total number of bonds formed, i.e. the “valency” of the interaction.<sup>72-74</sup> The best studied example of affinity-avidity regulation is the LFA-1/ICAM-1 bond (Fig. 8B). LFA-1 can regulate its affinity by altering its conformation from an inactive form to an active form and its avidity by clustering of different LFA-1 molecules on the cell membrane.<sup>74, 75</sup>

### Examples of adhesion regulation: ALCAM and DC-SIGN

**ALCAM** In our laboratory a CAM extensively studied is the activated leukocyte cell adhesion molecule (ALCAM) belonging to the IgSF. The homotypic ALCAM-ALCAM interaction is implicated in metastatic progression of different types of cancer.<sup>76-79</sup> The heterotypic interaction of ALCAM with CD6, an adhesion molecule belonging to the scavenger receptor superfamily, seems to play a role in the interaction between

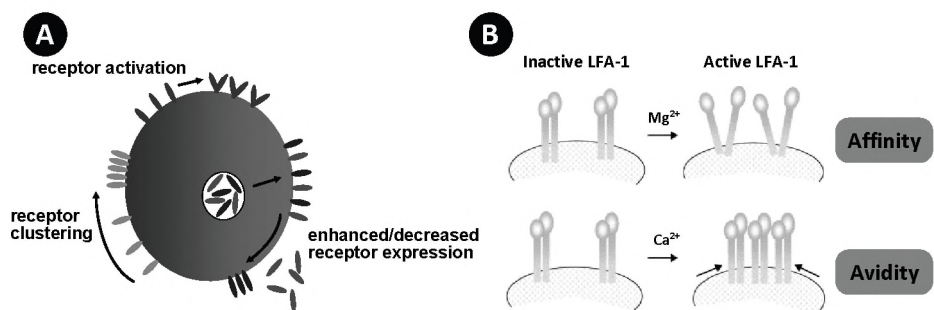


**Figure 8: Adhesion regulation**

(A) The cellular adhesion mechanism. (B) Alterations in affinity and avidity regulate LFA-1 mediated adhesion. Binding of LFA-1 to its ligand ICAM-1 is regulated by two distinct mechanisms.  $Mg^{2+}$ -dependent conformational changes may induce an alteration in the conformation of LFA-1, leading to increased binding affinity.  $Ca^{2+}$ -dependent multimerization of LFA-1 alters integrin avidity, leading to release of cytoskeleton restraints, which facilitates LFA-1 redistribution in the cell membrane. Adapted from Van Kooyk and Figdor, 2000, *Curr. Opin. Cell Biol.*<sup>74</sup>

a DC and a T cell at the formation of the immunological synapse.<sup>80</sup> ALCAM-mediated adhesion is dynamically regulated through the actin cytoskeleton.<sup>81</sup> Release from the actin cytoskeleton enhances mobility of the molecules and results in the formation of high avidity clusters of ALCAM molecules on the cell surface.<sup>81,82</sup> The different aspects of ALCAM affinity and avidity regulation will be further discussed in Chapter 4.

**DC-SIGN** The dendritic cell-specific intercellular adhesion molecule-3 (ICAM-3) grabbing non-integrin (DC-SIGN) is a C-type lectin receptor expressed by DCs and certain macrophages that binds a broad range of ligands including pathogen-derived ligands such as the human immunodeficiency virus-1 (HIV-1), *Candida albicans*, and *Mycobacterium tuberculosis*, but also endogenous ligands like ICAM-2 and ICAM-3.<sup>83-86</sup> DC-SIGN binds to these pathogens specifically by the use of its carbohydrate recognition domain (CRD) (Fig. 9A). The binding of DC-SIGN to specific pathogens is regulated by the (nano)organization of the molecules on the cell membrane (Fig. 9B).<sup>87</sup> For example, the binding of (small) HIV-1 virus particles onto immature DCs (imDCs) is only possible when DC-SIGN has formed nanoclusters with a size of 50-200 nm on the cell membrane.<sup>87</sup> By forming nanoclusters of DC-SIGN imDCs regulate their avidity to bind small nano-sized pathogens. The interaction of DC-SIGN with *Candida albicans* will be discussed in detail in Chapter 5.

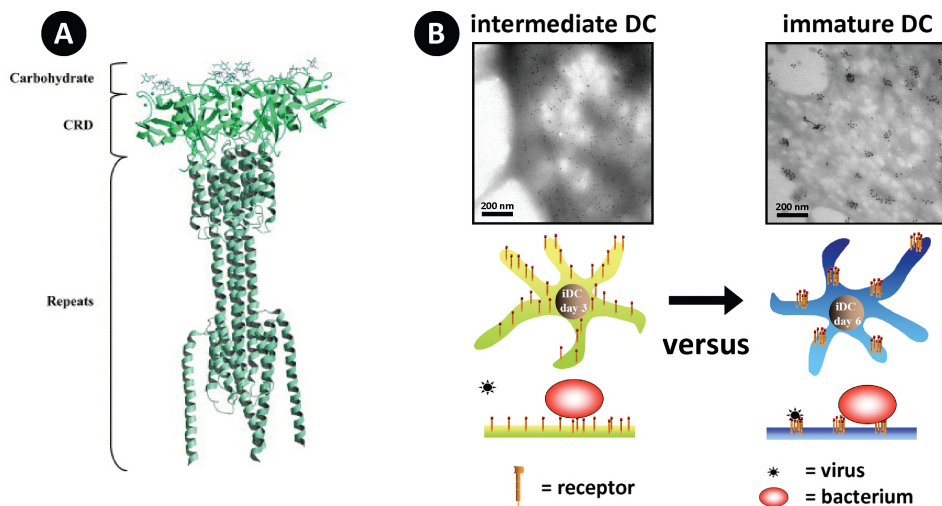


**Figure 9: DC-SIGN structure and organization**

(A) Protein structure of the outer-membrane DC-SIGN tetramer containing a repeat region, carbohydrate recognition domain (CRD) and bound carbohydrates. DC-SIGN binds to many different ligands, aside from ICAM-2, -3, macrophage-1 antigen (Mac-1), and carcinoembryonic antigen-related cell adhesion molecule-1 (CEACAM-1). Furthermore, it binds to different pathogenic carbohydrates of viruses as HIV, Ebola, Hepatitis C, and Dengue; bacteria as *Mycobacterium tuberculosis*; parasites as *Leishmania*; and fungi as *Candida albicans*. Adapted from Snyder et al., *J. Mol. Biol.*, 2005.<sup>88</sup> (B) The binding of small pathogens such as viruses depends critically on the organization of DC-SIGN on the membrane. Nanoclusters of DC-SIGN, which can only be seen on fully 'matured' immature DCs (day 6) and not on intermediate DCs (day 3), are important for the binding of small pathogens, the binding of larger pathogens is independent of this clustering. On DCs these nanoclusters are observed by TEM as 50-200 nm sized clusters of gold beads, that have been used to label the DC-SIGN molecules. Adapted from Cambi et al., *J. Cell Biol.*, 2004.<sup>83</sup>

## *Techniques to study cell adhesion regulation*

Several different methods have been developed to investigate ligand-receptor interactions. Cell adhesion assays using flow cytometry employing either fluorescent beads coated with purified ligand molecules, or fluorescently labeled ligand molecules provide a measure for the affinity of the binding of a ligand to a receptor.<sup>89,90</sup> With Surface Plasmon Resonance (SPR) based biosensors, the affinity is directly measured in terms of  $K_d$  values (dissociation constant).<sup>91, 92</sup> To study the overall adhesion of living cells to a substrate, plate adhesion assays can be used.<sup>82</sup> Another method to study the mobility of cells is a migration assay.<sup>93</sup> The modulation of avidity by the cell can be studied using high resolution imaging techniques visualizing dynamic CAM clustering. Besides confocal laser scanning microscopy (CLSM),<sup>94</sup> techniques like Fluorescence Resonance Energy Transfer (FRET),<sup>72, 73, 95</sup> Transmission Electron Microscopy (TEM),<sup>83, 96</sup> and Near-field Scanning Optical Microscopy (NSOM)<sup>97,98</sup> are applied. Fluorescence recovery after photobleaching (FRAP)<sup>73</sup> and Single Particle Tracking<sup>81,99</sup> have been used to study the diffusive properties of the CAMs in response to stimuli. When combining the afore-described approaches, the obtained data can be correlated to study affinity and avidity modulation.<sup>73, 83</sup>

Although the above-mentioned biochemical analyses of CAM binding properties remain an essential part of CAM interaction studies, they cannot provide information about the influence of internal and external forces to which adhesion receptors in the plasma membrane are constantly exposed. For example during cell migration, traction forces are generated inside the cell that are applied to the integrin/matrix-component linkage. The shear stress due to the blood-flow during selectin-mediated leukocyte rolling and subsequent transmigration across activated endothelium provides another example (Fig. 7). Spinning disk assays and dynamic flow chambers were used to study shear stress and yielded the first clues on how CAMs mechanically deal with stress.<sup>100</sup> The shear force that is exerted on the cells in these assays depends on parameters such as cell size, cell shape, and on how the cell is attached to the substrate. Therefore, the forces can only be estimated rather than exactly measured.<sup>101</sup> For a more controlled and quantitative approach to measure cell adhesion strength and downstream effects of this mechanical stimulation, single-cell methods are needed.

Several types of single-cell force assays are available to measure the strength of cell adhesion down to the single-molecule level. A method that mimics the interaction of two cells by bringing two lipid membranes close to each other and measure the interaction forces is the surface force apparatus (SFA).<sup>102, 103</sup> Three other assays for probing on living cells have been described. They all exploit optical microscopes to observe cells while force measurements are done, but differ in how cells are manipulated and forces are determined. Two methods use a micropipette to grasp and hold cells, and measure detachment forces using another micropipette, the bio-membrane force probe (BFP),<sup>38</sup> or use an optical laser trap (OT) to manipulate the second cell.<sup>99, 104-106</sup> The last technique is the earlier described single-cell force spectroscopy (SCFS) in which a cell-bearing AFM cantilever is exploited to assess cellular interactions with a functionalized surface, tissue or on another cell.<sup>34, 107-108</sup> Here, the deflection of the cantilever is used to measure interaction forces. Clearly, SCFS allows for the widest force range comprising the full force range encountered by cells. The possibility to probe the mechanics of CAM interactions on the surface of living cells with single-molecule sensitivity is expected to be of great value in studies on cell adhesion regulation. In this thesis, I focus on the use of AFM in measuring ligand-receptor interactions.

## *Aim and outline of this thesis*

**T**he Aim of this thesis was to explore the versatility of the AFM in the context of biomaterial science, surface chemistry and cell biology. The high precision and resolution of this technique were exploited to manipulate and measure at the nanometer and picoNewton scale. The AFM was used to image micro- and nanostructures that are applied in cell adhesive studies. In a different setting, the AFM was used to manipulate and, later on, to probe nanopatterns up to the atomic scale by a technique called nanografting. The high force sensitivity of the AFM was applied to measure adhesive properties of CAMs on a cell by addressing their affinity and avidity. Furthermore, the binding of pathogens to PRR receptors was studied, addressing affinity and spatial organization of the receptors on the cell membrane.

In **Chapter 2**, the high resolution of the AFM is exploited to image substrates relevant for biological applications in biomaterial sciences. The AFM's strength is shown by imaging micro- and nano-patterns with high accuracy and by its excellent molecular resolution on bio-molecules. Furthermore, this chapter illustrates the essence of AFM as a tool to investigate patterns intended for biological studies on adhesive behavior, cell signaling, and tissue embedding.

**Chapter 3** describes a uniform calibration method for AFM cantilevers, which is required for quantitative force measurements. By performing an interlaboratory round robin study, cantilever spring constant calibration methods are compared on different AFMs in different groups. The findings resulted in a fast and improved standard protocol to obtain reliable spring constants for different types of cantilevers.

**Chapter 4** describes the potential of AFM force spectroscopy on unraveling the influence of affinity versus avidity on the homo- and heterotypic ALCAM-mediated interactions. This leads to a better insight in the biological function of ALCAM based on its kinetic and mechanical properties. In **Chapter 5** AFM force spectroscopy is used to study the interaction of the pathogen receptor DC-SIGN with the fungus *Candida albicans*. The interaction of this C-type lectin, which specifically binds to carbohydrate epitopes of the fungus, is studied at the single molecule level and compared to other receptor-carbohydrate interactions.

**Chapter 6** describes the possibilities of nanografting to generate protein patterns of DC-SIGN and ALCAM to address the contribution of nano- and micro-clustering of CAMs on adhesion. We report on the immobilization strategy for His-tagged DC-SIGN and ALCAM on a SAM of NTA-terminated thiols. On this platform, proteins can be specifically bound and oriented. In **Chapter 7**, we show the nanografting of patterns within a self-assembled monolayer by AFM. The high accuracy of the AFM is demonstrated by measuring the topography with subnanometer resolution and by quantifying the molecular friction of these patterns. With AFM friction measurements different chemical endgroups can be recognized, as the endgroups possess specific friction 'signatures'. Furthermore, an interesting observation was that on layers consisting of thiols with acid- and amine-endgroups double layers are formed, that are stabilized via (non-covalent) hydrogen bonds between their COOH- or NH<sub>2</sub>-groups. These findings are described in **Chapter 8**.

Finally in **Chapter 9**, the results and significance of the findings described in this thesis are discussed. The future application and direction of nano- and micropatterning for cell biology and biomaterials are discussed. Furthermore, the results on the derived

dynamic Bell parameters of force spectroscopy studies, like those in Chapters 4 and 5, will be discussed in relation to other studies on CAMs and PRRs.

## References

1. **G. Binnig, H. Rohrer** (2000). Scanning tunneling microscopy (Reprinted from IBM Journal of Research and development, vol 30, 1986). *IBM Journal of Research and Development*, **44**, 279-293.
2. **G. Binnig, C. F. Quate, C. Gerber** (1986). Atomic force microscope. *Phys. Rev. Lett.*, **56**, 930-933.
3. **C. A. Putman, K. O. van der Werf, B. G. de Grooth, N. F. van Hulst, J. Greve, P. K. Hansma** (1992). New imaging mode in atomic-force microscopy based on the error signal. *Proc. SPIE*, **1639**, 198-204.
4. **S. Bahatyrova, R. N. Frese, C. A. Siebert, J. D. Olsen, K. O. Van Der Werf, R. Van Grondelle, R. A. Niederman, P. A. Bullough, C. Otto, C. N. Hunter** (2004). The native architecture of a photosynthetic membrane. *Nature*, **430**, 1058-1062.
5. **D. Ricci, P. C. Braga** (2002). Atomic Force Microscopy: Biomedical Methods and Applications. *Methods in Molecular Biology*.
6. **J. Liang, G. Scoles** (2007). Nanografting of alkanethiols by tapping mode atomic force microscopy. *Langmuir*, **23**, 6142-6147.
7. **N. H. Thomson, B. L. Smith, N. Almqvist, L. Schmitt, M. Kashlev, E. T. Kool, P. K. Hansma** (1999). Oriented, active Escherichia coli RNA polymerase: an atomic force microscope study. *Biophys. J.*, **76**, 1024-1033.
8. **K. Wadu-Mesthrige, N. A. Amro, J. C. Garno, S. Cruchon-Dupeyrat, G. Y. Liu** (2001). Contact resonance imaging - a simple approach to improve the resolution of AFM for biological and polymeric materials. *Appl. Surf. Sci.*, **175**, 391-398.
9. **O. Sahin, S. Magonov, C. Su, C. F. Quate, O. Solgaard** (2007). An atomic force microscope tip designed to measure time-varying nanomechanical forces. *Nat. Nanotechnol.*, **2**, 507-514.
10. **Y. Martin, H. K. Wickramasinghe** (1987). Magnetic Imaging by Force Microscopy with 1000-Å Resolution. *Appl. Phys. Lett.*, **50**, 1455-1457.
11. **A. Raab, W. H. Han, D. Badt, S. J. Smith-Gill, S. M. Lindsay, H. Schindler, P. Hinterdorfer** (1999). Antibody recognition imaging by force microscopy. *Nat. Biotechnol.*, **17**, 902-905.
12. **G. U. Lee, D. A. Kidwell, R. J. Colton** (1994). Sensing discrete streptavidin-biotin interactions with AFM. *Langmuir*, **10**, 354-361.
13. **G. U. Lee, L. A. Chrisey, R. J. Colton** (1994). Direct measurement of the forces between complementary strands of DNA. *Science*, **266**, 771-773.
14. **D. J. Muller, J. Helenius, D. Alsteens, Y. F. Dufrene** (2009). Force probing surfaces of living cells to molecular resolution. *Nat. Chem. Biol.*, **5**, 383-390.
15. **D. J. Muller, M. Krieg, D. Alsteens, Y. F. Dufrene** (2009). New frontiers in atomic force microscopy: analyzing interactions from single-molecules to cells. *Curr. Opin. Biotechnol.*, **20**, 4-13.
16. **E. L. Florin, V. T. Moy, H. E. Gaub** (1994). Adhesion forces between individual ligand-receptor pairs. *Science*, **264**, 415-417.
17. **V. T. Moy, E. L. Florin, H. E. Gaub** (1994). Intermolecular forces and energies between ligands and receptors. *Science*, **266**, 257-259.
18. **P. Hinterdorfer, W. Baumgartner, H. J. Gruber, K. Schilcher, H. Schindler** (1996). Detection and localization of individual antibody-antigen recognition events by atomic force microscopy. *Proc. Natl. Acad. Sci. USA*, **93**, 3477-3481.
19. **P. Hinterdorfer, Y. F. Dufrene** (2006). Detection and localization of single molecular recognition events using atomic force microscopy. *Nat. Methods*, **3**, 347-355.
20. **D. J. Muller, Y. F. Dufrene** (2008). Atomic force microscopy as a multifunctional molecular toolbox in nanobiotechnology. *Nat. Nanotechnol.*, **3**, 261-269.
21. **W. Baumgartner, P. Hinterdorfer, W. Ness, A. Raab, D. Vestweber, H. Schindler, D. Drenckhahn** (2000). Cadherin interaction probed by atomic force microscopy. *Proc. Natl. Acad. Sci. USA*, **97**, 4005-4010.
22. **X. Zhang, E. P. Wojcikiewicz, V. T. Moy** (2002). Force spectroscopy of the leukocyte function-associated antigen-1/intercellular adhesion molecule-1 interaction. *Biophys. J.*, **83**, 2270-2279.
23. **X. Zhang, D. F. Bogorin, V. T. Moy** (2004). Molecular basis of the dynamic strength of the sialyl Lewis X-selectin interaction. *ChemPhysChem*, **5**, 175-182.
24. **N. Almqvist, R. Bhatia, G. Primbs, N. Desai, S. Banerjee, R. Lal** (2004). Elasticity and adhesion force mapping reveals real-time clustering of growth factor receptors and associated changes in local cellular rheological properties. *Biophys. J.*, **86**, 1753-1762.

25. G. Pfister, C. M. Stroh, H. Perschinka, M. Kind, M. Knoflach, P. Hinterdorfer, G. Wick (2005). Detection of HSP60 on the membrane surface of stressed human endothelial cells by atomic force and confocal microscopy. *J. Cell Sci.*, **118**, 1587-1594.
26. V. Dupres, F. D. Menozzi, C. Locht, B. H. Clare, N. L. Abbott, S. Cuenot, C. Bompard, D. Raze, Y. F. Dufrene (2005). Nanoscale mapping and functional analysis of individual adhesins on living bacteria. *Nat. Methods*, **2**, 515-520.
27. G. Francius, S. Lebeer, D. Alsteens, L. Wildling, H. J. Gruber, P. Hols, S. De Keersmaecker, J. Vanderleyden, Y. F. Dufrene (2008). Detection, localization, and conformational analysis of single polysaccharide molecules on live bacteria. *ACS Nano*, **2**, 1921-1929.
28. M. I. Giannotti, G. J. Vancso (2007). Interrogation of single synthetic polymer chains and polysaccharides by AFM-based force spectroscopy. *ChemPhysChem*, **8**, 2290-2307.
29. M. Grandbois, M. Beyer, M. Rief, H. Clausen-Schaumann, H. E. Gaub (1999). How strong is a covalent bond? *Science*, **283**, 1727-1730.
30. R. Proksch, T. E. Schaffer, J. P. Cleveland, R. C. Callahan, M. B. Viani (2004). Finite optical spot size and position corrections in thermal spring constant calibration. *Nanotechnology*, **15**, 1344-1350.
31. J. L. Hutter, J. Bechhoefer (1993). Calibration of atomic-force microscope tips. *Rev. Sci. Instrum.*, **64**, 1868-1873.
32. J. E. Sader, J. W. M. Chon, P. Mulvaney (1999). Calibration of rectangular atomic force microscope cantilevers. *Rev. Sci. Instrum.*, **70**, 3967-3969.
33. M. Benoit, D. Gabriel, G. Gerisch, H. E. Gaub (2000). Discrete interactions in cell adhesion measured by single-molecule force spectroscopy. *Nat. Cell Biol.*, **2**, 313-317.
34. J. Helenius, C. P. Heisenberg, H. E. Gaub, D. J. Muller (2008). Single-cell force spectroscopy. *J. Cell Sci.*, **121**, 1785-1791.
35. C. Yuan, A. Chen, P. Kolb, V. T. Moy (2000). Energy landscape of streptavidin-biotin complexes measured by atomic force microscopy. *Biochemistry*, **39**, 10219-10223.
36. G. I. Bell (1978). Models for the specific adhesion of cells to cells. *Science*, **200**, 618-627.
37. E. Evans, K. Ritchie (1997). Dynamic strength of molecular adhesion bonds. *Biophys. J.*, **72**, 1541-1555.
38. E. Evans, K. Ritchie, R. Merkel (1995). Sensitive force technique to probe molecular adhesion and structural linkages at biological interfaces. *Biophys. J.*, **68**, 2580-2587.
39. R. Merkel, P. Nassoy, A. Leung, K. Ritchie, E. Evans (1999). Energy landscapes of receptor-ligand bonds explored with dynamic force spectroscopy. *Nature*, **397**, 50-53.
40. J. Wong, A. Chilkoti, V. T. Moy (1999). Direct force measurements of the streptavidin-biotin interaction. *Biomol. Eng.*, **16**, 45-55.
41. H. Grubmüller, B. Heymann, P. Tavan (1996). Ligand binding: molecular mechanics calculation of the streptavidin-biotin rupture force. *Science*, **271**, 997-999.
42. D. F. Tees, R. E. Waugh, D. A. Hammer (2001). A microcantilever device to assess the effect of force on the lifetime of selectin-carbohydrate bonds. *Biophys. J.*, **80**, 668-682.
43. E. Evans, D. Berk, A. Leung (1991). Detachment of agglutinin-bonded red blood cells. I. Forces to rupture molecular-point attachments. *Biophys. J.*, **59**, 838-848.
44. H. Janovjak, J. Struckmeier, D. J. Muller (2005). Hydrodynamic effects in fast AFM single-molecule force measurements. *Eur. Biophys. J.*, **34**, 91-96.
45. N. Maeda, T. J. Senden (2000). A method for the calibration of force microscopy cantilevers via hydrodynamic drag. *Langmuir*, **16**, 9282-9286.
46. X. Zhang, E. Wojcikiewicz, V. T. Moy (2002). Force spectroscopy of the leukocyte function-associated antigen-1/intercellular adhesion molecule-1 interaction. *Biophys. J.*, **83**, 2270-2279.
47. E. P. Wojcikiewicz, X. Zhang, A. Chen, V. T. Moy (2003). Contributions of molecular binding events and cellular compliance to the modulation of leukocyte adhesion. *J. Cell Sci.*, **116**, 2531-5239.
48. T. Betancourt, L. Brannon-Peppas (2006). Micro- and nanofabrication methods in nanotechnological medical and pharmaceutical devices. *Int. J. Nanomedicine*, **1**, 483-495.
49. K. Salaita, Y. H. Wang, C. A. Mirkin (2007). Applications of dip-pen nanolithography. *Nature Nanotechnology*, **2**, 145-155.
50. A. A. Tseng, S. Jou, A. Notargiacomo, T. P. Chen (2008). Recent developments in tip-based nanofabrication and its roadmap. *J. Nanosci. Nanotechnol.*, **8**, 2167-2186.
51. A. J. Torres, M. Wu, D. Holowka, B. Baird (2008). Nanobiotechnology and cell biology: Micro- and nanofabricated surfaces to investigate receptor-mediated signaling. *Ann. Rev. Biophys.*, **37**, 265-288.
52. D. Lehnert, B. Wehrle-Haller, C. David, U. Weiland, C. Ballestrem, B. A. Imhof, M. Bastmeyer (2004). Cell behaviour on micropatterned substrata: limits of extracellular matrix geometry for spreading and adhesion. *J. Cell Sci.*, **117**, 41-52.

53. S. C. Hsiao, A. K. Crow, W. A. Lam, C. R. Bertozzi, D. A. Fletcher, M. B. Francis (2008). DNA-Coated AFM Cantilevers for the Investigation of Cell Adhesion and the Patterning of Live Cells. *Angew. Chem. Int. Edit.*, **47**, 8473-8477.
54. Y. Mei, C. Cannizzaro, H. S. Park, Q. B. Xu, S. R. Bogatyrev, K. Yi, N. Goldman, R. Langer, D. G. Anderson (2008). Cell-Compatible, Multicomponent Protein Arrays with Subcellular Feature Resolution. *Small*, **4**, 1600-1604.
55. D. K. Hoover, E. J. Lee, M. N. Yousaf (2009). Total Internal Reflection Fluorescence Microscopy of Cell Adhesion on Patterned Self-Assembled Monolayers on Gold. *Langmuir*, **25**, 2563-2566.
56. K. Takeda, S. Akira (2005). Toll-like receptors in innate immunity. *Int. Immunol.*, **17**, 1-14.
57. R. Medzhitov, C. A. Janeway, Jr. (2002). Decoding the patterns of self and nonself by the innate immune system. *Science*, **296**, 298-300.
58. W. D. Hanley, D. Wirtz, K. Konstantopoulos (2004). Distinct kinetic and mechanical properties govern selectin-leukocyte interactions. *J. Cell Sci.*, **117**, 2503-2511.
59. W. Hanley, O. McCarty, S. Jadhav, Y. Tseng, D. Wirtz, K. Konstantopoulos (2003). Single molecule characterization of P-selectin/ligand binding. *J. Biol. Chem.*, **278**, 10556-10561.
60. B. J. Dzamba, M. A. Bolton, D. W. Desimone. (2001). The integrin family of cell adhesion molecules, in *Cell Adhesion* (Ed.: M. C. Beckerle).
61. M. L. Dustin (1998). Making a little affinity go a long way: a topological view of LFA-1 regulation. *Cell Adhes. Commun.*, **6**, 255-262.
62. E. P. Wojcikiewicz, X. Zhang, A. Chen, V. T. Moy (2003). Contributions of molecular binding events and cellular compliance to the modulation of leukocyte adhesion. *J. Cell Sci.*, **116**, 2531-2539.
63. F. Li, S. D. Redick, H. P. Erickson, V. T. Moy (2003). Force measurements of the  $\alpha_5\beta_1$  integrin-fibronectin interaction. *Biophys. J.*, **84**, 1252-1262.
64. X. Zhang, S. E. Craig, H. Kirby, M. J. Humphries, V. T. Moy (2004). Molecular basis for the dynamic strength of the integrin  $\alpha_4\beta_1$ /VCAM-1 interaction. *Biophys. J.*, **87**, 3470-3478.
65. H. Volkmer. (2001). The immunoglobulin superfamily of cell adhesion molecules, in *Cell Adhesion* (Ed.: M. C. Beckerle).
66. G. L. Radice, M. Takeichi. (2001). Cadherins, in *Cell Adhesion* (Ed.: M. C. Beckerle).
67. P. Panorchan, M. S. Thompson, K. J. Davis, Y. Tseng, K. Konstantopoulos, D. Wirtz (2006). Single-molecule analysis of cadherin-mediated cell-cell adhesion. *J. Cell Sci.*, **119**, 66-74.
68. E. Zamir, B. Geiger (2001). Molecular complexity and dynamics of cell-matrix adhesions. *J. Cell Sci.*, **114**, 3583-3590.
69. M. Balzar, H. A. Bakker, I. H. Briaire-de-Brujin, G. J. Fleuren, S. O. Warnaar, S. V. Litvinov (1998). Cytoplasmic tail regulates the intercellular adhesion function of the epithelial cell adhesion molecule. *Mol. Cell. Biol.*, **18**, 4833-4843.
70. R. R. Dubreuil, G. MacVicar, S. Dissanayake, C. Liu, D. Homer, M. Hortsch (1996). Neuroglian-mediated cell adhesion induces assembly of the membrane skeleton at cell contact sites. *J. Cell Biol.*, **133**, 647-655.
71. M. Lub, Y. van Kooyk, S. J. van Vliet, C. G. Figdor (1997). Dual role of the actin cytoskeleton in regulating cell adhesion mediated by the integrin lymphocyte function-associated molecule-1. *Mol. Biol. Cell*, **8**, 341-351.
72. C. V. Carman, T. A. Springer (2003). Integrin avidity regulation: are changes in affinity and conformation underemphasized? *Curr. Opin. Cell Biol.*, **15**, 547-556.
73. M. Kim, C. V. Carman, W. Yang, A. Salas, T. A. Springer (2004). The primacy of affinity over clustering in regulation of adhesiveness of the integrin  $\alpha_1\beta_2$ . *J. Cell Biol.*, **167**, 1241-1253.
74. Y. van Kooyk, C. G. Figdor (2000). Avidity regulation of integrins: the driving force in leukocyte adhesion. *Curr. Opin. Cell Biol.*, **12**, 542-547.
75. A. Cambi, B. Joosten, M. Koopman, F. de Lange, I. Beeren, R. Torensma, J. A. Fransen, M. Garcia-Parajo, F. N. van Leeuwen, C. G. Figdor (2006). Organization of the Integrin LFA-1 in Nanoclusters Regulates Its Activity. *Mol. Biol. Cell*, **17**, 4270-4281.
76. W. G. Degen, L. C. van Kempen, E. G. Gijzen, J. J. van Groningen, Y. van Kooyk, H. P. Bloemers, G. W. Swart (1998). MEMD, a new cell adhesion molecule in metastasizing human melanoma cell lines, is identical to ALCAM (activated leukocyte cell adhesion molecule). *Am. J. Pathol.*, **152**, 805-813.
77. L. C. van Kempen, J. J. van den Oord, G. N. van Muijen, U. H. Weidle, H. P. Bloemers, G. W. Swart (2000). Activated leukocyte cell adhesion molecule/CD166, a marker of tumor progression in primary malignant melanoma of the skin. *Am. J. Pathol.*, **156**, 769-774.
78. S. Choi, M. Kobayashi, J. Wang, H. Habelhah, F. Okada, J. Hamada, T. Moriuchi, Y. Totsuka, M. Hosokawa (2000). Activated leukocyte cell adhesion molecule (ALCAM) and annexin II are involved in the metastatic progression of tumor cells after chemotherapy with Adriamycin. *Clin. Exp.*



- Metastasis*, **18**, 45-50.
79. G. Kristiansen, C. Pilarsky, C. Wissmann, C. Stephan, L. Weissbach, V. Loy, S. Loening, M. Diemel, A. Rosenthal (2003). ALCAM/CD166 is up-regulated in low-grade prostate cancer and progressively lost in high-grade lesions. *Prostate*, **54**, 34-43.
  80. A. Grakoui, S. K. Bromley, C. Sumen, M. M. Davis, A. S. Shaw, P. M. Allen, M. L. Dustin (1999). The immunological synapse: a molecular machine controlling T cell activation. *Science*, **285**, 221-227.
  81. J. M. Nelissen, I. M. Peters, B. G. de Grooth, Y. van Kooyk, C. G. Figdor (2000). Dynamic regulation of activated leukocyte cell adhesion molecule-mediated homotypic cell adhesion through the actin cytoskeleton. *Mol. Biol. Cell*, **11**, 2057-2068.
  82. A. W. Zimmerman, J. M. Nelissen, S. E. Van Ernst-De Vries, P. H. Willems, F. De Lange, J. G. Collard, F. N. Van Leeuwen, C. G. Figdor (2004). Cytoskeletal restraints regulate homotypic ALCAM-mediated adhesion through PKC $\alpha$  independently of Rho-like GTPases. *J. Cell Sci.*, **117**, 2841-2852.
  83. A. Cambi, F. de Lange, N. M. van Maarseveen, M. Nijhuis, B. Joosten, E. M. van Dijk, B. I. de Bakker, J. A. Fransen, P. H. Bovee-Geurts, F. N. van Leeuwen, N. F. Van Hulst, C. G. Figdor (2004). Microdomains of the C-type lectin DC-SIGN are portals for virus entry into dendritic cells. *J. Cell Biol.*, **164**, 145-155.
  84. A. Cambi, K. Gijzen, J. M. de Vries, R. Torensma, B. Joosten, G. J. Adema, M. G. Netea, B. J. Kullberg, L. Romani, C. G. Figdor (2003). The C-type lectin DC-SIGN (CD209) is an antigen-uptake receptor for *Candida albicans* on dendritic cells. *Eur. J. Immunol.*, **33**, 532-538.
  85. T. B. Geijtenbeek, D. J. Krooshoop, D. A. Bleijs, S. J. van Vliet, G. C. van Duijnhoven, V. Grabovsky, R. Alon, C. G. Figdor, Y. van Kooyk (2000). DC-SIGN-ICAM-2 interaction mediates dendritic cell trafficking. *Nat. Immunol.*, **1**, 353-357.
  86. T. B. Geijtenbeek, D. S. Kwon, R. Torensma, S. J. van Vliet, G. C. van Duijnhoven, J. Middel, I. L. Cornelissen, H. S. Nottet, V. N. KewalRamani, D. R. Littman, C. G. Figdor, Y. van Kooyk (2000). DC-SIGN, a dendritic cell-specific HIV-1-binding protein that enhances trans-infection of T cells. *Cell*, **100**, 587-597.
  87. A. Cambi, M. Koopman, C. G. Figdor (2005). How C-type lectins detect pathogens. *Cell Microbiol.*, **7**, 481-488.
  88. G. A. Snyder, M. Colonna, P. D. Sun (2005). The structure of DC-SIGNR with a portion of its repeat domain lends insights to modeling of the receptor tetramer. *J. Mol. Biol.*, **347**, 979-989.
  89. T. B. Geijtenbeek, Y. van Kooyk, S. J. van Vliet, M. H. Renes, R. A. Raymakers, C. G. Figdor (1999). High frequency of adhesion defects in B-lineage acute lymphoblastic leukemia. *Blood*, **94**, 754-764.
  90. L. C. van Kempen, J. M. Nelissen, W. G. Degen, R. Torensma, U. H. Weidle, H. P. Bloemers, C. G. Figdor, G. W. Swart (2001). Molecular basis for the homophilic activated leukocyte cell adhesion molecule (ALCAM)-ALCAM interaction. *J. Biol. Chem.*, **276**, 25783-25790.
  91. J. G. Quinn, S. O'Neill, A. Doyle, C. McAtamney, D. Diamond, B. D. MacCraith, R. O'Kennedy (2000). Development and application of surface plasmon resonance-based biosensors for the detection of cell-ligand interactions. *Anal. Biochem.*, **281**, 135-143.
  92. N. J. Hassan, A. N. Barclay, M. H. Brown (2004). Frontline: Optimal T cell activation requires the engagement of CD6 and CD166. *Eur. J. Immunol.*, **34**, 930-940.
  93. G. J. Pilkington, R. Bjerkvig, L. De Ridder, P. Kaaijk (1997). In vitro and in vivo models for the study of brain tumour invasion. *Anticancer Res.*, **17**, 4107-4109.
  94. C. Cremer, T. Cremer (1978). Considerations on a Laser-Scanning-Microscope with High-Resolution and Depth of Field. *Microscopica Acta*, **81**, 31-44.
  95. M. Kim, C. V. Carman, T. A. Springer (2003). Bidirectional transmembrane signaling by cytoplasmic domain separation in integrins. *Science*, **301**, 1720-1725.
  96. G. Vereb, J. Matko, G. Vamosi, S. M. Ibrahim, E. Magyar, S. Varga, J. Szollosi, A. Jenei, R. Gaspar, Jr., T. A. Waldmann, S. Damjanovich (2000). Cholesterol-dependent clustering of IL-2R $\alpha$  and its colocalization with HLA and CD48 on T lymphoma cells suggest their functional association with lipid rafts. *Proc. Natl. Acad. Sci. USA*, **97**, 6013-6018.
  97. F. de Lange, A. Cambi, R. Huijbens, B. de Bakker, W. Rensen, M. Garcia-Parajo, N. van Hulst, C. G. Figdor (2001). Cell biology beyond the diffraction limit: near-field scanning optical microscopy. *J. Cell Sci.*, **114**, 4153-4160.
  98. M. Koopman, A. Cambi, B. I. de Bakker, B. Joosten, C. G. Figdor, N. F. van Hulst, M. F. Garcia-Parajo (2004). Near-field scanning optical microscopy in liquid for high resolution single molecule detection on dendritic cells. *FEBS Lett.*, **573**, 6-10.
  99. I. M. Peters, Y. van Kooyk, S. J. van Vliet, B. G. de Grooth, C. G. Figdor, J. Greve (1999). 3D single-particle tracking and optical trap measurements on adhesion proteins. *Cytometry*, **36**, 189-194.
  100. R. Alon, S. Chen, R. Fuhlbrigge, K. D. Puri, T. A. Springer (1998). The kinetics and shear threshold

- of transient and rolling interactions of L-selectin with its ligand on leukocytes. *Proc. Natl. Acad. Sci. USA*, **95**, 11631-11636.
101. **Y. Cai, M. P. Sheetz** (2009). Force propagation across cells: mechanical coherence of dynamic cytoskeletons. *Curr. Opin. Cell Biol.*, **21**, 47-50.
102. **D. E. Leckband, F. J. Schmitt, J. N. Israelachvili, W. Knoll** (1994). Direct force measurements of specific and nonspecific protein interactions. *Biochemistry*, **33**, 4611-4624.
103. **S. Sivasankar, W. Brieher, N. Lavrik, B. Gumbiner, D. Leckband** (1999). Direct molecular force measurements of multiple adhesive interactions between cadherin ectodomains. *Proc. Natl. Acad. Sci. USA*, **96**, 11820-11824.
104. **M. L. Bennink, S. H. Leuba, G. H. Leno, J. Zlatanova, B. G. de Groot, J. Greve** (2001). Unfolding individual nucleosomes by stretching single chromatin fibers with optical tweezers. *Nat. Struct. Biol.*, **8**, 606-610.
105. **L. J. Rinko, M. B. Lawrence, W. H. Guilford** (2004). The molecular mechanics of P- and L-selectin lectin domains binding to PSGL-1. *Biophys. J.*, **86**, 544-554.
106. **M. I. Snijder-Van As, B. Rieger, B. Joosten, V. Subramaniam, C. G. Figdor, J. S. Kanger** (2009). A hybrid total internal reflection fluorescence and optical tweezers microscope to study cell adhesion and membrane protein dynamics of single living cells. *J. Microsc.*, **233**, 84-92.
107. **J. te Riet, A. W. Zimmerman, A. Cambi, B. Joosten, S. Speller, R. Torensma, F. N. van Leeuwen, C. G. Figdor, F. de Lange** (2007). Distinct kinetic and mechanical properties govern ALCAM-mediated interactions as shown by single-molecule force spectroscopy. *J. Cell Sci.*, **120**, 3965-3976.
108. **O. H. Willemsen, M. M. Snel, A. Cambi, J. Greve, B. G. De Groot, C. G. Figdor** (2000). Biomolecular interactions measured by atomic force microscopy. *Biophys. J.*, **79**, 3267-3281.



# CHAPTER 2

---

## **The threshold at which substrate nanogroove dimensions may influence fibroblast alignment and adhesion**

*Walter A. Loesberg, Joost te Riet, Falco C.M.J.M. van Delft, Peter Schön, Carl G. Figdor, Sylvia Speller, Jack J.W.A. van Loon, X. Frank Walboomers, John A. Jansen*

*The capacity to blunder slightly is the real marvel of DNA. Without this special attribute, we would still be anaerobic bacteria and there would be no music.*

*Lewis Thomas*

The differences in morphological behaviour between fibroblasts cultured on smooth and nanogrooved substrata (groove depth: 5–350 nm, width: 20–1000 nm) have been evaluated *in vitro*. The aim of the study was to clarify to what extent cell guidance occurs on increasingly smaller topographies. Pattern templates were made using electron beam lithography, and were subsequently replicated in polystyrene cell culture material using solvent casting. The replicates were investigated with atomic force microscopy (AFM). After seeding with fibroblasts, morphological characteristics were investigated using scanning electron microscopy (SEM) and light microscopy, in order to obtain qualitative and quantitative information on cell alignment. AFM revealed that the nanogroove/ridge widths were replicated perfectly, although at deeper levels the grooves became more concave. The smooth substrata had no distinguishable pattern other than a roughness amplitude of 1 nm. Interestingly, microscopy and image analysis showed that fibroblast after 4 h had adjusted their shape according to nanotopographical features down to cut-off values of 100 nm width and 75 nm depth. After 24 h culturing time, fibroblasts would even align themselves on groove depths as shallow as 35 nm. It appears depth is the most essential parameter in cellular alignment on groove patterns with a pitch ratio of 1:1. On the smooth substrata, cells always spread out in a random fashion. Analysis of variance (ANOVA) demonstrated that both main parameters, topography and culturing time, were significant. We conclude that fibroblast cells cultured on nanotopography experience a threshold feature size of 35 nm, below this value contact guidance does no longer exist.

## Introduction

Biomaterials for tissue and cell engineering are successfully incorporated into neighbouring tissue when they not only match the tissue's mechanical properties, but also bring forth specific cell responses, thus controlling or guiding the tissue formation in contact with the biomaterial. The cellular response to a biomaterial may be enhanced by mimicking the surface topography formed by the extra cellular matrix (ECM) components of natural tissue.<sup>1</sup> This could be beneficiary in the field of tissue engineering, which aims at the (re)generation of new and functional tissues. These ECM components are of nanometer scale and a first step in this quest is the production of nano(meter scale) topography. Previous studies have already addressed cellular reactions to larger micrometer scale topography. Predominantly groove and ridge patterns were studied, on which cells responded by altering morphology, orientation, adhesion, and gene regulation. Nanogroove patterns of 10-100 nm thus far have not yet been studied, although Teixeira et al.<sup>2</sup> have studied cell behaviour on ridges 70 nm wide, with a pitch of 400 nm however, and a depth of 600 nm, and found cellular alignment along these grooves. Previous *in vitro* research has investigated nanocolumns produced by colloidal lithography or polymer demixing which caused changes in cell morphology, filopodia production, migration, and cytokine release.<sup>3</sup> From these studies, it has become clear that topography in the nanometer scale may be of importance in cell guiding.<sup>1, 3-5</sup> Despite the amount of control over the dimensions created by these techniques, however, they remain largely random. In addition, it is unknown to what extent cells will sense and adapt their morphology to an ordered topography if the dimensions become exceedingly small.

In this study, a nanogroove topography formed by electron beam lithography has been investigated. In order not to deviate too far from previously used patterns<sup>6-9</sup> ten nanogroove/ridge patterns with a 1:1 pitch ratio have been selected and compared to smooth controls.

We hypothesised that, if the topography is small enough, a cellular “point break” is reached, where cells no longer display contact guidance along nanogroove patterns. In order to verify this hypothesis, cell responses to such nanotopography fields have been investigated from a morphology point of view, using light microscopy and scanning electron microscopy (SEM), and subsequent image analysis.

## Materials and Methods

### Substrata

Silicon wafers, 15 cm (6 in) across, were spin coated with hydrogen silsesquioxane (HSQ) solutions in methyl isobutyl ketone (MIBK) (FOX-12, Dow Corning Corp., Midland, MI, USA) on a Karl Suss spinner at 1000 rpm during 10 s with closed lid, resulting in 100 nm thick HSQ layers. The wafers were exposed in a JEOL Electron Beam Pattern Generator (JBX-9300FS) to a 100 kV beam with a 500 pA beam current (4 nm spot size) using a 4 nm beam step size. The field patterns consisted of squares of 500×500  $\mu\text{m}^2$  containing 1:1 lines and spaces at various pitches. The wafers were developed by manual immersion at 20°C in a 0.26 M tetra methyl ammonium hydroxide developer (TMA238WA), rinsed in 1:9 v:v TMA238WA:H<sub>2</sub>O, rinsed in demineralised water and blown dry with N<sub>2</sub>.<sup>10-12</sup> For obtaining higher master structures, the e-beam patterned HSQ was used as a mask in a Reactive Ion Etching (RIE) process for silicon using a CF<sub>4</sub>/O<sub>2</sub> plasma.

One 250 nm deep groove pattern, with a 2  $\mu\text{m}$  pitch, was made using a photolithographic technique and subsequent etching in a silicon wafer as described by Walboomers et al.<sup>8</sup> Wafers with a smooth surface were used as controls. In all instances, the silicon wafers were used as template for the production of polystyrene (PS) substrata for cell culturing. Polystyrene was solvent cast in a manner described by Chesmel and Black.<sup>13</sup> The dimensions of all substrata are shown in Table 1. Polystyrene replicas were attached to 20 mm diameter cylinders with polystyrene-chloroform adhesive to create a cell culture dish. Shortly before use a radio frequency glow-discharge (RFGD) treatment using Argon was applied for 3 minutes at a pressure of  $2.0 \times 10^{-2}$  mbar (Harrick Scientific Corp., Ossining, NY, USA) and a power of 200 W in order to sterilise and promote cell attachment by improving the wettability of the substrata.

### Cell culture

Rat dermal fibroblasts (RDF) were obtained from the ventral skin of male Wistar rats as described by Freshney.<sup>14</sup>

**Table 1: Feature dimensions of topographically patterned substrata**

Field	Pitch ratio (nm; 1:1)	Depth (nm $\pm$ S.E.M.)	Roughness (nm $\pm$ S.E.M.)
A	1000	37.8 $\pm$ 0.6	17.3 $\pm$ 0.2
B	600	37.3 $\pm$ 0.7	16.3 $\pm$ 0.1
C	400	34.6 $\pm$ 1.4	14.9 $\pm$ 0.6
D	300	33.8 $\pm$ 1.6	13.5 $\pm$ 0.1
E	200	30.6 $\pm$ 1.1	11.6 $\pm$ 0.1
F	160	30.5 $\pm$ 1.1	9.4 $\pm$ 0.1
G	100	17.9 $\pm$ 1.0	6.7 $\pm$ 0.4
H	80	11 $\pm$ 0.6	4.8 $\pm$ 0.1
I	60	7.8 $\pm$ 0.6	4.5 $\pm$ 0.3
J	40	4.4 $\pm$ 0.5	3.6 $\pm$ 0.1
K	1000	153.3 $\pm$ 2.7	69.1 $\pm$ 1.0
L	600	158 $\pm$ 3.2	64.4 $\pm$ 0.7
M	400	149.2 $\pm$ 1.2	53.9 $\pm$ 1.8
N	300	119.9 $\pm$ 2.6	36.7 $\pm$ 1.3
O	200	77.4 $\pm$ 4.1	22.0 $\pm$ 0.5
P	160	51.9 $\pm$ 3.4	15.3 $\pm$ 0.3
Q	100	17.2 $\pm$ 3.5	9.2 $\pm$ 0.7
R	80	15.3 $\pm$ 1.9	8.7 $\pm$ 0.9
S	60	11.6 $\pm$ 1.1	8.3 $\pm$ 0.1
T	40	10.9 $\pm$ 1.1	6.6 $\pm$ 0.4
$\mu\text{m}$ -Groove	2000	353.9 $\pm$ 8.2	163.3 $\pm$ 10.5
Smooth	n/a	n/a	1.24 $\pm$ 0.14

Cells were cultured in Dulbecco's MEM containing Earle's salts (Gibco, Invitrogen Corp., Paisley, Scotland), L-glutamine, 10% FCS, gentamicin (50 µg/ml), in an incubator set at 37 °C with a humidified atmosphere. Cell passage 4-6<sup>th</sup> was used during the experiments. Onto the various substrata,  $3.5 \times 10^4$  cells/cm<sup>2</sup> were seeded into the culture dishes. For the analysis, after 4 or 24 h, the cell layers were washed three times with phosphate buffered saline (PBS) and prepared for further analysis immediately after retrieval.

### Atomic Force Microscopy (AFM)

Surface topography was quantitatively evaluated using a Dimension atomic force microscope (AFM; Dimension 3100, Veeco, Santa Barbara, CA). Tapping in ambient air was performed with 118 µm long silicon cantilevers (NW-AR5T-NCHR, NanoWorld AG, Wetzlar, Germany) with average nominal resonant frequencies of 317 kHz and average nominal spring constants of 30 N/m. This type of AFM probe has a high aspect ratio (7:1) portion of the tip with a nominal length of >2 µm and a half-cone angle of <5°. Nominal radius of curvature of the AFM probe tip was less than 10 nm. The probes are especially suited to characterize the manufactured nanogrooves.

Height images of each field/sample were captured in ambient air at 50% humidity at a tapping frequency of 266.4 kHz. The analysed field was scanned at a scan rate of 0.5 Hz and 512 scanning lines. Nanoscope imaging software (version 6.13r1, Veeco) was used to analyze the resulting images. Surface roughness (root mean squared (RMS), nm) and the depth (nm) were obtained and averaged of three random fields per substrate.

### Scanning electron microscopy (SEM)

SEM graphs of the HSQ master structures were made using a Philips XL40 FEG-SEM. To assess overall morphology of the fibroblasts, also SEM was performed. Cells were rinsed, fixed for 5 minutes in 2% glutaraldehyde, followed by 5 minutes in 0.1 M sodium-cacodylate buffer (pH 7.4), dehydrated in a graded series of ethanol, and dried in tetramethylsilane to air. Specimens were sputter-coated with gold and examined with a Jeol 6310 SEM (Tokyo, Japan). Multiple micrographs were taken of cells on each nanopattern.

### Image Analysis

For quantitative image analysis, samples were fixed in paraformaldehyde and stained with Methylene blue followed by examination with a Leica/Leitz DM RBE Microscope (Wetzlar, Germany) at magnification of 20×. Methylene blue micrographs were analysed with Scion Image software (Beta Version 4.0.2, Scion Corp., Frederick, MD, USA). In several cases, due to low contrast between cell staining and background, the orientation was determined manually with a Falmouth Marine three-limb Course Protractor with a 5-min accuracy. The orientation of fibroblasts on the different fields and patterns was examined and photographed. The criteria for cell selection were (1) the cell is not in contact with other cells and (2) the cell is not in contact with the image perimeter. The maximum cell diameter was measured as the longest distance between two edges within the cell borders. The angle between this axis and the grooves (or an arbitrarily selected line for smooth surfaces) was termed the orientation angle. If the average angle was 45° or more, cells were supposed to lie in a random orientation. Cell extensions like filopodia, which could confound the alignment measurement, were not included when assessing the cell orientation. For statistic analysis, cells oriented at <10° from the groove direction were considered to be aligned.<sup>15,16</sup> The number of cells that were measured per sample group ranged from 24 to 290.

### Statistical analysis

Data acquired from the micrographs of cell alignment were analysed using SPSS for Windows (Release 12.0.1, SPSS Inc., Chicago, USA). The effects of, and the interaction between both time and surface were analysed using Analysis of variance (ANOVA), including a modified least significant difference (Bonferroni) multiple range test to detect significant differences between two distinct groups. Probability (p) value ≤ 0.05 was considered to be significant.

## Results

### Atomic force microscopy

In Table 1, the dimension, depth, and roughness as measured by AFM of the patterns in all polystyrene duplicates are given. The nanofields are designated A till T, while the microgrooved and smooth surfaces are designated by their own names. Fig. 1 shows a

number of representative images. What can be seen in these images is, that although groove/ridge widths are fairly preserved at the top, at deeper levels the grooves became concave or even V-shaped. The smooth sample has no distinguishable pattern other than a RMS roughness of  $1.2 \pm 0.1$  nm, occasionally a spike is present on the surface, probably the result of blemishes on the original wafer.

### Scanning electron microscopy

Fig. 2 shows a number of representative SEM graphs of the HSQ on silicon template structures as made by means of electron beam lithography (and Reactive Ion Etching). The various nanotopographies were accurately replicated in the polystyrene substrata. When observing cell morphology, fibroblasts cultured on smooth substrata displayed a cell spreading which was considered random (Fig. 3A), while an orientation along the

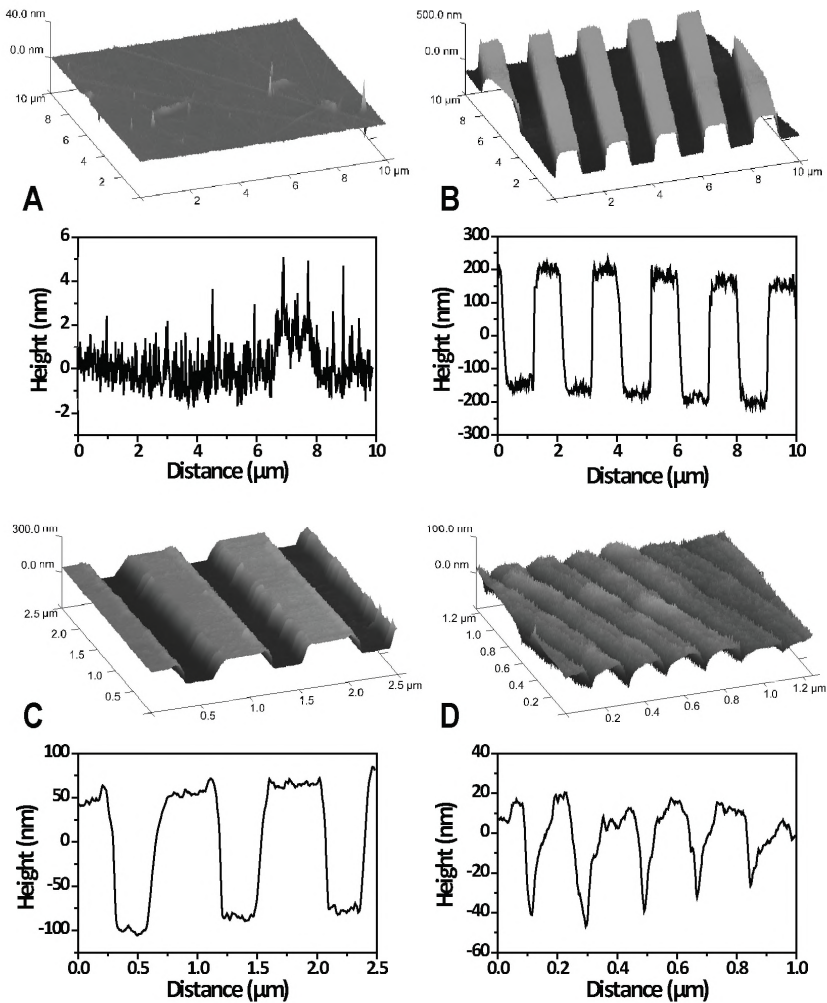


**Figure 1: AFM topography measurements of the substrates**

AFM graphs of topographies and height profiles of smooth (A), microgrooved (B), and nanogrooved substrates fields K and P (C and D, respectively).



groove direction was observed when cells were cultured on microgroove substrata (Fig. 3B). With decreasing pitch visual inspection made it clear that alignment was reduced. From field K to N, alignment of cells was still observed (Fig. 3C), on fields O till Q, however, cellular orientation was observed only rarely. Fields with the smallest pitch values (R, S, and T) resulted in cell morphology undistinguishable from the cells growing on the planar surface surrounding the textured fields, or the smooth control samples (Fig. 3D). Fibroblast alignment on fields A to J was virtually non-existent as opposed to, fields with the deeper groove depth (K, etc.) that did elicit alignment. Interestingly, time had a beneficial effect on cellular alignment; in all cases increased culture times (24 h vs. 4 h) led to an increase in orientation and/or more fields triggering alignment on the cell population (Field A in Fig. 3E, and F).

### Image analysis

Image analysis and subsequent statistical analysis performed confirmed that topography and culturing time were both significant factors in eliciting cellular orientation. Fig. 4 lists the various patterns and the mean angle of orientation they enticed to the fibroblasts. To designate the turning point after which alignment does not occur anymore, polynomial trend lines were drawn in the figures and the steepest parts were calculated. Fig. 4 presents these trend lines and illustrates the turning point between  $23^\circ$  and  $31^\circ$ .

Regarding topography: RDFs cultured on smooth substrata displayed a random cell spreading (average orientation angle around  $45^\circ$ ), while those cultured on the  $1\ \mu\text{m}$  wide groove pattern showed a clear alignment along the grooves for 82% of the

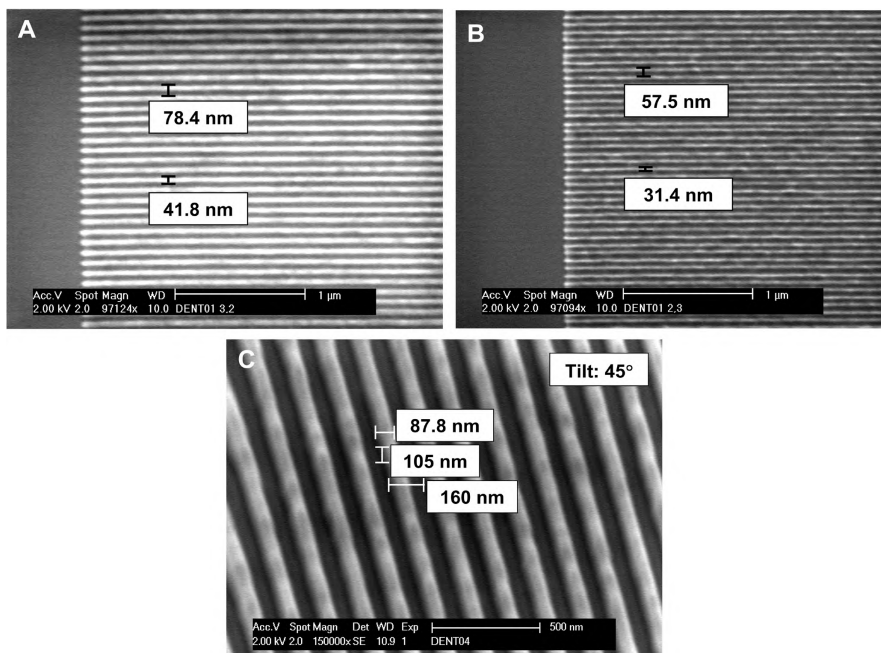


**Figure 2: SEM micrographs of templates made by electron beam lithography**

(A) Field H: 40 nm 1:1 lines and spaces in HSQ on silicon wafer. (B) Field I: 30 nm 1:1 lines and spaces in HSQ on silicon wafer and by electron beam lithography and reactive ion etching. (C) Field P: 80 nm 1:1 lines and spaces in HSQ/silicon on silicon wafer.

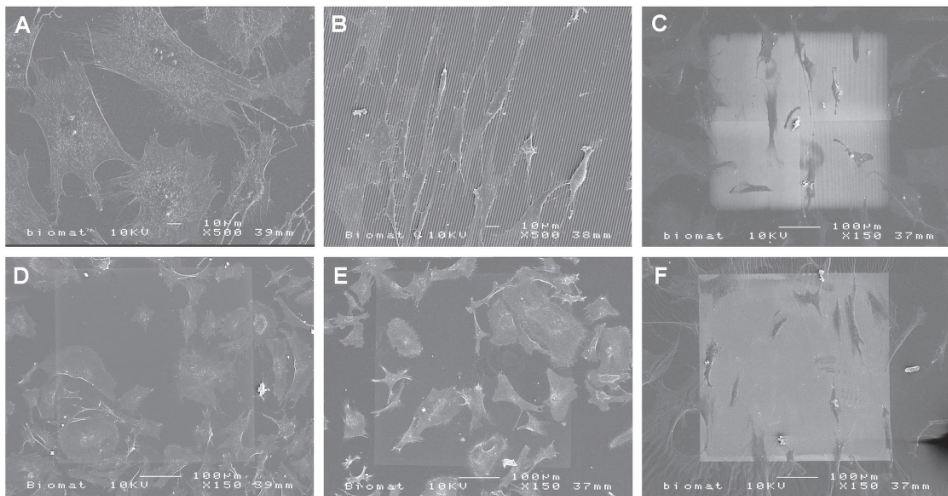


**Figure 3: SEM micrographs of RDFs cultured under various conditions**

(A) Smooth substratum with cells in a random fashion, (B) 1  $\mu\text{m}$  wide (350 nm deep) grooved substratum displaying aligned cells. (C) Field N (width 150 nm, depth 120 nm) still elicits cellular alignment to a majority of the cells compared to (D). Field R (width 40 nm, depth 15 nm) on which cells lay randomly spread. (E) Field A (width 500 nm, depth 35 nm) after 4 h of culturing and field A after 24 h of culturing (F). All micrographs were taken from 24 h samples, unless otherwise stated.

cells. Nanopatterns with depth 80–150 nm also resulted in cellular orientation on fields with larger pitch values (Fields K, L, M, and N). Nanopatterns with depths of 35 nm did not result in orientation of the fibroblasts at 4 h; however, when cultured for a prolonged period of time, the fields A and B did elicit cell alignment. Time played a key part in cell response towards the grooves; 24 h groups showed improved alignment compared to 4 h samples. As mentioned earlier, analysis of cells cultured on the deeper grooved nanopattern for 24 h showed an orientation trend, which gradually decreased with decreasing pitch width. After 24 h of culturing, the deep nanopattern resulted in enhanced alignment with the cut-off at 100 nm (Field O), after which cells appear not to be aligned anymore.

## Discussion

The aim of this study was to understand the morphological cell response of fibroblasts *in vitro*, particularly their orientation along a nanogroove pattern. Fibroblasts were cultured on polystyrene substrata, both smooth and grooved. In the latter case, both width and depth of the grooves have been varied. The patterns were characterized and cell behaviour was analysed using microscopic techniques. From our data it can be concluded that RDFs adjust their shape according to nanotopographical features down to a cut-off value of 100 nm width and a depth of 70 nm, which is a novel finding. Given sufficient culturing time, fibroblasts will even align themselves on groove depths as shallow as 35 nm, provided that ample ridge-surface (150 nm wide ridges) is available to the cells. It appears depth is the most essential parameter in cellular alignment on groove patterns with a pitch ratio of 1:1.

In order to obtain nanogroove patterns, electron beam lithography and RIE have been employed. In the latter technique, the phenomenon of diffusion limitation plays a role, especially in smaller grooves; the chemical reactants will insufficiently reach the

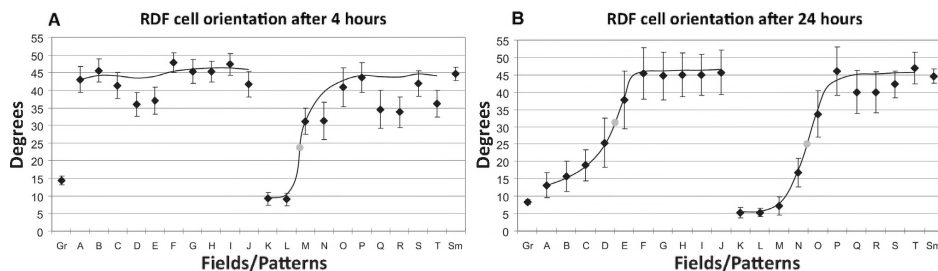


**Figure 4: The mean angle ( $\pm$  S.E.M.) showing the distribution of cellular orientation divided over time**

(A) Cellular orientation after 4 h culture shows alignment for the groove pattern and fields K and L. All other surfaces, smooth pattern and fields with small groove dimensions do not elicit orientation at this point. (B) After 24 h cell alignment has appeared or improved on the several patterns and fields. Polynomic trend line in black with the turning point in gray. Gr = 1  $\mu$ m groove pattern, Sm = smooth pattern, nanometric fields A through T (see also Table 1).

bottom of the proposed design of the grooves, resulting in shallower depths or grooves becoming more concave. Simply increasing the etching time in RIE may result in the desired depth locally, however, this would lead to the top edges of the ridges enduring more etching, resulting in a reduced sharpness and somewhat convex and concave profiles of, respectively, the wafer ridges and the ensuing polystyrene duplicates. The characteristics of the actual wafers were not the focus of our study, as our main interest is in the substrata onto which the cells are cultured. In addition, polystyrene casting could be influenced by capillary forces elicited by the nanogrooves which may affect the reproduction accuracy, although literature data concerning imprint lithography techniques suggest that 20 nm details can easily be accomplished when pressing a mould into polymers.<sup>17, 18</sup>

Another possible explanation for the concave appearance of the grooves, from fields E and O onwards, is the intrinsic limitation of AFM measurements related to tip convolution. Also, this phenomenon can have an effect on the reliability of the depth measurement. In order to minimize these effects during our AFM measurement, a high aspect ratio tip especially designed for scanning grooves was used.

SEM, cell staining, and subsequent image analysis all confirmed that fibroblasts were oriented on nanogrooved surfaces. Because the pitch dimensions used on both nanopattern wafers were equal, the difference in rate of cellular orientation was predominantly determined by the groove depth. These results are in accordance with work of Clark et al.<sup>15, 16</sup> on micrometric textures. They concluded that groove depth is much more important in alignment of cells than the spacing of the grooves. Even when nanoscale patterns were used, an increase in groove depth led to better orientation.<sup>19</sup> Teixeira et al.,<sup>2</sup> who cultured epithelial cells on patterned substrata showed an approximate 35% of cells aligned; this value could be the result of shallow ridge width (70 nm, pitch 400 nm) with appropriate depth (600 nm). However, it could also be that cell orientation is the result of both (or more) parameters. Current e-beam lithography permits the fabrication of large areas of features comparable in size to those found in fibrillar ECM. Individual collagen fibrils have diameters that are commonly in the range 20–100 nm although they often form larger aggregates.<sup>19, 20</sup> This study shows that fibroblast cells display meagre alignment on fields with ridge/groove widths of 100 nm or less. So, it is

possibly a combination of factors that lead to cell guidance by the environment (be it substrata or tissue) rather than simply one parameter.

Similar to Teixeira's results and our own work,<sup>9</sup> in this study it was observed that cells extend themselves while probing the substrata, since the grooves patterns are too narrow for the cells to get into contact with the bottom. The cellular extensions, probing the substrate surface, only found the ridges, resulting in extension of the cellular body along these ridges. Early responses of fibroblasts growing on textured substrata have been described before;<sup>21</sup> and cell orientation starts with the cell exploring the surroundings with the appearance of membrane extensions. Connective tissue cells need ECM in order to survive; since none is present, the aforementioned extensions are produced in all directions. Within hours, fitting anchor points are found and focal adhesion contacts are established with deposited ECM material, and the cell flattens and spreads, followed by the formation of filaments in the longitudinal direction.<sup>22, 23</sup> This study showed it was clear that cell alignment occurred immediately on Fields K, L, and 1  $\mu\text{m}$  grooves during cell spreading and in accordance with the grooves. An alternative view concerning cell guidance on such small features is that not the increasing amount of ECM proteins with time, but the lag time between guidance on a small scale (filopodia, lamellapodia) and the influence on the entire cell might perhaps explain the increase in orientation.<sup>24, 25</sup>

As explained earlier, having the ability to control cell behaviour is of great advantage in tissue engineering. And topography is just one method of gaining control. It is now clear that cells as a whole respond strongly to structured nanotopography to a cut-off value of 35 nm. However, as Dalby et al.<sup>25</sup> pointed out for filopodia and to some extent lamellapodia, this value may be as low as 10 nm when random distributed "nano islands" are applied to induce interaction.

By using a pattern design which surface is large enough to extract quantitative data, future research will, besides visualisation of cell cytoskeleton components and quantification of the cell's responses on a molecular level, look at the interaction of these groove dimensions and a dynamic force, like mechanical strain or fluid flow on cell conduct.

## Conclusion

Since e-beam lithography is able to generate diverse patterns, a new approach was made possible to conduct research on cell behaviour on a wide variety of fields. This in turn allowed us to ascertain the cellular divide as presented in this study. The gradual decrease in dimension values allowed us to investigate in more detail the fibroblasts response towards topography. It is proposed that criteria concerning cellular orientation go beyond an arbitrary value, since those values are derived from measurements on specified topographies. By approaching natural dimensions these theoretical standards are no longer valid. Cellular alignment is triggered by a combination of ridge width and groove depth and most likely by other external (dynamic) factors as well, such as mechanical stress or compression. In this static study, design groove depths below 35 nm or ridge widths smaller than 100 nm do not result in fibroblast alignment.

It is concluded that fibroblast cells, cultured upon increasingly smaller nanoscale topography, experience, in accordance with our hypothesis, a decisive point where they no longer demonstrate contact guidance. This threshold seems to be at a 35 nm for whole cell alignment.

## Acknowledgements

Dr. F.C. van den Heuvel performed Reactive Ion Etching of the master structures at the Philips Research MiPlaza facilities in Eindhoven. Scanning electron microscopy on fibroblast morphology was performed at the Microscopic Imaging Centre (MIC) of the Nijmegen Centre for Molecular Life Sciences (NCMLS), the Netherlands.

This research was supported by the Microgravity Research Program of NWO-Space Research Organization Netherlands (SRON Grant # MG-057 and MG-063) and NanoNed, the Dutch Nanotechnology Programme of the Ministry of Economic Affairs (Grant # BSIK-03006).

## References

1. **D. C. Miller, A. Thapa, K. M. Haberstroh, T. J. Webster** (2004). Endothelial and vascular smooth muscle cell function on poly(lactic-co-glycolic acid) with nano-structured surface features. *Biomaterials*, **25**, 53-61.
2. **A. I. Teixeira, G. A. Abrams, P. J. Bertics, C. J. Murphy, P. F. Nealey** (2003). Epithelial contact guidance on well-defined micro- and nanostructured substrates. *J. Cell Sci.*, **116**, 1881-1892.
3. **M. J. Dalby, M. O. Riehle, D. S. Sutherland, H. Agheli, A. S. G. Curtis** (2005). Morphological and microarray analysis of human fibroblasts cultured on nanocolumns produced by colloidal lithography. *Eur. Cell Mater.*, **9**, 1-8.
4. **M. J. Dalby, M. O. Riehle, H. J. H. Johnstone, S. Affrossman, A. S. G. Curtis** (2002). Polymer-demixed nanotopography: Control of fibroblast spreading and proliferation. *Tissue Eng.*, **8**, 1099-1108.
5. **M. J. Dalby, M. O. Riehle, D. S. Sutherland, H. Agheli, A. S. G. Curtis** (2004). Use of nanotopography to study mechanotransduction in fibroblasts - methods and perspectives. *Eur. J. Cell Biol.*, **83**, 159-169.
6. **D. M. Brunette, B. Chehroudi** (1999). The effects of the surface topography of micromachined titanium substrata on cell behavior in vitro and in vivo. *J. Biomech. Eng.-Trans. ASME*, **121**, 49-57.
7. **E. T. den Braber, J. E. de Ruijter, H. T. J. Smits, L. A. Ginsel, A. F. von Recum, J. A. Jansen** (1996). Quantitative analysis of cell proliferation and orientation on substrata with uniform parallel surface micro-grooves. *Biomaterials*, **17**, 1093-1099.
8. **X. F. Walboomers, H. J. E. Croes, L. A. Ginsel, J. A. Jansen** (1998). Growth behavior of fibroblasts on microgrooved polystyrene. *Biomaterials*, **19**, 1861-1868.
9. **W. A. Loesberg, X. F. Walboomers, J. van Loon, J. A. Jansen** (2005). The effect of combined cyclic mechanical stretching and microgrooved surface topography on the behavior of fibroblasts. *J. Biomed. Mater. Res. Part A*, **75A**, 723-732.
10. **F. van Delft** (2002). Delay-time and aging effects on contrast and sensitivity of hydrogen silsesquioxane. *J. Vac. Sci. Technol. B*, **20**, 2932-2936.
11. **F. van Delft, F. C. van den Heuvel, A. E. T. Kuiper, P. C. Thune, J. W. Niemantsverdriet** (2004). Micro-contact printing on oxide surfaces for model catalysts using e-beam written masters in hydrogen silsesquioxane. *Microelectron. Eng.*, **73-4**, 202-208.
12. **F. van Delft, J. P. Weterings, A. K. van Langen-Suurling, H. Romijn** (2000). Hydrogen silsesquioxane/novolak bilayer resist for high aspect ratio nanoscale electron-beam lithography. *J. Vac. Sci. Technol. B*, **18**, 3419-3423.
13. **K. D. Chesmel, J. Black** (1995). Cellular-responses to chemical and morphologic aspects of biomaterial surfaces .1. A novel in-vitro model system. *J. Biomed. Mater. Res.*, **29**, 1089-1099.
14. **R. I. Freshney** (1999). Culture of animal cells: a multimedia guide, Wiley, Chichester.
15. **P. Clark, P. Connolly, A. S. G. Curtis, J. A. T. Dow, C. D. W. Wilkinson** (1987). Topographical control of cell behavior .1. Simple step cues. *Development*, **99**, 439-448.
16. **P. Clark, P. Connolly, A. S. G. Curtis, J. A. T. Dow, C. D. W. Wilkinson** (1990). Topographical control of cell behavior .2. Multiple grooved substrata. *Development*, **108**, 635-644.
17. **S. Y. Chou, P. R. Krauss, P. J. Renstrom** (1996). Nanoimprint lithography. *J. Vac. Sci. Technol. B*, **14**, 4129-4133.
18. **J. Haisma, M. Verheijen, K. van den Heuvel, J. van den Berg** (1996). Mold-assisted nanolithography: A process for reliable pattern replication. *J. Vac. Sci. Technol. B*, **14**, 4124-4128.
19. **P. Clark, P. Connolly, A. S. G. Curtis, J. A. T. Dow, C. D. W. Wilkinson** (1991). Cell guidance by ultrafine topography in vitro. *J. Cell Sci.*, **99**, 73-77.
20. **G. A. Dunn, J. P. Heath** (1976). New hypothesis of contact guidance in tissue-cells. *Exp. Cell Res.*, **101**, 1-14.
21. **X. F. Walboomers, L. A. Ginsel, J. A. Jansen** (2000). Early spreading events of fibroblasts on microgrooved substrates. *J. Biomed. Mater. Res.*, **51**, 529-534.
22. **R. O. Hynes** (1999). Cell adhesion: old en new questions. *Trends Cell Biol.*, **9**, M33-37.
23. **R. O. Hynes, A. T. Destree** (1978). Relationships between fibronectin (LETS protein) and actin. *Cell*, **15**, 875-886.
24. **M. J. Dalby, N. Gadegaard, M. O. Riehle, C. D. W. Wilkinson, A. S. G. Curtis** (2004). Investigating filopodia sensing using arrays of defined nano-pits down to 35 nm diameter in size. *Int. J. Biochem. Cell Biol.*, **36**, 2005-2015.
25. **M. J. Dalby, M. O. Riehle, H. Johnstone, S. Affrossman, A. S. G. Curtis** (2004). Investigating the limits of filopodial sensing: a brief report using SEM to image the interaction between 10 nm high nano-topography and fibroblast filopodia. *Cell Biol. Int.*, **28**, 229-236.

# CHAPTER 3

---

## **Interlaboratory round robin on cantilever calibration for AFM force spectroscopy**

*Joost te Riet, Allard J. Katan, Christian Rankl, Stefan W. Stahl,  
Arend M. van Buul, In Yee Phang, Alberto Gomez-Casado,  
Jan W. Gerritsen, Alessandra Cambi, Alan E. Rowan,  
G. Julius Vancso, Pascal Jonkheijm, Jurriaan Huskens,  
Tjerk H. Oosterkamp, Hermann Gaub, Peter Hinterdorfer,  
Carl G. Figdor, Sylvia Speller*

*Gravitation is not responsible  
for people falling in love.*

*Albert Einstein*

Submitted for publication

**S**ingle-molecule force spectroscopy studies performed by Atomic Force Microscopes (AFMs) strongly rely on accurately determined cantilever spring constants. Hence, to calibrate cantilevers, a reliable calibration protocol is essential. Although the thermal noise method and the direct Sader method are frequently used for cantilever calibration, there is no consensus on the optimal calibration of soft and V-shaped cantilevers, especially those used in force spectroscopy. Therefore, in this study we aimed at establishing a novel approach to accurately calibrate compliant and V-shaped cantilevers. In a round robin experiment involving eight different laboratories we compared the thermal noise and the Sader method on ten commercial and custom-built AFMs. We found that spring constants of both rectangular and V-shaped cantilevers can accurately be determined with both methods, although the Sader method proved to be superior. Furthermore, we observed that simultaneous application of both methods on an AFM proved an accurate consistency check of the instrument and thus provides optimal and highly reproducible calibration. To illustrate the importance of optimal calibration, we show that for biological force spectroscopy studies, an erroneously calibrated cantilever can significantly affect the derived (bio)physical parameters. Taken together, our findings resulted in a fast and improved standard protocol to obtain reliable spring constants for different types of cantilevers.

## Introduction

The Atomic Force Microscope (AFM) is a sensitive force probe<sup>1</sup> with a resolution in the piconewton (pN) range, allowing to characterize inter- and intra-molecular forces. The study of single molecule bond dynamics by AFM, known as AFM force spectroscopy, is widely used to investigate biological and chemical interactions, providing insight into their intra-molecular energy landscapes.<sup>2, 3</sup> In 1994, for the first time individual ligand-receptor interactions between avidin and biotin were measured.<sup>4, 5</sup> Since then, force spectroscopy has been used to study, e.g. DNA structure<sup>6, 7</sup>, unfolding of native proteins,<sup>8, 9</sup> polymers,<sup>10</sup> covalent bonds,<sup>11</sup> rupture of supramolecular bonds,<sup>12</sup> and cell adhesion.<sup>13, 14</sup> All these force measurements rely on the use of well calibrated cantilevers, i.e. to know the absolute spring constant allowing one to quantify the forces. In addition, also many other AFM applications as nanostructuring,<sup>15</sup> elasticity mapping,<sup>10, 16</sup> and static as well as resonant imaging modes<sup>17</sup> depend on an accurately determined spring constant in order to quantify the physical forces probed properly.

Over the last decades, several methods have been proposed to determine AFM cantilever spring constants that can be grouped into three categories. Dimensional modeling methods require the precise knowledge of the cantilever dimensions and material properties to calculate the spring constant.<sup>18-20</sup> Static deflection methods use glass fibers,<sup>21, 22</sup> reference cantilevers,<sup>23, 24</sup> electrostatic forces,<sup>25</sup> or a piezosensor<sup>26</sup> to determine the spring constant by loading the cantilever with a known static force. Finally, there are different dynamic deflection methods that relate the spring constant to the cantilever's resonance behavior, such as the Cleveland method,<sup>27</sup> the thermal noise method,<sup>28</sup> the Sader method<sup>29, 30</sup> and laser Doppler vibrometry.<sup>31</sup>

All these methods were compared with each other and were discussed before.<sup>31-35</sup> Specifically, the thermal noise method – based on statistical mechanics – and the Sader method – based on fluid dynamics theory – were frequently investigated and have the highest application potential, also documented by their implementation in commercial AFMs. Relatively widespread use of these approaches are mainly related to the following

advantages: (i) the calibration of the cantilever is performed in situ; (ii) both methods are independent on the cantilever's material or coating; (iii) and they are (largely) nondestructive and noninvasive for the cantilevers. In addition, (iv) the AFM systems used need minimal hard- and software requirements; and finally, (v) both methods are quick and easy to learn. Furthermore, to apply the thermal noise method, it is important to use a calibration protocol with accurate correction factors, which can be adapted from literature.<sup>32, 36, 37</sup> These factors mainly concern differences between rectangular versus V-shaped cantilevers and the AFM's detection scheme.

The implementation of these two methods has been thoroughly described before,<sup>32, 33</sup> especially concerning technical and theoretical aspects. Both methods were compared by measuring rectangular-shaped cantilevers within a wide spring constant range (0.1-20 N/m).<sup>32</sup> However, in those studies V-shaped cantilevers were not calibrated. Other reports addressing V-shaped cantilevers did not consider the Sader method.<sup>34, 38</sup> In view of the increasing importance to derive quantitative forces for AFM force spectroscopy, a comparison between the methods addressing cantilevers frequently used in these studies – soft (<0.05 N/m) and V-shaped – has become necessary.

The aim of our study was to investigate potential differences between (commercial) instruments and laboratories, particularly paying attention to practical aspects of cantilever calibration. The experiments described in this article were performed sequentially, as a round robin experiment. In particular, we investigated the accuracy of the thermal noise and direct Sader method by calibrating cantilevers on different AFM systems operated by experienced users of different labs all using the same calibration protocol. Furthermore, two indirect methods by Gibson and Sader,<sup>29, 39</sup> which relate the spring constant of the rectangular to the V-shaped cantilever on one chip, were considered as alternatives. Finally, the effect of an incorrectly determined spring constant on the measured forces and micromechanical properties of a biological ligand-receptor bond was addressed. We conclude our study by proposing a fast and improved standard protocol to obtain reliable spring constants for different types of cantilevers.

## Materials & Methods

### Round robin experiment

The round robin study has been set up in collaboration between eight laboratories from three countries. In these labs different commercial and custom-built AFMs were used to study the same 30 cantilevers on 10 different chips, which were sent around from one lab to the next to sequentially determine their spring constants. The calibrations were performed by experienced users of the AFM systems according to a protocol pre-established by all participants, see Supporting Material.

#### Instruments

Ten different AFMs were used, owned by eight different labs. In Table 1, we summarize the characteristics of these AFMs. We include a symbol (roman number) to designate the AFMs throughout the study. A more detailed description of the instruments is given below. Furthermore, detailed information on the software used, the temperature, etc., can be found in Table S1 (Supporting Material).

**Multimode Nanoscope IIIa (Veeco, Santa Barbara, CA, USA).** Calibrations on the Nijmegen [I] and Enschede [III] AFM systems were performed on thermal noise data sampled at a rate of 62.5 kHz. In detail, false engage images (512×512) at a line rate of 61 Hz were exported, a power spectral density (PSD) analysis was performed on these data, to obtain all calibration parameters by a fit for further analysis. Calibrations on the Leiden system [II] were performed by routing the deflection data from the Signal Access Module to a 16 bit DAQ card (USB 6152, National Instruments) and recording it at a sample rate of 1.25 MS/s. Spectra were calculated from this data during acquisition using custom-written LabView software.

**Multimode Nanoscope IV (Veeco).** Calibrations on the Nijmegen system [IV] were performed by measuring



the thermal noise data at a sampling rate of 62.5 kHz via the Thermal Tune box in the software. Thermal noise spectra were exported and analyzed.

**Multimode Nanoscope IVa (Veeco).** Calibrations on the Enschede PicoForce system [V] were performed by measuring the thermal noise data at a sampling rate of 62.5 kHz via the Thermal Tune box in the software. InvOLS (inverse optical lever sensitivity (nm/V); also known as deflection sensitivity<sup>40</sup>) measurements were performed with closed z-loop. Thermal noise spectra were exported and analyzed.

**Multimode Nanoscope V (Veeco).** Calibrations on the Nijmegen system [VI] were performed by measuring the thermal noise data at a sampling rate of 200 kHz via the Thermal Tune box in the software, in which also the thermal noise spectra were analyzed via the Liquid (SHO) fitting procedure.

**JPK NanoWizard I (JPK, Berlin, Germany).** Calibrations on the Nijmegen system [VII] were performed by measuring the thermal noise at a sampling rate of 152 kHz via the JPK software, in which also the thermal noise spectra were analyzed.

**Agilent 5500 (Agilent, Chandler, AZ, USA).** Calibrations on the Linz system [VIII] were performed by obtaining the thermal noise data at a sampling rate of 220 kHz. Spectra generation and curve fitting was performed by a custom written software in MATLAB (The Mathworks, Natick, MA, USA).

**Custom-built system (CB) with Asylum MFP-3D controller (Asylum Research, Santa Barbara, CA, USA).** Calibrations on the Munich system [IX] were performed by obtaining the thermal noise data at a sampling rate of 5 MHz. Generation of spectra and curve fitting were performed in Igor 5.03 (Wavemetrics Inc., OR, USA) with software packages provided by Asylum Research.

**Custom-built system.** Thermal noise spectra on the Leiden system [X] were acquired on a high-speed digitizer with built-in FFT calculation (National Instruments PCI 5122), using a sample rate of 10 MS/s and a frequency resolution of 4 Hz.

Note that before the experiments, the z-calibration of all AFMs was checked using a calibration grid, or via interference measurements (for system IX).

### Cantilevers

The cantilevers used in this round robin study were 5 MLCT-AUHW (MicroLevers for ConTact mode with Au-coating from one Half Wafer, Veeco) and 5 MSCT-AUHW (Oxide-Sharpended MLCTs, Veeco). The nominal – i.e. given by the manufacturer – spring constants are given in Table 2. The cantilever dimensions were measured by a JEOL SEM (JSM-6301F) using an dedicated internal calibration grid to relate the dimensions measured by the SEM (Table 2).

Cantilevers were cleaned once before the calibration series by rinsing them three times with chloroform (Sigma-Aldrich, St. Louis, MO, USA) and subsequently with >98% ethanol (Sigma). Then the cantilevers were UV-cleaned for 20 minutes, rinsed with ethanol, MQ water and as a last step with ethanol. Finally, the cantilevers were dried in a  $N_2$  flow.

### The thermal noise method

In this method the cantilever is treated as a simple harmonic oscillator. The equi-partition theorem, which says each mode of the cantilever on average contains an amount of energy  $\frac{1}{2}k_bT$ , is then used to find the cantilever spring constant  $k$  by relating the thermal (i.e. Brownian) motion of the cantilever's fundamental mode to its thermal energy:<sup>28</sup>

**Table 1. Outline of used AFM systems**

Symbol	Abbreviation	System	Location
I	NS IIIa	Veeco Multimode Nanoscope IIIa	Nijmegen (NL)
II	NS IIIa	Veeco Multimode Nanoscope IIIa	Leiden (NL)
III	NS IIIa	Veeco Multimode Nanoscope IIIa	Enschede (NL)
IV	NS IV	Veeco Multimode Nanoscope IV	Nijmegen (NL)
V	NS IVa	Veeco Multimode Nanoscope IVa	Enschede (NL)
VI	NS V	Veeco Multimode Nanoscope V	Nijmegen (NL)
VII	JPK	JPK NanoWizard I	Nijmegen (NL)
VIII	Agilent 5500	Agilent 5500	Linz (A)
IX	CB	Custom-built based on Asylum MFP-3D	Munich (D)
X	CB	Custom-built	Leiden (NL)

**Table 2. Dimensions of the cantilevers\***

Cantilever	$L$ ( $\mu\text{m}$ )	$b$ ( $\mu\text{m}$ )	$d$ ( $\mu\text{m}$ )	$\theta$ ( $^\circ$ )	$k_{\text{nom}}$ (pN/nm)
B <sub>MLCT</sub>	203.8	20.38	$n/a$	$n/a$	20
C <sub>MLCT</sub>	324.2	20.81	226.6	18.6	10
D <sub>MLCT</sub>	219.6	20.26	154.9	18.6	30
B <sub>MSCT</sub>	203.3	20.12	$n/a$	$n/a$	20
C <sub>MSCT</sub>	321.4	21.24	222.1	18.6	10
D <sub>MSCT</sub>	217.6	21.05	153.0	18.6	30

\* Given dimensions are those determined of three randomly chosen cantilevers from one wafer

$$k = \frac{k_B T}{\langle z_c^2 \rangle} \quad (1)$$

where  $k_B$  is the Boltzmann constant,  $T$  the temperature, and  $\langle z_c^2 \rangle$  the mean square displacement of the cantilever. Later studies pointed out that two corrections were necessary.<sup>36, 37</sup> The first correction takes into account the non-ideal spring behavior of the cantilever, dividing its thermal energy over multiple oscillatory modes. For the primary mode correction factors of 0.971 and 0.965 were found for rectangular<sup>36</sup> and V-shaped cantilevers,<sup>37</sup> respectively. A second, more significant correction takes into account the optical lever detection scheme<sup>36</sup> in which the *angular* changes of the cantilever are measured rather than the absolute deflection. Since the curvature profile of a freely oscillating cantilever (used to collect the thermal noise data) differs from that of a supported one (used to measure InvOLS) the measured “displacement” is corrected. These also depend on the bending mode of the cantilever, for the primary mode the following formula was derived (with  $C = 0.817$  or  $0.764$  for rectangular and V-shaped cantilevers, respectively):<sup>36, 37</sup>

$$k = C \frac{k_B T}{\langle z_l^2 \rangle} \quad (2)$$

where  $\langle z_l^2 \rangle$  represents the “apparent” cantilever displacement measured by the optical lever scheme of the primary oscillation mode.

Further corrections were suggested, e.g. taking into account the finite spot size, the cantilever size, and the laser spot position on the cantilever.<sup>40, 41</sup> However for cantilevers longer than  $100 \mu\text{m}$  used in AFMs with a laser spot size smaller than  $20 \mu\text{m}$  and V-shaped cantilevers (i.e. such as is the case in our study) these corrections are insignificant.

To determine  $\langle z_c^2 \rangle$  of Eq. 2 the thermally driven oscillations of the cantilever are collected over time, followed by a power spectral density (PSD) analysis to get a thermal spectrum. The fundamental resonance peak is then fitted with a simple harmonic oscillator (SHO) model for the power:<sup>42</sup>

$$P(f) = y_0 + \frac{A_0 \cdot f_R^4}{(f^2 - f_R^2)^2 + \left(\frac{f \cdot f_R}{Q}\right)^2} \quad (3)$$

where  $y_0$  is the power of the white noise baseline,  $A_0$  the zero frequency power,  $f_R$  the resonance frequency and  $Q$  the quality factor. (We note that for highly damped systems,  $Q \leq 10$  as for example in liquid, an adapted SHO fit should be used<sup>38</sup>). The spring constant is then calculated by taking  $\langle z_c^2 \rangle$ , which represents the area under the curve of the SHO fit, as:<sup>32</sup>

$$\langle z_c^2 \rangle = \int_{f=0}^{\infty} P(f) \cdot df \quad (4)$$

with  $P(f)$  from Eq. 3, for Eq. 2 this results in:

$$k = \frac{2 \cdot C \cdot k_B T}{\pi \cdot A_0 \cdot f_R \cdot Q} \quad (5)$$

### The Sader method

With the direct Sader method the spring constant of a rectangular cantilever is determined by using its plan view dimensions, the density of the medium  $\rho$ , and viscosity of the medium  $\eta$  in which they are measured, and the corresponding resonance frequency  $f_R$  and quality factor  $Q$ .<sup>29</sup> The thickness  $t$  of the cantilever is not needed. Typically the Sader method is applied in air, in which  $Q > 10$ . Additionally, the length to width ratio

should be  $L/b > 3$ .<sup>43</sup> By fitting the thermal spectrum of a rectangular cantilever with the SHO model Eq. 3,  $f_R$  and  $Q$  are determined. (For liquid see<sup>38</sup>). The spring constant can then be described by:<sup>29</sup>

$$k = 7.5246 \cdot \rho \cdot b^2 \cdot L \cdot \Gamma_i(\text{Re}) \cdot f_R^2 \cdot Q \quad (6A)$$

$$\text{with Re} = \frac{\pi \cdot \rho \cdot b^2 \cdot f_R}{2\eta} \quad (6B)$$

where  $b$  is the width of the cantilever,  $L$  the length of the cantilever (see Fig. 1B), and  $\Gamma_i$  the imaginary part of the hydrodynamic function.<sup>44</sup>

This model is valid for any rectangular cantilever, for V-shaped cantilevers it is necessary to determine the individual dynamical response of each cantilever. This method is described by Sader et al.<sup>30</sup> In short, the response of the resonance frequency and damping factor are measured according to the Reynolds number, which is varied by changing the air pressure. In their study formulas are derived for the V-shaped cantilevers C and D from a MSCT/MLCT chip, which are the type of cantilevers studied in this paper.<sup>30</sup> The formulas for cantilever type C and D are respectively:

$$k = 140.94 \cdot \rho \cdot b_C^2 \cdot L_C \cdot \text{Re}^{-0.728+0.00915 \ln \text{Re}} f_R^2 \cdot Q \quad (7A)$$

$$k = 117.25 \cdot \rho \cdot b_D^2 \cdot L_D \cdot \text{Re}^{-0.700+0.0215 \ln \text{Re}} f_R^2 \cdot Q \quad (7B)$$

with  $b_C$  or  $b_D$  the width of one of the two cantilever beams (Fig. 1B),  $L_C$  or  $L_D$  the length of the cantilever and the Reynolds numbers as in Eq. 6B.

### Cantilever tilt

Usually cantilevers are mounted at a small angle (6-12°; see Table S1) with respect to the horizontal (scan) direction in an AFM to prevent contact between the cantilever chip and the sample. Forces, however, are applied in the direction of the movement of the cantilever, implying that they are also under an angle in respect to the cantilever.<sup>45</sup> For spring constants determined by the thermal noise method, this effect cancels out because the InvOLS is measured under an angle too. By the Sader method the *intrinsic* spring constant (i.e. the actual value) of the cantilever is determined. This implies that spring constants should be corrected by a factor  $1/\cos^2 \alpha$ , where  $\alpha$  is the tilt angle. However, to compare spring constants measured on several AFMs exhibiting different tilt angles, those obtained with the thermal noise method are corrected by a factor  $\cos^2 \alpha$ . So the relation between the effective (thermal noise) and intrinsic (Sader) spring constants is:

$$k_{\text{effective}} = \frac{k_{\text{intrinsic}}}{\cos^2 \alpha} \quad (8)$$

An additional correction is needed if the tip protruding from the cantilever is long compared to the cantilevers length.<sup>45</sup> However, this additional correction applies only to rectangular cantilevers and, moreover, in most cases results are identical to the results given by Eq. 8, including the present study.

## Results & Discussion

### Physical characteristics of the cantilevers used for calibration

Tested cantilevers are of the MSCT/MLCT-type; one of the most applied types of cantilevers in AFM force spectroscopy studies, due to their low spring constant, uniformity, robustness, and affordability. We choose to study only the softest cantilevers of the chip, i.e. B, C, and D. The dimensions of cantilevers B, C and D, needed for the Sader method, were determined by scanning electron microscopy (SEM). In the SEM image (Fig. 1A) the arrangement of cantilevers B (rectangular), C and D (V-shaped) is shown. The dimensions of each cantilever on three MLCT- and three MSCT-cantilever chips were determined and the mean values are given in Table 2 (see Fig. 1B for labels). The differences between the manufacturer's specifications and the measured dimensions of the cantilevers were smaller than  $\pm 1.9\%$  for length and  $\pm 7.9\%$  for width. Furthermore, cantilevers from the MLCT and MSCT chips are comparable in size with only a measured variation of  $\pm 3.9\%$  in width, which is similar to the measured error for SEM of  $\pm 3.3\%$ . While, it can be concluded that the manufacturer's nominal dimensions in this specific case are in good agreement with the measured ones, we observed that nominal values

provided by manufacturers are insufficiently accurate ( $\pm 10\text{--}25\%$ ). Therefore, a check of the dimensions is always recommended.

Another important parameter is temperature, as thermal fluctuations of the cantilever depend on it. The temperature at the location of the cantilever in its holder was measured in a working AFM and was usually found to be higher (up to  $6^\circ\text{C}$ ) than room temperature. Based on Eq. 5, neglecting this temperature difference would imply a systematic error of  $\sim 2\%$ . Therefore, actual (measured) temperatures were used in the present study.

### Calibration of the cantilever spring constant by the thermal noise method

Cantilevers are calibrated with the thermal noise method by using the protocol as given in the Supporting Material. After InvOLS measurements, thermal noise spectra were obtained with this protocol. In these spectra the fundamental resonance peak was fitted with the SHO model of Eq. 3, to obtain the resonance frequency  $f_R$ , the quality factor  $Q$ , the zero frequency power  $A_o$ , and the power of the white noise baseline  $y_o$  (Fig. 1C).

The spring constant of the longest type of cantilevers (C-type) was calculated with Eq. 5 using the derived parameters  $f_R$ ,  $Q$  and  $A_o$ . We decided not to calibrate the shorter B- and D-type cantilevers with the thermal noise method to prevent damage of the longer C-type cantilever. This damage might occur when measuring the InvOLS for the

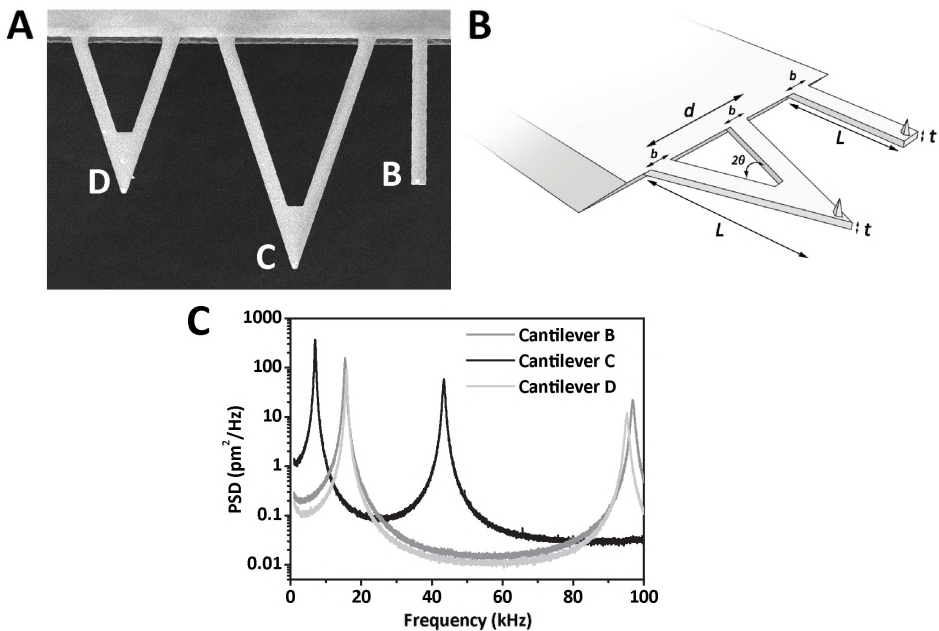


**Figure 1: Characteristics of the three types of studied cantilevers**

(A) SEM image of rectangular cantilever B and V-shaped cantilevers C and D on a MSCT chip. (B) Scheme of a rectangular and V-shaped cantilever with the symbols for the dimensions as used throughout the study. (C) Thermal noise spectra of cantilevers B, C, and D on chip MLCT1 as determined with AFM system VI at a sampling rate of 200 kHz. The PSD is semi-logarithmic scaled against the frequency to represent cantilevers mutual power relation. The primary and secondary thermal noise peaks are visible for all three cantilevers. In the spectra the white noise level is low, but shows a  $1/f$  noise floor. The resonance frequencies and quality factors of the primary peaks are  $f_R = 14.5, 6.3, 14.5$  kHz and  $Q = 23.1, 14.9, 25.6$  for cantilevers B, C, and D, respectively.

shorter cantilevers, during which the C-type cantilever would come into full contact with the substrate. In Fig. 2D, the result is shown of calibrating 10 C-type MLCT/MSCT-cantilevers (see Table S2D for corresponding values). In both Fig. 2D and Table S2D, the intrinsic spring constant is presented, i.e. corrected for cantilever tilt by Eq. 8. In Fig. 2D only the spring constants determined on AFMs [I-IX] are shown. On system X, which was optimized for fast sampling, it was impossible to perform calibrations with the thermal noise method; due to the small  $z$ -range of the piezo scanner the required InvOLS could not be determined, as the cantilever did not detach from the substrate, due to strong electrostatic interactions.

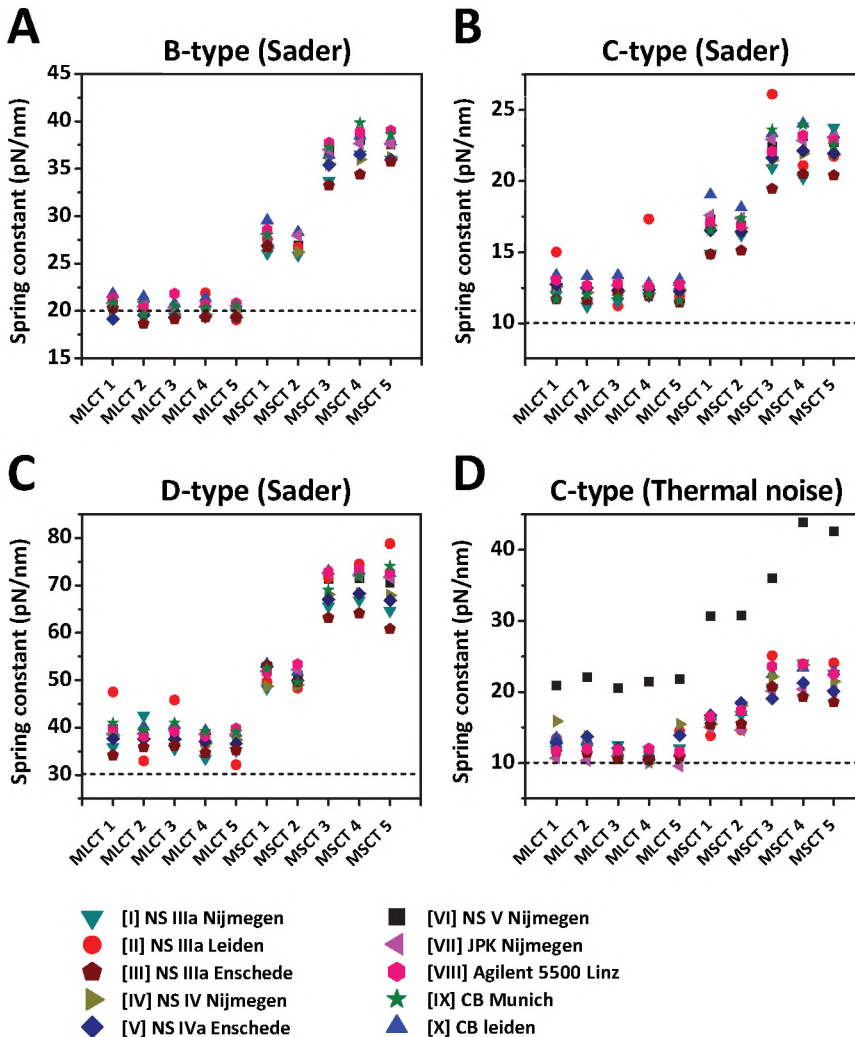


**Figure 2: Cantilever calibration with the thermal noise method and Sader method**

The mean spring constants ( $N = 5$ ) found for calibrating cantilevers of MLCT and MSCT chips on 10 AFM systems. (A) Using the Sader method to calibrate cantilevers of the B-type, (B) the C-type, (C) and the D-type. (D) Calibrating the C-type cantilevers with the thermal noise method. The different AFMs are represented by different symbols. The cantilever spring constants as given by the manufacturer are indicated by dotted lines (20, 10, 30 pN/nm).

When comparing the results obtained on the MLCT and MSCT cantilevers, cantilevers from the same wafer, i.e. MLCT 1–5, MSCT 1–2, and MSCT 3–5, were found to nearly exhibit the same spring constant, within an error of  $\sim 4\%$  (Fig. 2D). However, comparing batches these cantilevers vary substantially in spring constant. Moreover, the measured values of cantilevers MSCT 3–5 are more than double those of the nominal value given by the manufacturer (10 pN/nm). This illustrates the importance of manual cantilever calibration instead of simply taking the provided spring constant, which could lead to errors up to  $\sim 125\%$ .

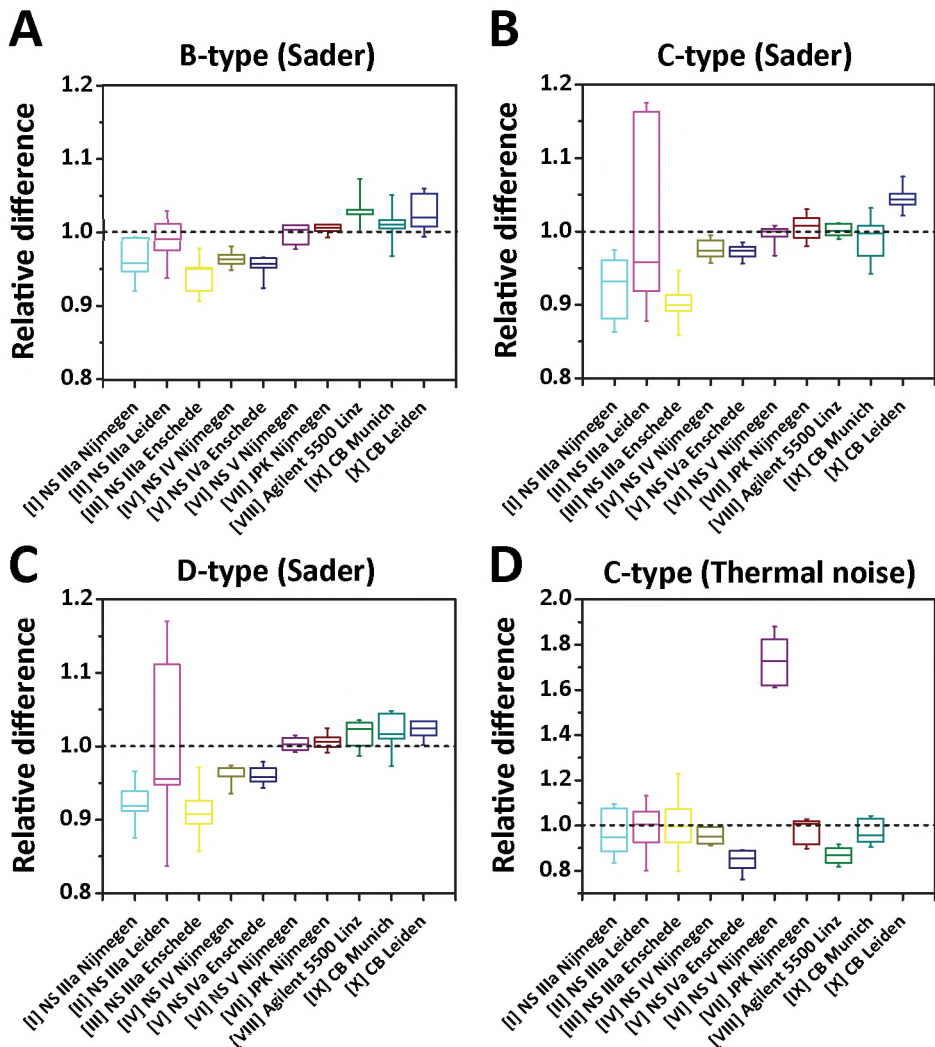


**Figure 3: Comparison of the accuracies of the AFMs**

Box plot in which the accuracies of 10 AFMs are compared by normalizing the found cantilever spring constants per system to the mean spring constant found for systems [IV-X] by the Sader method. The normalized value is set to 1 and is indicated by the dotted line in all plots. The accuracy of the systems found by applying the Sader method is plotted in, (A) in the case of the B-type, (B) C-type, and (C) D-type. (D) The accuracy of calibrating the C-type applying the thermal noise method. The borders of the boxes represent the 25-75% levels, the line in the box the median and the whiskers the 10-90% levels. Note the difference in scale.

### Calibration of the cantilever spring constant by the Sader method

In order to apply the (direct) Sader method, the resonance frequency  $f_r$  and the quality factor  $Q$  of the cantilevers must be determined first, which are obtained by fitting the thermal noise spectrum of the cantilever. From the obtained parameters and the dimensions of the cantilever (Table 2), the spring constant is calculated by using Eqs. 6 or 7.

For the C-type cantilevers the spring constants are instantly calculated from the earlier obtained thermal noise method data and are shown in Fig. 2B and Table S2B. The thermal noise spectra of cantilevers B and D were determined in a similar way, only the laser was re-aligned to these cantilevers, which were kept at all times well above the substrate. The corresponding spectra were analyzed to obtain  $f_r$  and  $Q$ . As  $A_o$  is not needed for further analysis, it was not necessary to measure the InvOLS in this case. In this way, it is now possible to also calibrate the shorter cantilevers on the chip. The spring constants of cantilevers B and D were determined on all 10 AFMs and are shown in Fig. 2A, C and Table S2A, C, for the B- and D-type of the 10 MLCT/MSCT-chips, respectively. The obtained values are less scattered, and have the same mean value as those of the thermal noise method.

### Comparison of the results obtained with the Sader method on different AFMs

To get a better insight in the performance of every AFM alone and to compare them with each other, the data were normalized to the mean spring constant calculated for every cantilever (Table 3). This calculation was executed on the data of all AFMs except the NS IIIa systems [I–III], which show many outliers. In addition, only data obtained with the Sader method were used, as the thermal noise method was only applied to C-type cantilevers.

The data obtained with the Sader method on the rectangular B-cantilevers show relatively uniform results on all AFM systems (Fig. 3A). The observed variation on the normalized spring constant is 1–3% for the different AFMs, and by considering all these results the variation in spring constant is within a  $\pm 6\%$  error in relation to the overall mean cantilever spring constant. For the V-shaped cantilevers of the C- and D-type, the results are in good agreement with the mean cantilever spring constant except for the results obtained on the three NS IIIa systems (Fig. 3B, C). Just keeping these three systems out of consideration for a moment; the variation in mean spring constants for each individual AFM is  $\pm 2\%$  for C-type as well as for D-type cantilevers, which is similar to those obtained for B-type cantilevers. Taking all these AFMs [IV–X] together, a deviation of  $\pm 5\%$  is found for both the C- and D-type cantilever. Now considering the normalized spring constants obtained on the NS IIIa systems, we observe a systematic error of  $-4\%$  ( $\pm 7\%$ ) (Fig. 3B,C). This implicates that the obtained spring constants are underestimated and less accurate, especially on system II. The explanation for this is that the thermal noise data were acquired differently on the NS IIIa systems with respect to AFMs IV–IX. The thermal noise data for I & III, and II were acquired internally and externally, respectively. As it is not a priori clear how many samplings are necessary to get a spectrum with an acceptable signal-to-noise ratio, the acquisition time may be a too short. This then results in less thermal noise data processed, and in spectra that can be fitted less accurately. The results from instruments I–III demonstrate this pitfall for spring constant calibrations. On the other hand, appropriate use of external data acquisition is shown by instrument X.

**Table 3. Spring constants of the cantilevers (pN/nm)\***

Chip name	B-type	C-type			D-type		
	$k_{mean}$	$k_{mean}$	Indirect Sader	Gibson	$k_{mean}$	Indirect Sader	Gibson
MLCT 1	20.7	12.9	9.9	9.9	39.1	31.0	30.8
MLCT 2	20.3	12.8	9.7	9.6	38.8	30.3	30.3
MLCT 3	20.3	12.8	9.8	10.1	39.1	30.4	31.0
MLCT 4	20.3	12.5	9.8	9.8	38.2	30.4	30.3
MLCT 5	20.3	12.6	9.7	9.8	38.4	30.4	30.0
MSCT 1	27.9	17.3	13.9	14.1	52.0	44.7	41.5
MSCT 2	27.3	16.9	13.6	13.6	51.0	43.8	40.7
MSCT 3	36.6	22.2	18.3	17.8	70.6	58.7	55.7
MSCT 4	37.9	23.0	18.9	18.3	71.2	60.8	58.2
MSCT 5	37.5	22.7	18.7	18.4	70.9	60.2	56.7

\* Mean values are determined on 10 different AFMs in 5 subsequent measurements (see also Table S2)

### Comparison of the results obtained with the thermal noise method on different AFMs

The data obtained with the thermal noise method indicate that the mean determined spring constants of the C-type cantilevers are equal to those determined by the Sader method (Fig. 3D). However, for most AFMs the error is significant ( $\pm 3$  to  $\pm 11\%$ ). Having a closer look at the calibrations with the NS IIIa systems I–III, the spring constants are more accurately determined with the thermal noise method than with the Sader method. In fact, the mean spring constants determined are not underestimated. However, AFM systems V, VI, and VIII performed badly applying this method and are systematically off from the mean. Most likely, for systems V and VIII this can be attributed to piezo-scanner calibration, as these systems are calibrated with a grid of which the given depth deviates from the true value, as determined afterwards. An error of  $\pm 5\%$  herein, which is reasonable from our own observations, leads to an error in the spring constant of  $\pm 10\%$  as the calibration error scales quadratically with the depth. Another cause for the observed higher variations might be static interactions due to charging under low humidity. Actually, the soft C-cantilevers hardly got off the substrate during the InvOLS measurement, leading to non-ideal force curves in which the InvOLS is under- or overestimated. The accuracy of the thermal noise method determined in this study agrees well with the estimated error of  $\pm 8\%$  reported by Ohler et al.,<sup>33</sup> which they mainly relate to the error in the InvOLS. In addition, we found that the error in z-calibration of the AFM has to be taken into account and advise to calibrate it with great care to avoid error propagation.

Still remains the overestimation by  $\sim 74\%$  of spring constants calibrated in system VI with the thermal noise method. In fact, on this system high quality calibrations could be performed with the Sader method (Fig. 3A–C). Moreover, this system was calibrated with the same calibration grid as systems I, IV and VII, suggesting that something completely different is the cause of this overestimation. Most likely, a defect in the implemented hard- or software related to the InvOLS measurements gives rise to this error, for which the system is under revision.

In conclusion, the above described cases of systems V, VI, and VIII nicely illustrate another interesting finding from our round robin experiment. The comparison with the other systems revealed systematic errors on these systems, which were not foreseen. Therefore, we recommend users to check consistency for the cantilever calibration on an AFM with more than one method to verify the evaluation implemented in the instrument.



### The Gibson and indirect Sader method for V-shaped cantilevers

Next to direct cantilever spring constant calibration, methods also exist in which the spring constant is determined indirectly. Different theories have been described in literature, in which the spring constant of one (rectangular) cantilever can be related to the spring constant of other cantilevers located on the same chip, assuming that the material properties and thickness for each cantilever on the chip are approximately the same.<sup>29,39</sup> These methods are described as alternatives for the calibration of cantilevers that could not be calibrated due to technical difficulties or with differently shaped cantilevers. In our case, this implies that for the MLCT/MSCT-cantilever chips, the spring constant obtained for the rectangular cantilever B can be used to calculate the spring constant of the V-shaped cantilevers C and D on the same chip. Two different methods were selected to compare the accuracy of such indirect calibration approaches to the direct Sader method and thermal noise methods. First, we applied the indirect method described by Sader et al.<sup>29</sup> that combines the Euler-Bernoulli beam theory<sup>46</sup> for rectangular cantilevers and the parallel beam approximation (PBA)<sup>47</sup> for V-shaped cantilevers. This leads to the following equation for the spring constants of cantilevers C and D from B:

$$k_{C/D} = \frac{2k_B \cdot L_B^3 \cdot d_{C/D}}{L_{C/D}^3 \cdot b_B} \cos\theta_{C/D} \left[ 1 + \frac{4b_{C/D}^3}{d_{C/D}^3} (3\cos\theta_{C/D} - 2) \right]^{-1} \quad (9)$$

where  $\theta_{C/D}$  is the half angle in between the two beams of the V-shaped cantilevers C or D and  $d_{C/D}$  the full width at the base of the cantilevers (Fig. 1B). Secondly, the indirect method described by Gibson et al.<sup>39</sup> was used, in which the spring constants of two cantilevers ( $k_1$  and  $k_2$ ) are related via:

$$k_1 = \frac{n_1 \cdot A_1}{n_2 \cdot A_2} \cdot \left( \frac{f_1}{f_2} \right)^2 \cdot k_2 \quad (10)$$

where,  $n_1/n_2$  is the ratio between the shape factors of the cantilevers,  $A_1/A_2$  between their areas and  $f_1/f_2$  between their resonance frequencies. The SEM images (Fig. 1A) were used to determine the areas of the cantilevers. The shape factors were derived by using data from Sader et al.,<sup>48</sup> from cantilever dimensions (Table 2) and a Poisson ratio of 0.24. For cantilever C related to B, this resulted in  $n_C \cdot A_C / n_B \cdot A_B = 2.486$  and for cantilever D in  $n_D \cdot A_D / n_B \cdot A_B = 1.467$ .

Subsequently, the spring constants for the C- and D-type cantilevers were calculated by Eqs. 9, 10 by using the earlier obtained spring constants of the B-type, and are given in Table 3. The spring constants calculated with the indirect Sader method are consequently  $21 \pm 2\%$  and  $18 \pm 3\%$  underestimated for cantilevers C and D, respectively. In addition, the results calculated with the Gibson method are also  $21 \pm 2\%$  underestimated for both C and D. However, when the similar shaped C- and D-cantilevers are compared, the spring constants extrapolated from one to the other are well related within a  $\pm 1\%$  error (data not shown). One explanation for the discrepancy of  $\sim 20\%$  between directly or indirectly obtained spring constants can be that in both indirect methods the V-shaped cantilever is considered as two beams connected under an angle, which does not account for their real shape.<sup>47</sup> Besides, both indirect methods assume a uniform material density of the cantilevers, although in reality they consist of stacked layers of  $\text{SiN}_4$  and gold. Probably, corrections to Eq. 9, as for example suggested by Hazel and Tsukruk,<sup>49</sup> would better describe V-shaped and bi-component cantilevers. In conclusion, indirect methods can

be used to calculate spring constants of cantilevers, only when the cantilevers have the same shape.

### Biological implications for AFM Force Spectroscopy

The importance of accurate calibration of an AFM cantilever becomes evident when AFM Force Spectroscopy is used to study, e.g. biological receptor-ligand interactions at the single molecule and/or single cell level. If in one study rupture forces of a ligand-receptor bond are measured with an erroneously calibrated cantilever, upon comparison with rupture forces from another study the conclusions drawn on the differences in dynamic compliance of the interactions might be wrong. Generally, these comparisons between rupture forces are done at a particular loading rate (rate of the increase in force). Furthermore, the rupture forces and loading rates are such related that data will appear as a straight line in a semi-logarithmical plot of the force spectrum (Fig. 4) which is described by the Bell model.<sup>50</sup> In this model, the mean rupture force  $F_{rup}$  is given by:

$$F_{rup} = \frac{k_B T}{x_\beta} \ln\left(\frac{x_\beta}{k_{off}^0 k_B T}\right) + \ln(r_f) \quad (11)$$

where  $k_{off}^0$  is the dissociation rate in the absence of a pulling force,  $x_\beta$  the mechanical bond-length, and  $r_f$  the loading rate.<sup>51, 52</sup> The Bell model parameters  $k_{off}^0$  and  $x_\beta$  characterize the micromechanical properties of the ligand-receptor interaction under study and model their intra-molecular energy landscapes.

Now, if we assume an error of  $\pm 20\%$  in cantilever spring constant – which is reasonable based on, e.g. piezo-scanner error ( $\pm 10\%$ ), rectangular instead of V-shaped correction factor ( $\pm 7\%$ ) and ignoring correction factors ( $\pm 31\%$ ) – then the error in the observed rupture forces and loading rates is  $\pm 20\%$ . In the spectra this error causes a linear shift up or down (Fig. 4; light and dark gray lines) of the data points. By fitting, we found that the error of  $\pm 20\%$  hardly influenced the Bell parameter  $k_{off}^0$ , but resulted in an error of  $\pm 20\%$  for  $x_\beta$ . As a consequence, we conclude that when micromechanical

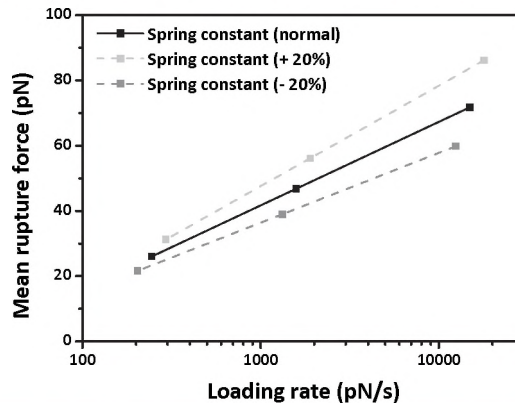


**Figure 4: The influence of under- or overestimated spring constants on the force spectrum**

The relation between the mean rupture force ( $F_{rup}$ ) and the loading rate ( $r_f$ ) is shown in a force spectrum. Plotted is the change in obtained force spectrum by an error in spring constant of  $\pm 20\%$ . The data presented in this example are those acquired for the cell adhesion ligand-receptor bond ALCAM-ALCAM, as obtained in Ref.<sup>54</sup> The corresponding Bell parameters are  $k_{off}^0 = 2.1 \text{ s}^{-1}$  and  $x_\beta = 0.37 \text{ nm}$ . The mean rupture forces as well as the loading rates are raised or lowered according to an error of  $+20\%$  (light gray) and  $-20\%$  (dark gray). By fitting the newly obtained force spectra, new Bell parameters are found for these two extremes, which are  $k_{off}^0 = 2.1 \text{ s}^{-1}$  and  $x_\beta = 0.31 \text{ nm}$  (for  $+20\%$ ) and  $k_{off}^0 = 2.1 \text{ s}^{-1}$  and  $x_\beta = 0.45 \text{ nm}$  (for  $-20\%$ ).

properties of ligand-receptors in AFM force spectroscopy are compared by means of their Bell parameters,<sup>53, 54</sup> it is safe to only compare the  $k_{off}^0$ -values from different studies, rather than the  $x_{\beta}$ -values or the rupture forces at a specific loading rate.<sup>14</sup> However, having a commonly adopted protocol with an high accuracy makes comparisons of different studies more trustworthy.

Force spectroscopy, but also other scientific areas applying AFM in which quantitative measurements of forces are needed, would benefit from a uniform calibration protocol leading to an increase in accuracy of the obtained parameters, independent on AFM, cantilever, and operator. For force spectroscopy, we here propose this improved fast and versatile method to calibrate *in situ* functionalized AFM cantilevers, preferably applied in air, although also possible in liquids. Upon application in liquid, damping of the cantilever becomes substantial and extra care should be taken in fitting and acquiring the data, especially due to commercial AFM limitations.<sup>38</sup> Note that InvOLS measurements performed in air are related to those in liquid by the difference in refractive indexes of the media.<sup>55</sup>

In view of our findings, a combination of the direct Sader method together with calculating the InvOLS (see also Supplementary Materials) – without getting into contact with a substrate, as described by Higgins et al.<sup>56</sup> – yields the best results.

## Conclusions

In a round robin experiment we compared cantilever calibration methods on different AFMs. By comparing the results obtained on a single AFM versus the mean of 10 AFMs we found that the accuracies are ~6% vs. ~15% for the thermal noise method and ~3% vs. ~7% for the direct Sader method. This demonstrates that – even in the case of using a well-defined protocol – ‘relative’ errors between AFMs can be substantial. The main cause for the error of the thermal noise method is that it suffers from systematic errors in determining the correct InvOLS, which can be mainly attributed to discrepancies in the z-calibrations of the AFM piezo scanner. On the other hand, the accuracy of the direct Sader method is predominantly defined by the quality of data acquisition of the thermal fluctuations of the cantilever. Another important factor is the accuracy of measuring the dimensions of the cantilever, especially the width, which normally can be measured with a ~3% accuracy by SEM. While this extra step of measuring the dimensions of every cantilever from a different wafer is intrinsic more time-consuming, clear advantages of the Sader method are: its higher accuracy and the time saved by calculating instead of measuring the InvOLS.

In addition, the simultaneous implementation and comparison of both calibration methods represents a convenient and effective way to check the proper hard- and software operation of an AFM instrument. Furthermore, the ‘sum’ of the both methods leads to a higher overall accuracy due to the elimination of systematic errors. In general, the systematic errors described in this study can be regarded as representative for errors encountered by any AFM user. It should be noted that, although this study focuses on soft cantilevers calibrated in air, the same two methods can be applied to stiffer cantilevers as well as to cantilevers in liquid.

Finally, we demonstrated that biophysical parameters obtained in force spectroscopy studies suffer from inaccurately derived spring constants. Therefore, a standard calibration protocol, as described in this report, will allow a more quantitative comparison of biophysical AFM results from different laboratories.

## Acknowledgments

This study was supported by NanoNed, the Dutch nanotechnology programme of the Ministry of Economic Affairs and in part financed by a BIO-LIGHT-TOUCH grant (FP6-2004-NEST-C-1-028781) and Immunomap grant (MRTN-CT-2006-035946) of the European Union to C.G.F. I.Y.P and G.J.V. thank the Dutch Polymer Institute for financial support (DPI-695). A.C. and P.J. were supported by VENI grants (916.66.028 and 700.57.401) of the Netherlands Organization for Scientific Research (NWO).

## References

1. **G. Binnig, C. F. Quate, C. Gerber** (1986). Atomic force microscope. *Phys. Rev. Lett.*, **56**, 930-933.
2. **P. Hinterdorfer, Y. F. Dufrène** (2006). Detection and localization of single molecular recognition events using atomic force microscopy. *Nat. Methods*, **3**, 347-355.
3. **F. Oesterhelt, D. Oesterhelt, M. Pfeiffer, A. Engel, H. E. Gaub, D. J. Muller** (2000). Unfolding pathways of individual bacteriorhodopsins. *Science*, **288**, 143-146.
4. **E. L. Florin, V. T. Moy, H. E. Gaub** (1994). Adhesion forces between individual ligand-receptor pairs. *Science*, **264**, 415-417.
5. **V. T. Moy, E. L. Florin, H. E. Gaub** (1994). Intermolecular forces and energies between ligands and receptors. *Science*, **266**, 257-259.
6. **M. Rief, H. Clausen-Schaumann, H. E. Gaub** (1999). Sequence-dependent mechanics of single DNA molecules. *Nat. Struct. Mol. Biol.*, **6**, 346-349.
7. **K. O. Greulich** (2005). Single-molecule studies on DNA and RNA. *ChemPhysChem*, **6**, 2458-2471.
8. **P. Frederix, P. D. Bosshart, A. Engel** (2009). Atomic Force Microscopy of Biological Membranes. *Biophysical Journal*, **96**, 329-338.
9. **M. Rief, M. Gautel, F. Oesterhelt, J. M. Fernandez, H. E. Gaub** (1997). Reversible unfolding of individual titin immunoglobulin domains by AFM. *Science*, **276**, 1109-1112.
10. **M. I. Giannotti, G. J. Vancso** (2007). Interrogation of single synthetic polymer chains and polysaccharides by AFM-based force spectroscopy. *ChemPhysChem*, **8**, 2290-2307.
11. **M. Grandbois, M. Beyer, M. Rief, H. Clausen-Schaumann, H. E. Gaub** (1999). How strong is a covalent bond? *Science*, **283**, 1727-1730.
12. **S. Zou, H. Schönherr, G. J. Vancso** (2005). Force spectroscopy of quadruple H-bonded dimers by AFM: dynamic bond rupture and molecular time-temperature superposition. *J Am Chem Soc*, **127**, 11230-11231.
13. **M. Benoit, D. Gabriel, G. Gerisch, H. E. Gaub** (2000). Discrete interactions in cell adhesion measured by single-molecule force spectroscopy. *Nat. Cell Biol.*, **2**, 313-317.
14. **J. Helenius, C. P. Heisenberg, H. E. Gaub, D. J. Muller** (2008). Single-cell force spectroscopy. *J. Cell Sci.*, **121**, 1785-1791.
15. **S. K. Kufer, E. M. Puchner, H. Gump, T. Liedl, H. E. Gaub** (2008). Single-molecule cut-and-paste surface assembly. *Science*, **319**, 594-596.
16. **H. G. Hansma, K. J. Kim, D. E. Laney, R. A. Garcia, M. Argaman, M. J. Allen, S. M. Parsons** (1997). Properties of biomolecules measured from atomic force microscope images: A review. *Journal of Structural Biology*, **119**, 99-108.
17. **R. Garcia, R. Perez** (2002). Dynamic atomic force microscopy methods. *Surface Science Reports*, **47**, 197-301.
18. **C. A. Clifford, M. P. Seah** (2005). The determination of atomic force microscope cantilever spring constants via dimensional methods for nanomechanical analysis. *Nanotechnology*, **16**, 1666-1680.
19. **J. M. Neumeister, W. A. Ducker** (1994). Lateral, Normal, and Longitudinal Spring Constants of Atomic-Force Microscopy Cantilevers. *Rev. Sci. Instrum.*, **65**, 2527-2531.
20. **J. E. Sader, L. White** (1993). Theoretical-Analysis of the Static Deflection of Plates for Atomic-Force Microscope Applications. *J. Appl. Phys.*, **74**, 1-9.
21. **Y. Q. Li, N. J. Tao, J. Pan, A. A. Garcia, S. M. Lindsay** (1993). Direct Measurement of Interaction Forces between Colloidal Particles Using the Scanning Force Microscope. *Langmuir*, **9**, 637-641.
22. **Y. I. Rabinovich, R. H. Yoon** (1994). Use of Atomic-Force Microscope for the Measurements of Hydrophobic Forces between Silanated Silica Plate and Glass Sphere. *Langmuir*, **10**, 1903-1909.
23. **A. Torii, M. Sasaki, K. Hane, S. Okuma** (1996). A method for determining the spring constant of cantilevers for atomic force microscopy. *Meas. Sci. Technol.*, **7**, 179-184.
24. **S. K. Jericho, M. H. Jericho** (2002). Device for the determination of spring constants of atomic force microscope cantilevers and micromachined springs. *Rev. Sci. Instrum.*, **73**, 2483-2485.
25. **K. H. Chung, S. Scholz, G. A. Shaw, J. A. Kramar, J. R. Pratt** (2008). SI traceable calibration of an instrumented indentation sensor spring constant using electrostatic force. *Rev. Sci. Instrum.*, **79**, 095105.
26. **E. D. Langlois, G. A. Shaw, J. A. Kramar, J. R. Pratt, D. C. Hurley** (2007). Spring constant calibration of atomic force microscopy cantilevers with a piezosensor transfer standard. *Rev. Sci. Instrum.*, **78**, 10.
27. **J. P. Cleveland, S. Manne, D. Bocek, P. K. Hansma** (1993). A Nondestructive Method for Determining the Spring Constant of Cantilevers for Scanning Force Microscopy. *Rev. Sci. Instrum.*, **64**, 403-405.
28. **J. L. Hutter, J. Bechhoefer** (1993). Calibration of Atomic-Force Microscope Tips. *Rev. Sci. Instrum.*, **64**, 1868-1873.
29. **J. E. Sader, J. W. M. Chon, P. Mulvaney** (1999). Calibration of rectangular atomic force microscope cantilevers. *Rev. Sci. Instrum.*, **70**, 3967-3969.

30. **J. E. Sader, J. Pacifico, C. P. Green, P. Mulvaney** (2005). General scaling law for stiffness measurement of small bodies with applications to the atomic force microscope. *J. Appl. Phys.*, **97**, 1249031-1249037.
31. **B. Ohler** (2007). Cantilever spring constant calibration using laser Doppler vibrometry. *Rev. Sci. Instrum.*, **78**, 0637011-0637015.
32. **S. Cook, T. E. Schaffer, K. M. Chynoweth, M. Wigton, R. W. Simmonds, K. M. Lang** (2006). Practical implementation of dynamic methods for measuring atomic force microscope cantilever spring constants. *Nanotechnology*, **17**, 2135-2145.
33. **B. Ohler** (2007). Practical Advice on the Determination of Cantilever Spring Constants. *Veeco Instrum. Inc. Internal Publ.* 1-12.
34. **N. A. Burnham, X. Chen, C. S. Hodges, G. A. Matei, E. J. Thoreson, C. J. Roberts, M. C. Davies, S. J. B. Tendler** (2003). Comparison of calibration methods for atomic-force microscopy cantilevers. *Nanotechnology*, **14**, 1-6.
35. **C. T. Gibson, D. A. Smith, C. J. Roberts** (2005). Calibration of silicon atomic force microscope cantilevers. *Nanotechnology*, **16**, 234-238.
36. **H. J. Butt, M. Jaschke** (1995). Calculation of Thermal Noise in Atomic-Force Microscopy. *Nanotechnology*, **6**, 1-7.
37. **R. W. Stark, T. Drobek, W. M. Heckl** (2001). Thermomechanical noise of a free v-shaped cantilever for atomic-force microscopy. *Ultramicroscopy*, **86**, 207-215.
38. **T. Pirzer, T. Hugel** (2009). Atomic force microscopy spring constant determination in viscous liquids. *Rev. Sci. Instrum.*, **80**, 035110.
39. **C. T. Gibson, D. J. Johnson, C. Anderson, C. Abell, T. Rayment** (2004). Method to determine the spring constant of atomic force microscope cantilevers. *Rev. Sci. Instrum.*, **75**, 565-567.
40. **R. Proksch, T. E. Schaffer, J. P. Cleveland, R. C. Callahan, M. B. Viani** (2004). Finite optical spot size and position corrections in thermal spring constant calibration. *Nanotechnology*, **15**, 1344-1350.
41. **T. E. Schaffer** (2005). Calculation of thermal noise in an atomic force microscope with a finite optical spot size. *Nanotechnology*, **16**, 664-670.
42. **D. A. Walters, J. P. Cleveland, N. H. Thomson, P. K. Hansma, M. A. Wendman, G. Gurley, V. Elings** (1996). Short cantilevers for atomic force microscopy. *Rev. Sci. Instrum.*, **67**, 3583-3590.
43. **J. W. M. Chon, P. Mulvaney, J. E. Sader** (2000). Experimental validation of theoretical models for the frequency response of atomic force microscope cantilever beams immersed in fluids. *J. Appl. Phys.*, **87**, 3978-3988.
44. **J. E. Sader** (1998). Frequency response of cantilever beams immersed in viscous fluids with applications to the atomic force microscope. *J. Appl. Phys.*, **84**, 64-76.
45. **J. L. Hutter** (2005). Comment on tilt of atomic force microscope cantilevers: effect on spring constant and adhesion measurements. *Langmuir*, **21**, 2630-2632.
46. **W. C. Young, R. G. Budynas, R. J. Roark** (2001). Roark's formulas for stress and strain.
47. **J. E. Sader** (1995). Parallel Beam Approximation for V-Shaped Atomic-Force Microscope Cantilevers. *Rev. Sci. Instrum.*, **66**, 4583-4587.
48. **J. E. Sader, I. Larson, P. Mulvaney, L. R. White** (1995). Method for the Calibration of Atomic-Force Microscope Cantilevers. *Rev. Sci. Instrum.*, **66**, 3789-3798.
49. **J. L. Hazel, V. V. Tsukruk** (1999). Spring constants of composite ceramic/gold cantilevers for scanning probe microscopy. *Thin Solid Films*, **339**, 249-257.
50. **G. I. Bell** (1978). Models for the specific adhesion of cells to cells. *Science*, **200**, 618-627.
51. **E. Evans, K. Ritchie** (1997). Dynamic strength of molecular adhesion bonds. *Biophys. J.*, **72**, 1541-1555.
52. **D. F. Tees, R. E. Waugh, D. A. Hammer** (2001). A microcantilever device to assess the effect of force on the lifetime of selectin-carbohydrate bonds. *Biophys. J.*, **80**, 668-682.
53. **P. Panorchan, M. S. Thompson, K. J. Davis, Y. Tseng, K. Konstantopoulos, D. Wirtz** (2006). Single-molecule analysis of cadherin-mediated cell-cell adhesion. *J. Cell Sci.*, **119**, 66-74.
54. **J. te Riet, A. W. Zimmerman, A. Cambi, B. Joosten, S. Speller, R. Torensma, F. N. van Leeuwen, C. G. Figdor, F. de Lange** (2007). Distinct kinetic and mechanical properties govern ALCAM-mediated interactions as shown by single molecule force spectroscopy. *J. Cell Sci.*, **120**, 3965-3976.
55. **E. Tocha, J. Song, H. Schonherr, G. J. Vancso** (2007). Calibration of friction force signals in atomic force microscopy in liquid media. *Langmuir*, **23**, 7078-7082.
56. **M. J. Higgins, R. Proksch, J. E. Sader, M. Polcik, S. Mc Endoo, J. P. Cleveland, S. P. Jarvis** (2006). Noninvasive determination of optical lever sensitivity in atomic force microscopy. *Rev. Sci. Instrum.*, **77**, 013701-013705.

Supporting Material: Tables

**Table S1: Detailed system information**

Abbreviation	System	Location	AFM software
NS IIIa	Veeco Multimode Nanoscope IIIa	Nijmegen (Figdor)	NS 4.43r6
NS IIIa	Veeco Multimode Nanoscope IIIa	Leiden (Oosterkamp)	NS 5.30
NS IIIa	Veeco Multimode Nanoscope IIIa	Enschede (Huskens)	NS 5.12r5
NS IV	Veeco Multimode Nanoscope IV	Nijmegen (Speller)	NS 6.12r1
NS IVa	Veeco Multimode Nanoscope IVa	Enschede (Vancso)	NS 6.13r1
NS V	Veeco Multimode Nanoscope V	Nijmegen (Speller)	NS 7.20r1
JPK	JPK NanoWizard I	Nijmegen (Rowan)	JPK v3.3.10
Agilent 5500	Agilent 5500	Linz (Hinterdorfer)	Custom-written in MATLAB
CB	Custom-built based on Asylum MFP-3D	Munich (Gaub)	Asylum/Igor 5.03
CB	Custom-built (CB)	Leiden (Oosterkamp)	Custom-written



Abbreviation	Spectral analysis software	Sampling rate	Temperature*	Cantilever tilt	Humidity	Extra system info
NS IIIa	IgorPro 6.0	62.5 kHz	24°C	12°	50%	JV-scanner
NS IIIa	Home-written in LabView	1.25 MS/s	29/32°C	12°	-	LN head
NS IIIa	IgorPro 6.0	62.5 kHz	27°C	12°	38%	EV-scanner
NS IV	Origin 8	62.5 kHz	29°C	12°	50%	EV-scanner, LN head
NS IVa	NS 6.13r1 ('SHO' button)	62.5 kHz	28°C	12°	38%	PF-scanner, LN head
NS V	NS 7.20r1 ('SHO' button)	200 kHz	29°C	12°	50%	EV-scanner
JPK	JPK v3.3.10	152 kHz	24°C	10°	45%	
Agilent 5500	Custom-written in MATLAB	220 kHz	22°C	8°	36%	
CB	Asylum/Igor 5.03	5 Mhz	22°C	6°	28%	CB-scanner
CB	Origin 7.5	10 MS/s	24/22°C	13°	-	

\* More than one temperature means measurements at different days

**Table S2 A: Spring constant of B-type cantilevers (pN/nm) (Sader method)**

Name	NS IIIa [I]	NS IIIa [II]	NS IIIa [III]	NS IV [IV]	NS IVa [V]	NS V [VI]	JPK [VII]	Agilent [VIII]	CB [IX]	CB [X]	Mean
MLCT 1-B	20.15	20.47	20.27	20.09	19.15	20.83	20.84	21.36	20.91	21.80	20.71
MLCT 2-B	20.68	20.85	18.67	19.89	19.56	20.54	20.47	20.28	19.61	21.47	20.26
MLCT 3-B	19.45	19.58	19.16	19.55	19.32	20.01	20.36	21.82	20.57	20.77	20.34
MLCT 4-B	20.21	21.89	19.33	19.62	19.38	20.54	20.45	20.70	20.37	21.33	20.34
MLCT 5-B	20.17	19.06	19.35	19.97	19.35	20.44	20.54	20.82	20.64	20.45	20.32
MSCT 1-B	26.07	27.59	26.76	26.63	26.89	27.23	28.13	28.57	28.01	29.54	27.86
MSCT 2-B	25.91	26.69	Broken	26.20	Broken	26.91	27.96	Broken	Broken	28.31	27.34
MSCT 3-B	33.72	36.38	33.23	35.52	35.39	36.99	37.02	37.75	37.26	36.43	36.62
MSCT 4-B	36.55	38.36	34.39	35.99	36.50	38.07	37.66	38.86	39.83	38.47	37.91
MSCT 5-B	35.99	37.69	35.73	36.17	35.97	37.55	37.64	39.03	38.59	37.84	37.54

**Table S2 B: Spring constant of C-type cantilevers (pN/nm) (Sader method)**

Name	NS IIIa [I]	NS IIIa [II]	NS IIIa [III]	NS IV [IV]	NS IVa [V]	NS V [VI]	JPK [VII]	Agilent [VIII]	CB [IX]	CB [X]	Mean
MLCT 1-C	12.04	15.02	11.69	12.58	12.72	12.98	12.73	13.06	13.00	13.38	12.91
MLCT 2-C	11.20	11.50	11.65	12.18	12.49	12.61	12.51	12.67	13.23	13.31	12.76
MLCT 3-C	11.57	11.23	12.11	12.24	12.35	12.35	12.68	12.80	13.19	13.38	12.78
MLCT 4-C	11.93	17.32	11.92	12.11	12.36	12.32	12.63	12.60	12.60	12.81	12.54
MLCT 5-C	12.23	11.91	11.46	12.39	12.27	12.12	12.69	12.71	12.39	13.07	12.55
MSCT 1-C	14.93	16.75	14.85	16.88	16.53	16.70	17.59	17.11	16.71	19.05	17.29
MSCT 2-C	16.21	16.36	15.12	16.71	16.45	16.15	17.38	16.87	16.25	18.13	16.87
MSCT 3-C	20.93	26.09	19.46	21.46	21.62	22.08	22.92	22.08	20.91	23.34	22.20
MSCT 4-C	20.23	21.09	20.47	21.93	22.14	22.39	22.84	23.20	22.90	24.03	22.95
MSCT 5-C	23.77	21.72	20.40	21.84	21.93	22.07	23.09	22.84	22.74	23.26	22.67

**Table S2 C: Spring constant of D-type cantilevers (pN/nm) (Sader method)**

Name	NS IIIa [I]	NS IIIa [II]	NS IIIa [III]	NS IV [IV]	NS IVa [V]	NS V [VI]	JPK [VII]	Agilent [VIII]	CB [IX]	CB [X]	Mean
MLCT 1-D	35.96	47.52	34.14	38.30	37.68	38.80	38.79	40.05	41.02	39.18	39.12
MLCT 2-D	42.52	32.96	35.89	37.59	37.54	39.32	38.72	38.23	39.62	40.21	38.75
MLCT 3-D	35.55	45.81	36.20	37.54	37.51	38.85	39.37	39.19	41.05	40.47	39.14
MLCT 4-D	33.44	36.43	34.67	36.63	37.05	38.29	38.57	38.26	39.22	39.32	38.19
MLCT 5-D	35.16	32.16	35.25	37.42	36.60	38.64	38.59	39.79	39.06	38.85	38.42
MSCT 1-D	48.32	49.68	53.09	48.67	52.90	52.93	51.88	51.66	52.57	53.38	52.00
MSCT 2-D	49.25	48.34	49.50	49.00	49.90	50.97	52.25	53.35	49.61	51.73	50.97
MSCT 3-D	65.58	71.63	63.15	68.08	67.01	71.39	72.66	72.85	69.05	72.98	70.58
MSCT 4-D	66.86	74.50	64.12	68.29	68.23	71.49	72.03	73.49	71.98	73.00	71.22
MSCT 5-D	64.63	78.81	60.80	67.86	66.86	70.50	71.74	72.70	74.07	72.49	70.89

**Table S2 D: Spring constant of C-type cantilevers (pN/nm) (Thermal noise method)**

Name	NS IIIa [I]	NS IIIa [II]	NS IIIa [III]	NS IV [IV]	NS IVa [V]	NS V [VI]	JPK [VII]	Agilent [VIII]	CB [IX]
MLCT 1-C	12.79	13.45	15.87	11.87	10.67	20.90	13.54	11.61	11.69
MLCT 2-C	13.71	12.81	13.69	12.15	10.35	22.03	13.12	11.39	11.99
MLCT 3-C	12.10	11.83	11.83	12.55	10.91	20.58	11.48	10.50	11.85
MLCT 4-C	10.46	11.63	10.01	11.85	10.11	21.45	11.37	10.46	12.03
MLCT 5-C	13.87	14.50	15.45	12.06	9.56	21.77	11.49	10.90	11.59
MSCT 1-C	16.70	13.83	15.44	15.88	15.04	30.66	16.49	15.40	16.52
MSCT 2-C	18.47	14.66	18.10	16.78	14.62	30.75	17.10	15.48	17.39
MSCT 3-C	19.06	25.12	22.11	20.25	20.16	35.97	22.43	20.73	23.62
MSCT 4-C	21.28	23.93	23.79	24.06	20.39	43.87	23.41	19.32	23.95
MSCT 5-C	20.08	24.08	21.46	22.61	20.19	42.61	22.86	18.55	22.53

## Supporting Material: Protocol for AFM spring constant calibration

### Start experiment (all methods)

- Check z-calibration of your AFM, for instance using a calibration grid.
- Write down before start: temperature (°C) at cantilever position in working AFM.
- Find the tilt angle off horizontal of the cantilever in its tip holder (e.g., for NanoScopes  $\alpha = 12^\circ$ ).
- Mount the cantilever into its holder, and align the laser-spot as close as possible to the end of the cantilever by a camera or microscope.
- Align the reflected laser beam onto the center of the photo detector and maximize the total intensity.

### 1. Thermal noise method

- Take force curves ( $N = 5$ ) of the cantilever in air on an ethanol cleaned silicon slide (or glass). Keep the deflection in the non-contact (flat) region at 0 V and the deflection in the contact region at a maximum of 1-2 V (< 200 nm). Set the deflection set-point at 0 V.<sup>#1</sup>
- Calculate the mean of the contact InvOLS (nm/V; sensitivity deflection) from the linear slope of the tip-sample contact region (in the approach curve). Enter this value in the software, if possible; and write it down.
- Raise the cantilever well above the substrate (>300  $\mu\text{m}$ ), without changing the laser position and re-center deflection to 0 V.<sup>#2</sup>
- When possible, before acquiring the thermal noise data enter the InvOLS and environmental temperature into the software. Also enter some correction parameters in your software to comply to the following formulas:<sup>#3</sup>

$$k = 0.817 \frac{k_B T}{\langle z_1^2 \rangle} \quad (\text{for rectangular cantilevers}) \quad (\text{S1a})$$

$$k = 0.764 \frac{k_B T}{\langle z_1^2 \rangle} \quad (\text{for V-shaped cantilevers}) \quad (\text{S1b})$$

(Note: The value you have to put into the software depends on AFM, for NSs set the 'deflection sensitivity correction' to 1.106 or 1.144, other AFMs: check manual)

- Acquire the thermal noise power spectrum of the cantilever ( $N = 5$ ) and, if possible, save the spectrum for later analysis.

### Calculating the spring constant:

- Fit the fundamental resonance peak in the spectrum with the SHO (simple harmonic oscillator) model.<sup>#4</sup> Write down the fitting parameters  $y_0$ ,  $A_0$ ,  $f_R$  and  $Q$  of the SHO fit:<sup>#5</sup>

$$P(f) = y_0 + \frac{A_0 \cdot f_R^4}{(f^2 - f_R^2)^2 + \left(\frac{f \cdot f_R}{Q}\right)^2} \quad (\text{S2})$$

- Find the spring constant using the software, or manually calculate it with:

$$k = \frac{1.634 \cdot k_B T}{\pi \cdot A_0 \cdot f_R \cdot Q} \quad (\text{for rectangular cantilevers}) \quad (\text{S3a})$$

$$k = \frac{1.528 \cdot k_B T}{\pi \cdot A_0 \cdot f_R \cdot Q} \quad (\text{for V-shaped cantilevers}) \quad (\text{S3b})$$

### Calibrating in liquid:

- Alternative to calibrating in air, the thermal noise method can be applied in liquid. This implies that the InvOLS measurement as well as the thermal noise should be acquired in this medium. The InvOLS in liquid is related to that in air by the refractive index of that liquid, for further reading see also Tocha et al., Langmuir, 23 (2007), 7078.
- Due to higher damping, the signal-to-noise ratio is lower in the PSD. In these highly damped systems,  $Q \leq 10$ , an adapted SHO fit should be used. For further reading on calibrating in liquid see Pirzer and Hugel, Rev. Sci. Instrum., 80 (2009), 035110.



**Note #1:** By calibrating at a  $\pm 0$  V deflection, using a 1-2 V trigger, and a 0 V setpoint in the deflection versus piezo distance curves, the photo detector and piezo scanner both stay in their linear regime.

**Note #2:** The laser position was kept unchanged, however the deflection was re-centered onto the detector (0 V), which had shifted due to the change in electrostatic interaction of the cantilever with the substrate.

**Note #3:** Where  $k_b$  is the Boltzmann constant,  $T$  the temperature and  $\langle z_1^2 \rangle$  the “virtual” cantilever displacement.

**Note #4:** In the thermal spectra also higher order peaks can be observed. Note that these can also be “false” peaks due to aliasing, which can be avoided by an anti-aliasing filter (see Cook et al., *Nanotechnology*, 17 (2006) 2135, for more information).

**Note #5:** Here  $y_0$  is the background noise,  $A_0$  the intercept for  $f=0$ ,  $f_R$  the resonance frequency and  $Q$  the quality factor. Besides, a SHO fit is better than a Lorentz fit, as sometimes implemented in the AFM software of commercial systems.

## 2. Sader method

### Before the calibration:

- Measure the plan-view dimensions of the cantilever by SEM or optical microscopy, and determine its length, its width and, for V-shaped, its width at the cantilever base.

### Calibration:

- Keep the cantilever well above the substrate ( $>300 \mu\text{m}$ ), and set the deflection to 0 V.<sup>#1</sup>
- Acquire the thermal noise power spectrum of the cantilever ( $N = 5$ ) and eventually save the spectrum for later analysis.
- Fit the fundamental resonance peak with the SHO (simple harmonic oscillator) model. Write down the fitting parameters  $f_R$  and  $Q$  of the SHO fit:<sup>#5</sup>

$$P(f) = y_0 + \frac{A_0 \cdot f_R^4}{(f^2 - f_R^2)^2 + \left(\frac{f \cdot f_R}{Q}\right)^2} \quad (S4)$$

### Alternative 1 (rectangular cantilever):

- Use the parameters  $f_R$  and  $Q$  to calculate the spring constant of a rectangular cantilever by using the formula:<sup>#6</sup>

$$k = 7.5246 \cdot \rho \cdot b^2 \cdot L \cdot \Gamma_1(\text{Re}) \cdot f_R^2 \cdot Q \quad (S5a)$$

$$\text{where } \text{Re} = \frac{\pi \cdot \rho \cdot b^2 \cdot f_R}{2\eta} \quad (S5b)$$

Use the length  $L$  and width  $b$  of the cantilever. (For cantilever B from a MLCT/MSCT chip, take values from Table 2). Take the temperature dependent values for  $\rho$ ,  $\eta$  from Table S3 or use the calculator on: <http://www.mh1.uwaterloo.ca/oldonlinetools/airprop/airprop.html>

- Calculate the spring constant by using Eq. S5, implemented in an own written software application (e.g. in MATLAB) or use the web tool of the Sader group on: <http://www.ampc.ms.unimelb.edu.au/afm/calibration.html>
- Correct the found intrinsic spring constant for cantilever tilt:<sup>#5</sup>

$$k_{\text{effective}} = \frac{K_{\text{intrinsic}}}{\cos^2 \alpha} \quad (S6)$$

### Alternative 2 (V-shaped cantilever C or D from a MLCT/MSCT-cantilever chip):

- Use the parameters  $f_R$  and  $Q$  to calculate the spring constant of V-shaped cantilevers C and D by using the formulas:<sup>#7</sup>

$$k = 140.94 \cdot \rho \cdot b_c^2 \cdot L_c \cdot \text{Re}^{-0.728 + 0.00915 \ln \text{Re}} \cdot f_R^2 \cdot Q \quad (\text{C-type}) \quad (S7a)$$

$$k = 117.25 \cdot \rho \cdot b_D^2 \cdot L_D \cdot \text{Re}^{-0.700 + 0.0215 \ln \text{Re}} \cdot f_R^2 \cdot Q \quad (\text{D-type}) \quad (S7b)$$

Calculate  $\text{Re}$  by Eq. S5b. Take the values for  $\rho$ ,  $\eta$ ,  $b_{C/D}$ ,  $L_{C/D}$  from Table 2&S3. <sup>#6</sup>

- Correct the found intrinsic spring constant for cantilever tilt with Eq. S6.

### Alternative 3 (other V-shaped or differently shaped cantilevers):

- Derive alternative formulas for Eq. S7, by using the method described in Sader et al., *J. Appl. Phys.* 97

(2005) 12490.

- After deriving the formulas, continue with Alternative 2.

**Calibrating in liquid:**

- See also thermal noise method in liquid. The Sader method can be applied in liquid too, the viscosity and density of water can be calculated by: <http://www.mhlt.uwaterloo.ca/old/onlinetools/airprop/airprop.html>

**Note #6:** This formula is derived in Sader et al., Rev. Sci. Instrum. 70 (1999) 3967, with replacing  $\omega_r = 2\pi \cdot f_r$ . Where  $b$  is the width of the cantilever,  $\Gamma_i$  the imaginary part of the hydrodynamic function,  $\rho$  the density and  $\eta$  the viscosity of the medium,  $L$  the length of the cantilever, and  $Re$  the Reynolds number. See also figure below.

**Note #7:** These formulas are derived in Sader et al., J. Appl. Phys. 97 (2005) 124903. With  $b_{c/D}$  the width of one of the two cantilever beams.

**Table S3: Viscosity and density of air at different temperatures**

Temperature (°C)	$\rho$ (kg/m <sup>3</sup> )	$\eta$ ( $\times 10^5$ kg/m s)
20	1.2047	1.8205
21	1.2006	1.8253
22	1.1965	1.8301
23	1.1925	1.8348
24	1.1885	1.8396
25	1.1845	1.8444
26	1.1805	1.8491
27	1.1765	1.8538
28	1.1726	1.8586
29	1.1687	1.8633
30	1.1649	1.8680
31	1.1610	1.8727
32	1.1572	1.8774
33	1.1534	1.8821
34	1.1496	1.8868
35	1.1459	1.8915

**Supporting Material: Calculation of the InvOLS**

A method to calibrate the inverse optical lever sensitivity (InvOLS [m/V]) of cantilevers without making contact with a substrate, is one using the thermal noise information obtained during calibration with the Sader method.<sup>56</sup> This is especially desirable in the case of functionalized cantilevers, where contact with the substrate is to be avoided.

To calculate the InvOLS, the spring constant  $k$  determined with the Sader method (Eqs. 6, 7) is used to relate the DC power response  $P_{DC}$  in [V<sup>2</sup>/Hz] - which is related to the zero frequency power  $A_0$  in [m<sup>2</sup>/Hz] via  $A_0 = \text{InvOLS}^2 \cdot P_{DC}$  - to the expected cantilever displacement  $\langle z_1^2 \rangle$  of Eq. 2.<sup>28</sup> Taking together Eqs. 5, 2 & 8, we can describe the InvOLS as:

$$\text{InvOLS} = \sqrt{\frac{2 \cdot C \cdot k_B T \cdot \cos^2 \alpha}{\pi \cdot k \cdot P_{DC} \cdot f_R \cdot Q}} \tag{S8}$$

with  $k$  the spring constant determined with the Sader method corrected for tilt  $\alpha$ , and  $C = 0.817$  or  $0.764$  for rectangular and V-shaped cantilevers, respectively. Furthermore, the parameters  $f_R$  and  $Q$  are those obtained by a fit of Eq. 3 to the fundamental resonance peak in the thermal spectrum. To determine  $P_{DC}$  there are two possibilities: (i) in the software of the AFM no InvOLS value was set and  $P_{DC}$  in [V<sup>2</sup>/Hz] can be directly derived, or (ii) an arbitrary value for the InvOLS was set and values are in [m<sup>2</sup>/Hz]. In the latter case  $A_0$  should be corrected by dividing with  $\text{InvOLS}^2$  to obtain  $P_{DC}$ .

For all spring constants determined with the direct Sader method given in Table S2, we calculated the corresponding InvOLS values with Eq. S8. In Table S4, the mean values are given of the calculated InvOLS values for the B-, C-, and D-type cantilevers. Furthermore, the directly measured InvOLS values determined with the thermal noise (TN) method are given. From Table S4, it is clear that the accuracy of the calculated InvOLS values is very precise (a small S.D.) and are as accurate as the measured ones. Furthermore, the InvOLS values obtained on the C-type cantilevers are similar for directly measured and calculated values within an error of  $\pm 8\%$ . This demonstrates the possibility to determine the InvOLS by calculation on every type of AFM as well as cantilever.

**Table S4: InvOLS values obtained for three types of cantilevers on eight AFMs\***

Type	Length ( $\mu\text{m}$ )	NS IIIa [I]	NS IIIa [II]	NS IIIa [III]	NS IV [IV]	NS IVa [V]	JPK [VII]	Agilent [VIII]	CB [IX]
B (Sader)	204	$52.1 \pm 2.1$	$52.9 \pm 3.1$	$45.1 \pm 1.3$	$54.0 \pm 4.2$	$58.5 \pm 2.7$	$35.8 \pm 3.3$	$49.0 \pm 3.0$	$200.6 \pm 12.2$
C (Sader)	323	$80.5 \pm 3.9$	$76.4 \pm 5.1$	$73.1 \pm 2.3$	$76.3 \pm 2.4$	$82.2 \pm 4.5$	$54.3 \pm 2.5$	$82.4 \pm 8.4$	$275.4 \pm 11.6$
C (TN)	323	$79.3 \pm 2.2$	$77.6 \pm 6.7$	$69.3 \pm 5.5$	$77.8 \pm 3.3$	$89.1 \pm 2.6$	$55.2 \pm 3.0$	$78.0 \pm 8.0$	$282.3 \pm 11.0$
D (Sader)	218	$56.3 \pm 3.8$	$53.2 \pm 3.5$	$49.8 \pm 1.6$	$53.6 \pm 0.9$	$58.6 \pm 2.8$	$37.9 \pm 1.7$	$55.7 \pm 9.0$	$196.7 \pm 7.0$
Difference*	-	+ 1.0%	- 1.5%	+ 5.5%	- 1.9%	- 7.7%	- 1.6%	+ 5.6%	- 2.4%

\* InvOLS values given are the mean values  $\pm$  S.D. (N=10) \* The difference (in %) between calculated (Sader) and measured (thermal noise = TN) InvOLS C-type values is given

If we plot the InvOLS values in relation to the cantilevers length  $L$ , we obtain a linear relation (Fig. S1). D’Costa and Hoh (*Rev. Sci. Instrum.*, 1995, 5096) described this phenomenon before and used it to gauge a photodetector. In our case, we also observe this relation between cantilever length and InvOLS in relation to the optical configuration of the AFM. In particular, we found a comparable relations between InvOLS and  $L$  for all NanoScope systems (within an error of  $\pm 7\%$ ). Yet, a different relation for the JPK system (Fig. S1). For the calibration of the InvOLS in general this gauging information helps to verify if measured values meet this linear curve, for example for cantilevers with different lengths. Besides, the proper alignment of the laser spot on the end of the cantilever can be verified.

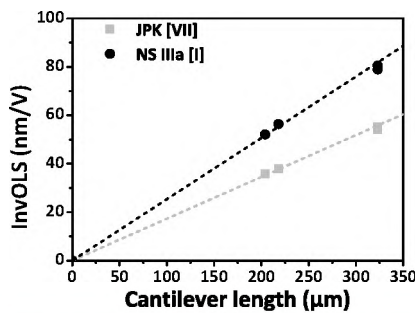


**Figure S1: The InvOLS is linearly related to the cantilever length**

The InvOLS values of AFMs [I & VII] are given for the Sader and thermal noise method for the B-, C-, and D-type cantilevers.

# CHAPTER 4

---

## **Distinct kinetic and mechanical properties govern homo- and heterotypic ALCAM mediated cell adhesion as shown by single-molecule force spectroscopy**

*Joost te Riet, Aukje W. Zimmerman, Alessandra Cambi, Ben Joosten, Sylvia Speller, Ruurd Torensma, Frank N. van Leeuwen, Carl G. Figdor, Frank de Lange*

*Kennis is van geen waarde, tenzij je hem in de praktijk brengt.*

*Heber J. Grant*

**T**he activated leukocyte cell adhesion molecule (ALCAM) mediates dynamic homotypic and heterotypic cellular interactions. Whereas homotypic ALCAM-ALCAM interactions have been implicated in the development and maintenance of tissue architecture and tumor progression, heterotypic ALCAM-CD6 interactions act to initiate and stabilize T cell - dendritic cell interactions affecting T cell activation. The ability to resist the forces acting on the individual bonds during these highly dynamic cellular contacts is thought to be crucial for the (patho)physiology of ALCAM-mediated cell adhesion. Here we used atomic force microscopy to characterize the relation between affinity, avidity, and the stability of ALCAM-mediated interactions under external loading, at the single-molecule level. Disruption of the actin cytoskeleton resulted in enhanced ALCAM binding avidity, without affecting the tensile strength of the individual bonds. Force spectroscopy revealed that the ALCAM-CD6 bond displayed a significantly higher tensile strength, a smaller reactive compliance and an up to hundredfold lower dissociation rate in the physiological force window in comparison to the homotypic interaction. These results indicate that homotypic and heterotypic ALCAM-mediated adhesion are governed by significantly distinct kinetic and mechanical properties providing novel insight into the role of ALCAM during highly dynamic cellular interactions.

## Introduction

Cell adhesion molecules mediate cell attachment and play an important role in maintaining tissue organization by facilitating tissue development, transmembrane signaling and cell-motility. Four major superfamilies of cell adhesion molecules have been identified so far: cadherin, selectin, integrin, and the immunoglobulin superfamily. Overall cell adhesive properties are tightly regulated and critically depend on the relative expression levels, molecular conformation (affinity) and on the local molecular density (valency) of adhesion receptors in the cell membrane.<sup>1-5</sup> The tumorigenic and metastatic phenotype of various cancers often are correlated with altered relative expression levels of these molecules.<sup>6,7</sup> In particular, the association between invasive growth of epithelial carcinomas and the loss of functional E-cadherin and the simultaneous expression of inappropriate cadherins is well documented.<sup>8-10</sup> Whereas it is well known that the release from the primary tumor usually is accompanied by a loss of homotypic cell adhesion, it is also clear that considerable mechanical stresses are imposed on the membranes of cells and their associated adhesion molecules, because the cells migrate and reversibly attach to other cells and the extracellular matrix. How the mechanical properties of the different adhesion receptor pairs govern the distinct migratory phenotypes of tumor cells is not well understood.

In addition to changes in cadherin expression, other adhesion molecules have been implicated in the phenotypic switch associated with enhanced tumor invasiveness. The Activated Leukocyte Cell Adhesion Molecule (ALCAM, CD166) is a member of the immunoglobulin superfamily of cell adhesion molecules, Ig-CAMs.<sup>11</sup> Similar to some other members of this family (e.g. NCAM, CEA), ALCAM mediates homotypic ALCAM-ALCAM adhesion,<sup>11-13</sup> but also heterotypic interactions with the T cell antigen CD6 have been described (Fig. 1A).<sup>11,14</sup> Bone marrow stromal cells and hematopoietic progenitor cells, neuronal cells and a large number of epithelial and endothelial cell types express significant levels of ALCAM, and contributions for homotypic ALCAM-mediated adhesion have been described for neural development, hematopoietic stem cell maturation and transendothelial monocyte migration.<sup>15-19</sup> ALCAM has been implicated in the onset and progression of melanoma,<sup>20-22</sup> bladder cancer,<sup>23</sup> prostate carcinoma,<sup>24</sup> breast cancer,<sup>25</sup>

and colorectal carcinoma.<sup>26</sup> The invasiveness of malignant melanoma correlates with enhanced ALCAM expression and this molecule is considered to be a prognostic marker in this disease.<sup>16, 20, 21, 27</sup>

Besides mediating homotypic interactions, ALCAM is the only known ligand for CD6 identified on immune cells. Recent work indicates that ALCAM localizes to the immunological synapse<sup>28</sup> in an antigen dependent manner<sup>29</sup> and that ALCAM-CD6 engagement plays a pivotal role both during early T cell-dendritic cell (DC) contact formation and in later stages of T cell activation.<sup>30</sup> In fact, several studies now point towards a role for CD6 as a co-stimulatory molecule in T cell activation.<sup>14, 30-34</sup> Recent intravital microscopy studies indicate that within lymphoid tissue naïve T cells scan the surface of DCs at relative cell speeds of up to 30  $\mu\text{m}/\text{min}$ .<sup>35</sup> Clearly, the ability to withstand shear at the molecular level is essential for establishing and maintaining productive DC-T cell contacts for prolonged periods of time.

These findings indicate a key role for ALCAM-mediated adhesion during highly dynamic cellular interactions. Mechanistically, this implies that ALCAM must be equipped to facilitate adhesion under different conditions of external loading. Previous work has focused on the affinity and avidity of ALCAM-mediated interactions.<sup>12-14</sup> Yet, how these properties relate to the stability of ALCAM-mediated bonds under mechanical stress is still poorly understood. Here, we address this issue using the atomic force microscope (AFM)<sup>36</sup> to measure ALCAM-mediated adhesion of living cells under varying loading conditions and with single-bond sensitivity. The AFM has been used successfully to study single molecule adhesion of isolated proteins,<sup>37, 38</sup> and later in studies towards cell adhesion phenomena - an approach that was first explored by Gaub and co-workers.<sup>39</sup> The use of force spectroscopy has meanwhile provided insight into the compliance of individual cell adhesion bonds to physiological-range external forces.<sup>40-44</sup>

We have adapted the AFM technology to study the stability of homo- and heterotypic ALCAM-mediated adhesion under loading. In the low-force regime the ALCAM-mediated interactions displayed similar dissociation kinetics. However, by applying physiologically relevant external forces we found that homo- and heterotypic ALCAM-mediated adhesion are governed by distinct kinetic and mechanical properties indicating that the ALCAM-CD6 bond is significantly more stable under mechanical stress. The reactive compliance and dissociation kinetics found for the ALCAM-CD6 interaction were similar in magnitude to those reported for selectin mediated bonds.<sup>45</sup> In contrast, the ALCAM-ALCAM bond displayed a significantly greater lability under force, also in comparison to homotypic E-cadherin-mediated interactions.<sup>43</sup>

## Materials and Methods

### Chemicals and antibodies

Chemicals were purchased from Sigma (St. Louis, MO) unless stated otherwise. The stock solution of cytochalasin D (CytD) was prepared in dimethylsulfoxide (DMSO) and stored at  $-20^{\circ}\text{C}$ . Anti-ALCAM monoclonal antibodies – AZN-L50 (IgG2A isotype) and AZN-L51 (IgG1 isotype) – were generated in our laboratory by immunizing BALB/C mice with K562-ALCAM. Goat-anti-human Fc-(Fab')<sub>2</sub> fragments were purchased from Jackson ImmunoResearch (Westgrove, PA), FITC-conjugated goat-anti-mouse (Fab')<sub>2</sub> fragments were purchased from Zymed Laboratories (San Francisco, CA). Recombinant ALCAM-Fc consisting of the extracellular domains of the ALCAM fused to the human IgG1 Fc tail was produced and purified as described elsewhere,<sup>12</sup> and recombinant CD6-Fc was purchased from R&D Systems (Minneapolis, MN).

### Cell lines and cultures

Culture media, serum and antibiotics were purchased from Gibco Invitrogen (Breda, The Netherlands). All

culture media were supplemented with 1% antibiotics/antimycotics. Myelomonocytic KG1a cells were cultured in Iscove's Modified Dulbecco's Medium containing 10% FCS as described.<sup>13</sup> Erythroleukemic K562 cells were cultured in RPMI 1640 containing 10% FCS. K562-ALCAM cells were generated and maintained as described elsewhere.<sup>12</sup> Human myeloid MUTZ-3 cells were cultured in 12-well plates in MEM $\alpha$  supplemented with ribonucleosides, deoxyribonucleosides, 20% FCS, 50  $\mu$ M  $\beta$ -mercaptoethanol and 10% 5637 conditioned medium.<sup>46, 47</sup>

### Flow cytometry

Cells were washed with PBA [phosphate buffered saline (PBS) containing 1% (w/v) bovine serum albumin (BSA) and 0.05% (w/v) Na<sub>2</sub>S<sub>2</sub>O<sub>3</sub>] and stained for 30 min at 4°C with AZN-L50 primary antibody (2–5  $\mu$ g/ml in PBA). Cells were washed with PBA and incubated with FITC-conjugated goat-anti-mouse (Fab')<sub>2</sub> secondary antibodies. After washing, cells were analyzed on a FACScan analyzer (Becton Dickinson, Oxnard, CA). The gates were set to exclude dead cells and 5000 gated cells were analyzed. Data are displayed as histograms of fluorescence intensity versus cell count.

### Radioactive cell labeling and immunoprecipitation

KG1a or control-3 cells were pre-incubated for 1 h in serum- and methionine/cysteine-free RPMI 1640 medium prior to labeling with Tran<sup>[35S]</sup>-Label (MP Biomedicals Inc., Irvine, CA), 250  $\mu$ Ci per 10 $\times$ 10<sup>6</sup> cells for 16 h at 37°C. Cells were washed once in phosphate buffered saline (PBS) and subsequently lysed in lysis buffer A (50 mM Tris pH 7.5, 0.5% Triton X-100, 300 mM NaCl, 1.5 mM MgCl<sub>2</sub>, 0.2 mM EDTA, 0.5 mM DTT, 1 mM PMSF, 1  $\mu$ g/ml leupeptin and aprotinin). Lysates were subjected to immunoprecipitation with 1  $\mu$ g of AZN-L51 antibody coupled to Protein G Sepharose 4 Fast Flow beads (Amersham Biosciences). Beads were washed three times in lysis buffer A and bound proteins were eluted by boiling in Laemmli sample buffer and subjected to 9% SDS-PAGE under reducing conditions. Radioactive proteins were detected by exposure to X-ray film (BioMax XAR; Kodak, USA).

### Immunoprecipitation and Western blot analysis

5 $\times$ 10<sup>6</sup> KG1a cells were lysed in lysis buffer B (50 mM HEPES pH 7.5, 150 mM NaCl, 1.5 mM MgCl<sub>2</sub>, 1 mM EDTA, 10% glycerol, 1% Triton X-100, 1 mM PMSF, 1  $\mu$ g/ml leupeptin and aprotinin). Immunoprecipitations were carried out with 1  $\mu$ g of AZN-L51 antibody coupled to Protein G Sepharose 4 Fast Flow beads. Bound proteins were eluted by boiling in Laemmli sample buffer, subjected to 12% SDS-PAGE under reducing conditions, and transferred onto a nitrocellulose membrane. To detect ALCAM and actin, membranes were incubated for 1 h with AZN-L50 or mouse monoclonal anti- $\beta$ -actin (Sigma), followed by 1 h incubation with a peroxidase-conjugated rabbit anti-mouse IgG (DAKO, Denmark) and proteins were visualized using an enhanced chemiluminescence system (Amersham Biosciences).

### AFM force measurements

Force measurements were made on living cells in force-distance mode (Fig. 1) using a MultiMode AFM (Nanoscope IIIa) equipped with a "J"- type piezoelectric translator (Veeco Instruments, Santa Barbara, CA). Triangular gold-coated silicon-nitride cantilevers were used with a nominal spring constant of 10 pN/nm as given by the manufacturer (MLCT-AUHW, Veeco Instruments). Cantilever deflection was determined from the difference in signal generated by a two-segment photodiode monitoring the reflection of a laser beam focused onto the endpoint of the cantilever (Fig. 1B). Each cantilever was calibrated before use by a nondestructive thermal oscillation method,<sup>48</sup> by using this method the uncertainty in the determination of the spring constant amounted to 3–4%, per cantilever. The experimentally determined spring constants of the used cantilevers were 15  $\pm$  2 pN/nm, and these values were used to obtain interaction forces using Hooke's law,  $F = k \times \Delta x$ . Here,  $F$  is the force (expressed in piconewtons, pN),  $k$  is the experimentally obtained spring constant (pN/nm), and  $\Delta x$  is the measured cantilever deflection (nm).

### Protein immobilization

ALCAM-Fc and CD6-Fc were immobilized on 13 mm plastic coverslips (Nalge Nunc, Rochester, NY). First, in an overnight (4°C) incubation, 10  $\mu$ g/ml goat anti-human Fc-(Fab')<sub>2</sub> fragments were absorbed to the coverslip surface in TSM (20 mM Tris, 150 mM NaCl, 1 mM CaCl<sub>2</sub>, 2 mM MgCl<sub>2</sub>, pH 8.0). Then the substrates were rinsed and subsequently incubated for 30 min in TSM/1% (w/v) BSA at 37°C to block the remaining exposed non-coated surface. After an additional washing step, the plates were incubated with 5  $\mu$ g/ml ALCAM-Fc or 5  $\mu$ g/ml CD6-Fc in TSM for 1 h at 37°C. Finally, the coated substrates were washed and transferred into the AFM

measuring chamber (MTFML, Veeco Instruments).

### Functionalization of AFM cantilevers with cells

Cells were attached to the AFM cantilever by concanavalin A (ConA)-mediated linkages essentially as described.<sup>41</sup> ConA coated cantilevers were prepared as follows. Cantilevers were first cleaned by immersion in acetone for 5 min, then rinsed with ethanol and subsequently dried in a microwave oven. Following an overnight incubation at 37°C in biotinylated BSA (biotin-BSA, 0.5 mg/ml in 100 mM NaHCO<sub>3</sub>, pH 8.6) the cantilevers were rinsed using PBS and exposed to 0.5 mg/ml (PBS, 30 min, 37°C) streptavidin (Pierce, Rockford, IL). Finally, the cantilevers were incubated in biotinylated conA (biotin-ConA, 0.2 mg/ml in PBS) for 30 min at 37°C and washed with PBS.

Cells kept in medium A (RPMI 1640, 10% FCS, 25 mM HEPES; pH 7.0) were seeded onto a clean uncoated glass coverslip and were picked up under the guidance of an optical microscope mounted on top of the AFM, using the AFM as a micromanipulator. For this, the ConA-functionalized cantilever was positioned over a target cell on the substrate and was approached to establish contact lasting at least one minute. During this time the applied indentation force was kept constant at about 2.5 nN. Upon retraction, the successful pick-up was readily scored by visual inspection, and, in these events, the cell was positioned right behind the AFM tip (Fig. 1C).

### Rupture force measurements and Force Spectroscopy

The cell bearing cantilever was brought into contact with the ligand-coated substrate (Fig. 1Ba-c) for a preset period of time (interaction time; 25°C, medium A). During this time, a force was exerted on the cell of no more than ~ 1 nN. Interaction times were such that a minimal, yet significant, ALCAM-specific adhesion was established (typically between 0.5-3 s, see Results). Upon retraction, the forces acting on the cantilever were recorded as a function of displacement of the ALCAM/CD6-coated substrate (Figs 1Bd-f, 1D). ALCAM-ALCAM and ALCAM-CD6 rupture forces were determined directly from the height of the sudden variations in binding force that are associated with bond rupture. The final ruptures in the force-distance curves were used for further analysis (Fig. 1D; see below). The area enclosed by the zero-force axis and the force-distance curve (Fig. 1D) was taken as a measure for the work ( $W=F \times d$ ) performed during the detachment phase.<sup>40, 49</sup> CytD treatments were performed in situ (2.5 µg/ml in medium A, 25 min). Specificity was verified by an in situ incubation with the function-blocking ALCAM-specific monoclonal antibody AZN-L50 (10 µg/ml, 25 min). Force curves were analyzed using Origin<sup>®</sup> Pro 6.1 (OriginLab Corporation, Northampton, MA). The same package was used for performing Student's t-test.

Force spectroscopy was applied to study how the rupture forces depend on the loading rate, i.e. the rate at which force builds up on the respective bonds. Loading rates (pN/s) were computed as the product of the slope of the force-distance curve (pN/nm) just before a rupture event – the effective force constant that takes the viscoelastic properties of the system into account<sup>50, 51</sup> – and the pulling velocity (nm/s). Pulling velocities were varied from 250-12,500 nm/s. The final ruptures in the force-distance curves were used for further analysis and for each of these events both the loading rate and the rupture force was determined (Fig. 1D). For each cell, complete force spectra were recorded under identical conditions on both substrates by switching the ligand-coated plate for one containing the other. Pulling rates were varied randomly and reproducibility over time was verified by repeating measurements using prior pulling rate settings. After each series, ALCAM specificity of the adhesion was checked using the blocking mAb AZN-L50.

At retraction speeds >1 µm/s the hydrodynamic drag on the cantilever resulted in damping and, as a result, smaller forces were recorded than were actually applied to rupture the bonds.<sup>40, 52, 53</sup> To compensate for this effect the data were corrected using a damping coefficient of 2 pN·s/µm.



## Results

### Using AFM to measure single ALCAM-mediated interactions on living cells

A schematic layout of the AFM adhesion measurements is depicted in Fig. 1B. Cell adhesion forces were measured by moving ALCAM or CD6 coated substrates alternately towards and away from an AFM cantilever to which a single ALCAM-expressing cell was attached by means of concanavalin A (ConA)-mediated linkages (Fig. 1B,C; see Materials and Methods). The detachment of the cell was recorded during retraction of

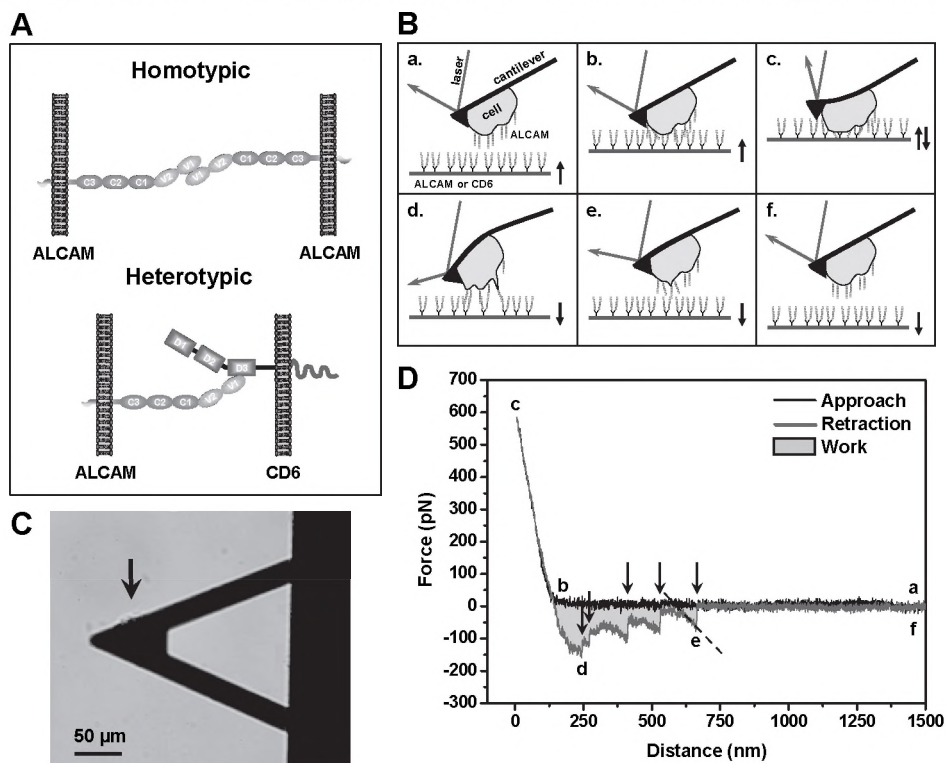


**Figure 1: ALCAM-mediated adhesion probed by AFM**

(A) Homo- and heterotypic ALCAM-mediated interactions. ALCAM contains five Ig-domains and the membrane-distal V1 Ig-domain mediates homotypic ALCAM-ALCAM interactions.<sup>21</sup> Heterotypic interaction to CD6, a member of the scavenger receptor cysteine rich (SRCR) protein family, are mediated by the ALCAM V1 Ig-domain and the third, membrane-proximal, SRCR domain (D3) of CD6.<sup>21</sup> (B) Schematic layout of the AFM experiment. Cells were attached to the AFM cantilever by a ConA-mediated linkage as detailed in Materials and Methods. An ALCAM expressing cell attached to the AFM cantilever interacts with a substrate coated with either ALCAM-Fc or CD6-Fc under the control of the AFM. First (a) the substrate is moved to the cantilever by the piezoelectric scanner until contact is made (b). Then the substrate is pressed onto the cell, causing the cantilever to bend, until a specified force limit is reached. During a preset period of time (interaction time) the cell and substrate are allowed to interact (c). Upon retraction the cell-substrate adhesion will cause the cantilever to bend in the other direction (d), until the force acting on the molecular bonds are large enough for bond rupture to occur (e). Finally, the cantilever returns to its resting position (f). (C) Example of a single K562-ALCAM cell (arrow), just visible in the shadow of the cantilever, attached to the end of the AFM probe. (D) A typical force-distance curve of an ALCAM-ALCAM interaction, showing single bond ruptures (arrows; K562-ALCAM on ALCAM coated substrate). In this trace the indices a-f correspond to those in Fig. 1B. From the slope just before the final rupture (dotted line) the loading rate acting on the bond is calculated. The area enclosed by the approach and retraction curve (shaded) is a measure for the work of de-adhesion under these conditions.

the substrate. The rupture of cell-substrate bonds caused subtle changes in cantilever deflection that provided a measure for the cell adhesion forces that were acting on the molecular level (Fig. 1D, arrows). The work needed to detach the cell from the substrate - derived from the area enclosed by the retraction curve and the zero-force axis - was taken as a measure for overall cell adhesion.<sup>40</sup> Homo- and heterotypic ALCAM-mediated adhesion were compared using the same cell and cantilever probing the distinct ligand-coated substrates.

#### **ALCAM is linked to the actin cytoskeleton**

KG1a and ALCAM-transfected K562 cells (K562-ALCAM) both express similar levels of ALCAM at the cell surface (Fig. 2A). Parental ALCAM-negative K562 and MUTZ-3 cells were used as negative controls in further experiments. We found that a 42 kDa protein co-precipitates with ALCAM from metabolically labeled KG1a cells, but not from ALCAM-negative MUTZ-3 cells (Fig. 2B). This 42 kDa protein was identified as  $\beta$ -actin by immunoprecipitation of ALCAM followed by Western blot analysis (Fig. 2C). Total cell lysate served as a control for total amounts of ALCAM and  $\beta$ -actin (not shown). Control IPs with either protein G beads alone or with a control antibody were negative for both ALCAM and  $\beta$ -actin, confirming the specificity of the interaction. These results confirm and extend our previously reported finding that ALCAM-mediated adhesion is directly regulated by the actin cytoskeleton.<sup>12, 13</sup>

#### **Avidity of ALCAM-mediated adhesion is controlled by the actin cytoskeleton**

We have previously shown by means of an optical trap based motility assay and fluorescence microscopy that modest disruption of the cortical actin cytoskeleton - using cytochalasin D (CytD) - results in enhanced lateral mobility of ALCAM and the formation of ALCAM clusters on the cell surface. Interestingly, CytD pretreatment further enhanced cell adhesiveness to ALCAM-Fc coated plates suggesting that the observed clustering effectively enhanced ALCAM binding avidity.<sup>12, 13</sup> Here we exploit the sensitivity of the AFM to determine to what extent the affinity of individual ALCAM-mediated interactions contributes to this effect.

Fig. 3A shows the effect of CytD on the work (shaded area) needed to detach a KG1a cell from an ALCAM-Fc coated plate. For clarity, the traces are shown with an offset. After the initial acquisition of force-distance curves, the cell was stimulated in situ with CytD and re-examined under identical experimental conditions. Subsequently, ALCAM-mediated adhesion was blocked using mAb AZN-L50. Similar experiments were performed to study the adhesion to CD6-Fc coated plates (curves not shown). The effect of CytD was most pronounced in the case of the homotypic interactions (Fig. 3B). We found that CytD treatment caused an up to twofold enhancement in overall cell adhesion. Subsequent incubation with mAb AZN-L50 blocked ~80% of total adhesion, i.e. back to the level of untreated cell adhesion in the presence of this antibody, indicating that the CytD-enhanced adhesion was ALCAM specific. Similar results were obtained on CD6-Fc coated plates, albeit that the enhancement in adhesion and subsequent blocking was slightly less pronounced. Overall, these results are in excellent agreement with our previous findings using a plate adhesion assay.<sup>12, 13</sup>

The ability of the AFM to measure binding forces on the molecular scale prompted us to re-examine whether CytD might also affect the affinity of the homo- and heterotypic interactions. Affinity changes are expected to result in concomitant changes in rupture force.<sup>40, 41</sup> Rupture forces were determined from the final rupture events, before and after

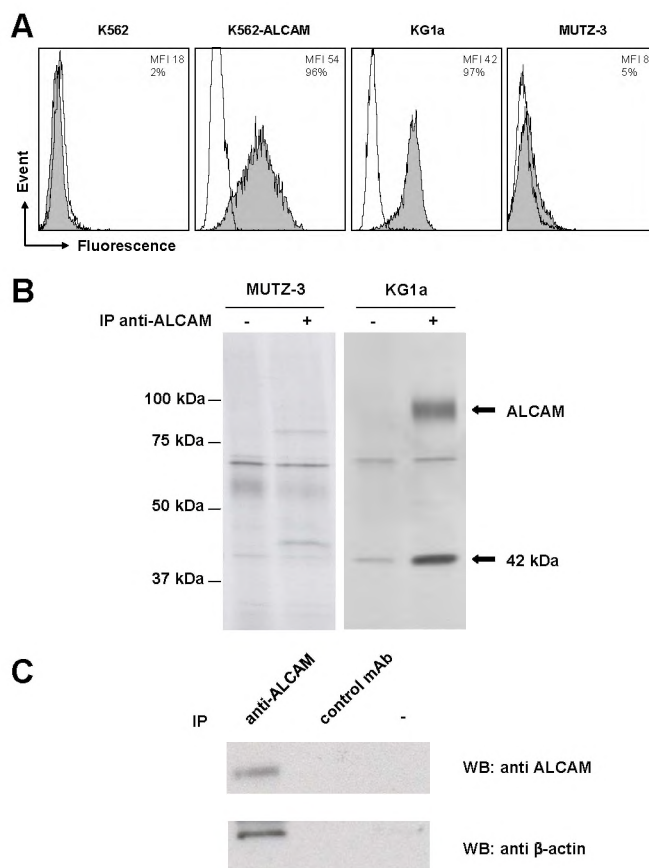


**Figure 2: ALCAM is associated with the actin cytoskeleton**

(A) Surface expression of ALCAM on K562, K562-ALCAM, KG1a and undifferentiated MUTZ-3 cells was analyzed by flow cytometry. Unfilled histograms represent isotype control staining and shaded histograms represent staining with ALCAM antibody AZN-L50. The mean fluorescence intensity (MFI) and percentage of positive cells are as indicated. (B) A 42 kDa protein coprecipitates with ALCAM from KG1a cells, as indicated by arrows. KG1a and undifferentiated MUTZ-3 control cells (no ALCAM expression) were incubated overnight with [<sup>35</sup>S]methionine/cysteine. ALCAM was immunoprecipitated from labeled cell lysates with 1  $\mu$ g of AZN-L51. Samples that were incubated with protein G beads alone (-) are shown as negative controls. (C) Identification of the coprecipitated protein by Western blot analysis. ALCAM and  $\beta$ -actin were detected using antibodies AZN-L50 and anti- $\beta$ -actin (clone AC-15), respectively. As a negative control lysates were incubated with an irrelevant control antibody (anti-hemagglutinin, clone 12CA5) or with protein G beads alone (-).

CytD or AZN-L50 treatment. However, in contrast to the effects on overall cell adhesion described above, the mean rupture forces for the homo- and heterotypic interactions were not affected by either treatment (Fig. 3C). These results clearly demonstrate that disruption of the actin cytoskeleton by CytD enhances ALCAM binding avidity without affecting the affinity of the individual ALCAM-mediated interactions.

#### The ALCAM-CD6 bond is more stable under external loading

Previous work focused on the affinity of ALCAM-mediated interactions using soluble ligand binding assays.<sup>13, 14</sup> Here we address the relative stability of single homo- vs heterotypic ALCAM-mediated bonds under conditions of external loading, i.e. under

conditions that mimic the forces acting on the cell adhesion molecules during dynamic cell-cell contacts.

To compare cell adhesion to different substrates, interaction times were adjusted to control the overall level of adhesion. The extent of adhesion between cell and substrate depended both on the interaction time and the force exerted on the cell during that time. Moreover, local variations in receptor density were anticipated to affect adhesion. It has been shown that short interaction times promote the detection of single-bond ruptures as opposed to the simultaneous rupture of multiple bonds.<sup>39, 42, 54, 55</sup> Control experiments were performed to determine the threshold level of adhesion in this assay. When a parental K562 cell - not expressing ALCAM - was lowered onto an ALCAM-Fc coated, or even an uncoated substrate, non-specific adhesion sometimes occurred (data not shown). However, although these events could not be distinguished from specific ruptures on the basis of rupture force alone (not shown), the apparent work of de-adhesion associated with these non-specific events was small, typically  $\leq 20 \times 10^{-18}$  J. Therefore, to further promote the capture of specific single-bond ruptures, interaction

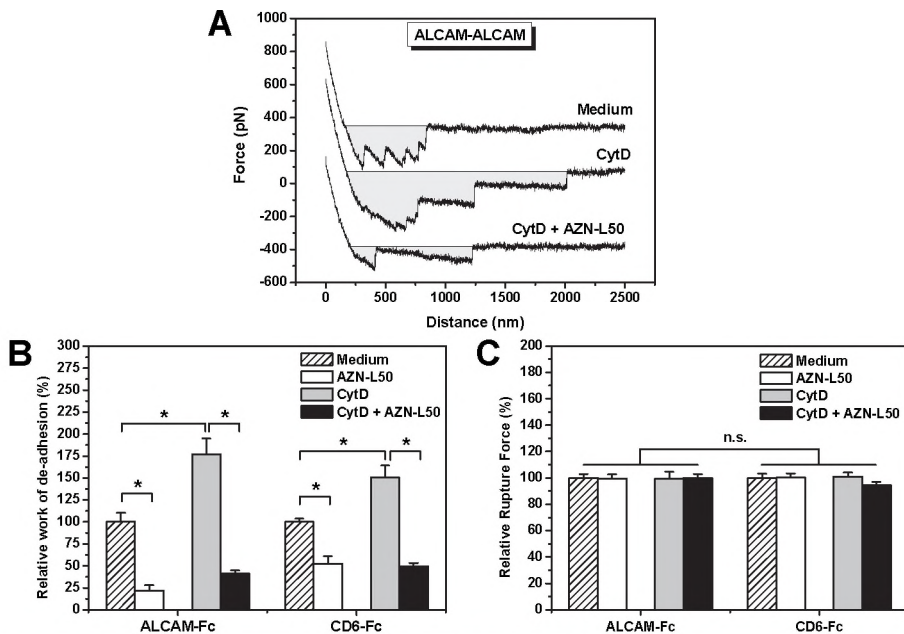


**Figure 3: The actin cytoskeleton regulates ALCAM binding avidity**

(A) Typical force-distance curves of the homotypic ALCAM-mediated interaction between a KG1a cell and an ALCAM-Fc coated plate, before (medium) and after treatment with the actin cytoskeleton inhibitor Cytochalasin D (CytD), and after a subsequent blocking step (CytD + mAb AZN-L50). For clarity, the traces are shown with an offset. The substrate retraction speed was set to 2.5  $\mu\text{m/s}$ . The work needed to detach the cell from the substrate (shaded areas), typically between  $1 \times 10^{-16}$  and  $3 \times 10^{-16}$  J for untreated cells, was taken as a measure for overall cell adhesion. (B) Whole cell analyses of the relative work of de-adhesion comparing the situation before treatment (medium) with that after incubation with the ALCAM function blocking mAb AZN-L50, or after incubation with CytD alone or followed by a subsequent AZN-L50 incubation. The relative work of de-adhesion was determined from over at least 25 traces per cell per condition (medium condition set to 100%). It can be seen that CytD treatment upregulates overall cell adhesion and that this adhesion is ALCAM-specific. (C) Single-bond level rupture force analyses. In contrast to the overall cell adhesion, the single-bond rupture forces under these loading conditions were found to be insensitive to the various treatments (relative force-scale;  $N > 30$ ). (Error bars represent s.e.m.; \* indicates significance to  $p < 0.05$ , n.s.: not significant). Trends were reproducibly observed in three independent experiments.

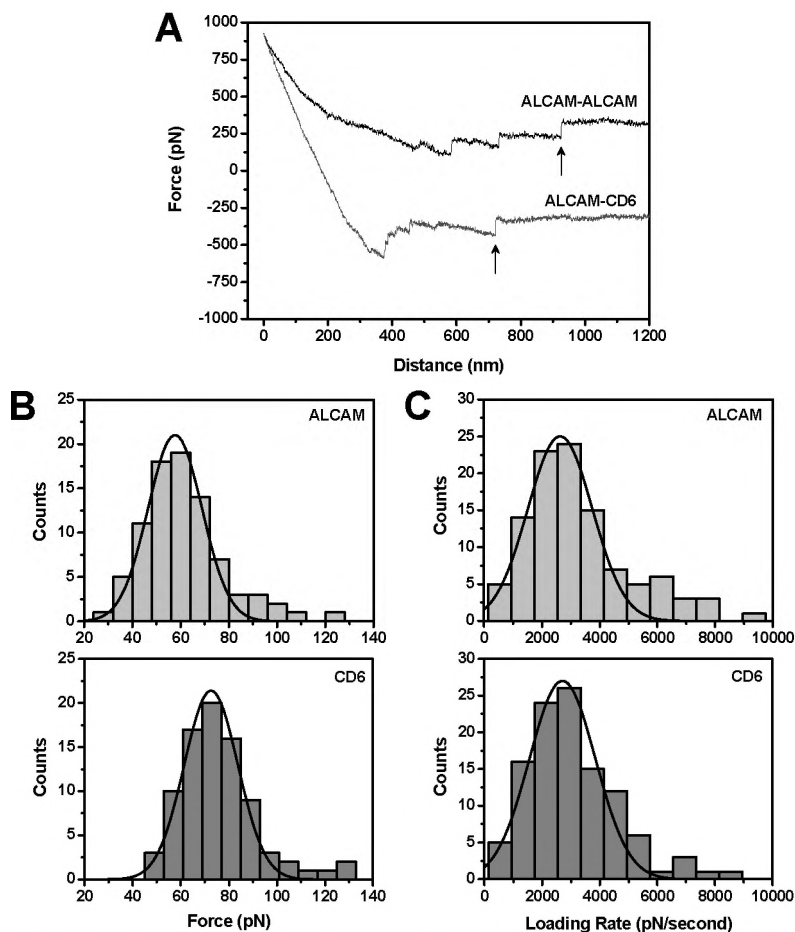


**Figure 4: Single molecule force measurements on living KG1a cells**

(A) Examples of force-distance curves obtained in the low adhesion regime ( $\sim 50 \times 10^{-18}$  J, see text). Final ruptures (arrows) were used for further analyses. The retraction speed was set to  $2.5 \mu\text{m/s}$ . (B) Statistical analysis of the rupture forces. The mean rupture forces ( $\pm$  s.e.m.) determined from these data were  $58 \pm 3$  pN and  $73 \pm 3$  pN for the ALCAM-ALCAM and ALCAM-CD6 bond respectively ( $p < 0.001$ ,  $N = 85$ ; see also Fig. 5). (C) Statistical analysis of the loading rates. The mean loading rates were found to be similar in magnitude, i.e.  $2632 \pm 112$  pN/s and  $2707 \pm 115$  pN/s for the homo- and heterotypic bonds respectively ( $N > 100$ ; not significant). A single Gaussian function (solid lines) could be fitted to the force and loading rate distributions which in all cases accounted for  $> 85\%$  of the events.

times were adjusted to obtain a detachment work of  $\sim 50 \times 10^{-18}$  J, sufficient to allow for a clearly visible block with the mAb AZN-L50. Typical force-distance curves acquired in this way are presented in Fig. 4A, and are again offset for clarity. To further reduce the chance of measuring multiple bond ruptures, only the final events (Fig. 4A, arrows) were used to extract the rupture force and loading rate data.<sup>56</sup> Fig. 4B,C show the statistical analysis compiled from more than 100 of these curves taken at a fixed substrate retraction speed. The rupture force (Fig. 4B) and loading rate (Fig. 4C) distributions could be fitted to a single Gaussian function, which in all cases accounted for over 85% of the events. We note that multiple bond ruptures would have resulted in multiple quantized peaks.<sup>39, 56</sup> Taken together, by performing the experiments under conditions of moderate adhesion

we find that over 85% of the events included in this assay represented single ALCAM-mediated bond ruptures.

When both homo- and heterotypic ALCAM-mediated bonds were loaded at a similar rate of 2700 pN/s (Fig. 4C), the mean rupture force determined for the ALCAM-CD6 bond was  $73 \pm 3$  pN, significantly higher than the  $58 \pm 3$  pN found for the homotypic interaction ( $\pm$  s.e.m.,  $p < 0.001$ ; Fig. 4B). These data show that relative to the homotypic interaction, the ALCAM-CD6 bond can resist higher forces indicating that this bond will be the more stable under conditions of dynamic cell-cell interactions.

### Distinct mechanical properties govern homo- and heterotypic ALCAM-mediated interactions

Force spectroscopy was applied to characterize and compare the biochemical and biophysical properties underlying the stability of individual ALCAM-mediated interactions under conditions of varying mechanical stress. Force spectra were obtained by examining the mean rupture forces determined as described above, but now for loading rates varying in the range from 300-20,000 pN/s – mimicking cell-cell speeds ranging from 0.2 - 13  $\mu$ m/s. Experiments were performed using both KG1a and K562-ALCAM cells and the resulting force spectra are displayed in Fig. 5A. Importantly, the similarity of the force-spectra obtained from both cell-types further substantiates the conclusion that exclusively ALCAM-mediated bond ruptures were probed.

The mean rupture forces found for both the homo- and heterotypic interactions increase linearly as a function of the natural logarithm of the loading rate. This behavior was first described by Bell.<sup>57</sup> In the Bell model, the mean rupture force  $F_{rup}$  is described by:

$$F_{rup} = \frac{k_B T}{x_\beta} \ln\left(\frac{x_\beta}{k_{off}^0 k_B T}\right) + \frac{k_B T}{x_\beta} \ln(r_f) \quad (1)$$

where  $k_{off}^0$  is the (unstressed) dissociation rate in the absence of a pulling force;  $x_\beta$  is the reactive compliance or mechanical bond-length;  $T$  is the absolute temperature;  $k_B$  is the Boltzmann constant, and  $r_f$  is the loading rate.<sup>52, 54, 58, 59</sup> The Bell model parameters  $k_{off}^0$  and  $x_\beta$ , characterizing the micromechanical properties of the homo- and heterotypic ALCAM-mediated interactions, were obtained by fitting the spectra to Eq. 1. Table 1 lists these parameters, and shows a comparison to other receptor-ligand pairs to put the ALCAM data into perspective (see Discussion). The data did not show a significant difference in unstressed dissociation rates – 1.9 vs 3.4  $s^{-1}$  for the homotypic and heterotypic bond, respectively. In contrast, the mechanical bond-length determined for the ALCAM-CD6 interaction was  $0.23 \pm 0.01$  nm, significantly shorter than the  $0.38 \pm 0.06$  nm we found for the ALCAM-ALCAM bond. Because these numbers are in the range of the bond lengths of a single Van der Waals interaction or hydrogen bond, the observed differences in mechanical bond-length likely reflect distinct (hydrogen) bonding patterns in both types of ALCAM-mediated interactions (Fig. 1A). Bonds with shorter  $x_\beta$  are more resistant to applied force. These findings, therefore, corroborate the previous conclusion that with respect to the homotypic interaction the ALCAM-CD6 bond is more resistant to applied force, and hence more stable under loading than the ALCAM-ALCAM bond.

In terms of interaction potentials, the unstressed dissociation rate  $k_{off}^0$  represents the rate-limiting step in the dissociation, i.e. the transition over the activation barrier, of the unstressed complex. The reactive compliance,  $x_\beta$ , then represents the reaction coordinate, and describes how far the bond can be stretched before it breaks.<sup>60, 61</sup> A schematic graphical representation of the data is shown in Fig. 5B (solid curves). The

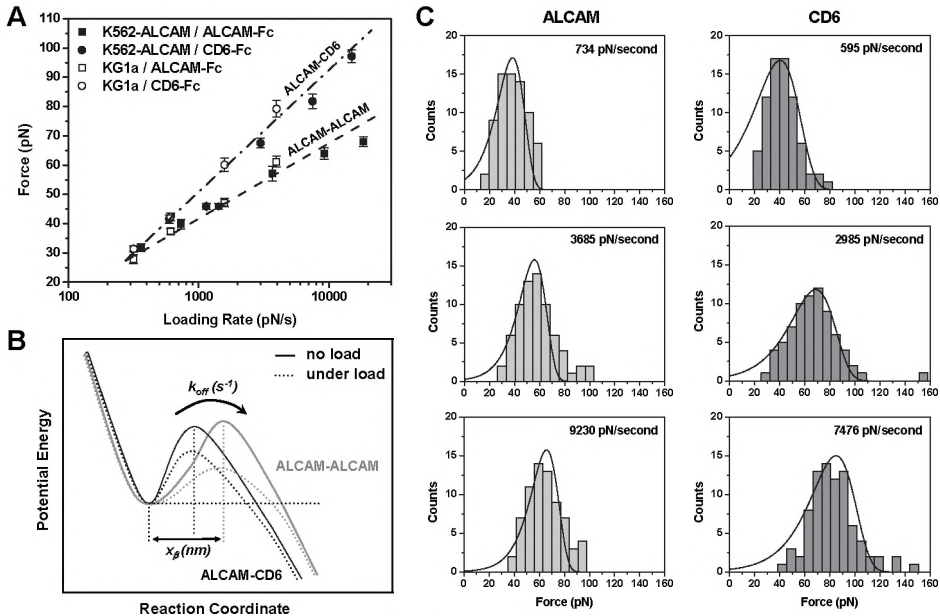


**Figure 5: Force spectra of ALCAM-mediated interactions**

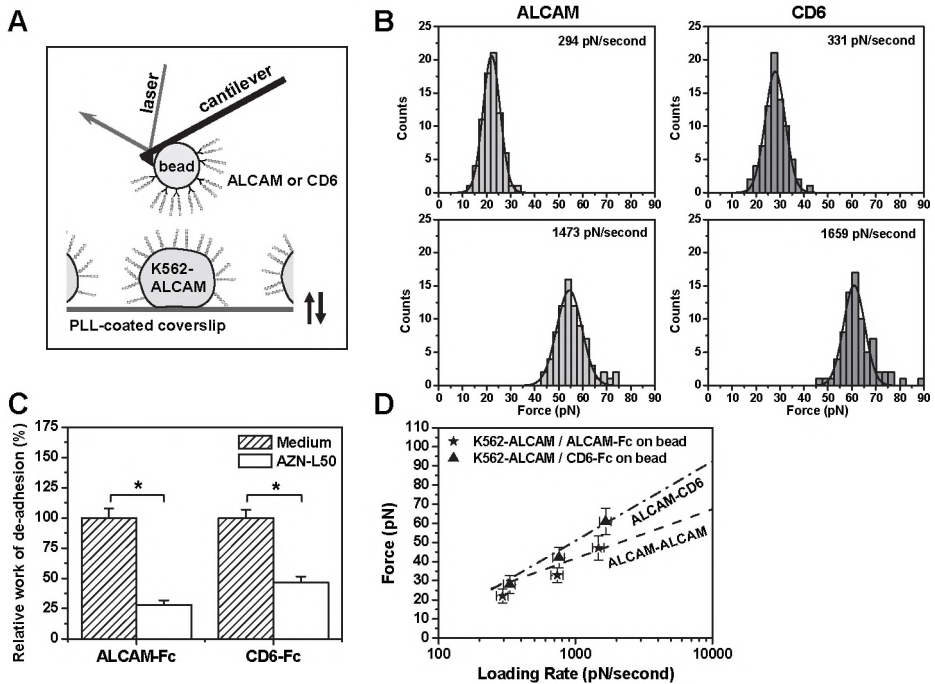
(A) The mean rupture forces for the homotypic (circle) and heterotypic (square) ALCAM-mediated interactions were found to increase linearly with the natural logarithm of the loading rate. This behavior is consistent with the Bell model (see text,  $R^2 > 0.95$ ). The results obtained using KG1a (white symbol) were similar to those using K562-ALCAM cells (black). At loading rates  $> 1500$  pN/s, the forces associated with ALCAM-CD6 bond rupture were significantly higher than those for the ALCAM-ALCAM interaction ( $N > 20$ ,  $p < 0.05$ ; error bars indicate s.e.m.). (B) Schematic representation of the significance of the Bell model parameters in terms of the energy barrier between the bound and unbound state. The situation when no force is applied (solid lines) or when external forces are applied to the bonds (dotted lines, see discussion) is represented. (C) Comparison of the histograms of rupture forces (K562-ALCAM cells,  $N > 70$ ; three loading rates) and the theoretical probability density distributions for the failure of single ALCAM-ALCAM and ALCAM-CD6 bonds.

linearity of the force spectra (Fig. 5A) indicates that in this loading rate regime the dissociation of ALCAM-mediated interactions is best described by a single activation energy barrier. In contrast, bi-phasic force spectra reflecting a double-barrier interaction potential have been reported [e.g. for E-cadherin-E-cadherin, LFA-1/ICAM-1 and E-, P-, or L-selectin/sLex (sialyl LewisX)].<sup>40, 43, 53, 62</sup> The Bell model predicts that with increasing loading forces, the activation energy barrier of the complex is suppressed and the dissociation rate constant increases. This is shown schematically in Fig. 5B and will be discussed below.

Fig. 5C shows a comparison of the histograms of rupture forces at three loading rates and the corresponding probability density distributions for the failure of single ALCAM-ALCAM and ALCAM-CD6 bonds that were calculated using the Bell model parameters derived from Fig. 5A using:<sup>55, 59</sup>

$$P(F_{rup}) = k_{off}^0 \exp\left(\frac{X_\beta F_{rup}}{k_B T}\right) \cdot \exp\left\{\frac{k_{off}^0 k_B T}{X_\beta r_f} \left[1 - \exp\left(\frac{X_\beta F_{rup}}{k_B T}\right)\right]\right\} \quad (2)$$

As can be seen in Fig. 5C, the theoretical distributions closely match the histograms of rupture forces at all three loading rates. The width of the distributions does not reflect experimental error, but is a manifestation of the underlying stochastic distribution of breakup times.<sup>52, 59, 63</sup> The small number of events beyond the predicted distributions,



### Supplementary Figure S1: ALCAM-mediated adhesion probed by a ligand coated, bead-modified AFM cantilever

(A) **Materials and methods.** 10 pN/nm cantilevers (MSCT; Veeco Instruments, Santa Barbara, CA) with a 10  $\mu\text{m}$  glass bead glued onto the tip were obtained from Novascan (Ames, IA). Individual cantilevers were calibrated using the thermal oscillation method. The beads were coated with streptavidin by the manufacturer and were further modified with biotinylated goat anti-human Fc-(Fab)<sub>2</sub> fragments and subsequently with purified recombinant ALCAM-Fc or CD6-Fc. The ALCAM- or CD6-coated cantilevers were used to probe the interaction with ALCAM expressed at the cell membrane of K562-ALCAM cells seeded on a poly-L-lysine-coated glass coverslip. Force measurements were performed on at least ten K562 cells in medium A. The interaction time between the bead and the cell was set to 3 s at a contact force of  $\sim 500$  pN.

(B) **Single molecule force measurements.** Histograms show the force distributions obtained by analyzing the final rupture events under two different pulling conditions. At a pulling velocity of 2.5  $\mu\text{m/s}$  the mean rupture force and loading rates ( $\pm$  s.e.m.;  $N > 75$ ) were  $22 \pm 1$  pN at  $294 \pm 27$  pN/s for the ALCAM-ALCAM bond and  $28 \pm 1$  pN at  $331 \pm 30$  pN/s for ALCAM-CD6. At a pulling velocity of 12.5  $\mu\text{m/s}$  this amounted to  $54 \pm 1$  pN at  $1473 \pm 135$  pN/s for ALCAM-ALCAM and to  $61 \pm 2$  pN at  $1659 \pm 152$  pN/s for ALCAM-CD6. While the mean loading rates obtained for both pulling conditions did not significantly differ, the ALCAM-CD6 bond ruptured at significantly higher forces than the homotypic interaction in both cases ( $p < 0.05$ ). A single Gaussian function (solid lines) could be fit to the force distributions which in all cases accounted for  $> 85\%$  of the events, indicating that predominantly single-molecule rupture events were analyzed, see main text.

(C) **Specificity of the interactions.** Analyses of the relative work of de-adhesion comparing the situation before treatment (dashed bars), with that after a 30 min incubation with the ALCAM function blocking mAb AZN-L50 (open bars). Both the homo- and heterotypic ALCAM-mediated interactions could be blocked indicating that the interactions were indeed ALCAM-specific. At least 25 traces per cell were analyzed per condition (medium condition set to 100%; error bars represent s.e.m.; \* indicates significance to  $p < 0.05$ .)

(D) **Bead-modified vs cell-functionalized cantilevers.** Comparison of the mean rupture forces determined using bead-modified AFM cantilevers (stars: ALCAM-ALCAM; triangles: ALCAM-CD6;  $\pm$  s.d.) and the data obtained using cell-functionalized cantilevers represented by the Bell model fit results taken from Fig. 5A). The data obtained using the bead-modified AFM cantilevers are in good agreement with the data obtained using the cell-functionalized AFM cantilevers.



<16% of events in all cases in Fig. 5C, can be accounted for by the simultaneous, i.e. un-resolved, rupture of multiple bond linkages.<sup>63</sup> Importantly, this analysis implies that indeed ~85% of the events represent the kinetically limited failure of single bonds.

Control experiments were performed to verify whether the attachment of the cells to the cantilevers by means of ConA-mediated linkages possibly activated the cells and affected the outcome of the single-molecule adhesion measurements. K562-ALCAM cells were seeded onto poly-L-lysine coated glass coverslips and probed with a 10  $\mu\text{m}$  ALCAM-Fc or CD6-Fc coated bead glued to an AFM cantilever (see supplementary material Fig. S1A). The interactions were found to be ALCAM-specific and showed a clear single-molecule signature (see supplementary material Fig. S1B,C). The mean rupture forces for both the homo- and heterotypic ALCAM-mediated interactions that were found under varying pulling conditions agree well with the data obtained using the cell-functionalized cantilevers (supplementary material Fig. S1D). These data show that the presented single-molecule level adhesion measurements are independent of the probing method.

Finally, the dissociation energies of single ALCAM-mediated interactions were derived from the net amount of work required to break the bonds, by calculating the product of rupture force and rupture length. The work to break a single ALCAM-ALCAM interaction - at 1000 pN/s, corresponding to a pulling speed of 700 nm/s – amounted to  $40 \text{ pN} \times 0.38 \text{ nm} \approx 4 k_B T$  (Fig. 5A;  $T = 300 \text{ K}$ ). Interestingly, under the same conditions, due to the higher unbinding force and the shorter reactive compliance, the net work to rupture an ALCAM-CD6 bond was  $50 \text{ pN} \times 0.23 \text{ nm} \approx 3 k_B T$ . Hence, despite the shorter mechanical bond-length, under physiologically relevant loading we found that the net work to break a single ALCAM-CD6 interaction was similar in magnitude to that found for the dissociation of the ALCAM-ALCAM complex. We note that in order to extract a transmembrane protein from the cell membrane, around 70 kcal/mol is required (i.e. about  $\sim 120 k_B T$  for a single protein).<sup>64</sup> Previous reports suggested that Ig-CAMs may cushion shear stresses at cell-cell contacts in the immune system by forced (reversible) unfolding of their Ig domains.<sup>65, 66</sup> However, under similar loading conditions these authors reported the net work to unfold an Ig domain to be in the 13-16  $k_B T$  regime.<sup>65</sup> Therefore, rather than inducing unfolding of the ALCAM Ig domains, we believe that shear related loading of ALCAM-mediated bonds *in vivo* will result in bond rupture, as suggested here.

In summary, we found that the dissociation of homo- and heterotypic ALCAM-mediated interactions are governed by distinct mechanical properties, revealing the molecular basis for the higher relative stability of the ALCAM-CD6 bond than the ALCAM-ALCAM bond under external loading.

## Discussion

ALCAM mediates cell adhesion during highly dynamic cellular interactions and hence under varying conditions of external loading. The relationship between the affinity and avidity of ALCAM-mediated interactions, and the ability of this molecule to facilitate productive cellular interactions under mechanical stress is poorly understood. We applied force spectroscopy to study the relative stability of single homo- and heterotypic ALCAM-mediated interactions, on living cells and in a dynamic setting mimicking cell-cell interactions at relative speeds ranging from 0.2 – 13  $\mu\text{m/s}$ .

Previous reports indicated that ALCAM-mediated adhesion of K562-ALCAM cells is dynamically regulated through the actin cytoskeleton. Treatment of the cells with

**Table 1: The kinetics and reactive compliance of ALCAM-mediated interactions placed in context**

System	$x_{\beta 2}$ (nm)	$k_{\alpha}^0$ (s <sup>-1</sup> )	$x_{\beta 2}$ (nm)	$k_{\alpha}^0$ (s <sup>-1</sup> )	Reference
ALCAM – ALCAM <sup>a</sup>	0.38 ± 0.06*	1.9 ± 0.8*			This work
ALCAM – CD6 <sup>a</sup>	0.23 ± 0.01*	3.4 ± 0.3*			This work
N-cadherin – N-cadherin <sup>b</sup>	0.77 ± 0.09	0.98 ± 0.46			Panorchan et al. <sup>43</sup>
E-cadherin – E-cadherin <sup>c</sup>	0.32 ± 0.07	1.09 ± 0.35	0.10 ± 0.02	4.00 ± 0.68	Panorchan et al. <sup>43</sup>
VE-cadherin – VE-cadherin <sup>b</sup>	0.42 ± 0.03	0.45 ± 0.12			Panorchan et al. <sup>67</sup>
P-selectin – PSGL-1 <sup>d</sup>	0.15 ± 0.01	0.22 ± 0.06			Hanley et al. <sup>42</sup>
LFA-1 – ICAM-1 (low affinity) <sup>e</sup>	0.15	4.0	0.018	57	Zhang et al. <sup>40</sup>
LFA-1 – ICAM-1 (high affinity) <sup>a</sup>	0.21	0.17	0.024	40	Zhang et al. <sup>40</sup>
E-selectin – sLeX <sup>f</sup>	0.5	0.3	0.09	65	Zhang et al. <sup>62</sup>

<sup>a</sup> loading rate 300 – 20,000 pN/second <sup>b</sup> loading rate 50 – 5000 pN/second <sup>c</sup> loading rate 100 – 500 pN/second (lower regime), 500 – 10,000 pN/second (higher regime) <sup>d</sup> loading rate 100 – 10,000 pN/second <sup>e</sup> loading rate 20 – 10,000 pN/second (lower regime), 10,000 – 50,000 pN/second (higher regime) <sup>f</sup> loading rate 100 – 10,000 pN/second (lower regime), 10,000 – 100,000 pN/second (higher regime)

\* Error estimation on the basis of a comparison between the data derived from both cell types

agents that disrupt the cortical cytoskeleton [e.g. the actin polymerization inhibitor cytochalasin D (CytD) or latrunculin A] significantly enhanced adhesion to ligand-coated plates.<sup>12, 13</sup> Here, we provide biochemical evidence that ALCAM can associate with  $\beta$ -actin. We further show by means of single-molecule resolution adhesion measurements that, although CytD treatment indeed enhances overall cell adhesion, it does not affect the tensile strength of the individual bonds. This unequivocally demonstrates that CytD affects ALCAM binding avidity rather than its affinity. Avidity enhancement could be due either to an enlarged cell-substrate contact area under force - facilitated by a possible loss of cortical tension - or enhanced microclustering of the more freely diffusing ALCAM molecules, as was suggested in the previous studies. Alternatively, avidity enhancement might occur through attenuated ALCAM-cytoskeleton interactions, influencing membrane separation from the cytoskeleton and hence the onset of tether formation.<sup>63</sup> Membrane tethers were suggested to dampen the shear forces in flow-chamber assays, enabling a longer duration of receptor-ligand attachment and thereby affecting binding avidity.<sup>63</sup> The exact cause of the avidity change is currently under investigation. By combining of AFM with confocal fluorescence microscopy, and using high-resolution whole-mount transmission electron microscopy<sup>2, 3</sup> we are currently exploring how the actomyosin cytoskeleton regulates these avidity changes.

By performing the AFM experiments under well-defined conditions of moderate adhesion, we were able to assign the observed sudden force jumps to single ALCAM-specific unbinding events. Indeed, apart from the fact that adhesion could be blocked using the ALCAM function-blocking mAb AZN-L50, significantly different force spectra were obtained for the ALCAM-ALCAM and ALCAM-CD6 bonds. Furthermore, the force-spectra were found to be essentially independent of the cell-type studied. Interestingly, this also indicates that the local membrane environment and the overall cell viscoelastic properties do not significantly affect the outcome of the single-molecule adhesion measurements. This is consistent with literature data showing that force spectra could be reproduced even after cells were fixed.<sup>42, 43, 52, 55</sup> The present observation that, on living cells, CytD does not affect the ALCAM-specific unbinding forces validates and extends these findings.

The equilibrium parameters for the ALCAM-ALCAM and ALCAM-CD6 interactions have previously been derived from surface-plasmon-resonance experiments and indicated a tenfold difference in dissociation rate (i.e. 5 s<sup>-1</sup> vs 0.5 s<sup>-1</sup>, respectively) for the homo- and heterotypic interaction respectively, and a hundred-fold higher affinity ( $K_D$ )

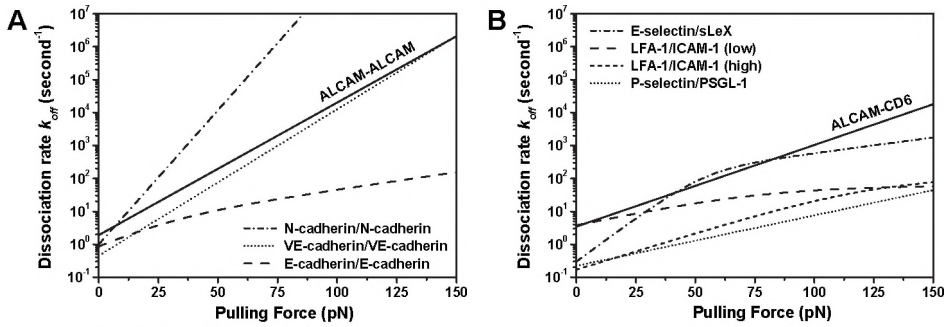


**Figure 6: Kinetic profiles of the ALCAM-mediated interactions placed in context**

The kinetic profiles of ALCAM-mediated interactions, based on the derived Bell model parameters, are compared to (A) homotypic E-, N-, and VE-cadherin mediated interactions, and (B) LFA-1/ICAM-1 (low and high affinity), P-selectin/PSGL-1 and E-selectin/sLex interactions (see text).

of ALCAM for CD6.<sup>14</sup> Interestingly, the unstressed dissociation rates derived here ( $1.9$  vs  $3.4 \text{ s}^{-1}$ , Table 1), although in overall agreement, do not show this relative difference. This is likely due to the fact that in our case the unstressed off-rates are derived by extrapolation from the higher loading regime. Here, the unbinding events might be forced through a specific pathway and hence may be expected to exhibit fewer degrees of freedom - a situation that is clearly distinct from that occurring in soluble ligand binding assays, and may be more physiological. By contrast, we found that the ALCAM-CD6 interaction displayed higher tensile strengths and a significantly smaller reactive compliance suggesting that this bond will be more resistant to applied force, and hence more stable under conditions of mechanical stress.

The stability of the adhesive bonds can be quantified by the dissociation rates of the interactions under conditions of external loading. The Bell model predicts that with increasing loading forces, the dissociation rate constants increase. The micromechanical properties derived here were used to compare the dissociation rates of the homo- and heterotypic ALCAM-mediated interactions under mechanical stress, and to place them in context. The force dependence of the dissociation rate of a bond displaying an inner and an outer activation barrier is given by:

$$k_{off} = 1 / \left[ \frac{1}{k_1^0} \exp\left(\frac{-Fx_{\beta_1}}{k_B T}\right) + \frac{1}{k_2^0} \exp\left(\frac{-Fx_{\beta_2}}{k_B T}\right) \right] \quad (3)$$

where the subscripts (1,2) indicate the outer and inner barrier respectively.<sup>53</sup> For ALCAM-mediated adhesion that only displaying a single activation barrier, the denominator only contains a single term only. Fig. 6 shows a comparison, based on the data listed in Table 1, of the kinetic profiles of the ALCAM-ALCAM and ALCAM-CD6 bonds with those of P-selectin/PSGL-1,<sup>42, 54</sup> E-selectin/sialyl Lewis X (sLeX),<sup>62</sup> low- and high affinity LFA-1/ICAM-1,<sup>40</sup> and homotypic E-, N-, and VE-cadherin interactions.<sup>43, 67</sup> Interestingly, although the dynamic force spectroscopy measurements did not show a significant difference in dissociation rates at low forces, with respect to the ALCAM-CD6 interaction a 10- to 100-fold higher lability for the homotypic ALCAM interaction is predicted in the 75 – 125 pN regime, likely representing the high-end of the physiologically relevant force range.<sup>55, 65</sup> A schematic representation of this finding is presented in Fig. 5B (dotted curves).

Homotypic ALCAM-mediated interactions have been implicated in the onset of melanoma, as besides the switching from E- to N- and VE-cadherin expression, ALCAM is also detected in early melanocytic transformation stages (reviewed by Swart et al.<sup>27</sup>). The ALCAM-positive metastatic phenotype of melanoma cells is characterized further by the absence of significant levels of the cadherins.<sup>27, 68</sup> Fig. 6A compares the force-response curves of homotypic ALCAM-mediated and E-, N- and VE-cadherin-mediated interactions. Although the unstressed dissociation rates of these molecules are similar in magnitude, ALCAM and VE-cadherin display an up to three orders of magnitude higher dissociation rate in the physiological force-window, with respect to E-cadherin. For N-cadherin this is already the case in the 30-40 pN range, and the relative lability of this bond under loading has been associated with the ability of breast tumor cells to break away from the primary tumor.<sup>43</sup> Similarly, expressing ALCAM rather than E-cadherin is anticipated to relieve the firm adhesive constraints facilitating transformed melanoma cells to escape the local tumor environment. The data further indicate that, under force, ALCAM will be able to sustain sufficient levels of adhesion. Hence, the kinetic and mechanical properties of the homotypic ALCAM-mediated interaction are consistent with a role for this bond promoting the migratory phenotype of melanoma cells.-

The heterotypic ALCAM-CD6 interaction, in the 20 - 120 pN force window (Fig. 6B), compares well – kinetically – with the rolling receptor pair E-Selectin/sLeX.<sup>62</sup> Besides its role in extravasation, E-selectin/sLeX interactions play a role in the vascular invasion and metastasis of human gallbladder adenocarcinoma.<sup>69</sup> P-selectin/PSGL-1 and LFA-1/ICAM-1 are involved in leukocyte rolling and firm adhesion to vascular endothelium during inflammation respectively. Clearly, high resistance to force is biologically important for the ability of these molecules to maintain cell-cell interactions in the blood flow. Consistent with their biological role these receptor pairs show significant smaller dissociation rates compared to the ALCAM-mediated interactions over the entire force-window. In DC-T cell interactions, ALCAM and CD6 are rapidly recruited to the contact site in an antigen dependent way, most likely under control of the actomyosin cytoskeleton,<sup>30, 70</sup> and the ALCAM-CD6 interaction reportedly has a dual function in that it both facilitates stable adhesion and provides a co-stimulatory signal.<sup>30</sup> The data presented here demonstrate that in the dynamic environment of the lymph node, this interaction is indeed sturdy enough to play a significant role in establishing early DC-T cell contact, in damping of shear stress and in providing long term stabilization to the highly organized structure of the immunological synapse.

Taken together, the single-molecule resolution adhesion measurements presented here have allowed us to obtain novel insight in the (patho)physiological role and regulation of ALCAM-mediated cell adhesion on a scale that was previously inaccessible. More generally, this work shows that measuring adhesion forces under external loading more accurately reflects differences between cell adhesion molecules that are not apparent in soluble ligand binding assays.

## Acknowledgements

JtR is supported by NanoNed, the Dutch nanotechnology programme of the Ministry of Economic Affairs. The Netherlands Organization of Scientific Research supports CGF through TOP Grant 9120.6030 and AC through Grant Veni 916.66.028 and SLW 33.302P. FdL received support through grant KUN OZ-2002-5 from the Radboud University Nijmegen Medical Centre. The authors thank Ben Ohler and Patrick Markus (Veeco Instruments) for their valuable technical support and Peter Schön for critical

reading of the manuscript. The Microscopic Imaging Centre (MIC) of the NCMLS is kindly acknowledged for providing facilities.

## References

1. **Y. van Kooyk, C. G. Figdor** (2000). Avidity regulation of integrins: the driving force in leukocyte adhesion. *Curr. Opin. Cell Biol.*, **12**, 542-547.
2. **A. Cambi, F. de Lange, N. M. van Maarseveen, M. Nijhuis, B. Joosten, E. M. van Dijk, B. I. de Bakker, J. A. Fransen, P. H. Bovee-Geurts, F. N. van Leeuwen, N. F. Van Hulst, C. G. Figdor** (2004). Microdomains of the C-type lectin DC-SIGN are portals for virus entry into dendritic cells. *J. Cell Biol.*, **164**, 145-155.
3. **A. Cambi, B. Joosten, M. Koopman, F. de Lange, I. Beeren, R. Torensma, J. A. Fransen, M. Garcia-Parajo, F. N. van Leeuwen, C. G. Figdor** (2006). Organization of the Integrin LFA-1 in Nanoclusters Regulates Its Activity. *Mol. Biol. Cell*, **17**, 4270-4281.
4. **C. V. Carman, T. A. Springer** (2003). Integrin avidity regulation: are changes in affinity and conformation underemphasized? *Curr. Opin. Cell Biol.*, **15**, 547-556.
5. **M. Kim, C. V. Carman, W. Yang, A. Salas, T. A. Springer** (2004). The primacy of affinity over clustering in regulation of adhesiveness of the integrin  $\alpha\beta_2$ . *J. Cell Biol.*, **167**, 1241-1253.
6. **G. Li, K. Satyamoorthy, F. Meier, C. Berking, T. Bogenrieder, M. Herlyn** (2003). Function and regulation of melanoma-stromal fibroblast interactions: when seeds meet soil. *Oncogene*, **22**, 3162-3171.
7. **D. Hanahan, R. A. Weinberg** (2000). The hallmarks of cancer. *Cell*, **100**, 57-70.
8. **R. B. Hazan, R. Qiao, R. Keren, I. Badano, K. Suyama** (2004). Cadherin switch in tumor progression. *Ann. N Y Acad. Sci.*, **1014**, 155-163.
9. **P. Cowin, T. M. Rowlands, S. J. Hatsell** (2005). Cadherins and catenins in breast cancer. *Curr. Opin. Cell Biol.*, **17**, 499-508.
10. **K. A. Knudsen, M. J. Wheelock** (2005). Cadherins and the mammary gland. *J. Cell Biochem.*, **95**, 488-496.
11. **M. A. Bowen, D. D. Patel, X. Li, B. Modrell, A. R. Malacko, W. C. Wang, H. Marquardt, M. Neubauer, J. M. Pesando, U. Francke** (1995). Cloning, mapping, and characterization of activated leukocyte-cell adhesion molecule (ALCAM), a CD6 ligand. *J. Exp. Med.*, **181**, 2213-2220.
12. **J. M. Nelissen, I. M. Peters, B. G. de Grooth, Y. van Kooyk, C. G. Figdor** (2000). Dynamic regulation of activated leukocyte cell adhesion molecule-mediated homotypic cell adhesion through the actin cytoskeleton. *Mol. Biol. Cell*, **11**, 2057-2068.
13. **A. W. Zimmerman, J. M. Nelissen, S. E. Van Emst-De Vries, P. H. Willems, F. De Lange, J. G. Collard, F. N. Van Leeuwen, C. G. Figdor** (2004). Cytoskeletal restraints regulate homotypic ALCAM-mediated adhesion through PKC $\alpha$  independently of Rho-like GTPases. *J. Cell Sci.*, **117**, 2841-2852.
14. **N. J. Hassan, A. N. Barclay, M. H. Brown** (2004). Frontline: Optimal T cell activation requires the engagement of CD6 and CD166. *Eur. J. Immunol.*, **34**, 930-940.
15. **D. D. Patel, S. F. Wee, L. P. Whichard, M. A. Bowen, J. M. Pesando, A. Aruffo, B. F. Haynes** (1995). Identification and characterization of a 100-kD ligand for CD6 on human thymic epithelial cells. *J. Exp. Med.*, **181**, 1563-1568.
16. **W. G. Degen, L. C. van Kempen, E. G. Gijzen, J. J. van Groningen, Y. van Kooyk, H. P. Bloemers, G. W. Swart** (1998). MEMD, a new cell adhesion molecule in metastasizing human melanoma cell lines, is identical to ALCAM (activated leukocyte cell adhesion molecule). *Am. J. Pathol.*, **152**, 805-813.
17. **H. Tanaka, T. Matsui, A. Agata, M. Tomura, I. Kubota, K. C. McFarland, B. Kohr, A. Lee, H. S. Phillips, D. L. Shelton** (1991). Molecular cloning and expression of a novel adhesion molecule, SC1. *Neuron*, **7**, 535-545.
18. **A. Masedunskas, J. A. King, F. Tan, R. Cochran, T. Stevens, D. Sviridov, S. F. Ofori-Acquah** (2006). Activated leukocyte cell adhesion molecule is a component of the endothelial junction involved in transendothelial monocyte migration. *FEBS Lett.*, **580**, 2637-2645.
19. **G. W. Swart** (2002). Activated leukocyte cell adhesion molecule (CD166/ALCAM): developmental and mechanistic aspects of cell clustering and cell migration. *Eur. J. Cell Biol.*, **81**, 313-321.
20. **L. C. van Kempen, J. J. van den Oord, G. N. van Muijen, U. H. Weidle, H. P. Bloemers, G. W. Swart** (2000). Activated leukocyte cell adhesion molecule/CD166, a marker of tumor progression in primary malignant melanoma of the skin. *Am. J. Pathol.*, **156**, 769-774.
21. **L. C. van Kempen, J. M. Nelissen, W. G. Degen, R. Torensma, U. H. Weidle, H. P. Bloemers, C. G. Figdor, G. W. Swart** (2001). Molecular basis for the homophilic activated leukocyte cell adhesion molecule (ALCAM)-ALCAM interaction. *J. Biol. Chem.*, **276**, 25783-25790.
22. **P. C. Lunter, J. W. van Kilsdonk, H. van Beek, I. M. Cornelissen, M. Bergers, P. H. Willems, G. N. van Muijen, G. W. Swart** (2005). Activated leukocyte cell adhesion molecule (ALCAM/CD166/MEMD), a novel actor in invasive growth, controls matrix metalloproteinase activity. *Cancer Res.*, **65**, 8801-8808.
23. **K. Tomita, A. van Bokhoven, C. F. J. Jansen, L. A. Kiemeneij, H. F. M. Karthaus, J. Vrieseema, M. J. G. Bussemakers, J. A. Witjes, J. A. Schalken** (2003). Activated Leukocyte Cell Adhesion Molecule (ALCAM) Expression is Associated with a Poor Prognosis for Bladder Cancer Patients. *UroOncology*, **3**, 121-129.
24. **G. Kristiansen, C. Pilarsky, C. Wissmann, C. Stephan, L. Weissbach, V. Loy, S. Loening, M. Dietel, A. Rosenthal** (2003). ALCAM/CD166 is up-regulated in low-grade prostate cancer and progressively lost in high-grade lesions. *Prostate*, **54**, 34-43.
25. **J. A. King, S. F. Ofori-Acquah, T. Stevens, A. B. Al-Mehdi, O. Fodstad, W. G. Jiang** (2004). Activated leukocyte cell adhesion molecule in breast cancer: prognostic indicator. *Breast Cancer Res.*, **6**, R478-487.
26. **W. Weichert, T. Knosel, J. Bellach, M. Dietel, G. Kristiansen** (2004). ALCAM/CD166 is overexpressed in colorectal carcinoma and correlates with shortened patient survival. *J. Clin. Pathol.*, **57**, 1160-1164.
27. **G. W. Swart, P. C. Lunter, J. W. Kilsdonk, L. C. Kempen** (2005). Activated leukocyte cell adhesion molecule

- (ALCAM/CD166): signaling at the divide of melanoma cell clustering and cell migration? *Cancer Metastasis Rev.*, **24**, 223-236.
28. **A. Grakoui, S. K. Bromley, C. Sumen, M. M. Davis, A. S. Shaw, P. M. Allen, M. L. Dustin** (1999). The immunological synapse: a molecular machine controlling T cell activation. *Science*, **285**, 221-227.
  29. **I. Gimferrer, M. Calvo, M. Mittelbrunn, M. Farnos, M. R. Sarrias, C. Enrich, J. Vives, F. Sanchez-Madrid, F. Lozano** (2004). Relevance of CD6-mediated interactions in T cell activation and proliferation. *J. Immunol.*, **173**, 2262-2270.
  30. **A. W. Zimmerman, B. Joosten, R. Torensma, J. R. Parnes, F. N. van Leeuwen, C. G. Figdor** (2006). Long-term engagement of CD6 and ALCAM is essential for T-cell proliferation induced by dendritic cells. *Blood*, **107**, 3212-3220.
  31. **R. M. Gangemi, J. A. Swack, D. M. Gavoria, P. L. Romain** (1989). Anti-T12, an anti-CD6 monoclonal antibody, can activate human T lymphocytes. *J. Immunol.*, **143**, 2439-2447.
  32. **S. Wee, G. L. Schieven, J. M. Kirihara, T. T. Tsu, J. A. Ledbetter, A. Aruffo** (1993). Tyrosine phosphorylation of CD6 by stimulation of CD3: augmentation by the CD4 and CD2 coreceptors. *J. Exp. Med.*, **177**, 219-223.
  33. **R. A. Rasmussen, S. L. Counts, J. F. Daley, S. F. Schlossman** (1994). Isolation and characterization of CD6 T cells from peripheral blood. *J. Immunol.*, **152**, 527-536.
  34. **L. M. Osorio, M. Rottenberg, M. Jondal, S. C. Chow** (1998). Simultaneous cross-linking of CD6 and CD28 induces cell proliferation in resting T cells. *Immunology*, **93**, 358-365.
  35. **T. R. Mempel, S. E. Henrickson, U. H. Von Andrian** (2004). T-cell priming by dendritic cells in lymph nodes occurs in three distinct phases. *Nature*, **427**, 154-159.
  36. **G. Binnig, C. F. Quate, C. Gerber** (1986). Atomic force microscope. *Phys. Rev. Lett.*, **56**, 930-933.
  37. **P. Hinterdorfer** (2002). Molecular recognition studies using the atomic force microscope. *Methods Cell Biol.*, **68**, 115-139.
  38. **O. H. Willemsen, M. M. Snel, A. Cambi, J. Greve, B. G. De Groot, C. G. Figdor** (2000). Biomolecular interactions measured by atomic force microscopy. *Biophys. J.*, **79**, 3267-3281.
  39. **M. Benoit, D. Gabriel, G. Gerisch, H. E. Gaub** (2000). Discrete interactions in cell adhesion measured by single-molecule force spectroscopy. *Nat. Cell Biol.*, **2**, 313-317.
  40. **X. Zhang, E. P. Wojcikiewicz, V. T. Moy** (2002). Force spectroscopy of the leukocyte function-associated antigen-1/intercellular adhesion molecule-1 interaction. *Biophys. J.*, **83**, 2270-2279.
  41. **E. P. Wojcikiewicz, X. Zhang, A. Chen, V. T. Moy** (2003). Contributions of molecular binding events and cellular compliance to the modulation of leukocyte adhesion. *J. Cell Sci.*, **116**, 2531-2539.
  42. **W. D. Hanley, D. Wirtz, K. Konstantopoulos** (2004). Distinct kinetic and mechanical properties govern selectin-leukocyte interactions. *J. Cell Sci.*, **117**, 2503-2511.
  43. **P. Panorchan, M. S. Thompson, K. J. Davis, Y. Tseng, K. Konstantopoulos, D. Wirtz** (2006). Single-molecule analysis of cadherin-mediated cell-cell adhesion. *J. Cell Sci.*, **119**, 66-74.
  44. **P. Hinterdorfer, Y. F. Dufrêne** (2006). Detection and localization of single molecular recognition events using atomic force microscopy. *Nat. Methods*, **3**, 347-355.
  45. **X. Zhang, S. E. Craig, H. Kirby, M. J. Humphries, V. T. Moy** (2004). Molecular basis for the dynamic strength of the integrin  $\alpha_5\beta_1$ /VCAM-1 interaction. *Biophys. J.*, **87**, 3470-3478.
  46. **K. D. Kim, S. C. Choi, Y. W. Noh, J. W. Kim, S. G. Paik, Y. Yang, K. Kim, 2nd, J. S. Lim** (2006). Impaired responses of leukemic dendritic cells derived from a human myeloid cell line to LPS stimulation. *Exp. Mol. Med.*, **38**, 72-84.
  47. **H. Quentmeier, A. Duschl, Z. B. Hu, B. Schnarr, M. Zaborski, H. G. Drexler** (1996). MUTZ-3, a monocytic model cell line for interleukin-4 and lipopolysaccharide studies. *Immunology*, **89**, 606-612.
  48. **J. L. Hutter, J. Bechhoefer** (1993). Calibration of atomic-force microscope tips. *Rev. Sci. Instrum.*, **64**, 1868-1873.
  49. **P. H. Puech, A. Taubenberger, F. Ulrich, M. Krieg, D. J. Muller, C. P. Heisenberg** (2005). Measuring cell adhesion forces of primary gastrulating cells from zebrafish using atomic force microscopy. *J. Cell Sci.*, **118**, 4199-4206.
  50. **E. Evans, K. Ritchie** (1999). Strength of a weak bond connecting flexible polymer chains. *Biophys. J.*, **76**, 2439-2447.
  51. **C. Yuan, A. Chen, P. Kolb, V. T. Moy** (2000). Energy landscape of streptavidin-biotin complexes measured by atomic force microscopy. *Biochemistry*, **39**, 10219-10223.
  52. **D. F. Tees, R. E. Waugh, D. A. Hammer** (2001). A microcantilever device to assess the effect of force on the lifetime of selectin-carbohydrate bonds. *Biophys. J.*, **80**, 668-682.
  53. **E. Evans, A. Leung, D. Hammer, S. Simon** (2001). Chemically distinct transition states govern rapid dissociation of single L-selectin bonds under force. *Proc. Natl. Acad. Sci. USA*, **98**, 3784-3789.
  54. **W. Hanley, O. McCarty, S. Jadhav, Y. Tseng, D. Wirtz, K. Konstantopoulos** (2003). Single molecule characterization of P-selectin/ligand binding. *J. Biol. Chem.*, **278**, 10556-10561.
  55. **F. Li, S. D. Redick, H. P. Erickson, V. T. Moy** (2003). Force measurements of the  $\alpha_5\beta_1$  integrin-fibronectin interaction. *Biophys. J.*, **84**, 1252-1262.
  56. **J. Wong, A. Chilkoti, V. T. Moy** (1999). Direct force measurements of the streptavidin-biotin interaction. *Biomol. Eng.*, **16**, 45-55.
  57. **G. I. Bell** (1978). Models for the specific adhesion of cells to cells. *Science*, **200**, 618-627.
  58. **R. Alon, S. Chen, R. Fuhlbrigge, K. D. Puri, T. A. Springer** (1998). The kinetics and shear threshold of transient and rolling interactions of L-selectin with its ligand on leukocytes. *Proc. Natl. Acad. Sci. USA*, **95**, 11631-11636.
  59. **E. Evans, K. Ritchie** (1997). Dynamic strength of molecular adhesion bonds. *Biophys. J.*, **72**, 1541-1555.
  60. **G. Hummer, A. Szabo** (2001). Free energy reconstruction from nonequilibrium single-molecule pulling experiments. *Proc. Natl. Acad. Sci. USA*, **98**, 3658-3661.
  61. **M. Rief, H. Grubmüller** (2002). Force spectroscopy of single biomolecules. *Chemphyschem*, **3**, 255-261.
  62. **X. Zhang, D. F. Bogorin, V. T. Moy** (2004). Molecular basis of the dynamic strength of the sialyl Lewis X-selectin interaction. *Chemphyschem*, **5**, 175-182.

63. **E. Evans, V. Heinrich, A. Leung, K. Kinoshita** (2005). Nano- to microscale dynamics of P-selectin detachment from leukocyte interfaces. I. Membrane separation from the cytoskeleton. *Biophys. J.*, **88**, 2288-2298.
64. **A. Chen, V. T. Moy** (2000). Cross-linking of cell surface receptors enhances cooperativity of molecular adhesion. *Biophys. J.*, **78**, 2814-2820.
65. **P. Carl, C. H. Kwok, G. Manderson, D. W. Speicher, D. E. Discher** (2001). Forced unfolding modulated by disulfide bonds in the Ig domains of a cell adhesion molecule. *Proc. Natl. Acad. Sci. USA*, **98**, 1565-1570.
66. **N. Bhasin, P. Carl, S. Harper, G. Feng, H. Lu, D. W. Speicher, D. E. Discher** (2004). Chemistry on a single protein, vascular cell adhesion molecule-1, during forced unfolding. *J. Biol. Chem.*, **279**, 45865-45874.
67. **P. Panorchan, J. P. George, D. Wirtz** (2006). Probing intercellular interactions between vascular endothelial cadherin pairs at single-molecule resolution and in living cells. *J. Mol. Biol.*, **358**, 665-674.
68. **K. Uhlenbrock, A. Eberth, U. Herbrand, N. Daryab, P. Stege, F. Meier, P. Friedl, J. G. Collard, M. R. Ahmadian** (2004). The RacGEF Tiam1 inhibits migration and invasion of metastatic melanoma via a novel adhesive mechanism. *J. Cell Sci.*, **117**, 4863-4871.
69. **H. Kashiwagi, H. Kijima, S. Dowaki, Y. Ohtani, K. Tobita, H. Yamazaki, M. Nakamura, Y. Ueyama, M. Tanaka, S. Inokuchi, T. Imaizumi, H. Makuuchi** (2004). Clinicopathological significance of sialyl Lex expression in human gallbladder carcinoma. *Oncol. Rep.*, **11**, 1139-1143.
70. **I. Gimferrer, A. Ibanez, M. Farnos, M. R. Sarrias, R. Fenutria, S. Rosello, P. Zimmermann, G. David, J. Vives, C. Serra-Pages, F. Lozano** (2005). The lymphocyte receptor CD6 interacts with syntenin-1, a scaffolding protein containing PDZ domains. *J. Immunol.*, **175**, 1406-1414.
71. **M. A. Bowen, A. A. Aruffo, J. Bajorath** (2000). Cell surface receptors and their ligands: in vitro analysis of CD6-CD166 interactions. *Proteins*, **40**, 420-428.

# CHAPTER 5

---

## **Mapping single interactions between DC-SIGN and *Candida albicans*- associated molecular patterns by AFM force spectroscopy**

*Joost te Riet, Inge M.J. Reinieren-Beeren,  
Sylvia Speller, Alessandra Cambi, Carl G. Figdor*

*A man who dares to waste  
one hour of time has not  
discovered the value of life.*

*Charles Darwin*

Manuscript in preparation



The fungus *Candida albicans* is the most common cause of mycotic infections in immunocompromised hosts. Little is known about the initial interactions between *Candida* and immune cell receptors, such as DC-SIGN, because detailed characterization at the structural level is lacking. Understanding these processes will ultimately provide relevant information to develop novel treatments. The C-type lectin DC-SIGN expressed on dendritic cells (DCs) recognizes specific *Candida*-associated molecular patterns. DC-SIGN binds to *Candida* via N-linked mannan sugar epitopes present in the cell wall of *Candida*. However, the exact binding epitope is not yet determined. Furthermore, there might be a role for DC-SIGN tetramerization and DC-SIGN nanoclustering on the affinity and avidity of the DC-SIGN–*C. albicans* bond, which is still unknown. Here, we exploit atomic force microscope force spectroscopy (AFM-FS) to gain better insight in the carbohydrate recognition of DC-SIGN. We demonstrate that slight differences in the N-mannan structure of *Candida* glycosylation mutants can be detected by AFM-FS, giving insight in the single bond affinity of the DC-SIGN–*Candida* interaction. Furthermore, biophysical Bell parameters determined for different carbohydrate-protein interactions exhibit a common dynamical response to forces (i.e. dynamical affinity) for this type of interactions. More detailed knowledge on the binding pocket of DC-SIGN–*Candida* will definitely lead to a better understanding of the carbohydrate recognition of C-type lectins and can ultimately contribute to the development of new anti-fungal drugs.

## Introduction

Ever since the diversity of carbohydrates found in mammalian cell surfaces was recognized, it has been speculated that unique combinations of sugars on individual cells might form the basis for specific adhesion events.<sup>1</sup> In the immune system the carbohydrate-binding C-type lectins (CLRs) and lectin-like receptors play an important role in the recognition of specific carbohydrate structures.<sup>2</sup> The cell adhesion molecule family of lectins can be divided into different subclasses according to their structural similarities and functional differences.<sup>2-4</sup> Well-understood examples of cell adhesion based on glycan-lectin interactions are those of the selectins. The E-, L-, and P-selectins mediate adhesion and homing of leukocytes to the peripheral tissues.<sup>2,4</sup> The tetrasaccharide sialyl-LewisX (sLeX) is the predominant carbohydrate recognized by E- and P-selectin. Furthermore, the slightly different tetrasaccharide sialyl 6-sulpho-LewisX (s6SLeX) is recognized by E- and P-selectin but also by L-selectin.<sup>2-5</sup> On the other hand, the CLR dendritic cell-specific intercellular cell adhesion molecule-3 (ICAM-3)-grabbing non-integrin (DC-SIGN) recognizes high-mannose containing structures and different Lewis antigens, such as LeX.<sup>2,6</sup> DC-SIGN, which is expressed on DCs, can function both as an adhesion receptor and as a phagocytic pathogen-recognition receptor.<sup>2,6,7</sup> Its Ca<sup>2+</sup>-dependent carbohydrate-recognition domain (CRD) binds to different ligands, such as ICAM-2, and -3 in DC-endothelium and DC-T cell interactions, respectively, but also many mannose-containing pathogens, such as viruses (HIV-1, Ebola, Hepatitis C), bacteria (*Mycobacterium tuberculosis*), parasites (*Leishmania*), and fungi (*Candida*).<sup>2</sup> The CRD interacts with specific carbohydrate moieties, e.g. LeX, mannan, and fucose, of the endogenous glycoproteins or exposed at the pathogen surface.<sup>2,8</sup>

Many studies focus on the interaction of DC-SIGN with the fungus *Candida*, which causes the most mycotic infections in severely immunocompromised patients.<sup>9-11</sup> Studies on the initial binding of different *Candida* species (e.g. *C. albicans*, *C. parapsilosis*, and *C. dubliniensis*) with DCs showed that DC-SIGN as well as the macrophage mannose receptor (MMR) are concerned with the detection of *Candida* cells.<sup>10,11</sup> The *Candida* cell wall is

almost exclusively composed of glycans (Fig. 1A). Glycans are synthesized as polymers of three types of monosaccharides: *D*-glucose, which forms  $\beta$ -(1,3)- and  $\beta$ -(1,6)-glucan, *N*-acetyl-*D*-glucosamine, which forms chitin, and *D*-mannose, giving rise to mannan.<sup>12, 13</sup> The outer layer of the *C. albicans* cell wall is enriched in mannoproteins, representing up to 30–40% of the cell wall dry weight,<sup>14</sup> while chitin,  $\beta$ -(1,3)- and  $\beta$ -(1,6)-glucan are more prominent in the inner layer (Fig. 1A). Binding studies of different *Candida* species and glycosylation mutants showed that the carbohydrate pattern recognized by DC-SIGN is within the *N*-linked mannan (protein glycosylation of an amine-group of asparagine or arginine).<sup>11</sup> Furthermore, the epitope necessary for binding to DC-SIGN was restricted to the  $\alpha$ -(1,2)-branched mannose residues. By varying cell wall composition *Candidas* can escape recognition by the host and might strongly influence the repertoire of PRRs that are able to interact.<sup>11</sup> Therefore, studying the affinity of PRRs, such as DC-SIGN, for different mutants of *C. albicans*, but also for synthetic glycans, that resemble those of the pathogen, might be interesting for the design of anti-fungal drugs.

In this study we explored the interaction of DC-SIGN with *C. albicans* by AFM-force spectroscopy in order to gain detailed insight in the specific carbohydrate structures recognized by the CRD of DC-SIGN. Therefore, an intact *C. albicans* cell was immobilized

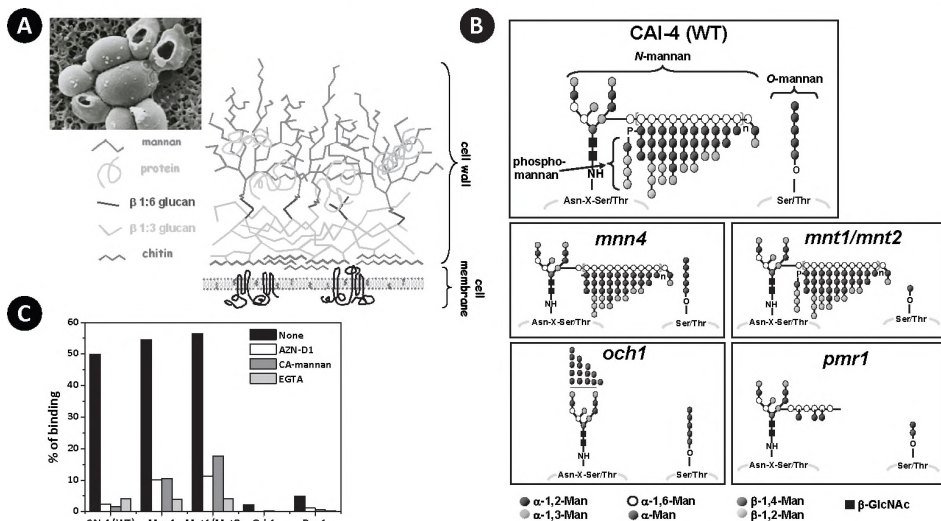


**Figure 1: Structure and binding of *Candida albicans***

(A) The fungus *C. albicans* has a cell membrane as well as a cell wall, like plant cells. This cell wall consists of a mixture of (glyco)proteins and carbohydrates, such as chitin,  $\beta$ -(1:3)- and  $\beta$ -(1:6)-glucans, and mannan. The mannan structures are part of the molecules likely to come into contact with other cells. The inset in the picture shows a scanning electron microscopy (SEM) image of 3–5  $\mu$ m sized *Candida* cells, the thick cell walls are visible. (B) Schematic representation of the different *N*- and *O*-linked mannan carbohydrate structure of different *C. albicans* glycosylation mutants. Compared to the wildtype (WT) variant CAI-4, the mutants lack or have mutations in the phospho-mannan side (*mnn4*), in the *O*-mannan structure (*mnt1/mnt2*), in the highly branched part of *N*-mannan (*och1*) and for *pmr1* parts of both the *O*- and *N*-mannan (see also text). The different colored beads represent the different monosaccharides given in the legend. (C) In a binding study, K562-DC-SIGN cells were incubated with FITC-labeled yeast cells of *C. albicans* wildtype and mutated strains in the presence or absence of blocking agents for 30 min at 37°C. The percentage of cells binding to *Candida* was determined by flow cytometry. Data are presented as means  $\pm$  S.D.

on the AFM cantilever. We clearly demonstrate the feasibility of measuring single receptor-ligand interactions with this method and the dynamical responses of the bonds upon applying picoNewton forces. Thereby, the subtle differences in affinity of DC-SIGN for different *C. albicans* mutants that differ in their carbohydrate make-up could be measured. We expect that these findings will ultimately provide relevant information on the manner by which CLRs, such as DC-SIGN, can specifically recognize and distinguish between endogenous ('self') and pathogen-associated ('non-self') carbohydrate structures. Which could ultimately contribute to better understand antifungal immune responses.

## Materials & Methods

### Chemicals and antibodies

Chemicals were purchased from Sigma (St. Louis, MO) unless stated otherwise. The anti-DC-SIGN monoclonal antibody AZN-D1 was used.<sup>7</sup> Recombinant DC-SIGN-Fc consisting of the extracellular domains of the DC-SIGN fused to the human IgG1 Fc tail was purchased from R&D Systems (Minneapolis, MN).

Mannan derived from *C. albicans* (CA-mannan) was a kind gift from Dr. G. Kogan (Institute of Chemistry of Slovak Academy of Sciences, Bratislava, Slovakia) and was isolated as previously described.<sup>15</sup>

### Candida albicans cells

*C. albicans*, strain UC820, a well described clinical isolate,<sup>16</sup> was maintained on agar slants at 4 °C. Strain UC820 was inoculated into 100 ml of Sabouraud broth and cultured for 24 h at 37 °C. *C. albicans* serotype B wildtype (LGH 1095) and  $\Delta mnn4$  were grown as reported elsewhere.<sup>17</sup> Briefly, starter cultures were grown in 10 ml of Sabouraud broth overnight at 30 °C. 1 ml of overnight culture was inoculated into 100 ml of Sabouraud broth and cultured at 30 °C until log phase is reached. After two washes with pyrogen-free saline by centrifugation at 1500×g, the number of yeast cells was counted in a hemocytometer and resuspended at  $1 \times 10^8$  cells/ml. Heat-kill was at 56 °C for 1 h, if it is required. Yeast cell suspensions were kept frozen at -80 °C until used. The homozygous null mutants in glycosylation genes were constructed in the *C. albicans* CAI-4 serotype A background by targeted gene disruption and their detailed generation is already published.<sup>11, 18</sup>

### Candida binding studies

The binding of K562-DC-SIGN cells to *Candida* yeast cells was measured by flow cytometry using the FACSCalibur (BD Biosciences) and performed as already described.<sup>10</sup> To test the effect of various reagents on ligand binding the following concentrations were used: different carbohydrates 150 µg/ml (unless otherwise indicated), EGTA 2 mM, isotype control (mouse IgG1), AZN-D1 anti-DC-SIGN (30 µg/ml). Incubations were performed in TSM (20 mM Tris, 150 mM NaCl, 1 mM CaCl<sub>2</sub>, 2 mM MgCl<sub>2</sub>, pH 8.0), and 1% bovine serum albumin, as already published.<sup>10</sup> FITC-labeled *Candida* was added in a cell/yeast ratio of 1:5. After 30 min of incubation at 37 °C, cell-yeast conjugates were analyzed by flow cytometry.

### AFM force measurements

Force measurements were made on cells in force-distance mode using a MultiMode AFM (Nanoscope IIIa) equipped with a "J" type piezoelectric translator (Veeco Instruments, Santa Barbara, CA). Triangular gold-coated silicon-nitride cantilevers were used with a nominal spring constant of 10 pN/nm as given by the manufacturer (MLCT-AUHW, Veeco Instruments). Each cantilever was calibrated before use by the calibration method described in Chapter 3. The experimentally determined spring constants of the used cantilevers were  $13 \pm 1$  pN/nm.

### Protein immobilization

DC-SIGN-Fc was immobilized on 12 mm glass coverslips (Menzel-Gläser, Braunschweig, Germany), divided in two halves by Dako pen (Dako Cytomation, Glostrup, Denmark), an uncoated and DC-SIGN-Fc coated part. First, in an overnight (4°C) incubation, 10 µg/ml goat anti-human Fc-(Fab')<sub>2</sub> fragments were absorbed to the coverslip surface in TSM. Then the substrates were rinsed and subsequently incubated for 30 minutes in TSM/1% (w/v) BSA at 37°C to block the remaining exposed non-coated surface. After an additional washing step, the plates were incubated with 5 µg/ml DC-SIGN-Fc in TSM for 1 hour at 37°C. Finally, the coated substrates were washed and transferred into the AFM liquid cell (MTFML, Veeco Instruments).

### Functionalization of AFM cantilevers with *C. albicans* cells

Cells were attached to the AFM cantilever by concanavalin A (ConA)-mediated linkages essentially as described.<sup>19</sup> ConA-coated cantilevers were prepared as follows. Cantilevers were first cleaned by immersion in chloroform for 5 minutes, then rinsed with ethanol and subsequently dried in a N<sub>2</sub>-flow. Following an overnight incubation at 37°C in biotinylated bovine serum albumin (biotin-BSA, 0.5 mg/ml in 100 mM NaHCO<sub>3</sub>, pH 8.6) the cantilevers were rinsed using PBS and exposed to 0.5 mg/ml (PBS, 30 minutes, 37°C) streptavidin (Pierce, Rockford, IL). Finally, the cantilevers were incubated in biotinylated concanavalin A (biotin-ConA, 0.2 mg/ml in TSM + 1 mM NiCl<sub>2</sub>) for 30 minutes at 37°C and washed with TSM.

Intact (heated killed) *C. albicans* cells kept in TSM were seeded onto the uncoated side of the glass coverslip by a 50 µl droplet. The DC-SIGN-Fc-coated side of the sample was also kept in a 50 µl TSM droplet. By closing the liquid cell with the cantilever holder the droplets merge and the cantilever can be used to pick up a cell on one side and to measure specific interactions on the other side, all in one droplet. An optical microscope mounted on top of the AFM was hereby used to position the ConA-functionalized cantilever over a target *C. albicans* cell on the substrate. Subsequently, contact was established between cantilever and cell for at least one minute. During this time the applied indentation force was kept constant at about 2.5 nN. Upon retraction, the successful pick-up was readily scored by visual inspection, and, in these events, the cell was positioned right behind the AFM tip (Fig. 2).

### Rupture-force measurements and force spectroscopy

The cell bearing cantilever was brought into contact with the ligand-coated substrate for a preset period of time (interaction time; 25°C, TSM). During this time, a force was exerted on the cell of no more than ~ 1 nN. Interaction times were such that a minimal, yet significant, DC-SIGN-specific adhesion was established (typically between 0.25-1 seconds). Upon retraction, the forces acting on the cantilever were recorded as a function of displacement of the DC-SIGN-coated substrate. DC-SIGN-*Candida* rupture forces were determined directly from the magnitude of the sudden variations in binding force that are associated with bond rupture. The final ruptures in the force-distance curves were used for further analysis (Fig. 3A). The area enclosed by the zero-force axis and the force-distance curve (Fig. 3A) was taken as a measure for the work ( $W=F \cdot d$ ) performed during the detachment phase.<sup>20, 21</sup> Specificity was verified by an *in situ* incubation with the function blocking DC-SIGN-specific monoclonal antibody AZN-D1 (30 µg/ml) and soluble *C. albicans* mannan (CA-mannan; 150 µg/ml) for 30 minutes. Force curves were analyzed using Origin<sup>®</sup> Pro 8.1 (OriginLab Corporation, Northampton, MA). The same package was used for performing Student's t-test.

Force spectroscopy was applied to study how the rupture forces depend on the loading rate, i.e. the rate at which force builds up on the respective bonds. Loading rates (pN/second) were computed as the product of the slope of the force-distance curve (pN/nm) just before a rupture event – the effective force constant that takes the viscoelastic properties of the system into account<sup>22, 23</sup> – and the pulling velocity (nm/second). Pulling velocities were varied in the range from 200–5,000 nm/second. The final ruptures in the force-distance curves were used for further analysis and for each of these events both the loading rate and the rupture force was determined. Pulling rates were varied randomly and reproducibility over time was verified by repeating measurements using prior pulling rate settings. After each series, DC-SIGN specificity of the adhesion was checked using a block of mAb AZN-D1 and soluble mannan.

At retraction speeds >1 µm/second the hydrodynamic drag on the cantilever resulted in substantial damping and, as a result, smaller forces were recorded than were actually applied to rupture the bonds.<sup>20, 24-26</sup> To compensate for this effect the data were corrected using a damping coefficient of 2.5 pN-second/µm.

## Results

### DC-SIGN binds different *Candida albicans* glycosylation mutants

The C-type lectin DC-SIGN is known to specifically bind to different carbohydrate structures of several pathogens. We tested the specific interaction of the fungus *Candida albicans* (Fig. 1A) with DC-SIGN, which is known to be mediated by highly structured glycans. Therefore, we analyzed the capacity of DC-SIGN to recognize and bind different glycosylation mutants of *C. albicans*. To better understand which structural elements of the fungal mannan are essential for the interaction between *Candida* and DC-SIGN, we exploited the well-defined isogenic mutants of *C. albicans* depleted in specific mannan structures.<sup>27</sup> In Fig. 1B, the *N*- and *O*-mannan structures of the wildtype *Candida* strain and the isogenic mutants are displayed. The *och1* mutant lacks the branched outer *N*-linked mannosyl chains,<sup>28</sup> while the *pmr1* mutant has defects both in *N*- and *O*-linked mannosylation.<sup>29</sup> The *mnn4* mutant only lacks phospho-mannan linked to the *N*-mannan,<sup>30</sup> and the double mutant *mnt1/mnt2* has intact *N*-mannan but lacks the 4 terminal *O*-linked  $\alpha$ -(1,2)-mannosyl residues.<sup>31</sup>

We used these mutants to analyze the interaction between K562-DC-SIGN cells and *Candida* mannan (Fig. 1C). The wildtype strain of *C. albicans* (CAI-4) has mannan structures that specifically bind to DC-SIGN as shown by the effective block by the anti-DC-SIGN monoclonal Ab (AZN-D1) and soluble *C. albicans* derived mannan (CA-mannan). Moreover, the interaction is  $\text{Ca}^{2+}$ -dependent as shown by the inhibition exerted by the  $\text{Ca}^{2+}$  chelator EGTA (Fig. 1C). Binding to DC-SIGN was severely reduced both in the *pmr1* and the *och1* mutant – both mutants lack large pieces of the *N*-mannan side group. In contrast, the absence of mannosylphosphate (*mnn4* mutant) or *O*-linked mannan (*mnt1/mnt2* mutant) had no effect on the interaction between DC-SIGN and *Candida*. These data clearly show that *N*-mannan is the only structure required for the recognition of *Candida* by DC-SIGN whereas *O*-linked or phospho-mannan structures are not recognized.

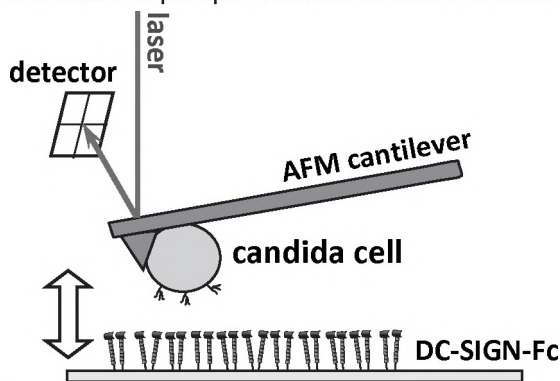


**Figure 2: Schematic set-up of the experiments**

An AFM cantilever coated with Concanavalin A (ConA) is used to pick up a *Candida albicans* cell, which is then positioned on the end of the cantilever next to the tip. To measure the interaction forces between the cell and the substrate, a laser beam is used that reflects from the tip of the cantilever onto a four-quadrant photo detector. If forces act on the cantilever it will deflect, this deflection is then measured with the detector and plotted by the software. Interactions of the *C. albicans* cell with DC-SIGN-Fc immobilized on a glass substrate are probed by moving the substrate closer and, subsequently, away from the cell. Many of these probing repetitions deliver the so-called set of ‘force-distance curves.’ These give information on the adhesion forces of the receptor-ligand interaction.

### Using AFM to measure single DC-SIGN-candida albicans interactions

The interactions of single *C. albicans* cells with DC-SIGN was probed with atomic force microscope force spectroscopy (AFM-FS). Therefore, a concanavalin A (ConA)-functionalized AFM cantilever was used to 'glue' a *Candida albicans* cell (size  $4.6 \pm 0.2 \mu\text{m}$ ;  $\pm$  S.E.M.) to the end of the cantilever (Fig. 2; see also Materials & Methods).<sup>19</sup> Subsequently, this cell-functionalized cantilever was used to measure interaction forces between the pathogen carbohydrate ligands of *C. albicans* and DC-SIGN molecules on the substrate.

### Measurement of specific DC-SIGN-Candida albicans mannan interactions

The affinity of DC-SIGN for its carbohydrate ligand on *C. albicans* can be measured with single-molecule sensitivity by AFM-FS. Therefore, an intact *C. albicans* cell immobilized onto the AFM cantilever is brought into contact with a DC-SIGN-Fc-coated substrate for 0.25–1.0 seconds. Upon retracting the cell from the substrate, which has adhered to the substrate, the detachment curves show discrete rupture steps (Fig. 3A). To determine whether that the adhesion is DC-SIGN specific, the interaction was blocked with anti-DC-SIGN antibody and soluble mannan. In presence of these inhibitors, the force curves clearly showed less interactions (Fig. 3B). Furthermore, the work needed to detach the cell from the substrate was measured both in the absence and in the presence of the inhibitors. From the force curves ( $N \geq 25$ ) the work needed for detachment (adhesion) was determined, by measuring the area enclosed by the retraction curve and the zero-force line (dotted lines; Fig. 3A, B). In Fig. 3C, the work needed for detachment (in aJ =  $10^{-18}$  J or Nm or nN·nm) was indeed significantly lower after the 30 min block (63% blocked), which implies that the interactions measured are specifically mediated by DC-SIGN. These findings are in line with the earlier described results for the binding studies of K562-DC-SIGN and *C. albicans* cells (Fig. 1C),<sup>11</sup> although inhibition was more profound in the latter case.

ConA, which is used to immobilize the *Candida* cell underneath the cantilever, is a plant lectin binding to glycoproteins containing  $\alpha$ -D-mannose and  $\alpha$ -D-glucose and could therefore possibly interfere with the specific binding of DC-SIGN to *C. albicans*. To exclude this, the ConA-coated cantilever was brought into contact with the DC-SIGN-Fc-coated substrate for 2 seconds and the work needed for detachment was measured before and after blocking with antibodies or soluble ligands. As indicated in Fig. 3D, blocking the interaction of ConA with soluble D-glucose or blocking the interaction with anti-DC-SIGN (AZN-D1) for 1 or 20 minutes showed no significant differences with respect to the untreated samples, demonstrating that no significant interactions between ConA and DC-SIGN-Fc are occurring in the conditions used.

Thus, ConA and DC-SIGN do not specifically bind and ConA can therefore be safely used to attach intact *C. albicans* to the cantilever.

### Measurement of single DC-SIGN interactions with *C. albicans* wildtype and *mnn4*-mutant

Previous studies on the interaction of DC-SIGN with *C. albicans* focused on the total adhesive (binding) properties of the bond,<sup>10, 11</sup> without addressing differences between affinity and avidity. Moreover, the different glycosylation mutations in mannan of *C. albicans* could be exploited to determine the exact binding epitope to DC-SIGN. Besides, subtle differences in the mannan structure could influence the affinity of the bond. Therefore, we exploited the sensitivity of AFM-FS to measure the affinity between DC-

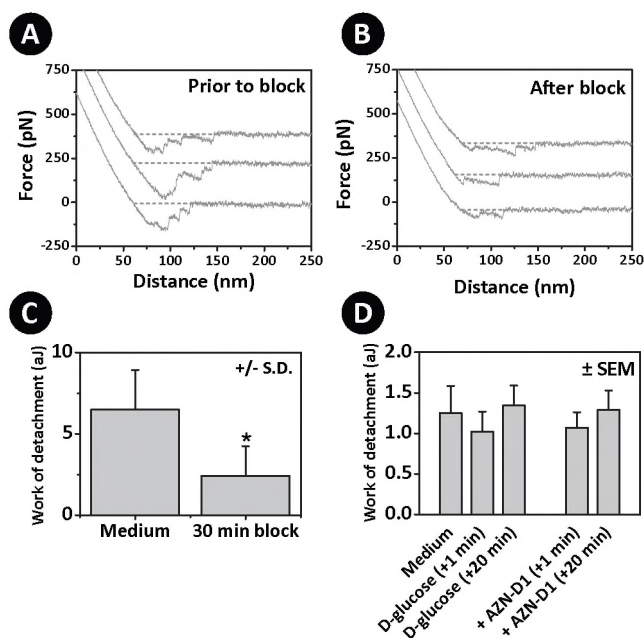


**Figure 3: Probing single DC-SIGN-*C. albicans* bonds with AFM-FS**

(A) Three examples of force-distance curves of the interaction of DC-SIGN with *C. albicans* (WT). In these curves single bond ruptures are visible as discrete steps. The area enclosed by the curve and the zero-force line (no contact regime; dotted line) is a read-out for the adhesion between the cell and the substrate; actually the work needed to detach *C. albicans*. (B) Three examples of force-distance curves of the same interaction as in (A) after a block for 30 minutes with 30  $\mu\text{g/ml}$  anti-DC-SIGN mAb AZN-D1 and 150  $\mu\text{g/ml}$  soluble CA-mannan. Still single bond ruptures are visible in some curves. However, the enclosed areas are smaller. (C) Analysis of force-distance curves ( $N \geq 25$ ) shows that the work needed for detachment (in  $\text{aJ} = 10^{-18} \text{ J}$ ) is significantly blocked with AZN-D1 + CA-mannan. This implies that the probed DC-SIGN-*C. albicans* interactions are specific (\*  $p < 0.05$ ). (D) The possible interaction of DC-SIGN and ConA is probed in a control experiment by measuring the work needed to detach the cantilever from the substrate. The conditions prior to the addition of DC-SIGN and ConA blocking agents - AZN-D1 and D-glucose, respectively - were compared with the conditions afterwards. Force-distance curves were measured before as well as after 1 and 30 minutes of *in situ* blocking ( $N \geq 40$ ).

SIGN and either wildtype (WT) mannan present on the wildtype *C. albicans* strain or a mannan with altered branching exposed on the *C. albicans mnn4* strain.

By applying AFM-FS, we first investigated the binding affinity of DC-SIGN for the *C. albicans* (WT). Therefore, the retraction speed of the cantilever was varied from 0.2–5.0  $\mu\text{m/s}$  and the resulting force curves were analyzed ( $N \geq 125$ ) for five different rates. The distribution of the rupture forces probed exhibits a single normal distribution at most rates, however, in some cases additional peaks are visible on the higher force flank (Fig. 4A, for example in the upper right panel). In other words, by performing the experiments under conditions of moderate adhesion (Materials & Methods) the primary peaks represent individual receptor-ligand ruptures, while the higher rupture forces probably represent double or multiple bond ruptures.<sup>19, 32, 33</sup> Next, we determined the loading rate corresponding to the applied rupture speeds. Therefore, during the analysis of the rupture forces from the force curves, the slope just before rupture was also measured.<sup>19</sup>

This slope represents the effective spring constant of the system, or the elasticity of the system related to the spring constant of the cantilever. By multiplying this effective spring constant (in pN/nm) with the retraction speeds (nm/s) the loading rate (in pN/s) on the bond is calculated, which is independent on the cell probed.

In Fig. 4B, the result is shown of the effective spring constant  $k_{eff}$  for all the ruptures measured at different retraction speeds, which in this case has a normal distribution with a maximum at 1.86 pN/nm. A comparison of the  $k_{eff}$  measured for every retraction speed separately showed no significant differences (data not shown), which is consistent because the effective spring constant is a system property.

In a similar set of experiments, the interaction of DC-SIGN with *C. albicans* glycosylation mutant *mnn4*, lacking the phospho-mannan side (Fig. 1B), was studied. The rupture force distributions at different loading rates showed again a predominantly single rupture behavior (Fig. 4C) and an effective spring constant of 1.10 pN/nm (Fig. 4D). Note that the effective spring constant determined in the *mnn4* experiment is lower than that of the former experiment described for *Candida* (WT). This is probably due to elasticity differences between single *Candida* cells. However, comparing the results obtained on different cells in different experiments ( $N = 3$ ,  $N = 2$ ) in both cases showed no significant differences in elasticity (data not shown). Measured effective spring constants are  $1.5 \pm 0.6$  pN/nm.

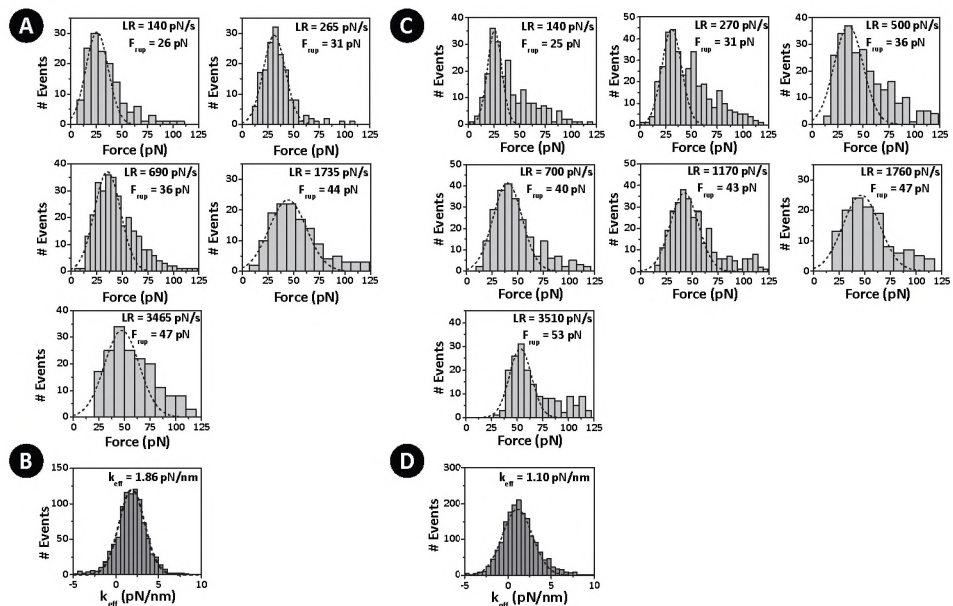


**Figure 4: Single-molecule force measurements on *C. albicans* cells**

(A) A histogram representation of the rupture forces obtained on *C. albicans* (WT) cells interacting with DC-SIGN-Fc at different retraction speeds (or loading rates; see text) ( $N \geq 125$ ). (B) Histogram of the effective spring constant  $k_{eff}$  of the probing system. The mean ( $\pm$  S.E.M.)  $k_{eff}$  determined was  $1.86 \pm 0.02$  pN/nm. The slopes just before ruptures are measured and plotted for all ruptures measured at different retraction speeds. The loading rate is the product of the retraction speed and the  $k_{eff}$  determined. (C) Histogram of the rupture forces obtained on *C. albicans* (*mnn4*) cells interacting with DC-SIGN-Fc (similar experiments as in (A);  $N \geq 175$ ). (D) Histogram of the effective spring constant, similar analysis as in (B). The mean ( $\pm$  S.E.M.)  $k_{eff}$  determined was  $1.10 \pm 0.04$  pN/nm.



The affinity of DC-SIGN for wildtype mannan and mannan lacking the phospho-mannan is similar

The dynamical response of the interaction of the DC-SIGN-*C. albicans* wildtype cell and the phospho-mannan lacking mutant *mnn4* is plotted in a force spectrum (Fig. 5). The determined rupture forces increase linearly from 25 pN to 55 pN as a function of the natural logarithm of the loading rate. This behavior was first described by Bell.<sup>34</sup> In the Bell model, the mean rupture force  $F_{rup}$  is described by:

$$F_{rup} = \frac{k_B T}{x_\beta} \ln\left(\frac{x_\beta}{k_{off}^0 k_B T}\right) + \frac{k_B T}{x_\beta} \ln(r_f) \quad (\text{Eq. 1})$$

where  $k_{off}^0$  is the (unstressed) dissociation rate in the absence of a pulling force;  $x_\beta$  is the reactive compliance or mechanical bond-length;  $T$  is the absolute temperature;  $k_B$  is the Boltzmann constant, and  $r_f$  is the loading rate.<sup>25, 35-37</sup> The Bell model parameters  $k_{off}^0$  and  $x_\beta$ , characterizing the micromechanical properties of the DC-SIGN-*Candida* (WT) and *mnn4* interactions, were obtained by fitting the spectral data to Eq. 1. Table 1 lists these parameters and shows a comparison to other receptor-ligand pairs to put the DC-SIGN-*Candida* data into perspective (see Discussion, Fig. 6). Furthermore, in Table 1 the dynamical parameters of other protein-carbohydrate (receptor-ligand) interactions are given of the viral entry receptor CD4 on leukocytes and the glycoprotein120 (gp120), that is present on the surface of HIV-1. The initial binding of CD4 and gp120 is exploited by HIV-1 to gain entry into the cell.<sup>38</sup> Similarly, the E-selectin-sLeX bond, represents a rolling receptor bond involved in leukocyte extravasation.<sup>2, 5</sup>

Interestingly, we observed that the measured rupture forces indicate that the DC-SIGN-*C. albicans* (*mnn4*) bonds are slightly stronger than the bonds of the wildtype *Candida* in a large regime of loading rates. However, at low loading rates this is not significant (Fig. 5). This slightly higher affinity of the bond is in line with the lower efficiency observed in cell-cell binding studies (Fig. 1C). An explanation for this slight

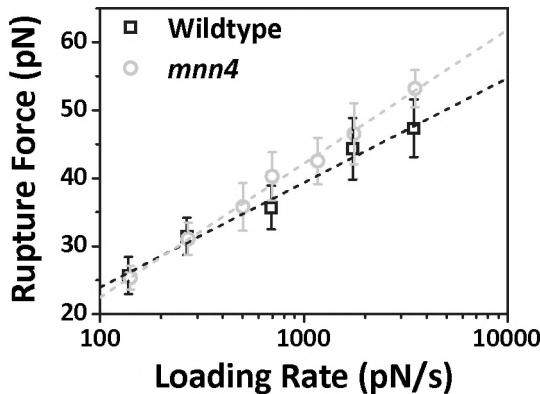


**Figure 5: Force spectra of the interaction of DC-SIGN with *C. albicans* (WT) and the *C. albicans* mutant *mnn4***

The mean rupture forces for the *Candida* (WT) and *mnn4* mutant DC-SIGN mediated interactions were found to increase linearly with the natural logarithm of the loading rate. This behavior is consistent with the Bell model ( $R^2 > 0.98$ ). Over the whole force regime measured, rupture forces were not significantly ( $p > 0.05$ ) different in both cases.

**Table 1: The dynamical parameters of the interactions**

System	$x_{\beta_1}$ (nm)	$k_1^o$ (s <sup>-1</sup> )	$x_{\beta_2}$ (nm)	$k_2^o$ (s <sup>-1</sup> )	Loading rate regime (pN/s)*	Reference
DC-SIGN - <i>Candida</i> CAI-4 (WT)	0.61	0.43	-	-	100 - 4,000	This study
DC-SIGN - <i>Candida</i> mnn4	0.48	0.83	-	-	100 - 4,000	This study
CD4 - gp120 (HIV-1)	0.34	3.73	-	-	200 - 1,000	Dubrowsky et al. <sup>38</sup>
E-selectin - sLex	0.5	0.3	0.09	65	200 - 10,000 - 100,000	Zhang et al. <sup>5</sup>

\* The given values correspond to the loading rates probed, if three values are given the middle one corresponds to the transition loading rate.

difference could be that the phospho-mannan structure in wildtype *C. albicans* slightly interferes within the CRD binding pocket of DC-SIGN by steric hindrance.

In summary, single receptor-ligand interactions between DC-SIGN and *C. albicans* cells can be probed with AFM-FS. Moreover, these interactions are specific and a slight difference between two mannan glycosylation structures is observed.

## Discussion

Infection of immunocompromised patients with the fungus *Candida albicans* is amongst the most common type of fungal infections and are important causes of morbidity and mortality.<sup>9</sup> Therefore, a better understanding of the interactions between invading fungi and immune cells is necessary. Especially, gaining insight in the carbohydrate recognition profile of C-type lectins (CLR), which are mainly responsible for the specific detection of the pathogen, will ultimately provide relevant information and may lead to the development of new drugs specifically targeting fungal cell wall antigens.

We previously demonstrated that DCs bind and internalize *C. albicans* through the CLR DC-SIGN,<sup>10</sup> and that N-linked mannosyl residues are essential for this interaction (Fig. 1C).<sup>11</sup> Moreover, the binding of *C. albicans* to DC-SIGN could be attributed to the carbohydrate recognition domain of DC-SIGN and to the  $\alpha$ -(1,2) branched mannose residues (Fig. 1B).<sup>11</sup> In the AFM-FS study described here, exploiting intact *C. albicans*, we could specifically study single receptor-ligand interactions between *C. albicans* attached on the cantilever and DC-SIGN immobilized on a substrate. The added value of probing the interaction of a whole pathogen rather than isolated ligand structures with AFM, is that the glycan structures on the cell wall are intact and have their native configuration. The isolation of mannan polysaccharides usually involves acetylosis, which cleaves specific linkages in the carbohydrate backbone, and could possibly alter the structure such that receptor binding is affected.<sup>39</sup>

Earlier studies on the interaction of DC-SIGN-*C. albicans* did not address the single receptor-ligand interactions, but only addressed the overall differences in binding of the *C. albicans* to DCs and K562-DC-SIGN cells.<sup>10,11,27</sup> As a result, they could not differentiate between affinity and avidity.<sup>19</sup> AFM-FS allows us to study the affinity of single bonds and determine the contribution of avidity in these interactions. Furthermore, by studying the dynamical response of the bonds when stressed by applying external forces, we can mimic the physiological environment in which DCs encounter invading *Candidas* at mucosal surfaces and in the skin.<sup>11</sup> Physiological loading rates expected for these type of interactions are up to 10<sup>4</sup> pN/s,<sup>40</sup> which matches the loading rate regime probed in Fig. 5. Moreover, the biophysical parameters derived on the receptor-ligand bond give a direct measure for the affinity of the bond.<sup>19,40,41</sup> The single rupture bond strength was in our case approximately 40 pN at a loading rate of 1000 pN/s, in the case of other protein-

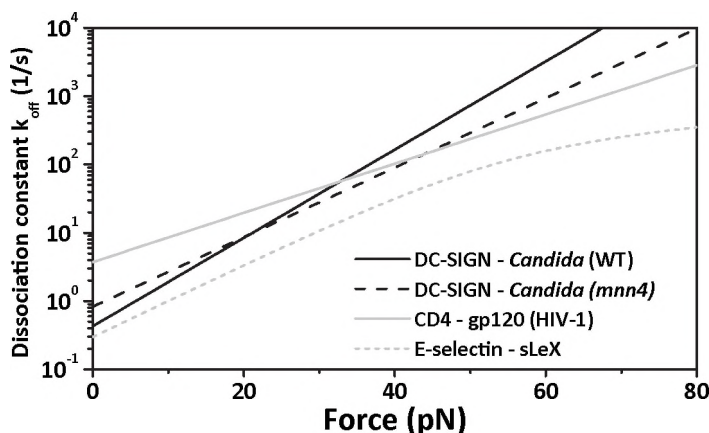


**Figure 6: Kinetic profiles of the DC-SIGN-*Candida* interactions in the context of related receptor-ligand interactions**

The kinetic profiles of the DC-SIGN-CAI-4 (WT) and DC-SIGN-mnn4 interactions, based on the derived Bell model parameters, are compared to CD4-gp120 (HIV-1) and E-selectin-sLeX interactions (see text). The force dependence of the dissociation rate of a bond displaying an inner and an outer activation barrier is described by:  $k_{off} = 1 / \{k_1^{0-1} \exp[-FX_{\beta_1}/k_B T] + k_2^{0-1} \exp[-FX_{\beta_2}/k_B T]\}$  where the subscripts 1 and 2 refer to the outer and inner barrier, respectively.<sup>26</sup>

carbohydrate interactions similar rupture forces were found; ~39 pN for the CD4-gp120 interaction and ~49 pN for E-selectin-sLeX.<sup>5, 38</sup>

Much better insight is obtained when the Bell parameters of the various related interactions are compared by plotting them in so-called kinetic profiles, which describe the dynamical response and stability of the bonds under conditions of external loading.<sup>26</sup> In Fig. 6, we compare the interactions of DC-SIGN - *C. albicans* both wildtype and *mnn4*, with those of CD4-gp120 and E-selectin-sLeX, using the parameters given in Table 1. The bonds all have comparable strengths over the force range plotted, although E-selectin-sLeX bonds are overall stronger – have lower dissociation rates. Related to the role of the E-selectin-sLeX bond in rolling and homing of leukocytes at and through the vascular endothelium, these bonds are likely subject to much higher forces than bonds involved in pathogen-leukocyte interactions. The CD4-gp120 bond is involved in the initial binding of HIV-1 to leukocytes, thereafter a co-receptor complex on the cell membrane is formed with CCR5 or CXCR4 (depending on cell type), to stabilize the bond and to provide virus entry into the host cell.<sup>38</sup> Dobrowsky et al.<sup>38</sup> used inactivated HIV-particles, that display the native structure of gp120 imbedded in the viral envelope. The use of an intact pathogen instead of an isolated protein, such as in the case of gp120 described in an earlier study by Chang et al.,<sup>42</sup> and in our case by probing the interaction with an intact *C. albicans*, will probably give more relevant information on the true physiological interaction. Interestingly, the kinetic responses of both bonds display similarities (Fig. 6), although the CD4-gp120 bond appears somewhat weaker at lower forces. The viruses are, however, approximately 30 times smaller, and therefore forces experienced by drag are probably also lower than those experienced by intact *C. albicans*. Finally, the dynamic response of DC-SIGN with the *Candida* wildtype and *mnn4* mutant are in the < 50 pN regime almost indiscernible, although the *mnn4* mutant is at higher forces >30 pN

somewhat stronger than the wildtype. However, as rupture forces probed were never higher than 55 pN, conclusive interpretations can only be made by probing higher forces at higher loading rates. Probing at higher loading rates would also establish if DC-SIGN only has a single barrier interaction, or a double barrier such as E-selectin.<sup>5, 19</sup> This inner barrier could, however, only be probed at loading rates >10,000 pN/s, whereas in this study we probed up to loading rates of 4000 pN/s.

Previous studies demonstrated that the binding of *C. albicans* specifically involves the CRD of the lectin receptor.<sup>11</sup> Within the CRD the aminoacid residue Asp(324), which chelates a Ca<sup>2+</sup>-ion, seems essential for binding of ligands, such as ICAM-3, LeX as well as gp120 and *C. albicans*.<sup>11, 43, 44</sup> A secondary bond mediated by Val(351) was only essential for the ICAM-3 and LeX bond,<sup>43, 44</sup> but not essential for the gp120 bond,<sup>43</sup> and only to a lesser extent for the *C. albicans* bond.<sup>11</sup> This suggests that the binding site for different ligands only partially overlap. Next to X-ray crystallography studies to model the structure of the binding site of the CRD,<sup>45</sup> AFM-FS is a powerful method to map the structure of the binding site or binding pocket of the CRD under physiological conditions, such as demonstrated by Zhang et al.,<sup>46</sup> for the integrin  $\alpha_4\beta_1$ -VCAM-1 interaction.

Finally, the intrinsic oligomerization of DC-SIGN<sup>47</sup> and its tendency to form nanoclusters<sup>48</sup> might provide additional control levels for the interaction of DC-SIGN with *C. albicans*. In the study described here, purified DC-SIGN-Fc molecules, which likely have oligomerized in solution, were immobilized on a substrate. From structural studies, it is known that DC-SIGN forms tetramers via its repeat regions, implying that four CRDs are very close.<sup>49, 50</sup> For the interaction of DC-SIGN with large glycan structures, such as those present on *C. albicans*, the binding structures will likely overlap and bind to all the CRDs. This will influence the cooperative affinity of the bonds. On cells clustering of DC-SIGN seems tightly regulated by the formation of nanoclusters on the cellular membrane. This might be another process exploited by cells to regulate adhesive processes. Therefore, studies exploiting two cells, one expressing DC-SIGN and the other the *C. albicans* cell, might help to understand the role of the cellular environment for the strength of the bond.<sup>41</sup>

In conclusion, we have shown how the strength of AFM-FS can be exploited to get detailed structural information on the binding of the pathogen receptor DC-SIGN and the pathogen *C. albicans*. With AFM-FS the dynamical strength of single molecular bonds can be probed, providing direct insight in subtle affinity differences between ligands. This knowledge will undoubtedly yield essential information on how CLRs expressed on DCs can recognize specific carbohydrate structures on pathogens.

## References

1. **S. Roseman** (2001). Reflections on glycobiology. *J. Biol. Chem.*, **276**, 41527-41542.
2. **A. Cambi, C. G. Figdor** (2003). Dual function of C-type lectin-like receptors in the immune system. *Curr. Opin. Cell Biol.*, **15**, 539-546.
3. **M. E. Taylor, K. Drickamer** (2007). Paradigms for glycan-binding receptors in cell adhesion. *Curr. Opin. Cell Biol.*, **19**, 572-577.
4. **M. Sperandio** (2006). Selectins and glycosyltransferases in leukocyte rolling in vivo. *FEBS J.*, **273**, 4377-4389.
5. **X. Zhang, D. F. Bogorin, V. T. Moy** (2004). Molecular basis of the dynamic strength of the sialyl Lewis X-selectin interaction. *Chemphyschem*, **5**, 175-182.
6. **Y. van Kooyk** (2008). C-type lectins on dendritic cells: key modulators for the induction of immune responses. *Biochem. Soc. Trans.*, **36**, 1478-1481.
7. **T. B. Geijtenbeek, R. Torensma, S. J. van Vliet, G. C. van Duijnhoven, G. J. Adema, Y. van Kooyk, C. G. Figdor** (2000). Identification of DC-SIGN, a novel dendritic cell-specific ICAM-3 receptor that supports primary immune responses. *Cell*, **100**, 575-585.
8. **Y. Guo, H. Feinberg, E. Conroy, D. A. Mitchell, R. Alvarez, O. Blixt, M. E. Taylor, W. I. Weis, K. Drickamer** (2004). Structural basis for distinct ligand-binding and targeting properties of the receptors DC-SIGN and DC-SIGNR. *Nat. Struct. Mol. Biol.*, **11**, 591-598.

9. M. M. McNeil, S. L. Nash, R. A. Hajjeh, M. A. Phelan, L. A. Conn, B. D. Plikaytis, D. W. Warnock (2001). Trends in mortality due to invasive mycotic diseases in the United States, 1980-1997. *Clin. Infect. Dis.*, **33**, 641-647.
10. A. Cambi, K. Gijzen, J. M. de Vries, R. Torensma, B. Joosten, G. J. Adema, M. G. Netea, B. J. Kullberg, L. Romani, C. G. Figdor (2003). The C-type lectin DC-SIGN (CD209) is an antigen-uptake receptor for *Candida albicans* on dendritic cells. *Eur. J. Immunol.*, **33**, 532-538.
11. A. Cambi, M. G. Netea, H. M. Mora-Montes, N. A. Gow, S. V. Hato, D. W. Lowman, B. J. Kullberg, R. Torensma, D. L. Williams, C. G. Figdor (2008). Dendritic cell interaction with *Candida albicans* critically depends on N-linked mannans. *J. Biol. Chem.*, **283**, 20590-20599.
12. J. Masuoka (2004). Surface glycans of *Candida albicans* and other pathogenic fungi: physiological roles, clinical uses, and experimental challenges. *Clin. Microbiol. Rev.*, **17**, 281-310.
13. J. Masuoka, K. C. Hazen (2004). Cell wall mannan and cell surface hydrophobicity in *Candida albicans* serotype A and B strains. *Infect. Immun.*, **72**, 6230-6236.
14. F. M. Klis, P. de Groot, K. Hellingwerf (2001). Molecular organization of the cell wall of *Candida albicans*. *Med. Mycol.*, **39 Suppl 1**, 1-8.
15. G. Kogan, V. Pavliak, L. Masler (1988). Structural studies of mannans from the cell walls of the pathogenic yeasts *Candida albicans* serotypes A and B and *Candida parapsilosis*. *Carbohydr. Res.*, **172**, 243-253.
16. C. B. Forsyth, H. L. Mathews (1996). Lymphocytes utilize CD11b/CD18 for adhesion to *Candida albicans*. *Cell Immunol.*, **170**, 91-100.
17. D. R. Singleton, J. Masuoka, K. C. Hazen (2005). Surface hydrophobicity changes of two *Candida albicans* serotype B mnn4delta mutants. *Eukaryot. Cell*, **4**, 639-648.
18. W. A. Fonzi, M. Y. Irwin (1993). Isogenic strain construction and gene mapping in *Candida albicans*. *Genetics*, **134**, 717-728.
19. J. te Riet, A. W. Zimmerman, A. Cambi, B. Joosten, S. Speller, R. Torensma, F. N. van Leeuwen, C. G. Figdor, F. de Lange (2007). Distinct kinetic and mechanical properties govern ALCAM-mediated interactions as shown by single-molecule force spectroscopy. *J. Cell Sci.*, **120**, 3965-3976.
20. X. Zhang, E. P. Wojcikiewicz, V. T. Moy (2002). Force spectroscopy of the leukocyte function-associated antigen-1/intercellular adhesion molecule-1 interaction. *Biophys. J.*, **83**, 2270-2279.
21. P. H. Puech, A. Taubenberger, F. Ulrich, M. Krieg, D. J. Muller, C. P. Heisenberg (2005). Measuring cell adhesion forces of primary gastrulating cells from zebrafish using atomic force microscopy. *J. Cell Sci.*, **118**, 4199-4206.
22. E. Evans, K. Ritchie (1999). Strength of a weak bond connecting flexible polymer chains. *Biophys. J.*, **76**, 2439-2447.
23. C. Yuan, A. Chen, P. Kolb, V. T. Moy (2000). Energy landscape of streptavidin-biotin complexes measured by atomic force microscopy. *Biochemistry*, **39**, 10219-10223.
24. H. Janovjak, J. Struckmeier, D. J. Muller (2005). Hydrodynamic effects in fast AFM single-molecule force measurements. *Eur. Biophys. J.*, **34**, 91-96.
25. D. F. Tees, R. E. Waugh, D. A. Hammer (2001). A microcantilever device to assess the effect of force on the lifetime of selectin-carbohydrate bonds. *Biophys. J.*, **80**, 668-682.
26. E. Evans, A. Leung, D. Hammer, S. Simon (2001). Chemically distinct transition states govern rapid dissociation of single L-selectin bonds under force. *Proc. Natl. Acad. Sci. USA*, **98**, 3784-3789.
27. M. G. Netea, N. A. Gow, C. A. Munro, S. Bates, C. Collins, G. Ferwerda, R. P. Hobson, G. Bertram, H. B. Hughes, T. Jansen, L. Jacobs, E. T. Buurman, K. Gijzen, D. L. Williams, R. Torensma, A. McKinnon, D. M. MacCallum, F. C. Odds, J. W. Van der Meer, A. J. Brown, B. J. Kullberg (2006). Immune sensing of *Candida albicans* requires cooperative recognition of mannans and glucans by lectin and Toll-like receptors. *J. Clin. Invest.*, **116**, 1642-1650.
28. S. Bates, H. B. Hughes, C. A. Munro, W. P. Thomas, D. M. MacCallum, G. Bertram, A. Atrih, M. A. Ferguson, A. J. Brown, F. C. Odds, N. A. Gow (2006). Outer chain N-glycans are required for cell wall integrity and virulence of *Candida albicans*. *J. Biol. Chem.*, **281**, 90-98.
29. S. Bates, D. M. MacCallum, G. Bertram, C. A. Munro, H. B. Hughes, E. T. Buurman, A. J. Brown, F. C. Odds, N. A. Gow (2005). *Candida albicans* Pmr1p, a secretory pathway P-type  $Ca^{2+}/Mn^{2+}$ -ATPase, is required for glycosylation and virulence. *J. Biol. Chem.*, **280**, 23408-23415.
30. R. P. Hobson, C. A. Munro, S. Bates, D. M. MacCallum, J. E. Cutler, S. E. Heinsbroek, G. D. Brown, F. C. Odds, N. A. Gow (2004). Loss of cell wall mannosylphosphate in *Candida albicans* does not influence macrophage recognition. *J. Biol. Chem.*, **279**, 39628-39635.
31. C. A. Munro, S. Bates, E. T. Buurman, H. B. Hughes, D. M. MacCallum, G. Bertram, A. Atrih, M. A. Ferguson, J. M. Bain, A. Brand, S. Hamilton, C. Westwater, L. M. Thomson, A. J. Brown, F. C. Odds, N. A. Gow (2005). Mnt1p and Mnt2p of *Candida albicans* are partially redundant alpha-1,2-mannosyltransferases that participate in O-linked mannosylation and are required for adhesion and virulence. *J. Biol. Chem.*, **280**, 1051-1060.
32. J. Wong, A. Chilkoti, V. T. Moy (1999). Direct force measurements of the streptavidin-biotin interaction. *Biomol. Eng.*, **16**, 45-55.
33. M. Benoit, D. Gabriel, G. Gerisch, H. E. Gaub (2000). Discrete interactions in cell adhesion measured by single-molecule force spectroscopy. *Nat. Cell Biol.*, **2**, 313-317.
34. G. I. Bell (1978). Models for the specific adhesion of cells to cells. *Science*, **200**, 618-627.
35. R. Alon, S. Chen, R. Fuhlbrigge, K. D. Puri, T. A. Springer (1998). The kinetics and shear threshold of transient and rolling interactions of L-selectin with its ligand on leukocytes. *Proc. Natl. Acad. Sci. USA*, **95**, 11631-11636.
36. E. Evans, K. Ritchie (1997). Dynamic strength of molecular adhesion bonds. *Biophys. J.*, **72**, 1541-1555.
37. W. Hanley, O. McCarty, S. Jadhav, Y. Tseng, D. Wirtz, K. Konstantopoulos (2003). Single molecule characterization of P-selectin/ligand binding. *J. Biol. Chem.*, **278**, 10556-10561.
38. T. M. Dobrowsky, Y. Zhou, S. X. Sun, R. F. Siliciano, D. Wirtz (2008). Monitoring early fusion dynamics of human immunodeficiency virus type 1 at single-molecule resolution. *J. Virol.*, **82**, 7022-7033.
39. N. Shibata, A. Suzuki, H. Kobayashi, Y. Okawa (2007). Chemical structure of the cell-wall mannan of *Candida*

- albicans* serotype A and its difference in yeast and hyphal forms. *Biochem. J.*, **404**, 365-372.
40. **E. A. Evans, D. A. Calderwood** (2007). Forces and bond dynamics in cell adhesion. *Science*, **316**, 1148-1153.
  41. **J. Helenius, C. P. Heisenberg, H. E. Gaub, D. J. Muller** (2008). Single-cell force spectroscopy. *J. Cell Sci.*, **121**, 1785-1791.
  42. **M. I. Chang, P. Panorchan, T. M. Dobrowsky, Y. Tseng, D. Wirtz** (2005). Single-molecule analysis of human immunodeficiency virus type 1 gp120-receptor interactions in living cells. *J. Virol.*, **79**, 14748-14755.
  43. **T. B. Geijtenbeek, G. C. van Duijnhoven, S. J. van Vliet, E. Krieger, G. Vriend, C. G. Figdor, Y. van Kooyk** (2002). Identification of different binding sites in the dendritic cell-specific receptor DC-SIGN for intercellular adhesion molecule 3 and HIV-1. *J. Biol. Chem.*, **277**, 11314-11320.
  44. **E. Van Liempt, A. Imberty, C. M. Bank, S. J. Van Vliet, Y. Van Kooyk, T. B. Geijtenbeek, I. Van Die** (2004). Molecular basis of the differences in binding properties of the highly related C-type lectins DC-SIGN and L-SIGN to Lewis X trisaccharide and *Schistosoma mansoni* egg antigens. *J. Biol. Chem.*, **279**, 33161-33167.
  45. **H. Feinberg, M. E. Taylor, W. I. Weis** (2007). Scavenger receptor C-type lectin binds to the leukocyte cell surface glycan Lewis(x) by a novel mechanism. *J. Biol. Chem.*, **282**, 17250-17258.
  46. **X. Zhang, S. E. Craig, H. Kirby, M. J. Humphries, V. T. Moy** (2004). Molecular basis for the dynamic strength of the integrin  $\alpha_5\beta_1$ /VCAM-1 interaction. *Biophys. J.*, **87**, 3470-3478.
  47. **D. A. Mitchell, A. J. Fadden, K. Drickamer** (2001). A novel mechanism of carbohydrate recognition by the C-type lectins DC-SIGN and DC-SIGNR. Subunit organization and binding to multivalent ligands. *J. Biol. Chem.*, **276**, 28939-28945.
  48. **A. Cambi, F. de Lange, N. M. van Maarseveen, M. Nijhuis, B. Joosten, E. M. van Dijk, B. I. de Bakker, J. A. Fransen, P. H. Bovee-Geurts, F. N. van Leeuwen, N. F. Van Hulst, C. G. Figdor** (2004). Microdomains of the C-type lectin DC-SIGN are portals for virus entry into dendritic cells. *J. Cell Biol.*, **164**, 145-155.
  49. **H. Feinberg, C. K. Tso, M. E. Taylor, K. Drickamer, W. I. Weis** (2009). Segmented helical structure of the neck region of the glycan-binding receptor DC-SIGNR. *J. Mol. Biol.*, **394**, 613-620.
  50. **G. A. Snyder, M. Colonna, P. D. Sun** (2005). The structure of DC-SIGNR with a portion of its repeat domain lends insights to modeling of the receptor tetramer. *J. Mol. Biol.*, **347**, 979-989.



# CHAPTER 6

---

## Measuring nanopatterns of His-tagged proteins by AFM

*Joost te Riet, Tim Smit, Inge M.J. Reinieren-Beeren,  
Alessandra Cambi, Sylvia Speller, Carl G. Figdor*

*It is a capital mistake to theorise  
before one has data. Insensibly one  
begins to twist facts to suit theories  
instead of theories to suit facts.*

*Sherlock Holmes*

Manuscript in preparation



The last decade, proceedings in patterning technologies have made it possible to construct molecular structures at the nanoscale. An interesting application of patterning proteins for immuno-cell-biology would be to mimic nano- and micro-clusters of cell adhesion molecules (CAMs) as observed on the cellular membrane, such as DC-SIGN (dendritic cell-specific ICAM-3-grabbing non-integrin) and ALCAM (activated leukocyte cell adhesion molecule) clusters. By mimicking these structures, it is possible to investigate the function of CAM clustering on adhesion regulation of cells. In this study, we investigated the chemistry needed to construct nanopatterns of DC-SIGN and ALCAM by atomic force microscopy (AFM) in self-assembled monolayers (SAMs), step-by-step. Therefore, AFM assisted nanografting is exploited to construct these nanostructures. To specifically immobilize proteins in an oriented fashion on a substrate N-nitrilotriacetic acid-histidine (NTA-His<sub>6</sub>) chemistry is used. The patterned SAMs consist of two components, one being an NTA-thiol which specifically binds to a His-tag of the protein, and the other a multi-ethylene glycol (EG)-thiol. With single molecule accuracy, we demonstrate by AFM that the His-tagged proteins DC-SIGN-His and ALCAM-His can be specifically bound to an NTA-containing SAM.

## Introduction

The last decade many new techniques have been developed to create and study micro- and nanometer scale objects. As application in life sciences especially micro- and nanopatterning is interesting to detect biomolecules, such as RNA or antibodies.<sup>1-3</sup> Whereas patterns at the microscale are currently used in diagnostic applications (e.g. microarrays or drug delivery devices), smaller submicron- and nano-structures better approach the size of cellular protein structures, such as the extracellular matrix.<sup>4</sup> The ability to pattern biomolecules at the 5-100 nanometer scale allows to study how cells respond to structures which approach the size of single molecules.<sup>5</sup> Up till now, a number of studies successfully demonstrated the feasibility of creating protein nanopatterns.<sup>5-10</sup> However, still two significant challenges often arise when creating protein nanostructures: i) which chemistry should be chosen for optimal protein immobilization and ii) how to obtain the ultrahigh resolution needed to construct these nanopatterns?

To immobilize proteins on a substrate many different strategies have been developed. These immobilization techniques can be divided in covalent vs. noncovalent coupling of the proteins as well as random vs. uniform orientation of the proteins.<sup>3, 11-13</sup> The simplest strategy is noncovalent physisorption of proteins by ionic, hydrophobic/hydrophilic and polar interactions.<sup>3</sup> Covalent coupling of proteins to a substrate can be achieved by many different chemical coupling strategies, for example, nonspecific binding to functional amino acid side groups such as amine-groups of lysines or carboxyl-groups of aspartic- or glutamic acids.<sup>3</sup> However, the abundance of these aminoacids in proteins does not allow any control in the orientation of proteins.<sup>13</sup> Other covalent coupling methods that involve specific binding sites exploit thiol-chemistry by cysteine-tags in the protein or the addition of an alkyne-group ( $\equiv\text{CH}$ ) to the protein to exploit “click” chemistry.<sup>3, 14</sup> Both methods add an orientation component, however they require protein modifications and irreversibly couple the proteins to the substrate. Bioaffinity immobilization strategies facilitate reversible coupling, for example applying avidin-biotin chemistry, DNA-directed coupling, antibodies, and NTA-His chemistry.<sup>3</sup> The latter method involves N-nitrilotriacetic acid-histidine (NTA-His<sub>6</sub>) coupling and is frequently used to uniformly orient proteins.<sup>3, 11, 15-17</sup> Anchoring of His-tagged proteins - proteins exposing a hexa-histidine tag on the C- or N-terminus - involves the chelation of a Ni<sup>2+</sup>-ion into an NTA-group by binding at four

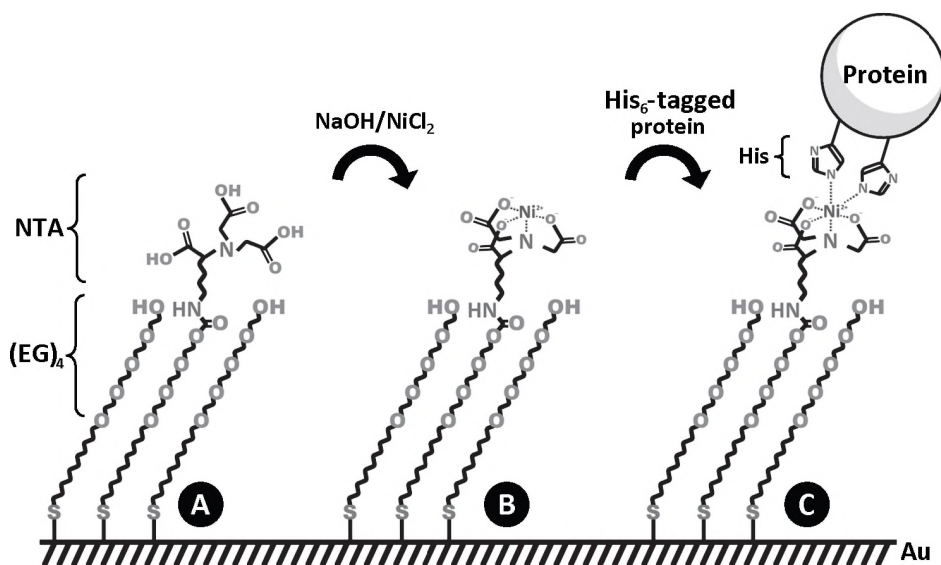


**Figure 1: Immobilizing proteins using NTA-His chemistry**

(A) A self-assembled monolayer (SAM) on gold of N-nitrilotriacetic acid (NTA) terminated thiols (HS-(CH<sub>2</sub>)<sub>11</sub>-(EG)<sub>3</sub>-NTA) mixed with ethylene glycol (EG) terminated thiols HS-(CH<sub>2</sub>)<sub>11</sub>-(EG)<sub>4</sub>-OH has NTA groups protruding from a tightly packed monolayer. (B) To activate the NTA-endgroup it is deprotonated with NaOH at pH 10. Subsequently, 40 mM of NiCl<sub>2</sub> is added to chelate the NTA-endgroup with a Ni<sup>2+</sup>-ion. This causes a conformational change. (C) Finally, the His<sub>6</sub>-tagged (tag of 6 histidine residues) proteins are added which results in 2 histidine aminoacids binding to the two remaining binding sites of the Ni<sup>2+</sup>-ion of the activated NTA.

sites, while the two remaining sites are available to bind two histidine residues of the tag (Fig. 1). In most cases, the protein has six histidine (His<sub>6</sub>) residues in its tag, instead of just two, to increase the total affinity by cooperativity.<sup>18</sup> It is well known that the affinity can even be enhanced by increasing the size of the tag to His<sub>10</sub> or by positioning of more NTA-groups in close conformation in an NTA-multimer.<sup>18, 19</sup> Molecules having NTA-endgroups can be covalently coupled to a glass or gold substrate. On both substrates these NTA-molecules are integrated in self-assembled monolayers (SAMs), which consist of mixed NTA-molecules with matrix or filler molecules to form a uniform SAM.<sup>3, 12, 13</sup> On gold, these NTA-endgroups are linked to an alkanethiol-tail which specifically binds to gold by forming an S-Au bond (Fig. 1). SAMs of alkanethiols usually form a 2D crystal structure on gold of closely packed hydrocarbon chains that are ~30° tilted with respect to the surface normal of the substrate.<sup>20-24</sup>

NTA-containing SAMs are usually made of a mixture of NTA-terminated thiols and filler molecules having ethylene glycol (EG) residues, such as HS-(CH<sub>2</sub>)<sub>11</sub>-(EG)<sub>3</sub>-OH or HS-(CH<sub>2</sub>)<sub>11</sub>-(EG)<sub>4</sub>-OH.<sup>15, 25, 26</sup> Molecules containing EG-residues are added for their protein adsorption-resistance. Therefore, on this mixed SAM His-tagged proteins only bind specifically to the NTA-molecules.<sup>25</sup> The total amount of proteins bound to the SAM surface is determined by the amount of NTA-groups present in the SAM.<sup>13, 27-29</sup> A second argument to use filler molecules is to increase the quality of the SAM, and this is realized by the oligo-EG-terminated thiols filling the space underneath the relatively large NTA-groups (Fig. 1).

Except of the simplicity of using gold-thiol chemistry to form uniform SAMs, a gold substrate is also a well defined platform to create nanostructures of thiolated molecules, especially by using AFM techniques, such as dip-pen nanolithography<sup>7, 30, 31</sup> and

nanografting.<sup>20, 32</sup> The latter method exploits AFM as a nanomanipulating tool to create nanostructures in a SAM as well as a microscope to image the created patterns (Fig 2). Nanografting is mostly used to understand the kinetics of self-assembly,<sup>33-36</sup> but also for grafting highly ordered biomolecules.<sup>10, 32, 37-39</sup> The availability of an internal scaffold *in situ* - a matrix SAM and atomic gold steps - allows for exact and precise study of the materials involved and provides quantitative measurements. In addition, the lateral friction experienced by the AFM tip when scanning the topography provides insight in the composition of the nanografted patch, such as, differences in molecular packing and chemical endgroup (Chapter 7). For example, AFM friction measurements have been used to detect protein ligand-binding events<sup>37</sup> and to study phospholipid bilayers.<sup>40</sup>

The aim of the study described in this chapter is to investigate the feasibility of immobilizing two types of proteins, DC-SIGN-His and ALCAM-His, onto thiol-bound nanoislands on gold using NTA-His chemistry and nanografting. The immobilization of uniformly oriented DC-SIGN molecules in nanoislands will enable the study of pathogen binding kinetics in relation to a threshold for binding of different sized pathogens (see also Chapter 1, Fig. 9). Nanografted patches of DC-SIGN represent a mimic of the 50-250 nm sized DC-SIGN nanoislands observed on dendritic cells.<sup>41</sup> In addition, creating nano- and micropatterns of ALCAM would help to better understand the benefit of micro-clustering for homotypic ALCAM-ALCAM as well as heterotypic ALCAM-CD6 interactions upon cell adhesion (Chapter 4).<sup>42</sup> In this Chapter, we describe the optimization of the chemical steps needed to immobilize DC-SIGN or ALCAM onto a substrate with NTA-His chemistry. The SAM structure of both chemical compounds is studied as separate SAMs and as mixed SAMs on a gold substrate with AFM. Furthermore, the self-assembly process of either conventionally (overnight) or by nanografting formed SAMs differ in their packing, the orientation of the molecules, and - for the mixed SAMs - in content. Furthermore, we show with AFM that DC-SIGN-His as well as ALCAM-His can be specifically immobilized on a SAM, on which it forms nano-clusters. This Chapter also discusses the difficulties encountered during the creation of nanopatterns and the critical chemical steps required to immobilize oriented proteins. Finally, the high resolution AFM images provide a novel

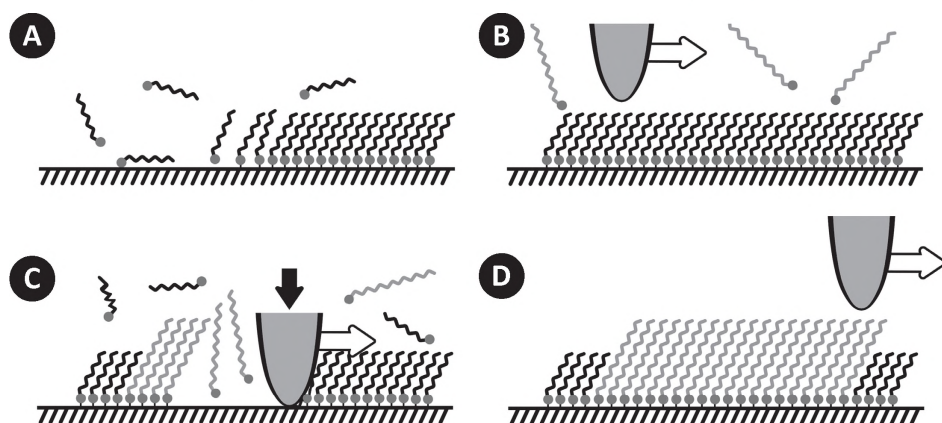


**Figure 2: Nanografting**

(A) A gold (Au(111)) sample is submerged in a 2-butanol thiol solution ( $\text{HSC}_8$  shown as example) for >18 hrs, after which an uniform SAM has formed. (B) The SAM can be studied with the AFM by scanning the sample using a low contact force ( $F_N \approx 6$  nN). (C) By increasing the contact force ( $F_N \approx 120$  nN), patches of the SAM are removed and under the supernatant allow the exchange with other thiol molecules in solution ( $\text{HSC}_{14}$  shown as example). (D) This results in a nanoscale graft which can be imaged again at a low contact force.

molecular insight in the crucial chemical steps to immobilize proteins with NTA-His chemistry that will be useful for future studies.

## Materials & Methods

### Chemicals and SAM preparation

All used chemicals were purchased from Sigma-Aldrich (St. Louis, MO) and used as received unless stated otherwise. Thiol solutions for SAM formation and grafting were prepared in >99.5% 2-butanol. The SAMs were prepared on an ultra-flat patch of template-stripped gold, which was prepared according to the procedure described by Hegner et al.<sup>43</sup> In short the procedure can be summarized in three steps: (i) First a 0.25 cm<sup>2</sup> piece of mica coated with a 300 nm thick layer of gold (Georg Albert PVD-Beschichtungen, Heidelberg, Germany) was glued to a clean glass slide, with its gold side pointing downwards, using a two-component epoxy glue (type 377, Epoxy Technology Inc., Waterloo, Belgium), leaving the mica side exposed to air. (ii) Subsequently, the sample was heated at 150 °C for 2 hrs, which activates the hardening process of the glue. (iii) Finally, the sample is submerged in a solution of tetrahydrofuran (THF) for 5 min after which it can be stripped at the gold - mica interface, removing the mica. After stripping, the sample was immediately submerged in a freshly prepared solution of 5 mM mixture of two thiols in 2-butanol. The 5 mM solution of the two mixed components HS-(CH<sub>2</sub>)<sub>11</sub>-(EG)<sub>3</sub>-NTA and HS-(CH<sub>2</sub>)<sub>11</sub>-(EG)<sub>4</sub>-OH (ProChimia Surfaces Sp, Poland) was used to form SAMs after incubation for >15 hrs. Thereafter, the sample was washed with ethanol (99.8%) and slightly dried in a gentle flow of nitrogen. To immobilize His-tagged proteins on SAMs containing NTA, the NTA endgroups are activated by first incubating the sample in a 1 mM NaOH MQ solution for 5 min and then in a 40 mM NiCl<sub>2</sub>/1mM NaOH MQ solution for 30 min at room temperature. Then, the sample is 3× rinsed with TSM buffer (20 mM Tris, 150 mM NaCl, 1 mM CaCl<sub>2</sub> and 2 mM MgCl<sub>2</sub> in MQ, pH 8.0) and the proteins are subsequently immobilized by adding a 200 µl droplet of 10 µg/ml ALCAM-His<sub>6</sub> or DC-SIGN-His<sub>6</sub> in TSM to the sample for 20 min. Finally, the sample was 3× rinsed with TSM + 0.1% TWEEN and mounted in the AFM for measurements. Buffers and solutions were freshly prepared and filtered using a 0.22 µm Millex GS filter (Millipore, IR).

### Atomic force microscopy

Imaging and nanografting was performed on two MultiMode AFMs with a Nanoscope IV and V controller (Veeco Industries, Santa Barbara, CA), both equipped with an E-type piezo scanner (XY-range ~12 µm) and a liquid-cell (MTFML, Veeco) holding the cantilever. Imaging and nanografting with the AFM were both performed with a Si<sub>3</sub>N<sub>4</sub> V-shaped NP-S cantilever (Veeco; cantilever A on the NP-S chip, nominal spring constant 0.58 N/m), which was cleaned by rinsing it with chloroform and by irradiation in UV light (20 min). Samples glued on a metal disk were mounted in the liquid-cell of the AFM and submerged in a 100 µL droplet of liquid.

**Nanografting:** Nanografting was performed at a high load of  $F_N \approx 120$  nN (~20 V) at 15 Hz (~60 µm/s). Imaging of the resulting nanografted patches was performed in contact mode under low load of  $F_N \approx 6$  nN (~1V deflection setpoint) at 1 Hz (~4 µm/s). To measure the friction, lateral force images in both trace and retrace were captured. Subsequently, these data were off-line analyzed by subtracting both channels (raw data) and dividing them by two to average. Finally, the data were converted into quantitative values using the method outlined below.

**SAM and protein imaging:** The samples were imaged in tapping mode with a drive frequency of 28-30 kHz for the NP-S cantilevers (type A) and a drive amplitude of 0.5 V.

In general, both AFM systems were regularly calibrated with a 1 × 1 µm<sup>2</sup> - 100 nm deep - calibration grid. All images obtained were analyzed in NS 6.13 & 7.20 (for Nanoscopes IV & V) and in Origin 8.

### Quantifying the AFM friction data

V-shaped NP-S cantilevers (Veeco) were calibrated by using both the Sader method<sup>44</sup> and the thermal oscillation method<sup>45</sup> with some minor adaptations to our needs. In short the vertical, torsional and lateral spring constant of the V-shaped cantilever were determined by the following method: The vertical spring constant was determined by using the included thermal tune software module of the NS V system (Veeco) by fitting the resonance peak with the simple harmonic oscillator model.<sup>46</sup> The system can process the data for resonances up to 100 kHz.<sup>47</sup> After a sensitivity deflection (InvOLS) calibration in air of the cantilever in the set-up (N=5), we used the Hutter and Bechhoefer method<sup>45</sup> - with the later described corrections for a V-shaped cantilever<sup>47, 48</sup> - to determine the vertical spring constant. The torsional and physically related lateral spring constant for

a V-shaped cantilever can be calculated by using the parallel beam approach for a composite ceramic-gold cantilever.<sup>49-52</sup> The following formulas were used for the lateral and torsional spring constant:

$$k_{lat} = \frac{4}{3\cos^2\theta + 6 \cdot (1 + \nu) \cdot \sin^2\theta} \left(\frac{L}{H}\right)^2 \cdot k_z \text{ and } k_{tors} = k_{lat} H^2, \text{ respectively}$$

where  $\theta$  is the inner angle between the cantilever beam and the substrate,  $\nu$  the Poisson ratio,  $L$  the length of the cantilever,  $H$  the height of the tip and  $k_z$  the vertical spring constant. For the used NP-S cantilever (cantilever A of the chip) the (nominal) dimensions given by the manufacturer are:  $\theta = 62^\circ$ ,  $\nu = 0.24$  (for  $\text{Si}_3\text{N}_4$ ),<sup>53</sup>  $L = 115 \mu\text{m}$ ,  $w = 25 \mu\text{m}$  (width),  $H = 3 \mu\text{m}$ ,  $\Delta L = 4 \mu\text{m}$  (tip set-back),  $t = 0.6 \mu\text{m}$  (thickness), and  $R = 10\text{-}20 \text{ nm}$  (tip radius). We determined an overall vertical spring constant of  $k_z = 252 \pm 19 \text{ pN/nm}$  ( $\pm$  S.D.;  $N = 6$ ; all chips from one wafer) by the method described above. By using the formulas we determined a lateral spring constant of  $k_{lat} = 159 \pm 20 \text{ N/m}$  and a torsional spring constant of  $k_{tors} = (2.06 \pm 0.15) \times 10^{-9} \text{ Nm/rad}$ . We determined a vertical InvOLS for the set-up in 2-butanol of  $23.76 \pm 0.43 \text{ nm/V}$  ( $\pm$  S.D.) and a horizontal InvOLS of  $0.77 \pm 0.10 \text{ nm/V}$  ( $\pm$  S.D.), which leads to an overall conversion rate for the photodetector data (in Volt) to the contact force (in Newton) of  $5.98 \pm 0.46 \text{ nN/V}$  and for the friction force of  $0.123 \pm 0.017 \text{ nN/mV}$ .

### Confocal microscopy of SAMs

Glass samples coated with a thin 40% transparent layer of gold (20 nm) were purchased from sSens (art. no. 12-3-00; Hengelo, NL). Samples were cleaned with Piranha solution (3:1  $\text{H}_2\text{SO}_4$ : $\text{H}_2\text{O}_2$ ) and subsequently rinsed with MQ and ethanol. Four different samples were made: i) 0% NTA-SAM, ii) 10% NTA-SAM, iii) 10% NTA-SAM + imidazole, and iv) 10% NTA-SAM + isotype Ab. In which (ii) is the sample of interest, and (i, iii, and iv) are the different negative controls. The different samples are loaded with ALCAM-His according to the procedure described before, only sample (iii) was treated with a 200 mM imidazole solution in TSM for 20 min after loading with ALCAM-His. Samples were labeled with subsequent anti-ALCAM (AZN-L50 Ab), an IgG(H+L)-biotin Ab and finally a PE-Cy5-streptavidin tandem dye (excitation at 488 nm, emission at 680 nm). Sample (iv) was labeled with an isotype Ab (IgG2a) instead of AZN-L50. After each consecutive step the samples were washed 3x times with TSM + 0.1% TWEEN. As final step the samples were embedded in mowiol (+2.5%  $\text{NaN}_3$ ).

Samples were analyzed with a confocal scanning laser scanning microscope (Zeiss LSM 510; Carl Zeiss, Germany) with a pinhole of 1 a.u. (arbitrary unit) and detector gain of 600 and 800 a.u.

## Results and Discussion

### Nanografting NTA-containing self-assembled monolayers (NTA-SAMs)

To make SAMs that can be used to immobilize proteins with NTA-His chemistry, the two components  $\text{HSC}_{11}(\text{EG})_4\text{-OH}$  and  $\text{HSC}_{11}(\text{EG})_3\text{-NTA}$  (from now abbreviated as “ $(\text{EG})_4\text{-thiol}$ ” and “ $\text{NTA-thiol}$ ”; Fig. 3) were used. Little is known on the formation and packing of SAMs containing  $(\text{EG})_4\text{-}$  and/or  $\text{NTA-thiols}$ . Therefore, we use nanografting to study these molecules. Several nanografted patches were created in a  $\text{HS-(CH}_2)_8\text{-CH}_3$  ( $\text{HSC}_9$ ) matrix of both components separately as well as mixed at different ratios in a 2-butanol solution. Hereby, the tip of an AFM cantilever is used to scratch a  $500 \times 500 \text{ nm}^2$  sized hole in the  $\text{HSC}_9$  matrix using a high force ( $>120 \text{ pN}$ ), at the same moment this hole is filled with thiols from the solution. As a result, a  $500 \times 500 \text{ nm}^2$  nanografted patch is formed consisting of the molecules from the solution, which can be imaged with the AFM cantilever at a lower

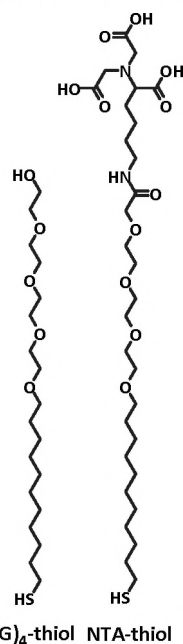


**Figure 3: Molecular structure**

The molecule  $\text{HS(CH}_2)_{11}\text{-(OC}_2\text{H}_4)_4\text{-OH}$  ( $(\text{EG})_4\text{-thiol}$  and  $\text{HS(CH}_2)_{11}\text{-(OC}_2\text{H}_4)_3\text{-NTA}$  abbreviated as  $\text{NTA-thiol}$ .

force of  $\sim 6$  pN (Fig. 2). AFM images of the resulting nanografted patches of NTA:(EG)<sub>4</sub>-thiol ratios of 0%:100%, 2.5%:97.5%, 20%:80%, 50%:50%, and 100%:0% are shown in Fig. 4. In particular, Fig. 4E summarizes the measured relative heights in relation to the HSC<sub>9</sub> matrix and Fig. 4F the corresponding friction of the different nanografted patches. First of all, the observed height of the 100% (EG)<sub>4</sub>-thiol (0% NTA) nanografted patch is only 0.94 nm, thus lower than expected (1.47 nm) for 30° tilted molecules (Table 1). In this case, the observed height for the (EG)<sub>4</sub>-nanografted patch would correspond with  $\sim 46^\circ$  tilted molecules (which is a similar orientation as mercapto-alkanols adopt on gold, see Chapter 7). Another possibility is that the molecules are compressed, are not fully extended, or present gauged conformations.<sup>54, 55</sup> However, the pressure exerted by the AFM tip could deform the molecules predominantly within their relatively flexible (EG)<sub>4</sub>-parts (Fig. 1).<sup>19, 56</sup> It is to be noted, that this flexibility of the EG-layer allows these oligo-EG SAMs to resist protein adsorption, probably because water molecules stabilize the EG-layer.<sup>57, 58</sup> However, in our set-up water molecules are absent, because the experiment

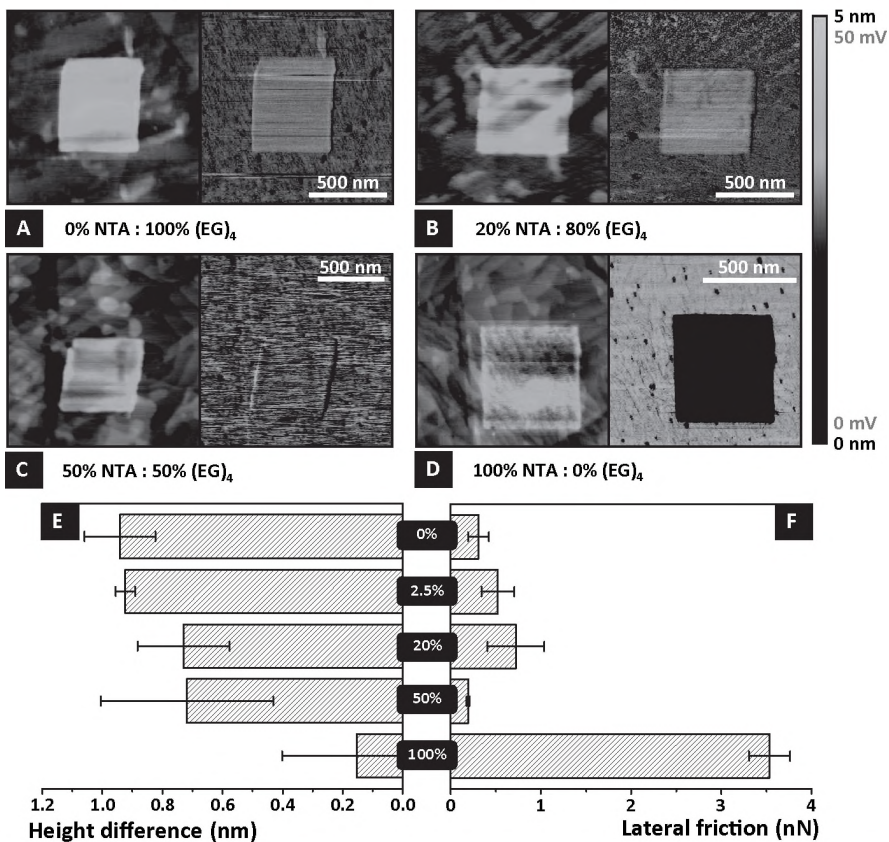


**Figure 4: Nanografting different mixtures of NTA- and (EG)<sub>4</sub>-thiols**

A series of  $500 \times 500$  nm<sup>2</sup> nanografted patches was made from different NTA:(EG)<sub>4</sub>-mixed solutions which were grafted in a HSC<sub>9</sub> SAM matrix. (A) The topography image (left panel) of a 0%-containing NTA-nanografted patch and the corresponding friction (right panel, retrace). (B) Similar for a nanografted patch of 20% NTA-, (C) 50% NTA- and (D) 100% NTA-thiols. (E) The relative heights of the nanografted patches from (A-D) plus a 2.5:97.5% mix in relation to the HSC<sub>9</sub> matrix. (F) The corresponding lateral friction of the nanografted patches. The number of samplings per patch is  $N \geq 5$ . All images were acquired in contact mode. All data are  $\pm$  S.D.

**Table 1: The observed and expected heights of the nanografted patches**

Type of nanografted patch and SAM matrix	Observed height (nm)	Expected height at 30° tilt (nm)	Corresponding tilt (°)
(EG) <sub>4</sub> -thiol in HSC <sub>9</sub>	0.94 ± 0.12	1.47	46
NTA-thiol in HSC <sub>9</sub>	0.15 ± 0.24	2.02	70
NTA-thiol in HSC <sub>16</sub>	1.22 ± 0.23	1.26	31
Hole in NTA-SAM	-3.0 ± 0.6	-3.3	39

was performed in 2-butanol. Therefore, the orientation and stability of the molecules might be influenced by the absence of water molecules stabilizing the SAM, and could also be responsible for the lower apparent heights measured.

Secondly, grafting the reverse 'mixture' of 100%NTA:0%(EG)<sub>4</sub>-thiols in a HSC<sub>9</sub> SAM matrix results in an observed height difference of only 0.15 nm, which is much lower than the expected height difference of 2.0 nm (Table 1). Besides, the nanografted patch's roughness of ± 0.24 nm and high friction of 3.53 ± 0.22 nN suggests that the monolayer of NTA-thiols has many structural defects. This is probably due to the large NTA endgroups which prevent a tight packing of the molecules resulting in NTA-thiols with non-uniform orientations. In contrast, grafting the molecules in a HSC<sub>16</sub> SAM matrix instead of a HSC<sub>9</sub> leads to a relative nanografted patch height of 1.22 nm, which almost exactly corresponds to a ~30° tilted orientation (Fig. 5A, B). Subsequently, the friction of the nanografted patch in a HSC<sub>16</sub> matrix is 1.8× reduced compared to the one in a HSC<sub>9</sub> matrix, which implicates that the NTA-thiols in the nanografted patch are better oriented and packed. Thus, longer alkyl chains of the SAM seem to better stabilize the longer

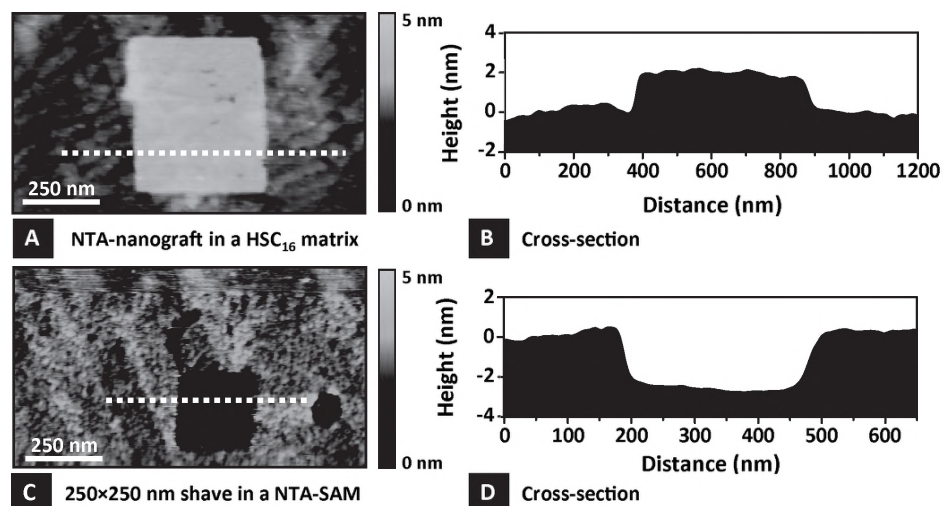


**Figure 5: NTA-thiols form different SAMs in an unconstrained environment or when grafted in a HSC<sub>16</sub> matrix**

(A) NTA-thiols grafted in a HSC<sub>16</sub> SAM matrix, (B) results in a relative height - cross-section as indicated in (A) - for the nanografted patch of 1.22 ± 0.23 nm which corresponds nicely to 30° tilted NTA-thiols (1.26 nm). (C) A SAM grown on gold from a 5 mM NTA-thiol solution overnight results in a 100% pure NTA-SAM. The topography image reveals a SAM with a relatively rough surface (RMS = 0.36 nm). After shaving an area of 250 × 250 nm<sup>2</sup> results in a hole in the SAM. (D) A cross-section as indicated in (C) results in a depth of the shave of -3.0 ± 0.6 nm. This depth corresponds roughly with a 30° tilted NTA-thiol (3.3 nm). All images were acquired in contact mode. Given values are ± S.D.

NTA molecules by interchain Van der Waals interactions, especially the flexible EG-part, which results in stretched and better packed NTA-thiols.

To check if the time needed to form a SAM can influence the orientation of the NTA-thiols, a SAM of NTA-thiols was made by growing a monolayer overnight from a 5 mM NTA solution on Au(111). The resulting SAM is as rough as the SAM in a nanografted patch ( $\pm 0.36$  nm vs.  $\pm 0.24$  nm). Furthermore, shaving a  $250 \times 250$  nm<sup>2</sup> patch (i.e. grafting in pure 2-butanol) revealed a hole in the SAM with an apparent depth of -3.0 nm (Fig. 5C, D). This depth is approximately as expected for the height difference between a 30° tilted molecule and the bare gold surface (Table 1). From these results we conclude that the NTA-thiols form monolayers. However, these tend to collapse, probably because they are less densely packed.

If the results obtained on mixed (EG)<sub>4</sub>:NTA-thiol nanografted patches (Fig. 4) are correlated, the apparent heights of the mixed NTA/(EG)<sub>4</sub>-patches at ratios of 2.5%, 20% and 50% NTA-thiols decrease slightly with increasing NTA-thiol concentration. Simultaneously, the friction of these mixed nanografted patches has increased slightly. However, taken all together these nanografted patches from different mixtures show more similarity to the 100% (EG)<sub>4</sub>-nanografted patch than to the 100% NTA-nanografted patch. This suggests that the mixed nanografted patches contain very little or no NTA-thiols. An explanation could be the confined self-assembly during nanografting. Xu et al.<sup>33</sup> proposed that during nanografting thiols adopt directly a standing-up configuration in contrast to self-assembly from solution (conventional self-assembly), where molecules first align parallel to the surface before orienting into their standing-up configuration.<sup>33</sup> This implies that conventional self-assembly takes several hours before molecules form a uniform SAM and in the case of spatial confined self-assembly only several minutes. Besides, the self-assembly process is faster for smaller than for longer molecules in the case of HSC<sub>n</sub>-molecules, although longer molecules form better organized SAMs.<sup>33, 54, 55</sup> Therefore, we assume that when a mixture of NTA- and (EG)<sub>4</sub>-thiols is used for grafting, the smaller (EG)<sub>4</sub>-molecules bind faster to gold than the NTA-thiols with their large NTA-endgroups. As a result, the reaction equilibrium shifts in favor of the binding of (EG)<sub>4</sub>-thiols and results in almost pure (EG)<sub>4</sub>-nanografted patches. Thus, although NTA-thiols are present in solution during grafting, the resulting nanografted patches do not reflect the mixed composition of the solution. Attempts to improve the quality of the nanografted patches by lowering the nanografting speed 10 times did not lead to different results.

In conclusion, our findings suggest that the formation of mixed nanografted patches containing NTA-thiols is suboptimal due to different binding dynamics of NTA- and (EG)<sub>4</sub>-thiols. Furthermore, SAMs containing only NTA-thiols have an irregular packing with non-uniformly oriented molecules in contrast to SAMs of (EG)<sub>4</sub>-thiols, which form nicely packed SAMs. The reason for NTA-thiols to form unstable SAMs is probably the large size of their NTA-endgroups; to form ordered SAMs the presence of (EG)<sub>4</sub>-thiols is necessary.

### Specific binding of His-tagged proteins on an NTA-SAM

Previous studies have shown that NTA-SAMs (NTA-containing SAMs) can form from a mixed 10%NTA:90%(EG)<sub>4</sub>-solution.<sup>15, 25, 26</sup> Herein, mixed monolayers are grown of NTA- and (EG)<sub>4</sub>-thiols in a conventional fashion (overnight). On the resulting SAMs His-tagged proteins, such as RNA-polymerase,<sup>15</sup> can be specifically bound. In order to verify that the NTA-His chemistry could also be applied in the case of ALCAM-His, a couple of 10%



NTA-SAM samples was prepared on semitransparent gold-glass slides. Subsequently, ALCAM-His was immobilized on these samples and thereafter ALCAM was specifically fluorescently labeled with a marker and analyzed under a confocal microscope (data not shown). We found that ALCAM-His specifically bound to a 10% NTA-SAM and that on treating these samples with imidazole, which disrupts the binding of His to NTA, the ALCAM molecules could be specifically removed, as expected. However, we observed that a small fraction ( $\pm 15\%$ ) of the ALCAM-His aspecifically bound to a 0% NTA-SAM, indicating that the  $(EG)_4$ -thiols are not as adsorption-resistant as expected.<sup>3, 13, 57, 59</sup> It has to be noted, that the aspecific adsorption of SAMs is usually tested by measuring the amount of bound material to the SAM of standard proteins, such as BSA, IgG, or lysozyme, by surface plasmon resonance (SPR).<sup>29</sup> For example, Hahn et al.<sup>29</sup> demonstrated that  $(EG)_4$ -SAMs are long enough to sufficiently block aspecific binding of the above mentioned proteins, whereas the smaller  $(EG)_3$ -SAMs are not. So, in this case only one EG-repeat ( $\sim 0.3$  nm) extra was enough to block aspecific interactions of standard proteins. In our case, where “more complex” proteins, such as ALCAM-His, were used, the  $(EG)_4$ -thiols might be unable to sufficiently block the adsorption. Besides, other factors like the composition of the buffer, pH, the concentration of the proteins, and possible degradation of the  $(EG)_4$ -thiols could also play a role in the observed level of aspecific adsorption.<sup>26, 29</sup> Finally, our negative control with an isotype Ab did only show a small background binding ( $\pm 4\%$ ), so probably the overall aspecific binding of proteins on  $(EG)_4$ -thiols is between this 4% and the earlier mentioned 15%.

In summary, we have shown that NTA-His chemistry can be applied in the case of SAMs formed in a conventional fashion. However, it would be interesting to study the immobilization of His-tagged proteins on these SAMs in more detail. For that, AFM was exploited. First, SAMs were formed from solutions of NTA- and  $(EG)_4$ -thiols mixed at different NTA: $(EG)_4$  ratios of 0:100%, 2:98%, and 50:50%. The total concentration of all solutions was kept at 5 mM and a SAM was formed on gold Au (111) (>15 hrs). In Fig. 6A, an AFM image of a SAM containing only  $(EG)_4$ -molecules displays a nicely uniform layer, because the underlying Au(111) structure is clearly visible, exhibiting etch holes and atomic plains. The SAM containing 2% NTA-thiols has a similar quality as the previous one, but displays a small number of bright dot-like features (Fig. 6B; white arrows). In the 50% NTA-containing SAM, these dots are much more abundant (Fig. 6C). This clearly indicates that there is a relation between the concentration of NTA-thiols and the number of protrusions visible in the SAM. Considering the difference in molecular structure of the NTA-thiols and the  $(EG)_4$ -thiols, it can be expected that the  $HSC_{11}(EG)_3$ NTA-thiols (3.6 nm long) protrude from the  $HSC_{11}(EG)_4$ OH-thiol matrix (2.9 nm long). In fact, the NTA endgroup is relatively bulky ( $\sim 0.75$  nm) compared to the OH endgroup of the  $(EG)_4$ -terminated thiols ( $\sim 0.1$  nm) (Fig. 1). Therefore, the small bright dots are most likely the NTA groups, as also proposed by Thomson et al.<sup>26</sup> Analysis of the size of the bright dots reveals an average diameter of  $25.6 \pm 6.9$  nm and an height of  $2.0 \pm 0.82$  nm. Herewith, our data confirm findings of Thomson et al. and Gamsjaeger et al., who measured height differences of 1.66 nm and 2.5 nm, respectively.<sup>15, 26</sup> Nevertheless, the expected height difference between the  $(EG)_4$ -SAM and the NTA-thiols upon a  $30^\circ$  tilt orientation of both molecules would be  $\sim 0.75$  nm, which is lower than the observed height difference. However, by assuming that both types of molecules adopt different orientations,<sup>15</sup> the  $(EG)_4$ -thiols  $30$ - $45^\circ$  and the NTA-thiols perpendicular to the surface, the apparent height of  $\sim 2$  nm can be explained.

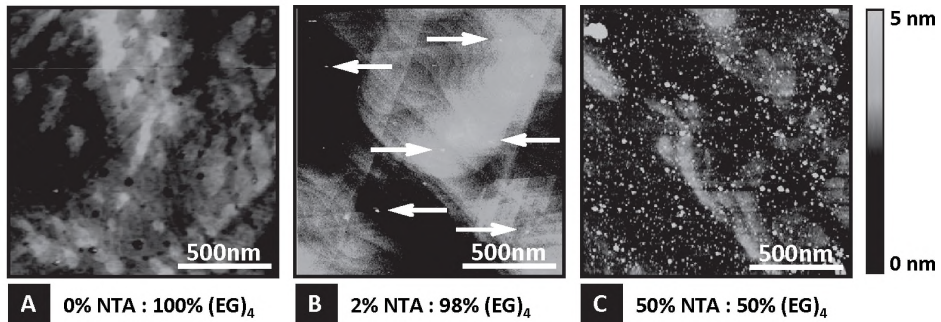


**Figure 6: SAMs of mixed NTA- and (EG)<sub>4</sub>-thiols**

(A) The topography of a 100% pure (EG)<sub>4</sub>-thiol SAM reveals a smooth SAM surface with the underlying gold structure clearly visible; in particular etch holes and atomic steps are visible. (B) A 2% NTA-SAM (98% (EG)<sub>4</sub>-thiols) shows some bright circular features which have an average diameter and height of  $25.6 \pm 6.9$  nm and  $2.0 \pm 0.8$  nm, respectively. Also here the underlying gold structure is clearly visible. (C) A mixed 50:50% SAM of both thiol-components displays a surface with many bright dots which have a diameter of  $23.9 \pm 6.2$  nm and a height of  $2.3 \pm 1.0$  nm. The underlying gold structure is now barely visible. All images were acquired in tapping mode. Statistics on dots:  $N > 20$  dots per image were analyzed with  $N = 5$  cross-sections per dot. All data presented are  $\pm$  S.D.

In addition to the height, the measured dot diameter of 25.6 nm is much larger than the diameter of a single NTA-molecule (0.75 nm). Yet, the convolution with the tip shape has to be taken into account. Convolution refers to the broadening of a feature, due to probing it with a tip of finite sharpness. In our case the tip has a radius of 10-20 nm, and so the convolution accounts for a broadening of 12-17 nm for a 2.0 nm high dot. As a result the dots with corrected diameters of 8.6-13.6 nm can maximally contain 100-300 NTA-thiol molecules per dot, if they are densely packed. In conclusion, this estimation demonstrates that NTA-thiols form small nanoclusters, which implies that NTA- and (EG)<sub>4</sub>-thiols partly phase segregate during SAM formation.

### Immobilizing His-tagged proteins on SAMs

To bind His-tagged DC-SIGN and ALCAM onto the NTA-containing SAMs, the 10% NTA-samples were first treated (*ex situ*) with 1 mM NaOH and subsequently incubated with 40 mM NiCl<sub>2</sub> solutions to activate the NTA groups (Fig. 1). Finally, 10  $\mu$ g/ml ALCAM-His or DC-SIGN-His was immobilized on the activated SAM. When rinsed and mounted in the AFM, the samples were submerged in a droplet of fresh TSM buffer and imaged in tapping mode. In Fig. 7A two different sizes of dots are visible on a SAM after immobilizing DC-SIGN-His: small dots with  $18.7 \pm 3.4$  nm diameter and  $2.3 \pm 1.1$  nm high (Fig. 7D), similarly to the size of the NTA nanoclusters as observed prior to the DC-SIGN-His addition (Fig. 6); and larger dots (Fig. 7A; white arrows) with  $34.6 \pm 6.3$  nm diameter and a height of  $9.0 \pm 1.8$  nm, significantly different from the putative NTA nanoclusters (Fig. 7E). The sample was treated subsequently with 40 mM imidazole for 1 hr. After the imidazole treatment the larger dots disappear, whereas some small dots remain (Fig. 7B). Subsequently, after the imidazole treatment the surface was reloaded with Ni<sup>2+</sup> and DC-SIGN-His (5  $\mu$ g/ml) could be immobilized again, showing the reversibility of the coupling (Fig. 7C). Therefore, we expect that the larger dots are specifically bound DC-SIGN-His proteins which are non-covalently coupled to NTA. In addition, similar experiments with ALCAM-His resulted also in two different populations of dots (Fig. 7D, F). The small dots

are  $26.0 \pm 6.7$  nm in diameter and have a height of  $1.7 \pm 0.65$  nm, most likely representing the NTA clusters again. The larger dots, which are probably bound ALCAM molecules, have a diameter of  $45.0 \pm 10.0$  nm and a height of  $4.4 \pm 1.4$  nm. The observed variation in diameter of the NTA-nanoclusters is probably due to the variation in sharpness of the AFM cantilever tip, in the case of the ALCAM-His sample being slightly blunter than for the DC-SIGN-His sample.

In conclusion, the two significantly different populations of nanoclusters observed in AFM topography images are those of nanoclustered NTA-thiols (small dots) and those of nanoclustered DC-SIGN-His or ALCAM-His molecules (large dots). We assume that the His-tagged proteins bind non-covalently and specifically onto the NTA-nanoclusters and form the larger clusters.

### Number of proteins in the clusters

The number of proteins present in clusters can be estimated by knowing their partial specific volume  $v_p$  ( $\text{cm}^3/\text{g}$ ) and the molecular weight  $M$  (kDa) of the proteins.<sup>60</sup> In general, for proteins a partial specific volume of  $0.733 \text{ cm}^3/\text{g}$  can be taken.<sup>60</sup> The molecular weight of DC-SIGN-His is 44 kDa and of ALCAM-His 60 kDa. By assuming that the proteins are spherically shaped, a minimum radius of 2.3 nm is calculated for a single DC-SIGN-His molecule and 2.6 nm for an ALCAM-His molecule. Upon comparison with the observed heights, which are  $9.0 \pm 1.8$  nm (DC-SIGN-His) and  $4.5 \pm 1.5$  nm (ALCAM-His), it can be

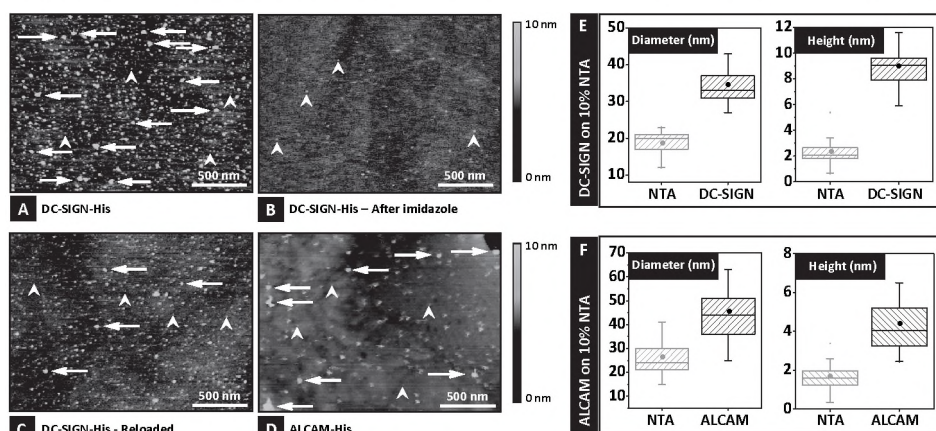


**Figure 7: His-tagged proteins immobilized on a 10% NTA SAM**

A gold sample having a 10% NTA SAM is incubated with  $10 \mu\text{g}/\text{mL}$  DC-SIGN-His and ALCAM-His for 20 min in TSM buffer. (A) Topography of the 10% NTA sample after incubation with DC-SIGN. A high amount of bright features (dots) are visible. Two types of dots are visible. The smaller dots probably correspond to NTA clusters (indicated with small arrows) and the larger dots probably have bound DC-SIGN-His (indicated with large arrows). The latter dots are  $34.6 \pm 6.3$  nm in diameter and  $9.0 \pm 1.8$  nm in height. (B) After a treatment with 40 mM imidazole, the majority of the DC-SIGN dots seem to have disappeared. The remaining dots are likely NTA clusters. (C) After the imidazole treatment the surface was again treated with  $\text{Ni}^{2+}$  and DC-SIGN-His ( $\sim 5 \mu\text{g}/\text{ml}$ ), and DC-SIGN could be specifically immobilized again. Although, the amount of dots is lower due to the lower concentration. (D) Topography image of the surface after ALCAM-His incubation. The larger dots (indicated with large arrows) represent immobilized ALCAM. ALCAM dots were determined to be  $47.7 \pm 8.8$  nm in diameter and  $4.5 \pm 1.5$  in height. (E, F) Box plots of the diameter and height of the two populations of dots, DC-SIGN and ALCAM, respectively. A Student t-test on the data showed that in all cases both populations are significantly different. A total number of 40 dots per image were analyzed. All values are  $\pm$  S.D.

concluded that the height of the ALCAM-His clusters is approximately as expected (5.2 nm diameter), whereas the DC-SIGN-His clusters are two times larger than expected (4.6 nm diameter). From literature, however, it is known that DC-SIGN(-His) forms tetramers,<sup>61</sup> and that in its tetrameric form DC-SIGN has a  $\sim 8 \times 8 \times 2$  nm sized carbohydrate recognition domain (CRD)-head and a  $\sim 2 \times 2 \times 7$  nm sized tail/repeat region ("ball-on-a-stick" model), which exactly matches the observed height.<sup>61</sup> Finally, an estimation of the amount of proteins in a cluster, taking into account the tip deconvolution, gives a maximum amount of 1-10 DC-SIGN-His monomers or 1-3 tetramers per dot and 15-30 ALCAM-His molecules per dot. That ALCAM-His molecules form larger clusters than DC-SIGN-His molecules is not surprising, because ALCAM molecules tend to multimerize.<sup>62</sup>

In conclusion, His-tagged proteins can be specifically immobilized on NTA-SAMs on which they form small nanoclusters with diameters of 20-40 nm. These nanoislands of His-tagged proteins only contain a couple of proteins which can be probed by AFM with almost single molecule resolution.

## Conclusions

By using NTA-His chemistry we have shown that it is possible to immobilize His-tagged proteins on a SAM formed on gold by specifically binding the proteins to NTA-groups. A SAM formed by 10% NTA-thiols mixed with 90%  $(EG)_4$ -thiols shows nanoclusters that contain 100-300 NTA-thiols. With tapping mode AFM bound His-tagged proteins were imaged on these SAMs and we calculated that each NTA-nanocluster bound 1-3 DC-SIGN-His tetramers or 15-30 ALCAM-His molecules (Fig. 7). The composition and orientation of the different SAM compounds have been studied by making nanografted patches of pure and mixed SAMs of NTA- and  $(EG)_4$ -thiols. In nanografted patches both thiols appear to orient at a tilt  $>30^\circ$ , which is higher than expected for thiols on gold. (Fig. 4) Probably the flexible  $(EG)$ -linker in the molecules bent due to the performed force, which resulted in relatively lower nanografted patches when probed with AFM. Furthermore, upon nanografting of mixed thiol-solutions, self-assembly of thiol-molecules within the created nanografted patch is favored by binding of  $(EG)_4$ -thiols instead of NTA-thiols. Because of the size and complexity of the NTA-thiols we assume that these thiols have a much lower binding rate which results in the almost pure  $(EG)_4$ -thiol nanografted patches observed. Nanografting seems therefore not to be the best technique to produce nanopatches of mixtures of complex thiols. Another minor difficulty is that a small fraction of His-tagged proteins bound aspecifically to the adsorption-resistant  $(EG)_4$ -thiols. Probably, by proper washing and use of longer oligo-EG linkers in the thiols this aspecific adsorption can be blocked.<sup>29</sup>

NTA-His chemistry is a useful strategy to immobilize proteins on a SAM in an oriented fashion for future applications. However, knowing that with nanografting patterning of NTA-thiols is not attainable, other strategies have to be explored to enable large scale nanopatterns of proteins. Nevertheless, our studies have shown that nanografting represents a powerful method to study the step-by-step chemistry involved in the construction of complex nanostructures.

## Acknowledgements

This work was supported by NanoNed, the Dutch nanotechnology programme of the Ministry of Economic Affairs. The authors like to thank Hans Elemans for NMR analysis of the thiols. In addition, Ben Joosten and Koen van den Dries are acknowledged for kindly assisting with the confocal laser scanning microscope.

## References

1. **S. Bodovitz, T. Joos, J. Bachmann** (2005). Protein biochips: the calm before the storm. *Drug Discovery Today*, **10**, 283-287.
2. **M. M. Stevens, J. H. George** (2005). Exploring and engineering the cell surface interface. *Science*, **310**, 1135-1138.
3. **F. Rusmini, Z. Zhong, J. Feijen** (2007). Protein immobilization strategies for protein biochips. *Biomacromolecules*, **8**, 1775-1789.
4. **C. S. Chen, J. Tan, J. Tien** (2004). Mechanotransduction at cell-matrix and cell-cell contacts. *Annu. Rev. Biomed. Eng.*, **6**, 275-302.
5. **M. Arnold, E. A. Cavalcanti-Adam, R. Glass, J. Blummel, W. Eck, M. Kantlehner, H. Kessler, J. P. Spatz** (2004). Activation of integrin function by nanopatterned adhesive interfaces. *Chemphyschem*, **5**, 383-388.
6. **D. Aydin, M. Schwieder, I. Louban, S. Knoppe, J. Ulmer, T. L. Haas, H. Walczak, J. P. Spatz** (2009). Micro-Nanostructured Protein Arrays: A Tool for Geometrically Controlled Ligand Presentation. *Small*, **5**, 1014-1018.
7. **K. Salaita, Y. H. Wang, C. A. Mirkin** (2007). Applications of dip-pen nanolithography. *Nature Nanotech.*, **2**, 145-155.
8. **J. Groll, K. Albrecht, P. Gasteier, S. Riethmueller, U. Ziener, M. Moeller** (2005). Nanostructured ordering of fluorescent markers and single proteins on substrates. *ChemBiochem*, **6**, 1782-1787.
9. **G. J. Zhang, T. Tani, T. Zako, T. Hosaka, T. Miyake, Y. Kanari, T. Funatsu, I. Ohdomari** (2005). Nanoscale patterning of protein using electron beam lithography of organosilane self-assembled monolayers. *Small*, **1**, 833-837.
10. **J. J. Yu, B. Nolting, Y. H. Tan, X. Li, J. Gervay-Hague, G. Y. Liu** (2006). Polyvalent interactions of HIV-gp120 protein and nanostructures of carbohydrate ligands. *NanoBioTechnology*, **1**, 201-210.
11. **P. Maury, M. Escalante, M. Peter, D. N. Reinhoudt, V. Subramaniam, J. Huskens** (2007). Creating nanopatterns of His-tagged proteins on surfaces by nanoimprint lithography using specific NINTA-histidine interactions. *Small*, **3**, 1584-1592.
12. **T. Wink, S. J. van Zuilen, A. Bult, W. P. van Bunnik** (1997). Self-assembled monolayers for biosensors. *Analyst*, **122**, 43R-50R.
13. **P. Jonkheijm, D. Weinrich, H. Schroder, C. M. Niemeyer, H. Waldmann** (2008). Chemical strategies for generating protein biochips. *Angew. Chem., Int. Ed.*, **47**, 9618-9647.
14. **A. J. Dirks, J. J. L. M. Cornelissen, F. L. van Delft, J. C. M. van Hest, R. J. M. Nolte, A. E. Rowan, F. P. J. T. Rutjes** (2007). From (bio)molecules to biohybrid materials with the click chemistry approach. *Qsar & Combinatorial Science*, **26**, 1200-1210.
15. **R. Gamsjaeger, B. Wimmer, H. Kah, A. Tinazli, S. Picuric, S. Lata, R. Tampe, Y. Maulet, H. J. Gruber, P. Hinterdorfer, C. Romanin** (2004). Oriented binding of the His(6)-tagged carboxyl-tail of the L-type Ca<sup>2+</sup> channel  $\alpha(1)$ -subunit to a new NTA-functionalized self-assembled monolayer. *Langmuir*, **20**, 5885-5890.
16. **P. D. Pollheimer, M. Kastner, A. Ebner, D. Blaas, P. Hinterdorfer, H. J. Gruber, S. Howorka** (2009). Receptor Arrays for the Selective and Efficient Capturing of Viral Particles. *Bioconj. Chem.*, **20**, 466-475.
17. **F. Kienberger, G. Kada, H. J. Gruber, V. Pastushenko, C. Riener, M. Trieb, H. G. Knaus, H. Schindler, P. Hinterdorfer** (2000). Recognition Force Spectroscopy Studies of the NTA-His6 Bond. *Single Mol.*, **1**, 59-65.
18. **A. Tinazli, J. L. Tang, R. Valiokas, S. Picuric, S. Lata, J. Piehler, B. Liedberg, R. Tampe** (2005). High-affinity chelator thiols for switchable and oriented immobilization of histidine-tagged proteins: A generic platform for protein chip technologies. *Chemistry - A European Journal*, **11**, 5249-5259.
19. **S. Lata, J. Piehler** (2005). Stable and functional immobilization of histidine-tagged proteins via multivalent chelator headgroups on a molecular poly(ethylene glycol) brush. *Anal. Chem.*, **77**, 1096-1105.
20. **S. Xu, G. Y. Liu** (1997). Nanometer-scale fabrication by simultaneous nanoshaving and molecular self-assembly. *Langmuir*, **13**, 127-129.
21. **M. D. Porter, T. B. Bright, D. L. Allara, C. E. D. Chidsey** (1987). Spontaneously Organized Molecular Assemblies .4. Structural Characterization of Normal-Alkyl Thiol Monolayers on Gold by Optical Ellipsometry, Infrared-Spectroscopy, and Electrochemistry. *J. Am. Chem. Soc.*, **109**, 3559-3568.
22. **L. H. Dubois, R. G. Nuzzo** (1992). Synthesis, Structure, and Properties of Model Organic-Surfaces. *Ann. Rev. Phys. Chem.*, **43**, 437-463.
23. **N. Camillone, C. E. D. Chidsey, G. Y. Liu, G. Scoles** (1993). Superlattice Structure at the Surface of a Monolayer of Octadecanethiol Self-Assembled on Au(111). *J. Chem. Phys.*, **98**, 3503-3511.
24. **P. Fenter, A. Eberhardt, P. Eisenberger** (1994). Self-Assembly of N-Alkyl Thiols as Disulfides on Au(111). *Science*, **266**, 1216-1218.
25. **G. B. Sigal, C. Bamdad, A. Barberis, J. Strominger, G. M. Whitesides** (1996). A self-assembled monolayer for the binding and study of histidine-tagged proteins by surface plasmon resonance. *Anal. Chem.*, **68**, 490-497.
26. **N. H. Thomson, B. L. Smith, N. Almqvist, L. Schmitt, M. Kashlev, E. T. Kool, P. K. Hansma** (1999). Oriented, active Escherichia coli RNA polymerase: an atomic force microscope study. *Biophys. J.*, **76**, 1024-1033.
27. **K. Uchida, H. Otsuka, M. Kaneko, K. Kataoka, Y. Nagasaki** (2005). A reactive poly(ethylene glycol) layer to achieve specific surface plasmon resonance sensing with a high S/N ratio: the substantial role of a short underbrushed PEG layer in minimizing nonspecific adsorption. *Anal. Chem.*, **77**, 1075-1080.
28. **M. Furuya, M. Haramura, A. Tanaka** (2006). Reduction of nonspecific binding proteins to self-assembled monolayer on gold surface. *Bioorg. Med. Chem.*, **14**, 537-543.
29. **C. D. Hahn, A. Tinazli, M. Holz, C. Leitner, F. Frederix, B. Lackner, N. Muller, C. Klampfl, R. Tampe, H. J. Gruber** (2007). Pragmatic studies on protein-resistant self-assembled monolayers. *Monatshfte Für Chemie*, **138**, 245-252.
30. **D. S. Ginger, H. Zhang, C. A. Mirkin** (2004). The evolution of dip-pen nanolithography. *Angew. Chem., Int. Ed.*, **43**,

- 30-45.
31. **R. D. Piner, J. Zhu, F. Xu, S. H. Hong, C. A. Mirkin** (1999). "Dip-pen" nanolithography. *Science*, **283**, 661-663.
  32. **M. Liu, N. A. Amro, G. Y. Liu** (2008). Nanografting for surface physical chemistry. *Ann. Rev. Phys. Chem.*, **59**, 367-386.
  33. **S. Xu, P. E. Laibinis, G. Y. Liu** (1998). Accelerating the kinetics of thiol self-assembly on gold - A spatial confinement effect. *J. Am. Chem. Soc.*, **120**, 9356-9361.
  34. **A. Ivanisevic, K. V. McCumber, C. A. Mirkin** (2002). Site-directed exchange studies with combinatorial libraries of nanostructures. *J. Am. Chem. Soc.*, **124**, 11997-12001.
  35. **J. J. Yu, Y. H. Tan, X. Li, P. K. Kuo, G. Y. Liu** (2006). A nanoengineering approach to regulate the lateral heterogeneity of self-assembled monolayers. *J. Am. Chem. Soc.*, **128**, 11574-11581.
  36. **M. Castronovo, F. Bano, S. Raugel, D. Scaini, M. Dell'Angela, R. Hudej, L. Casalis, G. Scoles** (2007). Mechanical stabilization effect of water on a membrane-like system. *J. Am. Chem. Soc.*, **129**, 2636-2641.
  37. **C. Staii, D. W. Wood, G. Scoles** (2007). Verification of Biochemical Activity for Proteins Nanografted on Gold Surfaces. *J. Am. Chem. Soc.*, **130**, 640-646.
  38. **M. Z. Liu, N. A. Amro, C. S. Chow, G. Y. Liu** (2002). Production of nanostructures of DNA on surfaces. *Nano Lett.*, **2**, 863-867.
  39. **K. Wadu-Mesthrige, S. Xu, N. A. Amro, G. Y. Liu** (1999). Fabrication and imaging of nanometer-sized protein patterns. *Langmuir*, **15**, 8580-8583.
  40. **G. Oncins, S. Garcia-Manyes, F. Sanz** (2005). Study of frictional properties of a phospholipid bilayer in a liquid environment with lateral force microscopy as a function of NaCl concentration. *Langmuir*, **21**, 7373-7379.
  41. **A. Cambi, F. de Lange, N. M. van Maarseveen, M. Nijhuis, B. Joosten, E. M. van Dijk, B. I. de Bakker, J. A. Fransen, P. H. Bovee-Geurts, F. N. van Leeuwen, N. F. Van Hulst, C. G. Figdor** (2004). Microdomains of the C-type lectin DC-SIGN are portals for virus entry into dendritic cells. *J. Cell Biol.*, **164**, 145-155.
  42. **J. M. Nelissen, I. M. Peters, B. G. de Groot, Y. van Kooyk, C. G. Figdor** (2000). Dynamic regulation of activated leukocyte cell adhesion molecule-mediated homotypic cell adhesion through the actin cytoskeleton. *Mol. Biol. Cell*, **11**, 2057-2068.
  43. **M. Hegner, P. Wagner, G. Semenza** (1993). Ultralarge Atomically Flat Template-Stripped Au Surfaces for Scanning Probe Microscopy. *Surf. Sci.*, **291**, 39-46.
  44. **J. E. Sader, I. Larson, P. Mulvaney, L. R. White** (1995). Method for the Calibration of Atomic-Force Microscope Cantilevers. *Rev. Sci. Instrum.*, **66**, 3789-3798.
  45. **J. L. Hutter, J. Bechhoefer** (1993). Calibration of Atomic-Force Microscope Tips. *Rev. Sci. Instrum.*, **64**, 1868-1873.
  46. **J. E. Sader, J. W. M. Chon, P. Mulvaney** (1999). Calibration of rectangular atomic force microscope cantilevers. *Rev. Sci. Instrum.*, **70**, 3967-3969.
  47. **B. Ohler** (2007). Cantilever spring constant calibration using laser Doppler vibrometry. *Rev. Sci. Instrum.*, **78**, 0637011-0637015.
  48. **R. W. Stark, T. Drobek, W. M. Heckl** (2001). Thermomechanical noise of a free v-shaped cantilever for atomic-force microscopy. *Ultramicroscopy*, **86**, 207-215.
  49. **A. Noy, C. D. Frisbie, L. F. Rozsnyai, M. S. Wrighton, C. M. Lieber** (1995). Chemical Force Microscopy - Exploiting Chemically-Modified Tips to Quantify Adhesion, Friction, and Functional-Group Distributions in Molecular Assemblies. *J. Am. Chem. Soc.*, **117**, 7943-7951.
  50. **J. E. Sader** (1995). Parallel Beam Approximation for V-Shaped Atomic-Force Microscope Cantilevers. *Rev. Sci. Instrum.*, **66**, 4583-4587.
  51. **J. E. Sader, R. C. Sader** (2003). Susceptibility of atomic force microscope cantilevers to lateral forces: Experimental verification. *Appl. Phys. Lett.*, **83**, 3195-3197.
  52. **J. L. Hazel, V. V. Tsukruk** (1999). Spring constants of composite ceramic/gold cantilevers for scanning probe microscopy. *Thin Solid Films*, **339**, 249-257.
  53. **W. Alexander, J. F. Shackelford** (2001). CRC Materials Science and Engineering Handbook (p.537). *CRC Handbooks*.
  54. **J. C. Love, L. A. Estroff, J. K. Kriebel, R. G. Nuzzo, G. M. Whitesides** (2005). Self-assembled monolayers of thiolates on metals as a form of nanotechnology. *Chem. Rev.*, **105**, 1103-1169.
  55. **C. Vericat, M. E. Vela, R. C. Salvarezza** (2005). Self-assembled monolayers of alkanethiols on Au(111): surface structures, defects and dynamics. *Phys. Chem. Chem. Phys.*, **7**, 3258-3268.
  56. **E. Barrena, C. Ocal, M. Salmeron** (2000). Molecular packing changes of alkanethiols monolayers on Au(111) under applied pressure. *J. Chem. Phys.*, **113**, 2413-2418.
  57. **S. Chen, J. Zheng, L. Li, S. Jiang** (2005). Strong resistance of phosphorylcholine self-assembled monolayers to protein adsorption: insights into nonfouling properties of zwitterionic materials. *J. Am. Chem. Soc.*, **127**, 14473-14478.
  58. **K. L. Prime, G. M. Whitesides** (1993). Adsorption of Proteins onto Surfaces Containing End-Attached Oligo(Ethylene Oxide) - a Model System Using Self-Assembled Monolayers. *J. Am. Chem. Soc.*, **115**, 10714-10721.
  59. **E. Ostuni, R. G. Chapman, R. E. Holmlin, S. Takayama, G. M. Whitesides** (2001). A survey of structure-property relationships of surfaces that resist the adsorption of protein. *Langmuir*, **17**, 5605-5620.
  60. **H. P. Erickson** (2009). Size and Shape of Protein Molecules at the Nanometer Level Determined by Sedimentation, Gel Filtration, and Electron Microscopy. *Biol. Proc. Online Epub*.
  61. **G. A. Snyder, M. Colonna, P. D. Sun** (2005). The structure of DC-SIGNR with a portion of its repeat domain lends insights to modeling of the receptor tetramer. *J. Mol. Biol.*, **347**, 979-989.
  62. **L. C. van Kempen, J. M. Nelissen, W. G. Degen, R. Torensma, U. H. Weidle, H. P. Bloemers, C. G. Figdor, G. W. Swart** (2001). Molecular basis for the homophilic activated leukocyte cell adhesion molecule (ALCAM)-ALCAM interaction. *J. Biol. Chem.*, **276**, 25783-25790.



# CHAPTER 7

---

## Molecular friction as a tool to identify functionalized alkanethiols

*Joost te Riet, Tim Smit, Jan W. Gerritsen, Alessandra Cambi,  
Johannes A.A.W. Elemans, Carl G. Figdor, Sylvia Speller*

*You cannot teach a man anything;  
you can only help him find  
it within himself.*

*Galileo Galilei*



By using the nanografting method, well-defined nanoscale patches of alkanethiols were constructed in a self-assembled monolayer (SAM) matrix on an atomically flat gold (Au(111)) surface. A series of nanografted patches, composed of alkanethiols with different endgroups ( $-\text{CH}_3$ ,  $-\text{CF}_3$ ,  $-\text{OH}$ ,  $-\text{SH}$ ,  $-\text{COOH}$  and  $-\text{NH}_2$ ), were analyzed in detail by a combination of atomic force microscopy (AFM) height and quantitative lateral friction measurements. By constructing a series of nanografted patches of methyl-terminated thiols with various chain lengths, it was shown that the absolute friction of the nanografted patches was always smaller than that of the surrounding SAM matrix, demonstrating that, because of the spatially confined self-assembly during nanografting, SAMs show less defects. In addition, the friction gradually increased for decreasing alkane chain length as expected, although a subtle odd–even effect was observed. The study of thiols with functionalized endgroups ( $-\text{CF}_3$ ,  $-\text{OH}$ ,  $-\text{SH}$ ,  $-\text{COOH}$  and  $-\text{NH}_2$ ) gave specific insights in orientation, packing, and structure of the molecules in the SAMs. Depending on the thiol endgroups, these nanografted patches exhibited large and specific differences in lateral friction force, which offers the unique possibility to use the friction as a molecular recognition tool for thiol-based self-assembled monolayers.

## Introduction

In the recent decade, the ability to create structures with dimensions below the micrometer scale has greatly increased the demand for and number of applications of nanosized structures, which requires the development of new methods to manipulate and control the properties of materials down to the molecular level. There are a number of widely available techniques to create well-defined nanoscale structures on surfaces, such as electron beam lithography (EBL),<sup>1</sup> methods based on chemical vapor deposition (CVD),<sup>2</sup> and scanning probe microscopy (SPM)-assisted lithography, such as dip-pen nanolithography (DPN),<sup>3, 4</sup> nanoshaving, and nanografting.<sup>5, 6</sup> Many of these techniques rely on atomic force microscopy (AFM) for quality control or pattern creation. Since its invention in 1986,<sup>7</sup> AFM has made enormous contributions to the study and development of nanoscale processes, commonly by using it as a topography imaging tool by scanning the sample with a small ( $\sim 10$  nm in diameter) tip attached to a cantilever. First introduced by Xu and Liu<sup>6</sup> in 1997, nanografting was presented as a new method for fabricating nanosized structures by using the AFM not only as an imaging tool, but also as a nanomanipulator to create patterns on a surface using the same cantilever to graft and image. The nanografting technique offers a highly precise control over pattern creation and surface distribution with high lithographic resolution ( $\sim 10$  nm and beyond). The versatility of a self-assembled monolayer (SAM) of alkanethiols<sup>8</sup> makes it ideal for pattern transfer.<sup>9, 10</sup> The specific binding to gold (Au(111)) of alkanethiols or other thiolated molecules is enabled via strong and specific sulfur–gold bonds, so that uniform SAMs of high quality are formed. From structural studies by, for example, scanning tunneling microscopy (STM) and reflectance absorption infrared spectroscopy (RAIRS), it is known that alkanethiols form a SAM on a gold surface with their hydrocarbon chains oriented in an *all-trans* conformation with a lattice constant of  $\sim 0.50$  nm.<sup>6, 9, 11–16</sup> Moreover, they predominantly present a  $(\sqrt{3} \times \sqrt{3})R30^\circ$ -based structure (although also a  $c(4 \times 2)$  superlattice has been observed) in which the hydrocarbon chains are closely packed and tilted under an angle of  $\sim 30^\circ$  with respect to the surface normal.

An AFM cantilever is used to nanograft patterns in a SAM matrix by applying a high load force ( $>100$  nN),<sup>17</sup> either in contact mode<sup>6</sup> or in tapping mode.<sup>18</sup> Under these conditions, the AFM tip locally “shaves” patches of thiol molecules away from the relatively soft SAM

matrix (Figure 1). Subsequently, the exposed gold is refilled with other thiol molecules from a supernatant solution. The resulting nanografted patch in the SAM matrix can then be imaged with the same cantilever under a lower load force. This method has been discussed in depth before,<sup>6, 18, 19</sup> and with respect to EBL, CVD, or DPN it has many advantages, for example, the ability of working *in situ* in liquid, without the need for tip modification, and with high accuracy and versatility. Disadvantages of the method are its relatively slow construction speed and small manipulation area, but for studying SAM characteristics at the nanoscale these are of minor importance. Nanografting has provided researchers with new possibilities for the fabrication of nanosized patterns which can be applied to better understand the kinetics of self-assembly,<sup>17, 20-22</sup> but also to specifically organize biomolecules (e.g., proteins and DNA),<sup>23-27</sup> nanoparticles,<sup>28</sup> 3D nanostructures,<sup>29</sup> and bicomponent mixtures.<sup>21</sup> The availability over internal calibration *in situ* (the atomic steps in gold and the matrix SAM) allows quantitative height measurements of the materials involved.

An AFM cantilever tip that scans the topography of a sample in contact mode exerts a load force and gets slightly torsionally deformed while scanning in the lateral direction. This deformation is interpreted as the lateral friction force between tip and sample. This friction is a complex interplay of different physical and chemical factors. The amount of friction the tip experiences depends on the scan speed, the load force  $F_N$ , the type of probe used, and, most importantly, the composition and structure of the sample.<sup>19, 30</sup> In the case of a surface covered with a SAM, important sample properties are its roughness

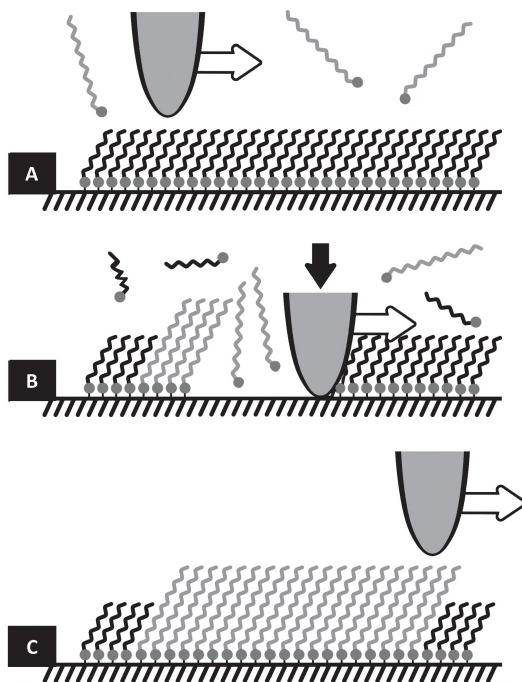


**Figure 1. Schematic representation of the nanografting procedure**

(A) A Au(111) sample covered with a uniform SAM (in this case HSC<sub>9</sub>) is studied under a supernatant solution with AFM by scanning with a low contact force ( $F_N \approx 6$  nN). (B) By increasing the contact force to 120 nN and increasing the speed, patches of the SAM can be removed and exchanged by other thiol molecules from solution (in this case HSC<sub>14</sub>). (C) A nanoscale graft has been formed within the matrix SAM which can be imaged again at a low contact force.

and packing density, the surface tension, and the number of defects (e.g., crystal edges, grain boundaries and gauche effects) present in the SAM.<sup>9</sup> In addition, the nature of the supernatant solution, or the absence of it (i.e., ambient or vacuum), can influence the surface tension between endgroups in a SAM and therefore also the friction.<sup>17, 31</sup> Friction mapping can thus provide valuable information about the composition and specific chemical<sup>32-37</sup> and biological<sup>26, 38</sup> properties of a surface layer at the nanoscale.

In this article, a combination of nanografting and lateral friction measurements is used to study in a quantitative manner the formation and identity of nanografted SAM patches of alkanethiols with different endgroups, such as  $-\text{CH}_3$ ,  $-\text{CF}_3$ ,  $-\text{OH}$ ,  $-\text{SH}$ ,  $-\text{NH}_2$ , and  $-\text{COOH}$ . All these measurements are carried out in a liquid environment of 2-butanol, which has the benefit over working in ambient conditions, because the layer on top of the SAM is well-defined and the SAM is in its native state. A thoroughly performed study on methyl-terminated alkanethiols expands the knowledge on the effect of the confined space of nanografting. In particular, the friction changes characteristically. Furthermore, we demonstrate that the ease of using a matrix SAM as internal standard allows to us get direct insight into the orientation and packing of the different (functionalized) alkanethiols within the nanografted patches. In addition, we will show that by using AFM to measure friction it is possible to quantitatively distinguish differences in the chemical nature of the endgroups of thiols by measuring their specific frictional properties in a nanografted SAM patch.

## Materials and Methods

### Chemicals used and SAM preparation

All chemicals used (Table 1) were purchased from Sigma-Aldrich (St. Louis, MO) and used as received unless stated otherwise. Thiol solutions for SAM formation and grafting were prepared in >99.5% 2-butanol. The SAMs were prepared on an ultraflat patch of template-stripped gold, which was prepared according to the procedure described by Hegner et al.<sup>60</sup> In short, it can be summarized in three steps: (i) First, a 0.25 cm<sup>2</sup> piece of mica coated with a 300 nm thick layer of gold (Georg Albert PVD-Beschichtungen, Heidelberg, Germany) was glued to a clean glass slide, with its gold side pointing downward, using a two-component epoxy glue (type 377, Epoxy Technology Inc., Waterloo, Belgium), leaving the mica side exposed to air. (ii) Subsequently, the sample was heated at 150 °C for 2 h, which activates the hardening process of the glue. (iii) Finally, the sample was submerged in a solution of tetrahydrofuran (THF) for 5 min, after which it can be stripped at the gold–mica interface, removing the mica. After stripping, the sample was immediately submerged in a freshly prepared solution of 5 mM of alkanethiol in 2-butanol. After incubation for  $\geq 18$  h in the thiol solution,<sup>9</sup> the gold sample was washed with ethanol (99.8%) and dried with a gentle flow of nitrogen.

### Atomic Force Microscopy

Imaging and nanografting were performed using two Veeco MultiMode AFMs with a Nanoscope IV and V controller (Veeco Industries, Santa Barbara, CA), both equipped with an E-type piezo scanner ( $XY$ -range  $\sim 12$   $\mu\text{m}$ ) and a liquid-cell (MTFML, Veeco) holding the cantilever. The AFM system was calibrated by using a  $1 \times 1$   $\mu\text{m}^2$  (100 nm-deep) calibration grid. After calibration, the sample was placed in the liquid-cell and subsequently submerged in a 50  $\mu\text{L}$  droplet of a 5 mM 2-butanolic solution of an alkanethiol. The whole sample and droplet were then enclosed by a fluorosilicate O-ring (FSFCO-10, Veeco). A laser beam was focused on the end point of a V-shaped  $\text{Si}_3\text{N}_4$  NP-S cantilever (Veeco; cantilever A on the NP-S chip, nominal spring constant 0.58 N/m), which had been cleaned by rinsing with chloroform and by irradiation with UV light (20 min.). Moreover, directly prior to every experiment, the cantilever was rinsed with ethanol (99.8%). The laser beam was deflected onto a four-quadrant photosensitive detector; the monitored vertical deflection was interpreted as the topography, while the horizontal deflection, caused by the torsional deformation of the cantilever when its tip scans over the surface, was interpreted as the lateral friction force between tip and sample.

Imaging was performed in contact mode, under a low load force of  $F_n \approx 6$  nN ( $\sim 1$  V deflection set point) at 1 Hz ( $\sim 4$   $\mu\text{m/s}$  for a  $2 \times 2$   $\mu\text{m}^2$  image). The pressure that the tip then exerts is  $\sim 0.5$  GPa, as calculated by the Hertzian

model<sup>54</sup> assuming a tip radius of 15 nm and a contact area of 12 nm<sup>2</sup>. Nanoshaving of the SAM was performed at a high load force of  $F_N \approx 120$  nN ( $\sim 20$  V) at 15 Hz ( $\sim 60$   $\mu\text{m/s}$ ), and the exerted pressure was  $\sim 10$  GPa. Data and images were analyzed by using NanoScope 6.13 and 7.20 (for NS IV and V) and Origin 8 software. The friction was determined from both trace and retrace of the lateral force images; these data were analyzed off-line by subtracting both channels (raw data), dividing by 2 for averaging, and subsequently converted into friction data (nN) using the method outlined below. For statistics, the height data were analyzed by taking consecutive cross sections (sampling over 20–50 lines) via step size determination on the edges of the nanografted patch on a single gold terrace within the software. Per image,  $N \geq 5$  of these samplings were performed. Subsequently, at least three images per nanografted patch were analyzed per experiment (up and down scans), and also at least three independent experiments in total (all with different cantilevers, to exclude the possibility that differences in friction are caused by differences in tip shape). The friction was determined only in the  $450 \times 450$  nm<sup>2</sup> center region of the  $500 \times 500$  nm<sup>2</sup> nanografted patches to eliminate edge effects. Furthermore, the friction was collected for the same amount and set of images as the topography analysis with a sampling of three on every image. In addition to the friction measurements of the nanografted patches, in all experiments, also the friction of the SAM matrix was determined in order to ascertain the quality and reliability of the measurements and, when necessary, to exclude measurements from further analysis. For all analyzed data, errors given are  $\pm$  S.D.

### Quantifying the AFM data

V-shaped NP-S cantilevers (Veeco) were calibrated combining the Sader method<sup>61</sup> and the thermal oscillation method,<sup>62</sup> with some minor practical adaptations. In short, the vertical, torsional, and lateral spring constants of the V-shaped cantilever were determined by the following method. The vertical spring constant was determined by using the included thermal tune software module of the NS V system (Veeco) by fitting the primary resonance peak with the simple harmonic oscillator model.<sup>63</sup> The system can process the data for resonances up to 100 kHz.<sup>64</sup> After a deflection sensitivity (from now designated as InvOLS; inverse optical lever sensitivity) calibration in air of the cantilever mounted in the set-up ( $N = 5$ ), we used the Hutter and Bechhoefer method,<sup>62</sup> with the later described corrections for a V-shaped cantilever,<sup>64, 65</sup> to determine the vertical spring constant. The torsional and physically related lateral spring constant for a V-shaped cantilever was calculated by using the parallel beam approach for a composite ceramic-gold cantilever.<sup>66–69</sup> The following formulas were used to calculate the lateral spring constant,

$$k_{\text{lat}} = \frac{4}{3\cos^2\theta + 6 \cdot (1 + \nu)\sin^2\theta} \left(\frac{L}{H}\right)^2 \cdot k_z$$

and the torsional spring constant,  $k_{\text{tors}} = k_{\text{lat}} H^2$

where  $\theta$  is the inner angle between the cantilever beam and the substrate,  $\nu$  is the Poisson ratio,  $L$  is the length of the cantilever,  $H$  is the height of the tip and  $k_z$  is the vertical spring constant. For the used NP-S cantilever (cantilever A of the chip), the (nominal) dimensions given by the manufacturer are  $\theta = 62^\circ$ ,  $\nu = 0.24$  (for  $\text{Si}_3\text{N}_4$ ),<sup>70</sup>  $L = 115$   $\mu\text{m}$ ,  $w = 25$   $\mu\text{m}$  (width),  $H = 3$   $\mu\text{m}$ ,  $\Delta L = 4$   $\mu\text{m}$  (tip set-back),  $t = 0.6$   $\mu\text{m}$  (thickness), and  $R = 10$ – $20$  nm (tip radius). We determined an overall vertical spring constant of  $k_z = 252 \pm 19$  pN/nm ( $\pm$  S.D.;  $N = 6$ ; all chips from one wafer) by the method described above (note the 57% difference with the manufacturers data). By using the formulas above, we calculated a lateral spring constant of  $k_{\text{lat}} = 159 \pm 20$  N/m and a torsional spring constant of  $k_{\text{tors}} = (2.06 \pm 0.15) \times 10^9$  Nm/rad. We determined a vertical InvOLS for the set-up in 2-butanol (note: different from that in air<sup>71</sup>) of  $23.76 \pm 0.43$  nm/V ( $\pm$  S.D.) and a horizontal InvOLS of  $0.77 \pm 0.10$  nm/V ( $\pm$  S.D.), which leads to an overall conversion rate for the photodetector data (in volts) to the contact force (in newtons) of  $5.98 \pm 0.46$  nN/V and for the friction force of  $0.123 \pm 0.017$  nN/mV.

### Molecular model

The apparent height of the molecules in the SAM was calculated using data from literature;<sup>72</sup> bond lengths are 0.1523 nm (C–C), 0.2293 nm (S–Au), 0.1815 nm (C–S), 0.1338 nm (C–O), 0.1208 nm (C=O), and 0.1438 nm (C–N) and the angle between the Au–S–C and C–C–C bonds in the alkyl backbone is in both cases  $109.5^\circ$ . With these data, the expected lengths of the alkanethiols were calculated using ChemBio3D Ultra 11.0. Subsequently, by taking into account a  $30^\circ$  tilt (if not stated otherwise) for the molecules,<sup>9, 14</sup> the apparent height or thickness of the layer is calculated.

## Results and Discussion

### Nanografting alkanethiols in a self-assembled monolayer

Figure 1 shows a cartoon that illustrates the nanografting experiments that have been performed to study functionalized SAMs of alkanethiols. On an ultraflat template-stripped piece of gold (terraces of  $200 \times 200 \text{ nm}^2$ ), a SAM of  $\text{HSC}_8$  (see Table 1 for abbreviations used) was grown from a 5 mM solution of the thiol in 2-butanol. After an incubation time of  $\geq 18 \text{ h}$ , a uniform SAM had been formed. The SAM sample, from now designated as SAM matrix, was then placed in an AFM liquid-cell containing another thiol in 2-butanol for grafting ( $\text{HSC}_{14}$  in this example). Subsequently, the SAM sample was imaged by AFM in contact mode (Figure 1A), for which a typical force and speed were chosen to avoid compression and deformation of the monolayers (see Experimental Section for details).<sup>17</sup> Next, an atomically flat part of the surface was selected and a graft was made by shaving the SAM at a high load force, and after that the uncovered gold was immediately filled with thiols from the  $\text{HSC}_{14}$  solution (Figure 1B). After the formation of the graft, the sample was imaged at low force again, and features such as height difference between the patch and SAM or lateral force can be determined (Figure 1C).

### Quantification of the height of nanografted patches

In Figure 2, AFM images of two  $500 \times 500 \text{ nm}^2$  nanografted patches are shown, one of a positive (protruding with respect to the background) nanografted patch of  $\text{HSC}_{18}$  in a  $\text{HSC}_8$  SAM matrix (Figure 2A) and the other one of a negative (lower than background) nanografted patch of  $\text{HSC}_9$  in a  $\text{HSC}_{18}$  matrix (Figure 2B). From the topographies, it is clear that after the grafting procedure other thiols have adsorbed onto the exposed gold, which are most probably those present in the supernatant solution. To confirm this assumption, the height differences between the nanografted patches and the SAM matrix were determined. Relative height differences of  $+1.10 \pm 0.18$  and  $-1.02 \pm 0.12 \text{ nm}$

**Table 1. List of molecules that were used for the formation of SAMs and nanografted patches in our experiments**

Chemical name	Molecular formula	Abbreviated as
1-pentanethiol	$\text{HS-(CH}_2)_4\text{-CH}_3$	$\text{HSC}_5$
1-hexanethiol	$\text{HS-(CH}_2)_5\text{-CH}_3$	$\text{HSC}_6$
1-heptanethiol	$\text{HS-(CH}_2)_6\text{-CH}_3$	$\text{HSC}_7$
1-octanethiol	$\text{HS-(CH}_2)_7\text{-CH}_3$	$\text{HSC}_8$
1-nonanethiol	$\text{HS-(CH}_2)_8\text{-CH}_3$	$\text{HSC}_9$
1-decanethiol	$\text{HS-(CH}_2)_9\text{-CH}_3$	$\text{HSC}_{10}$
1-undecanethiol	$\text{HS-(CH}_2)_{10}\text{-CH}_3$	$\text{HSC}_{11}$
1-dodecanethiol	$\text{HS-(CH}_2)_{11}\text{-CH}_3$	$\text{HSC}_{12}$
1-tetradecanethiol	$\text{HS-(CH}_2)_{13}\text{-CH}_3$	$\text{HSC}_{14}$
1-pentadecanethiol	$\text{HS-(CH}_2)_{14}\text{-CH}_3$	$\text{HSC}_{15}$
1-hexadecanethiol	$\text{HS-(CH}_2)_{15}\text{-CH}_3$	$\text{HSC}_{16}$
1-octadecanethiol	$\text{HS-(CH}_2)_{17}\text{-CH}_3$	$\text{HSC}_{18}$
6-mercapto-1-hexanol	$\text{HS-(CH}_2)_6\text{-OH}$	$\text{HSC}_{6\text{OH}}$
9-mercapto-1-nonanol	$\text{HS-(CH}_2)_9\text{-OH}$	$\text{HSC}_{9\text{OH}}$
11-mercapto-1-undecanol	$\text{HS-(CH}_2)_{11}\text{-OH}$	$\text{HSC}_{11\text{OH}}$
1,8-octanedithiol	$\text{HS-(CH}_2)_8\text{-SH}$	$\text{HSC}_{8\text{SH}}$
3,3,4,4,5,5,6,6,7,7,8,8,9,9,10,10,10-heptafluoro-1-decanethiol	$\text{HS-(CH}_2)_2\text{-(CF}_2)_7\text{-CF}_3$	$\text{HSC}_{9\text{CF}_3}^{\text{F}}$
12-mercapto-1-dodecanoic acid	$\text{HS-(CH}_2)_{11}\text{-COOH}$	$\text{HSC}_{11\text{COOH}}$
11-amino-1-undecanethiol	$\text{HS-(CH}_2)_{11}\text{-NH}_2$	$\text{HSC}_{11\text{NH}_2}$

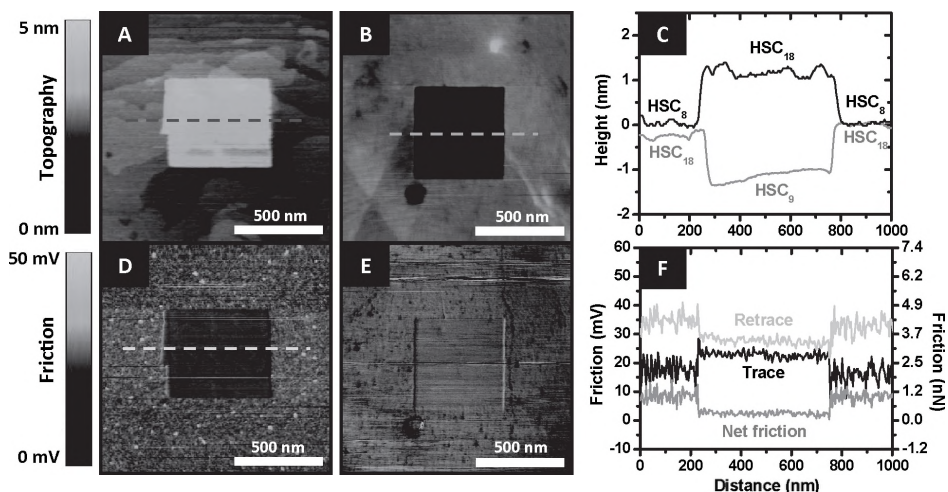


**Figure 2. Nanografting of “positive” and “negative” patches**

(A) AFM topography image of a freshly nanografted “positive”  $\text{HSC}_{18}$  patch grafted in a  $\text{HSC}_8$  matrix in 2-butanol. The light square represents the nanografted patch, which appears higher in the topography than the surrounding SAM matrix. (B) AFM topography image of a nanografted “negative”  $\text{HSC}_9$  patch, which appears lower than the surrounding  $\text{HSC}_{18}$  matrix. (C) Cross sections of the topography of the nanografted patches, as indicated by the dashed lines in images (A) and (B). (D and E) Friction images (retrace) corresponding to images (A) and (B), respectively. (F) Cross sections of the trace and retrace of the friction channel, as indicated by the dashed line in (D). The raw friction data indicated in black (trace) and light gray (retrace) are subtracted and divided by 2 yielding a net friction for the SAM matrix ( $\text{HSC}_8$ ) of  $8.6 \pm 1.9$  mV ( $1.05 \pm 0.24$  nN) and for the nanografted patch ( $\text{HSC}_{18}$ ) of  $2.4 \pm 0.7$  mV ( $0.30 \pm 0.09$  nN). All data are  $\pm$  S.D.

were found for the positive and negative grafts, respectively (Figure 2C; see Experimental Section for analysis). These values are in good agreement with the expected differences of +1.08 and -0.97 nm, which were calculated by the model described in the Experimental Section.

In the topographical images (Figure 2A), atomic gold steps with step sizes of  $0.235 \pm 0.06$  nm are clearly visible, values which correspond well to the known Au(111) step size of 0.235 nm.<sup>39</sup> The presence of these steps provides us with a reliable z-calibration of the AFM system at the sub-nanometer scale and demonstrates the high quality and accuracy of the measurements.

### Quantification of the friction on nanografted patches

When scanning the samples simultaneously with the topography, the friction was probed. In these friction images, the lateral response (torsion) of the AFM cantilever scanning under a  $90^\circ$  angle with respect to the cantilever long edge axis in contact with the molecular layer is shown. Friction is a unique approach to probe material’s and molecular properties at the nanoscale level. In Figure 2D and E, friction images corresponding to the topography images of Figure 2A and B, respectively, are shown, revealing differences in roughness of the SAM matrix with respect to the SAM nanografted patch. In Figure 2F, cross sections are shown that demonstrate the determination of the net lateral friction. Although coupling between friction and topography cannot be fully excluded, to minimize its influence, the friction of the nanografted patches has been determined in their central region only (see Experimental Section for details). For the nanografted patches shown in Figure 2A and B, friction forces of  $0.30 \pm 0.09$  and  $0.43 \pm 0.06$  nN were

found for the positive and negative graft, respectively, and  $1.05 \pm 0.24$  and  $0.60 \pm 0.06$  nN for their respective matrices. Remarkably, in both cases, the friction of the grafts was lower than that of the matrix. Furthermore, the friction was lower for progressively longer molecules in the nanografted patches as well as in the matrix, which triggered us to study this property in further detail (see below).

### Tilting of methyl-terminated thiols in a nanografted patch

By systematically investigating a series of nanografted alkanethiols with a chemically inert methyl-endgroup, the role of the alkane chain length on the topography was elucidated. A full range of HSC<sub>*n*</sub>-type molecules was investigated, with their alkane chain length varying from  $n = 5$  to 18 carbon atoms (Table 1), thereby expanding the studies that have been performed earlier by the Liu group.<sup>19,40</sup> A series of positive  $500 \times 500$  nm<sup>2</sup> nanografted patches was grafted into a HSC<sub>8</sub> SAM matrix, which all formed fully covered patches. By measuring the step size of each of the nanografted patches, relative

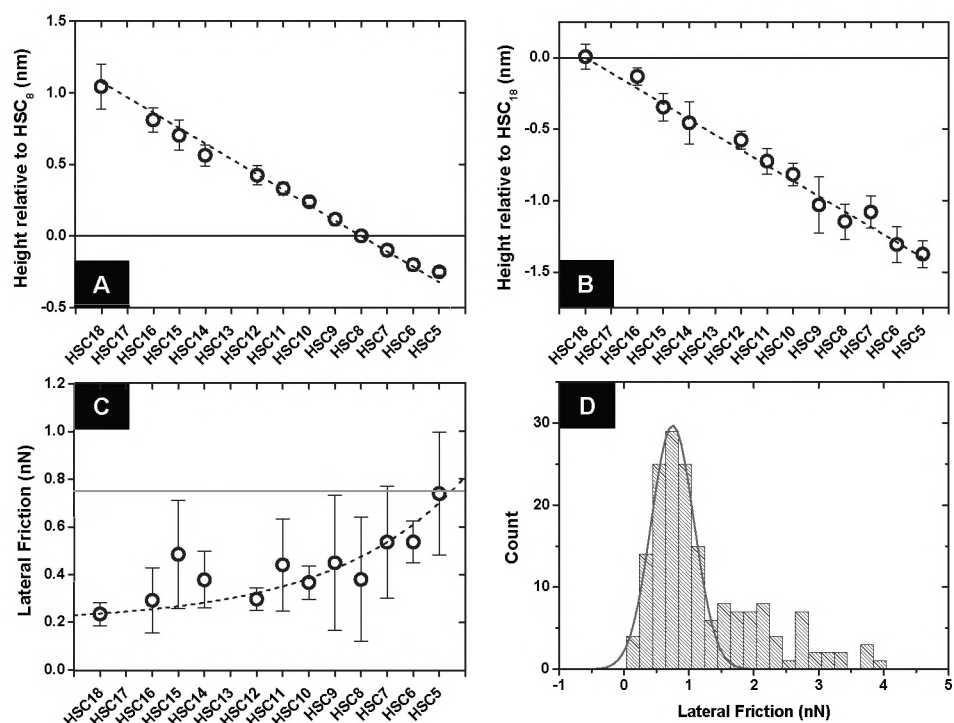


**Figure 3. Relation of the height and friction on thiol chain length**

(A) Plot of the heights of “positive” nanografted patches (HSC<sub>18</sub> to HSC<sub>5</sub>) grafted into a SAM matrix of HSC<sub>8</sub>; the dotted line represents the theoretically expected height values. (B) Plot of the heights of the “negative” nanografted patches (HSC<sub>18</sub> to HSC<sub>5</sub>) grafted into a matrix of HSC<sub>18</sub>. (C) Plot of the friction experienced by the tip while probing the methyl-terminated nanografted patches in a HSC<sub>8</sub> matrix. The dotted trendline illustrates the slight increase in friction upon a decrease in thiol chain length. The mean lateral friction of the HSC<sub>8</sub> matrix is represented by the blue line. (D) Histogram displaying the lateral friction of the SAM matrix (HSC<sub>8</sub>) for  $N = 200$  measurements in 2-butanol, measured at a normal force of 6 nN and a scan speed of  $\sim 4$   $\mu\text{m/s}$ . Fitting with a Gaussian (solid blue line) results in a mean lateral friction of  $0.75 \pm 0.33$  nN. Note that the values  $> 1.5$  nN probably represent cases in which measurement conditions were suboptimal, such as sample or tip contaminations. Number of samplings  $N \geq 10$ , all data  $\pm$  S.D.

height differences with respect to the matrix were found ranging from  $+1.04 \pm 0.16$  nm for the graft of HSC<sub>18</sub> to  $-0.25 \pm 0.03$  nm for the graft of HSC<sub>5</sub> (Figure 3A). To prove that these relative heights are independent of the surrounding SAM matrix, a control experiment was performed by constructing a series of negative nanografted patches, using the same thiols but now grafted into a HSC<sub>18</sub> SAM matrix. The measured relative height differences of these grafts with respect to the matrix ranged from  $+0.01 \pm 0.09$  nm for HSC<sub>18</sub> to  $-1.37 \pm 0.09$  nm for HSC<sub>5</sub> (Figure 3B). As expected, the relative height difference between the graft and the matrix varies linearly as a function of the length of the molecules for both the positive and negative grafts. The data points were fitted with the expected height differences, as calculated by our model (see Experimental Section) which assumes a tilt angle of  $30^\circ$  (Figure 3A, B), revealing a good agreement for both the positive and negative grafts ( $R^2 = 0.990$  and  $0.985$ , respectively). Alternatively, when the measured data were fitted to obtain the tilt angle, angles of  $35.3 \pm 1.3^\circ$  and  $31.2 \pm 1.8^\circ$  were found for the positive and negative nanografted patches, respectively. The slightly higher angle calculated for the positive grafts can be explained by collapsing (having a terminal gauche) of the long extending alkanethiols over the edges of the nanografted patch,<sup>41</sup> in particular those of thiols HSC<sub>14</sub> to HSC<sub>18</sub> (see Figure 3A). A fit excluding these molecules results in an angle of  $30.7 \pm 2.8^\circ$ , which indicates that our model, assuming a tilt angle of  $30^\circ$ , used to calculate the expected height values is correct. However, most importantly, it demonstrates the high accuracy by which nanografting can be used to determine the orientation of molecules in a SAM.

#### Friction of methyl-terminated thiols in a nanografted patch

In addition to the topography, the friction of the methyl-terminated nanografted patches and its relation to thiol chain length were investigated in 2-butanol (Figure 3C). Although no large differences in lateral force were measured for the different nanografted HSC<sub>*n*</sub> patches, a clear trend was observed (shown in Figure 3C, dotted trend line): grafts of shorter thiol molecules produce slightly higher friction values than the longer thiols (e.g.,  $0.24 \pm 0.05$  nN for HSC<sub>18</sub> and  $0.74 \pm 0.26$  nN for HSC<sub>5</sub>). This observation can be explained by the higher susceptibility of the grafts of shorter thiols to thermal excitation and pressure exerted by the tip.<sup>37,42</sup> In AFM friction studies performed under ambient conditions, it was found that the friction for HSC<sub>*n*</sub> molecules rapidly decreases till alkyl chains with a length of  $n=12$ , after which the friction only slightly decreases.<sup>42,43</sup> Furthermore, simulations show that gauche effects and kinks decrease in HSC<sub>*n*</sub> SAMs with increasing alkyl chain lengths at least up to a length of  $n=16$ .<sup>44,45</sup> An important factor is that SAMs of the shorter thiols exhibit a substantial disorder due to less van der Waals interactions, which contribute  $4\text{--}8$  kJ mol<sup>-1</sup> per methylene group to the overall stabilization of the SAM,<sup>9,13,46</sup> between their hydrocarbon chains. This facilitates the presence of more SAM and molecular defects (e.g., domain boundaries, missing rows, kinks, and other distortions in the chains) and causes an increased friction probed by the tip that presses on the SAM.<sup>46</sup> However, from our data, it can be concluded that none of the nanografted patches have collapsed and all molecules retain their alignment at a  $\sim 30^\circ$  tilt with respect to the surface normal (Figure 3A, B). Thus, especially the higher amount of defects in the SAM in the shorter nanografted thiol patches is proposed to cause the higher friction.

In addition to the friction of the nanografted patches, also the friction caused by the HSC<sub>8</sub> and HSC<sub>18</sub> SAM matrices was analyzed. Figure 3D shows a histogram of the observed lateral friction of the HSC<sub>8</sub> matrix, measured over  $N=200$  samplings. The normal



distribution of the data was fitted with a Gaussian curve, which reveals an average friction of  $0.75 \pm 0.33$  nN. In an analogous manner, an average friction of  $0.62 \pm 0.28$  nN was found for the HSC<sub>18</sub> matrix (data not shown). These observed friction forces, which were determined at  $F_N \approx 6$  nN, correspond well with AFM data previously gathered by Houston et al.,<sup>47</sup> who found a friction of  $0.75 \pm 0.15$  nN for a HSC<sub>16</sub> SAM at 6 nN in 2-butanol. The observed spreading in data (Figure 3D) can be mainly attributed to local variations in the gold substrate and the SAM, but also to variation between AFM cantilevers, especially in the sharpness of the tip.

When the friction values of the nanografted patches, which vary from  $0.24 \pm 0.04$  nN (HSC<sub>18</sub>) to  $0.74 \pm 0.26$  nN (HSC<sub>5</sub>), are compared to those of the HSC<sub>8</sub> SAM matrix, they are systematically lower (Figure 3C). This observation indicates that the nanografted patches, in contrast to the matrix SAMs, have a smoother surface, which can be explained by the fact that the self-assembly of the graft thiols during the nanografting is spatially confined.<sup>20</sup> While grafting, the AFM tip uncovers the gold and allows the thiols present in solution to bind to the surface, a process that occurs  $\sim 10$  times faster than the formation of an ordinary SAM matrix.<sup>20</sup> Xu et al. hypothesized that the tip effectively acts as a guide that forces and preorganizes the thiols to be placed in a standing-up configuration.<sup>20</sup> In contrast, a matrix SAM in an unconstrained environment is formed slowly over a period of hours, allowing the thiols to first adsorb parallel to the surface before they align to the known favorable  $30^\circ$  orientation. This relatively slow equilibration process not only causes the SAM to have multiple domains in which the thiols adopt an inhomogeneous orientation at the domain boundaries,<sup>46</sup> but it also results in a larger amount of monolayer defects,<sup>20, 46</sup> which probably contribute to an increase in friction probed by the cantilever. Finally, the friction differences obtained between matrix and nanografted SAM demonstrate in another way the higher ordering of the SAM when it is spatially confined, as proposed by Xu et al.<sup>20</sup>

#### Odd–even effects on the friction of methyl-terminated thiols in a nanografted patch

In Figure 3C another phenomenon is visible: the friction for grafts of thiol molecules with an odd number of carbon atoms in their chains is slightly higher than that of grafts of thiols with one carbon atom more or less. This is a so-called odd–even effect,<sup>9, 48</sup> which is proposed to be visible in the friction as a result of the difference in orientation of the methyl endgroups. Although this odd–even effect is not very pronounced at the used load force of 6 nN, we were able to measure it, whereas Mikulski et al.<sup>48</sup> calculated that a significant odd–even effect would only be noticed at a much higher load force ( $F_N > 50$  nN). We assume that the high quality of our spatially confined SAMs, as well as the controlled liquid environment, contribute to exhibiting, for the first time, this odd–even effect of methyl-terminated alkanethiols in the friction. Furthermore, it demonstrates the high sensitivity of our method to detect such small differences at the molecular level.

#### Topography and friction of SAMs of thiols with functional endgroups

Besides the length and packing of the thiol molecules in a nanografted patch, the type of thiol endgroup (exposed to the tip) will have a profound effect on the tip–sample interaction.<sup>49</sup> In order to determine this effect, single  $500 \times 500$  nm<sup>2</sup> nanografted patches of thiols of the HSC<sub>n</sub>X-type, having a variety of functional endgroups ( $X = -CF_3$ ,  $-OH$ ,  $-SH$ ,  $-NH_2$ ,  $-COOH$ ), were investigated. Each experiment was performed under strictly controlled conditions, the only variable between the patches being the thiol molecule

grafted. In a  $\text{HSC}_8$  SAM matrix, the following molecules were grafted:  $\text{HSC}_9^{\text{F}}\text{CF}_3$ ,  $\text{HSC}_{11}\text{OH}$ ,  $\text{HSC}_8\text{SH}$ ,  $\text{HSC}_{11}\text{NH}_2$ , and  $\text{HSC}_{11}\text{COOH}$  (Table 1). After imaging, the data from a series of measurements ( $N \geq 10$ ) were analyzed to obtain the height difference and friction (Figure 4).

### SAMs of fluorocarbon thiols

For the graft of  $\text{HSC}_9^{\text{F}}\text{CF}_3$  molecules (Figure 4A), a height difference of  $+0.37 \pm 0.07$  nm with respect to the matrix was found (Figure 4F), which is in good agreement with the calculated height difference of +0.39 nm. However, it has to be remarked that  $\text{HSC}_9^{\text{F}}\text{CF}_3$  has not only a  $\text{CF}_3$ -endgroup but also seven fluorinated carbon atoms extra in its chain ( $\text{HS}-(\text{CH}_2)_2-(\text{CF}_2)_7-\text{CF}_3$ ), which influences its SAM formation. A SAM from the fluorocarbon  $\text{HSC}_9^{\text{F}}\text{CF}_3$  is different at some points (crystal structure  $c(7 \times 7)$ , lattice constant  $\sim 0.59$  nm, and chain tilt  $16^\circ$ )<sup>50-52</sup> from its hydrocarbon counterpart with the same length,  $\text{HSC}_9\text{CH}_3$  (crystal structure  $(\sqrt{3} \times \sqrt{3})R30^\circ$ , lattice constant  $\sim 0.50$  nm, and chain tilt  $30^\circ$ ). Nevertheless, the lateral friction of  $0.35 \pm 0.05$  nN (Figure 4G) found for the patch of  $\text{HSC}_9^{\text{F}}\text{CF}_3$  is similar to that of  $\text{HSC}_{10}$  ( $0.37 \pm 0.07$  nN). This is a remarkable finding, since in friction studies comparing thiols of the type  $\text{HSC}_n\text{CF}_3$ , a molecule with

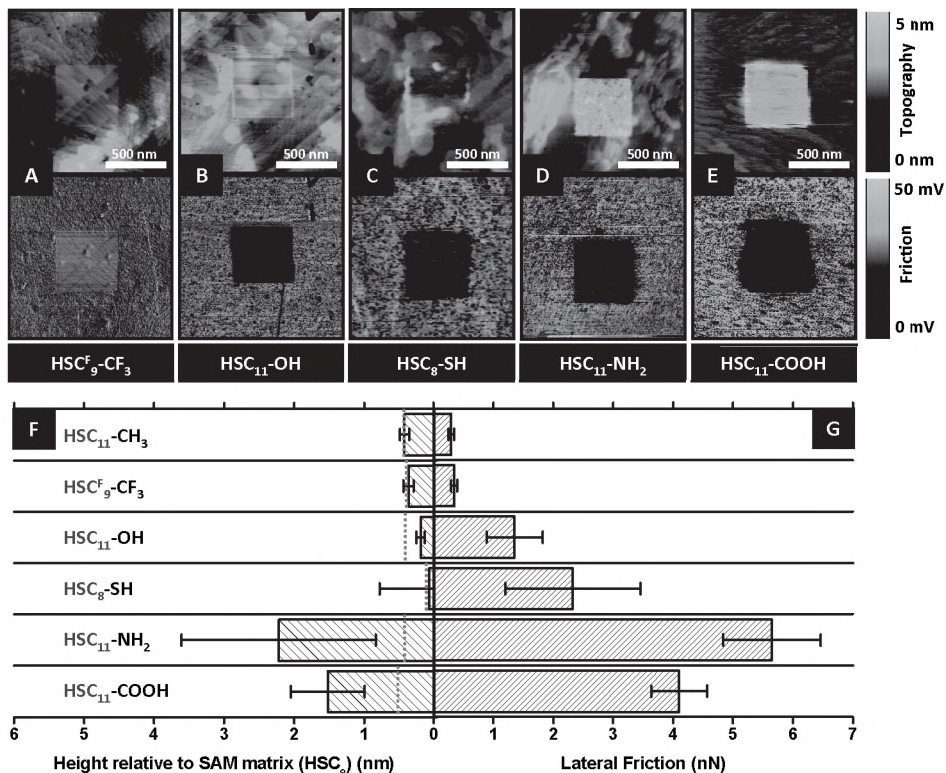


**Figure 4. Nanografting functionalized alkanethiols**

AFM topography (top row) and friction images (retrace, bottom row) of nanografted patches with thiols with various endgroups (A)  $\text{HSC}_9^{\text{F}}\text{CF}_3$ , (B)  $\text{HSC}_{11}\text{OH}$ , (C)  $\text{HSC}_8\text{SH}$ , (D)  $\text{HSC}_{11}\text{NH}_2$  and (E)  $\text{HSC}_{11}\text{COOH}$ . All images were recorded in a 2-butanol supernatant solution, with a normal load force of  $\sim 6$  nN and at a scan speed of  $\sim 4$   $\mu\text{m/s}$ . (F) Relative heights, expected height (based on  $30^\circ$  tilt) indicated by blue dotted line, and (G) corresponding lateral friction values of the different nanografted patches, displayed in bar diagrams. All data are  $\pm$  S.D. ( $N \geq 10$ ).

only one fluorinated carbon atom in its endgroup, and  $\text{HSC}_n\text{CH}_3$  it was found that the friction is higher for the  $\text{HSC}_n\text{CF}_3$ -type.<sup>33, 47, 53</sup> For example, Houston et al.<sup>47</sup> found a 3–4× higher friction for  $\text{HSC}_{15}\text{CF}_3$  than for  $\text{HSC}_{15}\text{CH}_3$ . This observation is, however, explainable: from studies on  $\text{HSC}_n\text{CF}_3$  SAMs, it is known that they display similar lattice constants and structures as their hydrocarbon counterparts of the  $\text{HSC}_n\text{CH}_3$  type.<sup>33, 52</sup> Nonetheless, thiols of the  $\text{HSC}_n\text{CF}_3$ -type have larger  $\text{CF}_3$ -endgroups than their counterparts (0.57 nm for  $\text{CF}_3$  versus 0.42 nm for  $\text{CH}_3$ )<sup>52</sup> which will presumably cause discontinuities in the packing of the thiol molecules within the monolayer. We therefore assume that for our measurements the  $\text{HSC}_9\text{CF}_3$  molecules within their patch are similarly well-packed as  $\text{HSC}_{10}$  molecules, resulting in similar observed friction values, in contrast to the studies on molecules with solely a  $\text{CF}_3$ -endgroup. However, in comparing these results, one should also consider differences in adhesion between tip and molecules due to difference in surface dipole effects,<sup>52</sup> which at this stage leaves a direct comparison between our results and those of Houston et al.<sup>47</sup> unresolved.

### SAMs of hydroxyl-terminated thiols

The relative height difference between the nanografted  $\text{HSC}_{11}\text{OH}$  patches (Figure 4B) and the  $\text{HSC}_8$  SAM matrix was determined to be  $+0.19 \pm 0.05$  nm. This value is significantly lower than the expected value of +0.42 nm according to our calculations, which would indicate that the tilt angle of the thiol with the surface normal is higher than the assumed  $30^\circ$ , or collapsing of the thiols on the edges. To further study this behavior and to see if it is dependent on the load force or the length of the thiol, different molecules of the  $\text{HSC}_n\text{OH}$  type (with  $n=6, 9, 11$ ) were studied. These molecules were grafted into either a  $\text{HSC}_8$  or a  $\text{HSC}_{18}$  SAM matrix, and the grafts were subsequently imaged in a load force regime of 3–12 nN. The observed height differences are summarized in Table 2. By calculating the tilt angle that would correspond to the observed height differences, it turned out that in both SAM matrices the two shorter thiols ( $\text{HSC}_6\text{OH}$  and  $\text{HSC}_9\text{OH}$ ) would be tilted more than the  $\text{HSC}_{11}\text{OH}$  molecules. This phenomenon had been observed before by Castronovo et al.,<sup>17</sup> who described how hydroxyl-terminated thiols in a nanografted patch could be easily compressed and forced under certain angles with respect to the surface normal. Tilt angles of  $43^\circ$  and  $59^\circ$  were found, which is in line with a carbon chain-interlocking model, which roughly describes the quantized tilting of hydrocarbon chains in steps of  $\sim 15^\circ$ .<sup>54, 55</sup> For our nanografted patches, tilt angles of  $53$ – $60^\circ$  were calculated for the shorter thiols  $\text{HSC}_6\text{OH}$  and  $\text{HSC}_9\text{OH}$ , for loads from 3 to 12 nN (see Table 2). Furthermore, we calculated a tilt angle of  $\sim 44^\circ$  for  $\text{HSC}_{11}\text{OH}$  thiols in nanografted patches in a  $\text{HSC}_8$  SAM matrix and of  $\sim 29^\circ$  in a  $\text{HSC}_{18}$  SAM matrix, which in the latter case means that the thiols in the grafts are aligned with the matrix molecules and indicates that the surrounding matrix can support the molecules in the grafts. The

**Table 2. Observed height differences and corresponding tilt angles for nanografted patches of OH-terminated alkanethiols**

Type of nanografted patches	Relative height (nm)	Calculated tilt angle ( $^\circ$ )
$\text{HSC}_6\text{OH}$ in $\text{HSC}_8$	$-0.45 \pm 0.12$	$58.31 \pm 8.13$
$\text{HSC}_9\text{OH}$ in $\text{HSC}_8$	$-0.29 \pm 0.08$	$59.80 \pm 4.01$
$\text{HSC}_{11}\text{OH}$ in $\text{HSC}_8$	$+0.19 \pm 0.15$	$43.82 \pm 7.98$
$\text{HSC}_6\text{OH}$ in $\text{HSC}_{18}$	$-1.46 \pm 0.13$	$53.08 \pm 9.63$
$\text{HSC}_9\text{OH}$ in $\text{HSC}_{18}$	$-1.31 \pm 0.14$	$56.95 \pm 7.09$
$\text{HSC}_{11}\text{OH}$ in $\text{HSC}_{18}$	$-0.71 \pm 0.16$	$29.44 \pm 11.11$

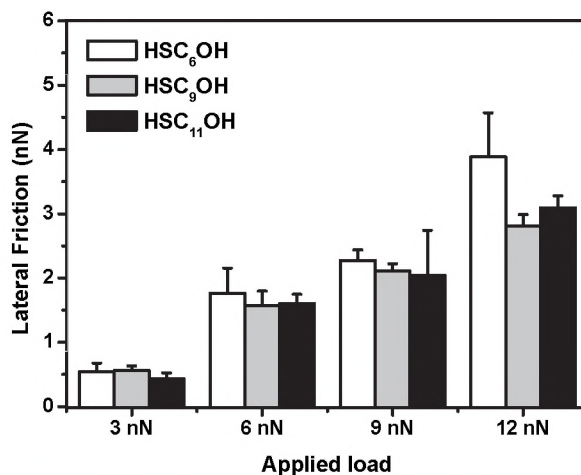


**Figure 5. Friction of nanografted patches of OH-terminated alkanethiols**

Lateral friction experienced by the AFM tip of nanografted patches of hydroxyl-terminated alkanethiols (HSC<sub>*n*</sub>OH) with different chain lengths ( $n = 6, 9, 12$ ), measured at varying applied load forces of 3–12 nN in 2-butanol and with scan speed of  $\sim 4 \mu\text{m/s}$ . Data have been collected on nanografted patches in both a HSC<sub>8</sub> and HSC<sub>18</sub> SAM matrix. All data are  $\pm$  S.D. ( $N \geq 20$ ).

HSC<sub>11</sub>OH thiols nanografted in the HSC<sub>8</sub> matrix molecules stick out above the matrix, so instead of having only a different tilt they can also have collapsed over the edges.<sup>41</sup>

Also the lateral friction of the nanografted patches of the hydroxyl-terminated thiols was measured at different load forces of 3–12 nN and in the two matrix SAMs (Figure 5). At increasing load force, for all nanografted patches, an approximate linear increase in lateral friction was observed, which is, as expected, independent of the SAM matrix (data not shown). Typically, at a load of 6 nN, the friction values measured for the grafts are about 3 times higher than those measured for grafts of thiols with methyl endgroups. In analogy with the trend observed for nanografted patches of methyl-terminated thiols, the friction increases slightly with decreasing thiol length. In line with earlier observations, we propose that the higher compressibility and decrease in packing of the SAM, induced by, for example, endgroup size and electrostatic interactions between the endgroups, is an important cause for the 3× higher friction.

#### SAMs of dithiols

The nanografted patch of dithiol HSC<sub>8</sub>SH (Figure 4C) exhibits a relative height difference of  $+0.13 \pm 0.65 \text{ nm}$  with respect to the matrix, which at first glance corresponds well with the theoretical height difference of  $+0.15 \text{ nm}$ . However, the large variation in the measurement indicates a decreased smoothness when compared to that of the earlier described nanografted patches. Explanations for this relative roughness might be the connection of two or more HSC<sub>8</sub>SH molecules through intermolecular S–S bonds,<sup>56, 57</sup> and the binding of both thiol groups of the same molecule to the gold surface.<sup>57</sup> As a consequence, the friction value of the HSC<sub>8</sub>SH graft ( $2.32 \pm 1.13 \text{ nN}$ , Figure 4G) is 5× higher than that observed for HSC<sub>9</sub>. In addition, throughout the graft, the friction is not fully uniform, which also corroborates the previously mentioned disorders in the patch.

### SAMs of amine- and acid-terminated thiols

Finally, the characteristics of nanografted patches containing amine- and acid-terminated alkanethiols were determined (Figure 4D, E). Height differences of  $+2.22 \pm 1.39$  and  $+1.52 \pm 0.53$  nm were measured between the HSC<sub>8</sub> matrix and the HSC<sub>11</sub>NH<sub>2</sub> and HSC<sub>11</sub>COOH grafts, respectively. These height differences are much larger than expected because calculations predicted values of only  $+0.42$  and  $+0.52$  nm for HSC<sub>11</sub>NH<sub>2</sub> and HSC<sub>11</sub>COOH, respectively. A plausible explanation for this observation can be the occurrence of bilayer formation via intermolecular hydrogen bonding between the amine or carboxylic acid groups, as has also been observed by Wang et al.<sup>58</sup> These findings will be described and discussed in more detail elsewhere.<sup>59</sup> The measured lateral forces of  $5.65 \pm 0.81$  nN for the graft of HSC<sub>11</sub>NH<sub>2</sub> and  $4.10 \pm 0.47$  nN for the graft of HSC<sub>11</sub>COOH both show a huge increase (19-fold and 14-fold, respectively) in friction compared to that of the graft of methyl-terminated thiols with a similar length (HSC<sub>12</sub>). It is assumed that this increase in friction cannot solely be attributed to the difference in endgroup but is mainly caused by the formation of the bilayer structure. We propose that the second layer, connected to the underlying layer via hydrogen bonds, is less resistant to pressure exerted by the tip and has more defects.

### Concluding remarks on nanografted functional alkanethiols

In conclusion, the friction values of the nanografted patches composed of thiols with functional endgroups are higher than those of grafts of methyl-terminated thiols. Considering the similarity of the thiol alkyl chain backbones of the different thiols, the differences in friction might be attributed to the size of the endgroup as well as to interactions between the endgroups, for example, hydrogen bonds, and their impact on intermolecular packing of the thiols. Obviously, these parameters are not independent, and at this stage we cannot discriminate properly between the different factors that contribute to the overall friction. In particular, the case of HSC<sub>9</sub>CF<sub>3</sub> illustrates the effect of chain packing on the friction. If this packing is suboptimal, like in the case of fluoro/hydrocarbon chains, the friction increases. Furthermore, for thiols with functionalized endgroups, there is probably also an effect induced by interactions between endgroups and AFM tip (e.g., hydrophobic/hydrophilic) or by specific interactions between the endgroup and the solvent. The latter factor is of course very important, because it can, for example, be expected that a relatively polar solvent such as 2-butanol will interact more favorably with polar thiol endgroups than an apolar solvent, and this difference might have a profound effect on the friction properties of a monolayer. Therefore, although we expect that the friction tool can also be successfully applied to differentiate between nanografted patches of different thiols in other solvents, each of these systems must be investigated separately in order to establish their specific friction characteristics.

### Recognition of the functional endgroups in multigrfts

The ability to recognize grafts of functionalized alkanethiols by their topographical and frictional “signatures”, opens the possibility to use AFM as a true surface identification tool. To investigate this, a set of grafts, each of which contains thiols with a different endgroup, was created within the same HSC<sub>8</sub> SAM matrix. Figure 6A shows an AFM image of such a multigrft with nanografted patches of HSC<sub>11</sub>NH<sub>2</sub>, HSC<sub>11</sub>OH, and HSC<sub>18</sub> thiols. It was constructed by rinsing the sample *in situ* after creating each nanografted patch. Subsequently, the nanografting procedure was repeated at a different spot at the sample with a supernatant solution containing a different thiol. Height differences

with respect to the matrix of  $+1.09 \pm 0.19$ ,  $+0.22 \pm 0.05$ , and  $+2.53 \pm 0.32$  nm were measured for the nanografted patches of HSC<sub>18</sub>, HSC<sub>11</sub>-OH, and HSC<sub>11</sub>-NH<sub>2</sub>, respectively. These values are similar to those determined earlier for the single nanografted patches. However, more interestingly, the corresponding friction image (Figure 6C) clearly reveals a different friction “signature” for each of the nanografted patches. Values of  $0.6 \pm 0.2$ ,  $2.1 \pm 0.5$  and  $8.0 \pm 1.3$  nN were obtained for the grafts of HSC<sub>18</sub>, HSC<sub>11</sub>-OH, and HSC<sub>11</sub>-NH<sub>2</sub>, respectively (Figure 6D). These results nicely demonstrate that the frictional “signatures” of the nanografted patches (ratio 1:3:14) constitute a useful source of identification.

By comparing the multigrift with the single nanograft experiments, it can be safely concluded that in both cases the observed lateral friction differences are caused by inherent differences in graft properties, which are directly related to their molecular structure and not by experimental variables between individual measurements. However, more interestingly, it is clear that with the described method nanografted patches of thiols with different endgroups can be specifically recognized by probing their friction.

## Conclusions

From a series of well-defined nanografted patches of methyl-terminated alkanethiols with various lengths, height differences of single carbon atoms were observed, implying a sub-nanometer precision in height. The measurements further revealed that in both positive and negative nanografted patches the thiols are oriented in an *all-trans* configuration under an angle of 30° with respect to the surface normal, which extends

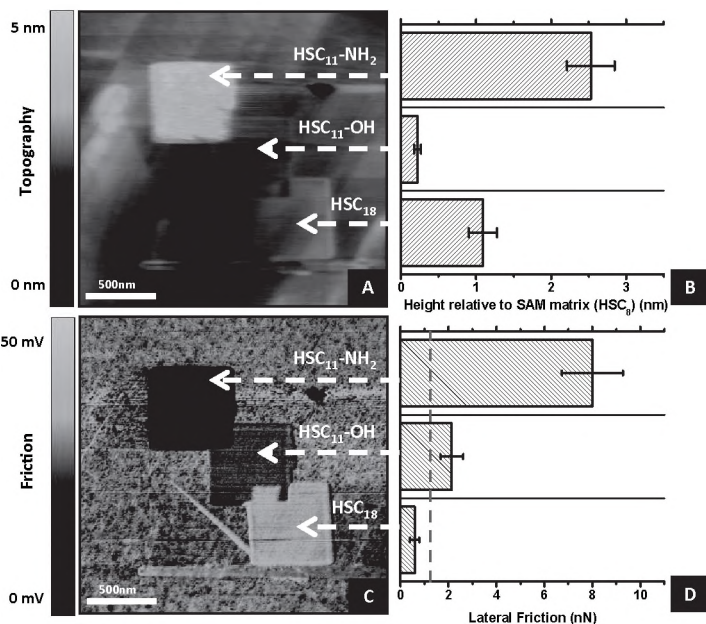


**Figure 6.** Multigrift of HSC<sub>18</sub>, HSC<sub>11</sub>-OH, and HSC<sub>11</sub>-NH<sub>2</sub>

(A) AFM topography image of a multigrift of HSC<sub>18</sub>, HSC<sub>11</sub>-OH, and HSC<sub>11</sub>-NH<sub>2</sub> (in creation order) recorded at load force of  $\sim 8.5$  nN and scan speed of  $\sim 4$   $\mu\text{m/s}$  in 2-butanol. (B) Observed heights of the nanografted patches relative to the HSC<sub>8</sub> SAM matrix. (C) Corresponding friction (retrace) image showing the different friction signatures of the grafts of  $-\text{CH}_3$ ,  $-\text{OH}$ , and  $-\text{NH}_2$  terminated thiols ( $N = 10$ ). (D) Average lateral friction values of the nanografted patches. The friction of the SAM matrix is indicated by the blue dashed line ( $1.21 \pm 0.14$  nN). All data are  $\pm$  S.D.

on results of earlier studies. Quantitative lateral force measurements showed that the friction of the nanografted patches was always lower than that of the surrounding matrix SAM. This effect can be attributed to the spatially confined self-assembly process during nanografting described by Xu et al.<sup>20</sup> and is clear evidence of the fact that the topographical roughness is directly correlated to this process. Furthermore, the friction of the nanografted patches decreased with increasing thiol length, which is mainly attributed to differences in packing of hydrocarbon chains. The ability to probe a subtle odd–even effect on the friction highlights the sensitivity of the method for detecting differences in molecular packing within a monolayer on the sub-nanometer scale.

The same techniques were applied to analyze SAMs of thiols with a variety of functional endgroups. While the topographies of the nanografted patches composed of thiols with  $-\text{CF}_3$  and  $-\text{SH}$  endgroups were as expected, the grafts of thiols with  $-\text{OH}$  endgroups appeared to be compressed, with the thiol molecules tilted under angles of  $\sim 43^\circ$  and  $\sim 59^\circ$ , depending on their chain length. This SAM compression is explained by hydroxyl endgroup induced surface tension and weaker van der Waals interactions, resulting in an increase in disorder in the packing of the molecules in the nanografted patches. Strong indications were found for the formation, via hydrogen bonding interactions, of bilayers in the nanografted patches constructed of thiols with  $-\text{NH}_2$  and  $-\text{COOH}$  endgroups. For each of the nanografted patches, highly characteristic friction values were found, which increase for thiols with endgroup  $\text{CH}_3 \leq \text{CF}_3 < \text{OH} \leq \text{SH} < \text{COOH} \leq \text{NH}_2$ . This has opened the possibility of using the lateral friction as a unique recognition tool to identify the building blocks of a nanografted patch, which was confirmed by the fact that multiple nanografted patches of thiols with different endgroups in the same matrix SAM could be accurately assigned by their specific friction characteristics.

## Acknowledgements

J.t.r. is supported by NanoNed, the Dutch nanotechnology programme of the Ministry of Economic Affairs. A.C. is supported by a VENI grant (916.66.028) of The Netherlands Organization for Scientific Research (NWO). J.A.A.W.E. thanks the Council for the Chemical Sciences of The Netherlands Organization for Scientific Research (CW-NWO) for a VIDI grant. C.G.F. is supported by a BIO-LIGHT-TOUCH grant (FP6-2004-NEST-C-1-028781) and Immunomap grant (MRTN-CT-2006-035946) of the European Union. Arend M. van Buul is acknowledged for kindly providing us with 11-amino-1-undecanethiol.

## References

1. A. N. Broers (1981). Resolution Limits of PMMA Resist for Exposure with 50 Kv Electrons. *J. Electrochem. Soc.*, **128**, 166-170.
2. W. A. Bryant (1977). Fundamentals of Chemical Vapor-Deposition. *J. Mater. Sci.*, **12**, 1285-1306.
3. R. D. Piner, J. Zhu, F. Xu, S. H. Hong, C. A. Mirkin (1999). "Dip-pen" nanolithography. *Science*, **283**, 661-663.
4. K. Salaita, Y. H. Wang, C. A. Mirkin (2007). Applications of dip-pen nanolithography. *Nat. Nanotechnol.*, **2**, 145-155.
5. J. J. Shi, J. X. Chen, P. S. Cremer (2008). Sub-100 nm Patterning of supported bilayers by nanoshaving lithography. *J. Am. Chem. Soc.*, **130**, 2718-2719.
6. S. Xu, G. Y. Liu (1997). Nanometer-scale fabrication by simultaneous nanoshaving and molecular self-assembly. *Langmuir*, **13**, 127-129.
7. G. Binnig, C. F. Quate, C. Gerber (1986). Atomic force microscope. *Phys. Rev. Lett.*, **56**, 930-933.
8. R. G. Nuzzo, D. L. Allara (1983). Adsorption of Bifunctional Organic Disulfides on Gold Surfaces. *J. Am. Chem. Soc.*, **105**, 4481-4483.
9. J. C. Love, L. A. Estroff, J. K. Kriebel, R. G. Nuzzo, G. M. Whitesides (2005). Self-assembled monolayers of thiolates on metals as a form of nanotechnology. *Chem. Rev.*, **105**, 1103-1169.
10. R. K. Smith, P. A. Lewis, P. S. Weiss (2004). Patterning self-assembled monolayers. *Prog. Surf. Sci.*, **75**, 1-68.
11. P. Fenter, A. Eberhardt, P. Eisenberger (1994). Self-Assembly of N-Alkyl Thiols as Disulfides on Au(111). *Science*, **266**, 1216-1218.

12. **N. Camillone, C. E. D. Chidsey, G. Y. Liu, G. Scoles** (1993). Superlattice Structure at the Surface of a Monolayer of Octadecanethiol Self-Assembled on Au(111). *J. Chem. Phys.*, **98**, 3503-3511.
13. **L. H. Dubois, R. G. Nuzzo** (1992). Synthesis, Structure, and Properties of Model Organic-Surfaces. *Annu. Rev. Phys. Chem.*, **43**, 437-463.
14. **M. D. Porter, T. B. Bright, D. L. Allara, C. E. D. Chidsey** (1987). Spontaneously Organized Molecular Assemblies .4. Structural Characterization of Normal-Alkyl Thiol Monolayers on Gold by Optical Ellipsometry, Infrared-Spectroscopy, and Electrochemistry. *J. Am. Chem. Soc.*, **109**, 3559-3568.
15. **G. E. Poirier, E. D. Pylant** (1996). The self-assembly mechanism of alkanethiols on Au(111). *Science*, **272**, 1145-1148.
16. **G. E. Poirier, M. J. Tarlov** (1994). The c(4x2) Superlattice of N-Alkanethiol Monolayers Self-Assembled on Au(111). *Langmuir*, **10**, 2853-2856.
17. **M. Castronovo, F. Bano, S. Raugai, D. Scaini, M. Dell'Angela, R. Hudej, L. Casalis, G. Scoles** (2007). Mechanical stabilization effect of water on a membrane-like system. *J. Am. Chem. Soc.*, **129**, 2636-2641.
18. **J. Liang, G. Scoles** (2007). Nanografting of alkanethiols by tapping mode atomic force microscopy. *Langmuir*, **23**, 6142-6147.
19. **M. Liu, N. A. Amro, G. Y. Liu** (2008). Nanografting for Surface Physical Chemistry. *Annu. Rev. Phys. Chem.*, **59**, 367-386.
20. **S. Xu, P. E. Laibinis, G. Y. Liu** (1998). Accelerating the kinetics of thiol self-assembly on gold - A spatial confinement effect. *J. Am. Chem. Soc.*, **120**, 9356-9361.
21. **J. J. Yu, Y. H. Tan, X. Li, P. K. Kuo, G. Y. Liu** (2006). A nanoengineering approach to regulate the lateral heterogeneity of self-assembled monolayers. *J. Am. Chem. Soc.*, **128**, 11574-11581.
22. **A. Ivanisevic, K. V. McCumber, C. A. Mirkin** (2002). Site-directed exchange studies with combinatorial libraries of nanostructures. *J. Am. Chem. Soc.*, **124**, 11997-12001.
23. **M. Castronovo, S. Radovic, C. Grunwald, L. Casalis, M. Morgante, G. Scoles** (2008). Control of Steric Hindrance on Restriction Enzyme Reactions with Surface-Bound DNA Nanostructures. *Nano Lett.*, **8**, 4140-4145.
24. **S. W. Chung, A. D. Presley, S. Elhadj, S. Hok, S. S. Hah, A. A. Chernov, M. B. Francis, B. E. Eaton, D. L. Feldheim, J. J. Deyoreo** (2008). Scanning Probe-based Fabrication of 3D Nanostructures via Affinity Templates, Functional RNA, and Meniscus-mediated Surface Remodeling. *Scanning*, **30**, 159-171.
25. **E. Mirmontaz, M. Castronovo, C. Grunwald, F. Bano, D. Scaini, A. A. Ensafi, G. Scoles, L. Casalis** (2008). Quantitative Study of the Effect of Coverage on the Hybridization Efficiency of Surface-Bound DNA Nanostructures. *Nano Lett.*, **8**, 4134-4139.
26. **C. Staii, D. W. Wood, G. Scoles** (2008). Verification of Biochemical Activity for Proteins Nanografted on Gold Surfaces. *J. Am. Chem. Soc.*, **130**, 640-646.
27. **D. J. Zhou, X. Z. Wang, L. Birch, T. Rayment, C. Abell** (2003). AFM study on protein immobilization on charged surfaces at the nanoscale: Toward the fabrication of three-dimensional protein nanostructures. *Langmuir*, **19**, 10557-10562.
28. **J. C. Garno, Y. Y. Yang, N. A. Amro, S. Cruchon-Dupeyrat, S. W. Chen, G. Y. Liu** (2003). Precise positioning of nanoparticles on surfaces using scanning probe lithography. *Nano Lett.*, **3**, 389-395.
29. **J. F. Liu, S. Cruchon-Dupeyrat, J. C. Garno, J. Frommer, G. Y. Liu** (2002). Three-dimensional nanostructure construction via nanografting: Positive and negative pattern transfer. *Nano Lett.*, **2**, 937-940.
30. **G. J. Leggett, N. J. Brewer, K. S. L. Chong** (2005). Friction force microscopy: towards quantitative analysis of molecular organisation with nanometre spatial resolution. *Phys. Chem. Chem. Phys.*, **7**, 1107-1120.
31. **L. Y. Li, S. F. Chen, S. Y. Jiang** (2003). Nanoscale frictional properties of mixed alkanethiol self-assembled monolayers on Au(111) by scanning force microscopy: Humidity effect. *Langmuir*, **19**, 666-671.
32. **L. Shuang, P. Cao, R. Colorado, X. P. Yan, I. Wenzl, O. E. Shmakova, M. Graupe, T. R. Lee, S. S. Perry** (2005). Local packing environment strongly influences the frictional properties of mixed CH<sub>3</sub>- and CF<sub>3</sub>-terminated alkanethiol SAMs on Au(111). *Langmuir*, **21**, 933-936.
33. **H. I. Kim, T. Koini, T. R. Lee, S. S. Perry** (1997). Systematic studies of the frictional properties of fluorinated monolayers with atomic force microscopy: Comparison of CF<sub>3</sub>- and CH<sub>3</sub>-terminated films. *Langmuir*, **13**, 7192-7196.
34. **S. Cruchon-Dupeyrat, S. Porthun, G. Y. Liu** (2001). Nanofabrication using computer-assisted design and automated vector-scanning probe lithography. *Appl. Surf. Sci.*, **175**, 636-642.
35. **H. I. Kim, J. E. Houston** (2000). Separating mechanical and chemical contributions to molecular-level friction. *J. Am. Chem. Soc.*, **122**, 12045-12046.
36. **Y. H. Liu, T. Wu, D. F. Evans** (1994). Lateral Force Microscopy Study on the Shear Properties of Self-Assembled Monolayers of Dialkylammonium Surfactant on Mica. *Langmuir*, **10**, 2241-2245.
37. **X. D. Xiao, J. Hu, D. H. Charych, M. Salmeron** (1996). Chain length dependence of the frictional properties of alkylsilane molecules self-assembled on Mica studied by atomic force microscopy. *Langmuir*, **12**, 235-237.
38. **G. Oncins, S. Garcia-Manyes, F. Sanz** (2005). Study of frictional properties of a phospholipid bilayer in a liquid environment with lateral force microscopy as a function of NaCl concentration. *Langmuir*, **21**, 7373-7379.
39. **C. A. Lang, M. M. Dovek, J. Nogami, C. F. Quate** (1989). Au(111) Autoepitaxy Studied by Scanning Tunneling Microscopy. *Surf. Sci.*, **224**, L947-L955.
40. **S. Xu, S. Miller, P. E. Laibinis, G. Y. Liu** (1999). Fabrication of nanometer scale patterns within self-assembled monolayers by nanografting. *Langmuir*, **15**, 7244-7251.
41. **W. J. Price, P. K. Kuo, T. R. Lee, R. Colorado, Jr., Z. C. Ying, G. Y. Liu** (2005). Probing the local structure and mechanical response of nanostructures using force modulation and nanofabrication. *Langmuir*, **21**, 8422-8428.
42. **A. Lio, D. H. Charych, M. Salmeron** (1997). Comparative atomic force microscopy study of the chain length dependence of frictional properties of alkanethiols on gold and alkylsilanes on mica. *J. Phys. Chem. B*, **101**, 3800-3805.



43. **M. T. McDermott, J. B. D. Green, M. D. Porter** (1997). Scanning force microscopic exploration of the lubrication capabilities of n-alkanethiolate monolayers chemisorbed at gold Structural basis of microscopic friction and wear. *Langmuir*, **13**, 2504-2510.
44. **O. Alexiadis, V. A. Harmandaris, V. G. Mavrantzas, L. Delle Site** (2007). Atomistic simulation of alkanethiol self-assembled monolayers on different metal surfaces via a quantum, first-principles parametrization of the sulfur-metal interaction. *J. Phys. Chem. C*, **111**, 6380-6391.
45. **O. Alexiadis, K. C. Daoulas, V. G. Mavrantzas** (2008). An efficient Monte Carlo algorithm for the fast equilibration and atomistic simulation of alkanethiol self-assembled monolayers on a Au(111) substrate. *J. Phys. Chem. B*, **112**, 1198-1211.
46. **C. Vericat, M. E. Vela, R. C. Salvarezza** (2005). Self-assembled monolayers of alkanethiols on Au(111): surface structures, defects and dynamics. *Phys. Chem. Chem. Phys.*, **7**, 3258-3268.
47. **J. E. Houston, C. M. Doelling, T. K. Vanderlick, Y. Hu, G. Scoles, I. Wenzl, T. R. Lee** (2005). Comparative study of the adhesion, friction, and mechanical properties of CF<sub>3</sub>- and CH<sub>3</sub>-terminated alkanethiol monolayers. *Langmuir*, **21**, 3926-3932.
48. **P. T. Mikulski, L. A. Herman, J. A. Harrison** (2005). Odd and even model self-assembled monolayers: links between friction and structure. *Langmuir*, **21**, 12197-12206.
49. **S. Park, Y. W. Kim, J. C. Lim, H. S. Ahn, S. J. Park** (2003). Nano- and microscale friction behaviors of functionalized self-assembled monolayers. *J. Ind. Eng. Chem.*, **9**, 16-24.
50. **C. A. Alves, M. D. Porter** (1993). Atomic-Force Microscopic Characterization of a Fluorinated Alkanethiolate Monolayer at Gold and Correlations to Electrochemical and Infrared Reflection Spectroscopic Structural Descriptions. *Langmuir*, **9**, 3507-3512.
51. **E. Ostuni, R. G. Chapman, R. E. Holmlin, S. Takayama, G. M. Whitesides** (2001). A survey of structure-property relationships of surfaces that resist the adsorption of protein. *Langmuir*, **17**, 5605-5620.
52. **D. Barriet, T. R. Lee** (2003). Fluorinated self-assembled monolayers: composition, structure and interfacial properties. *Curr. Opin. Colloid Interface Sci.*, **8**, 236-242.
53. **H. I. Kim, M. Graupe, O. Oloba, T. Koini, S. Imaduddin, T. R. Lee, S. S. Perry** (1999). Molecularly specific studies of the frictional properties of monolayer films: A systematic comparison of CF<sub>3</sub>-, (CH<sub>3</sub>)<sub>2</sub>CH-, and CH<sub>3</sub>-terminated films. *Langmuir*, **15**, 3179-3185.
54. **E. Barrena, C. Ocal, M. Salmeron** (2000). Molecular packing changes of alkanethiols monolayers on Au(111) under applied pressure. *J. Chem. Phys.*, **113**, 2413-2418.
55. **E. Barrena, C. Ocal, M. Salmeron** (2001). Structure and stability of tilted-chain phases of alkanethiols on Au(111). *J. Chem. Phys.*, **114**, 4210-4214.
56. **J. Liang, L. G. Rosa, G. Scoles** (2007). Nanostructuring, Imaging and molecular manipulation of dithiol monolayers on au(111) surfaces by atomic force Microscopy. *J. Phys. Chem. C* **111**, 17275-17284.
57. **J. J. Yu, J. N. Ngunjiri, A. T. Kelley, J. C. Garno** (2008). Nanografting versus solution self-assembly of alpha,omega-alkanedithiols on Au(111) investigated by AFM. *Langmuir*, **24**, 11661-11668.
58. **H. Wang, S. F. Chen, L. Y. Li, S. Y. Jiang** (2005). Improved method for the preparation of carboxylic acid and amine terminated self-assembled monolayers of alkanethiolates. *Langmuir*, **21**, 2633-2636.
59. **J. te Riet** unpublished results. *unpublished results*.
60. **M. Hegner, P. Wagner, G. Semenza** (1993). Ultralarge Atomically Flat Template-Stripped Au Surfaces for Scanning Probe Microscopy. *Surf. Sci.*, **291**, 39-46.
61. **J. E. Sader, I. Larson, P. Mulvaney, L. R. White** (1995). Method for the Calibration of Atomic-Force Microscope Cantilevers. *Rev. Sci. Instrum.*, **66**, 3789-3798.
62. **J. L. Hutter, J. Bechhoefer** (1993). Calibration of Atomic-Force Microscope Tips. *Rev. Sci. Instrum.*, **64**, 1868-1873.
63. **J. E. Sader, J. W. M. Chon, P. Mulvaney** (1999). Calibration of rectangular atomic force microscope cantilevers. *Rev. Sci. Instrum.*, **70**, 3967-3969.
64. **B. Ohler** (2007). Cantilever spring constant calibration using laser Doppler vibrometry. *Rev. Sci. Instrum.*, **78**, 0637011-0637015.
65. **R. W. Stark, T. Drobek, W. M. Heckl** (2001). Thermomechanical noise of a free v-shaped cantilever for atomic-force microscopy. *Ultramicroscopy*, **86**, 207-215.
66. **A. Noy, C. D. Frisbie, L. F. Rozsnyai, M. S. Wrighton, C. M. Lieber** (1995). Chemical Force Microscopy - Exploiting Chemically-Modified Tips to Quantify Adhesion, Friction, and Functional-Group Distributions in Molecular Assemblies. *J. Am. Chem. Soc.*, **117**, 7943-7951.
67. **J. E. Sader** (1995). Parallel Beam Approximation for V-Shaped Atomic-Force Microscope Cantilevers. *Rev. Sci. Instrum.*, **66**, 4583-4587.
68. **J. E. Sader, R. C. Sader** (2003). Susceptibility of atomic force microscope cantilevers to lateral forces: Experimental verification. *Appl. Phys. Lett.*, **83**, 3195-3197.
69. **J. L. Hazel, V. V. Tsukruk** (1999). Spring constants of composite ceramic/gold cantilevers for scanning probe microscopy. *Thin Solid Films*, **339**, 249-257.
70. **W. Alexander, J. F. Shackelford** (2001). CRC Materials Science and Engineering Handbook (p.537). *CRC Handbooks*.
71. **E. Tocha, J. Song, H. Schönherr, G. J. Vancso** (2007). Calibration of friction force signals in atomic force microscopy in liquid media. *Langmuir*, **23**, 7078-7082.
72. **D. R. Lide** (2008-2009). Handbook of Chemistry and Physics. 89th Edition.

# CHAPTER 8

---

## **AFM topography and friction studies of hydrogen-bonded bilayers of functionalized alkanethiols**

*Joost te Riet, Tim Smit, Michiel J.J. Coenen,  
Jan W. Gerritsen, Alessandra Cambi,  
Johannes A.A.W. Elemans, Sylvia Speller, Carl G. Figdor*

*The secret to creativity is knowing  
how to hide your sources.*

*Albert Einstein*

Submitted for publication

**A**tomic Force Microscope (AFM) assisted nanografting was exploited to construct – in a liquid – well-defined nanoscale patches of amino- and carboxyl-terminated alkanethiols in a SAM matrix on an atomically flat gold (Au(111)) surface. By means of AFM the nanografted patches of these thiols were studied in detail by a combination of height and quantitative lateral friction measurements. The functionalized thiols form well-ordered self-assembled bilayers, with uniformly oriented and packed molecules, consisting of a first layer adsorbed to the gold surface via thiol-gold bonds, and a second layer stably bound to the first via COOH–HOOC or NH<sub>2</sub>–H<sub>2</sub>N intermolecular hydrogen bonds.

## Introduction

Amino- and carboxyl-terminated self-assembled monolayers (SAMs) represent ideal platforms for chemically and biologically functionalized surfaces, mainly because of their capability to react and/or interact with other chemical functional groups via covalent coupling, or via non-covalent hydrogen bonding and electrostatic interactions. From structural studies it is known that alkanethiols, including amino- and carboxyl-terminated ones, form SAMs on gold surfaces with their hydrocarbon chains oriented in an *all-trans* conformation with a lattice constant of  $\sim 5.0$  Å. They are predominantly organized in a  $(\sqrt{3} \times \sqrt{3})R30^\circ$ -based structure and a  $c(4 \times 2)$  superlattice in which the hydrocarbon chains are closely packed and tilted under an angle of  $\sim 30^\circ$  with respect to the surface normal.<sup>1-6</sup> However, many conflicting results have been reported for the characterization of highly ordered SAMs of carboxyl-terminated alkanethiols, in contrast to for example unfunctionalized thiols. In particular the proper experimental conditions for the construction of the functionalized SAMs continues to be an ongoing topic of debate.<sup>6-10</sup> In addition, in contact angle measurements different wettabilities of SAMs of amino- and carboxyl-terminated alkanethiols have been observed, indicating hydrophilic but also hydrophobic top surfaces.<sup>6,7</sup> Scanning tunneling microscopy (STM) and infrared spectroscopy measurements on dry carboxyl-terminated SAMs prepared from an ethanolic solution revealed a high degree of disorder in some cases. The quality of such SAMs strongly improved upon the addition of acetic acid,<sup>8,9</sup> occasionally with 10% water,<sup>11</sup> or with CF<sub>3</sub>COOH followed by a rinse of an NH<sub>4</sub>OH solution.<sup>7</sup> The observed disorder in the SAMs was partially attributed to the occurrence of intermolecular hydrogen bonding between the carboxyl-termini, which could occur as head-to-head dimers of molecules within the layer, as dimers with single molecules on top of the monolayer, or as linear chains of neighboring COOH-groups.<sup>7,8</sup>

SAM formation of NH<sub>2</sub>- and COOH-terminated alkanethiols can be studied by nanografting, a method in which nanosized structures are fabricated by using an AFM cantilever to create patterns on a surface.<sup>4,12</sup> During the nanografting procedure, patches of thiol molecules are locally ‘shaved’ away with an AFM tip from a SAM matrix on an ultraflat gold substrate (Fig. S1). The exposed gold patches are subsequently refilled with other thiol molecules from a supernatant solution, resulting in a nanografted patch. The same cantilever is used to graft and to image, thus all procedures are carried out *in situ* and under liquid. During the nanografting, the thiols self-assemble in a spatially confined environment, which strongly reduces the amount of disorder present in the resulting nanografted patch.<sup>13</sup> These highly ordered patches can subsequently serve as ideal samples to study the molecular packing and orientation of alkanethiols at the molecular level in a liquid environment.<sup>14</sup> By AFM topography imaging, the nanografted patches can be studied with quantitative atomic height resolution, with the matrix SAM and

atomic gold steps serving as internal calibration. In addition to the topography, probing the lateral friction of the nanografted patches by the AFM tip provides insight in the composition and specific chemical properties of the SAM.<sup>1, 12, 14-20</sup>

In this paper a novel approach to characterize layers of carboxyl- and amino-functionalized alkanethiols on gold will be presented. We combine nanografting and lateral friction measurements to investigate, in a quantitative fashion, the nature of nanografted patches of those alkanethiols in a liquid, and in particular reveal the effect of intermolecular hydrogen bonding on the formation of stable monolayer and bilayer structures.

## Materials & Methods

### Chemicals used and SAM preparation

All chemicals used (Table 1) were purchased from Sigma-Aldrich (St. Louis, MO) and used as received unless stated otherwise. Thiol solutions for SAM formation and grafting were prepared in >99.5% 2-butanol. The SAMs were prepared on an ultraflat patch of template-stripped gold, which was prepared according to the procedure described by Hegner et al.<sup>21</sup> In short, the procedure can be summarized in three steps: (i) First, a 0.25 cm<sup>2</sup> piece of mica coated with a 300 nm thick layer of gold (Georg Albert PVD-Beschichtungen, Heidelberg, Germany) was glued to a clean glass slide, with its gold side pointing downward, using a two-component epoxy glue (type 377, Epoxy Technology Inc., Waterloo, Belgium), leaving the mica side exposed to air. (ii) Subsequently, the sample was heated at 150 °C for 2 h, which activates the hardening process of the glue. (iii) Finally, the sample was submerged in a solution of tetrahydrofuran (THF) for 5 min, after which it can be stripped at the gold–mica interface, removing the mica. After stripping, the sample was immediately submerged in a freshly prepared solution of 5 mM of alkanethiol in 2-butanol. After incubation for >18 h in the thiol solution, the gold sample was washed with ethanol (99.8%) and dried with a gentle flow of nitrogen.

### Atomic Force Microscopy

Imaging and nanografting were performed using a MultiMode AFM with a Nanoscope IV controller (Veeco, Santa Barbara, CA, USA) equipped with an E-type piezo scanner (XY-range ~12 μm) and a liquid-cell (MTFML,

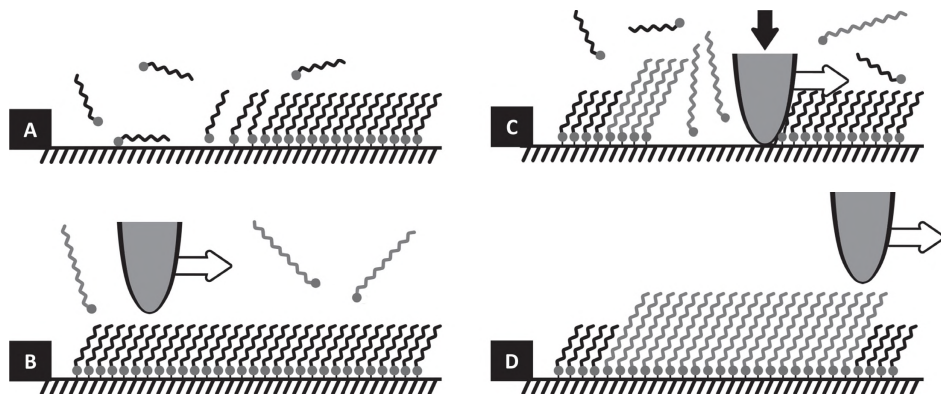


**Figure S1. Schematic representation of the nanografting procedure**

(A) A Au(111) sample is submerged in a 2-butanol solution of thiols (in this case HSC<sub>6</sub>) and after >18 h a uniform self-assembled monolayer (SAM) has formed. (B) The SAM under a supernatant solution is studied with AFM by scanning with a low contact force ( $F_N \approx 6$  nN). (C) By increasing the contact force to 120 nN and increasing the speed, patches of the SAM can be removed and exchanged by other thiol molecules from solution (in this case HSC<sub>14</sub>). (D) A nanografted patch has been formed within the matrix SAM, which can be imaged again at a low contact force. Now, features such as height difference between the patch and SAM or lateral force can be determined.

Veeco) holding the cantilever. The AFM system was calibrated by using a  $1 \times 1 \mu\text{m}^2$  (100 nm-deep) calibration grid. After calibration the sample was placed in the liquid-cell and subsequently submerged in a 50  $\mu\text{l}$  droplet of a 5 mM 2-butanolic solution of an alkanethiol. The whole sample and droplet were then enclosed by a fluorosilicate O-ring (FSFCO-10, Veeco). A laser beam was focused on the end point of a V-shaped  $\text{Si}_3\text{N}_4$  NP-S cantilever (Veeco; cantilever A on the NP-S chip, nominal spring constant 0.58 N/m), which had been cleaned by rinsing with chloroform and by irradiation with UV light (20 min). Moreover, directly prior to every experiment the cantilever was rinsed with ethanol (99.8%). The laser beam was deflected onto a four-quadrant photosensitive detector, the monitored vertical deflection was interpreted as the topography while the horizontal deflection, caused by the torsional deformation of the cantilever when its tip scans over the surface, was interpreted as the lateral friction force between tip and sample.

Imaging was performed in contact mode, under a low load force of  $F_N \approx 6 \text{ nN}$  ( $\sim 1 \text{ V}$  deflection set point) at 1 Hz ( $\sim 4 \mu\text{m s}^{-1}$  for a  $2 \times 2 \mu\text{m}^2$  image), these conditions were chosen to avoid compression and deformation of the monolayers.<sup>22</sup> The pressure that the tip then exerts is  $\sim 0.5 \text{ GPa}$ , as calculated by the Hertzian model<sup>23</sup> assuming a tip radius of 15 nm and a contact area of  $12 \text{ nm}^2$ . Nanoshaving of the SAM was performed at a high load force of  $F_N \approx 120 \text{ nN}$  ( $\sim 20 \text{ V}$ ) at 15 Hz ( $\sim 60 \mu\text{m s}^{-1}$ ), and the exerted pressure is  $\sim 10 \text{ GPa}$ .

Data and images were analyzed by using NanoScope 6.13 and Origin 8 software. The friction was determined from both trace and retrace of the lateral force images, these data were analyzed off-line by subtracting both channels (raw data) and divided by 2 for averaging, and subsequently converted into friction data (nN) using the method outlined below. For statistics, the height data were analyzed by taking consecutive cross sections (sampling over 20-50 lines) via step size determination on the edges of the nanografted patch on a single gold terrace within the software. Per image,  $N \geq 5$  of these samplings were performed. Subsequently, at least three images per nanografted patch were analyzed per experiment (up and down scans), and also at least three independent experiments in total (all with different cantilevers, to exclude the possibility that differences in friction are caused by differences in tip shape). The friction was determined only in the  $450 \times 450 \text{ nm}^2$  center region of the  $500 \times 500 \text{ nm}^2$  nanografted patches to eliminate edge effects. Furthermore, the friction was collected for the same amount and set of images as the topography analysis with a sampling of three on every image. In addition to the friction measurements of the nanografted patches in all experiments, the friction of the SAM matrix was determined in order to ascertain the quality and reliability of the measurements and, when necessary, to exclude measurements from further analysis. For all analyzed data, errors given are  $\pm \text{S.D.}$

### Quantifying the AFM data

V-shaped NP-S cantilevers (Veeco) were calibrated combining the Sader method<sup>24</sup> and the thermal oscillation method,<sup>25</sup> with some minor practical adaptations. In short, the vertical, torsional, and lateral spring constants of the V-shaped cantilever were determined by the following method. The vertical spring constant was determined by using the thermal tune software module of the NS V system (Veeco) by fitting the primary resonance peak with the simple harmonic oscillator model.<sup>26</sup> The system can process the data for resonances up to 100 kHz.<sup>27</sup> After a deflection sensitivity (from now designated as InvOLS; inverse optical lever sensitivity) calibration in air of the cantilever mounted in the setup ( $N = 5$ ), we used the Hutter and Bechhoefer method<sup>25</sup> - with the later described corrections for a V-shaped cantilever,<sup>27,28</sup> to determine the vertical spring constant. The torsional and physically related lateral spring constant for a V-shaped cantilever was calculated by using the parallel beam approach for a composite ceramic-gold cantilever.<sup>29-32</sup> The following formulas were used to calculate the lateral spring constant,

$$k_{\text{lat}} = \frac{4}{3\cos^2\theta + 6 \cdot (1 + \nu)\sin^2\theta} \left(\frac{L}{H}\right)^2 \cdot k_z$$

and the torsional spring constant,  $k_{\text{tors}} = k_{\text{lat}} H^2$

where  $\theta$  is the inner angle between the cantilever beam and the substrate,  $\nu$  is the Poisson ratio,  $L$  is the length of the cantilever,  $H$  is the height of the tip and  $k_z$  is the vertical spring constant. For the used NP-S cantilever (cantilever A of the chip), the (nominal) dimensions given by the manufacturer are  $\theta = 62^\circ$ ,  $\nu = 0.24$  (for  $\text{Si}_3\text{N}_4$ ),<sup>33</sup>  $L = 115 \mu\text{m}$ ,  $w = 25 \mu\text{m}$  (width),  $H = 3 \mu\text{m}$ ,  $\Delta L = 4 \mu\text{m}$  (tip set-back),  $t = 0.6 \mu\text{m}$  (thickness), and  $R = 10\text{--}20 \text{ nm}$  (tip radius). We determined an overall vertical spring constant of  $k_z = 252 \pm 19 \text{ pN/nm}$  ( $\pm \text{S.D.}$ ;  $N = 6$ ; all chips from one wafer) by the method described above (note the 57% difference with the manufacturers data). By using the formulas above, we calculated a lateral spring constant of  $k_{\text{lat}} = 159 \pm 20 \text{ N/m}$  and a torsional spring constant of  $k_{\text{tors}} = (2.06 \pm 0.15) \times 10^9 \text{ Nm/rad}$ . We determined a vertical InvOLS for the set-up in 2-butanol

(note: different from that in air<sup>34</sup>) of  $23.76 \pm 0.43$  nm/V ( $\pm$  S.D.) and a horizontal InvOLS of  $0.77 \pm 0.10$  nm/V ( $\pm$  S.D.), which leads to an overall conversion rate for the photodetector data (in volts) to the contact force (in newtons) of  $5.98 \pm 0.46$  nN/V and for the friction force of  $0.123 \pm 0.017$  nN/mV.

### Molecular model

The apparent height of the molecules in the SAM was calculated using data from literature;<sup>35</sup> bond lengths are 1.523 Å (C-C), 2.293 Å (S-Au), 1.815 Å (C-S), 1.338 Å (C-O), 1.208 Å (C=O), 1.438 Å (C-N) and the angle between the Au-S-C and C-C-C bonds in the alkyl backbone is in both cases 109.5°. The hydrogen bond between COOH-dimers is 3.72 Å (C-C distance) and 3.07 Å (N-N distance), as was found in literature and verified with DFT:B3LYP/3-21G calculations using the GAMESS<sup>36</sup> interface of ChemBio3D Ultra 11.0. With these data, the expected lengths of the alkanethiols were calculated using ChemBio3D Ultra 11.0. Subsequently, by taking into account a 30° tilt (if not stated otherwise) for the molecules,<sup>1,37</sup> the apparent height or thickness of the layer was calculated.

## Results and Discussion

Using the nanografting method,<sup>4</sup>  $500 \times 500$  nm<sup>2</sup> patches of 11-mercapto-1-undecanol (HSC<sub>11</sub>OH), 11-amino-1-undecanethiol (HSC<sub>11</sub>NH<sub>2</sub>), 11-mercapto-1-undecanoic acid (HSC<sub>10</sub>COOH) and 16-mercapto-1-hexadecanoic acid (HSC<sub>15</sub>COOH) were created from a 2-butanolic solution of the thiols in a matrix SAM of 1-octanethiol (HSC<sub>8</sub>) on an atomically flat Au(111) surface (see Table 1 for nomenclature). Each of these experiments was performed under strictly controlled conditions, the only variable between the patches being the thiol molecule grafted. HSC<sub>11</sub>OH, HSC<sub>11</sub>NH<sub>2</sub>, and HSC<sub>10</sub>COOH have a similar chain length and if they self-assemble at the expected ~30° tilt<sup>1</sup> with respect to the surface normal of the gold, the apparent height of their patches should be similar (Table 1). However, the topographies of the nanografted patches of HSC<sub>11</sub>NH<sub>2</sub> and HSC<sub>10</sub>COOH are clearly higher than that of the HSC<sub>8</sub> matrix (Fig. 1A-C (top panels)), whereas the nanografted patch of HSC<sub>11</sub>OH is just slightly higher (Fig. 1E). Remarkably, the patches of the NH<sub>2</sub>- and COOH-terminated alkanethiols are even 2.1× and 1.5× higher than expected. A different orientation of these thiols on the surface cannot explain this substantially higher apparent height. Interestingly, also the lateral friction of their nanografted patches appears to be 3-4× higher than that of the patch of HSC<sub>11</sub>OH (Fig. 1A-D, lower panels, Fig. 1F).

**Table 1. List of molecules that were used for the formation of SAMs and nanografted patches in our experiments**

Chemical name	Molecular formula	Abbreviated as	Molecular length at 30° tilt (nm)*
1-octanethiol	HS-(CH <sub>2</sub> ) <sub>7</sub> -CH <sub>3</sub>	HSC <sub>8</sub>	1.19
1-dodecanethiol	HS-(CH <sub>2</sub> ) <sub>11</sub> -CH <sub>3</sub>	HSC <sub>12</sub>	1.62
11-mercapto-1-undecanol	HS-(CH <sub>2</sub> ) <sub>11</sub> -OH	HSC <sub>11</sub> OH	1.61
11-amino-1-undecanethiol	HS-(CH <sub>2</sub> ) <sub>11</sub> -NH <sub>2</sub>	HSC <sub>11</sub> NH <sub>2</sub>	1.62
8-mercapto-1-octanoic acid	HS-(CH <sub>2</sub> ) <sub>7</sub> -COOH	HSC <sub>7</sub> COOH	1.28
11-mercapto-1-undecanoic acid	HS-(CH <sub>2</sub> ) <sub>10</sub> -COOH	HSC <sub>10</sub> COOH	1.58
12-mercapto-1-dodecanoic acid	HS-(CH <sub>2</sub> ) <sub>11</sub> -COOH	HSC <sub>11</sub> COOH	1.71
15-mercapto-1-pentadecanoic acid	HS-(CH <sub>2</sub> ) <sub>14</sub> -COOH	HSC <sub>14</sub> COOH	2.01
16-mercapto-1-hexadecanoic acid	HS-(CH <sub>2</sub> ) <sub>15</sub> -COOH	HSC <sub>15</sub> COOH	2.02
1-hexadecanoic acid	CH <sub>3</sub> -(CH <sub>2</sub> ) <sub>14</sub> -COOH	C <sub>15</sub> COOH	n/a
1-octadecanoic acid	CH <sub>3</sub> -(CH <sub>2</sub> ) <sub>16</sub> -COOH	C <sub>17</sub> COOH	n/a

\* The calculated lengths are those of alkanethiols bound on Au (111) along the surface normal, assuming a 30° tilt of the carbon chain with the surface normal, and including the S-Au binding distance of 0.23 nm.

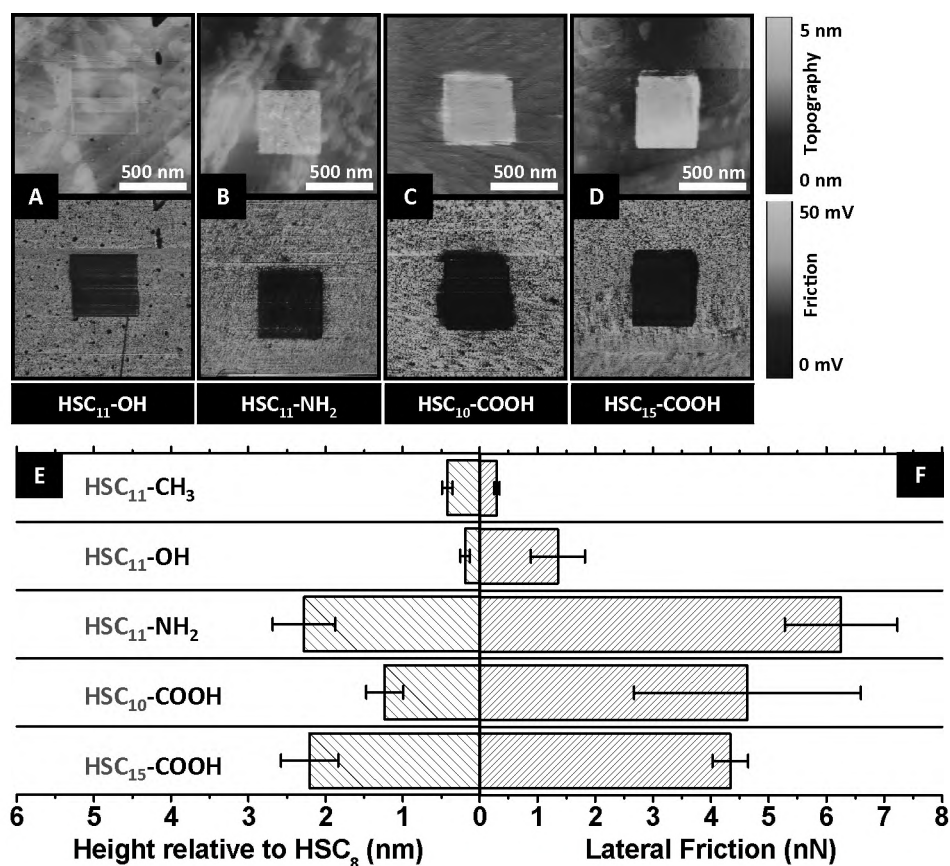


**Figure 1. AFM topography and friction images of nanografted patches**

AFM topography (top row) and friction images (retrace; bottom row) of nanografted patches of thiols with various endgroups in a matrix SAM of HSC<sub>8</sub>; (A) HSC<sub>11</sub>-OH, (B) HSC<sub>11</sub>-NH<sub>2</sub>, (C) HSC<sub>10</sub>-COOH, and (D) HSC<sub>15</sub>-COOH. All images were recorded in a 2-butanol supernatant solution, with a normal load force of  $\sim 6$  nN and at a scan speed of  $\sim 4$   $\mu\text{m/s}$ . (E) Relative heights and (F) corresponding lateral friction values of the different nanografts, displayed in bar diagrams. The friction of the HSC<sub>8</sub> matrix is  $0.75 \pm 0.33$  nN. Note that for the retrace friction images a darker color implies higher friction

As explanation for these observations, we propose the formation of bilayer structures in the case of patches of HSC<sub>11</sub>-NH<sub>2</sub> and HSC<sub>10</sub>-COOH via intermolecular hydrogen bonding between the amino or carboxylic acid headgroups of the layer of adsorbed thiols and thiols from solution. Bilayer formation readily can explain the higher appearance of the patches in the topography. Also the observed higher friction values are in line with such a model. As a result of the relatively weak link between the two layers, which is based on non-covalent hydrogen bonding interactions, it can be expected that the top layer is more dynamic than the bottom one, thereby exhibiting more packing defects and a lower stability upon exerting pressure by the scanning of the AFM tip. All these effects can contribute to a higher lateral friction.

To investigate the bilayer formation further, a series of HSC<sub>n</sub>-COOH alkanethiols ( $n=7,10,11,14,15$ ) was grafted. The relative heights of these nanografted patches (compared to HSC<sub>8</sub>) increases linearly with the length of the molecule (Fig. 2A). In

addition, the mean relative heights exactly match a model in which the first layer has a 30° tilt, and the second layer an extra ~30° tilt compared to the first layer. The result is a total tilt of ~60° for the second layer. Remarkably, this is an angle alkanethiols like to adopt according to the carbon chain-interlocking model (steps of ~15°).<sup>23</sup> Both types of thiols fit this model – those with an odd number of carbon atoms in their alkyl chain (HSC<sub>7</sub>COOH, HSC<sub>11</sub>COOH, HSC<sub>15</sub>COOH), where the COOH-group is in plane, as well as thiols with even numbers of carbon atoms in their chain (HSC<sub>10</sub>COOH, HSC<sub>14</sub>COOH), where the COOH-group is out of plane. However, the lateral friction clearly differs characteristically between the patches of the ‘odd’ and ‘even’ thiols (Fig. 2B). The friction on patches of the ‘even’ thiols is slightly higher than that on the odd ones. While for the former the measured variation in friction is 4–6× higher than for the latter. These observations indicate that bilayers of ‘even’ HSC<sub>n</sub>COOH-molecules are less stable than bilayers of their ‘odd’ analogues, which can be rationalized by the larger sterical hindering between neighboring molecules upon the formation of COOH—HOOC cyclic dimers in the case of the ‘even’ HSC<sub>n</sub>COOH-type thiols (Fig. 3A,B).

All of the HSC<sub>n</sub>COOH nanografted bilayer patches exhibit a ~3× higher friction than that of the monolayer patch of HSC<sub>11</sub>OH (Fig. 1F, 2B). It can be expected that the bottom layer SAM bound to the gold surface is closely packed, as has been described before,<sup>6</sup> consequently the large increase in friction can be mainly attributed to the presence of the second layer of HSC<sub>n</sub>COOH-molecules. This layer is expected to be dynamic and less well stabilized by Van der Waals interactions, as the first one, leading to imperfect packing. Further evidence for this greater instability is supplied by the slight increase in friction observed upon lengthening the alkyl chain of the HSC<sub>n</sub>COOH-molecules (Fig. 2B, dotted trendline), which in conventional SAMs of thiols would lead to a better monolayer packing and lower friction values.<sup>1, 38</sup>

To verify that the bilayer formation relies on COOH⋯HOOC and not on COOH⋯HS hydrogen bonding, nanografted patches were created of HSC<sub>10</sub>COOH and 9 equivalents of 1-hexadecanoic acid (C<sub>15</sub>COOH) or 1-octadecanoic acid (C<sub>17</sub>COOH) in 2-butanol. The

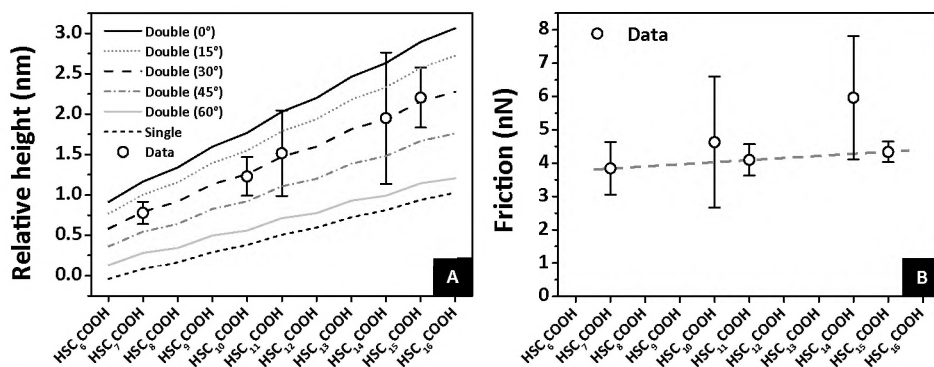


**Figure 2. Height and friction of different nanografted HSC<sub>n</sub>COOH patches**

(A) Relative height of nanografted patches of HSC<sub>n</sub>COOH ( $n = 7, 10, 11, 14, 15$ ) in an HSC<sub>8</sub> matrix. The different lines indicate the expected heights according to a single layer or a double layer model with different interlayer angles of 0°, 15°, 30°, 45° and 60°. (B) Corresponding lateral friction values of the nanografts. The trend line indicates the increase in friction observed for ‘odd’ HSC<sub>n</sub>COOH molecules.



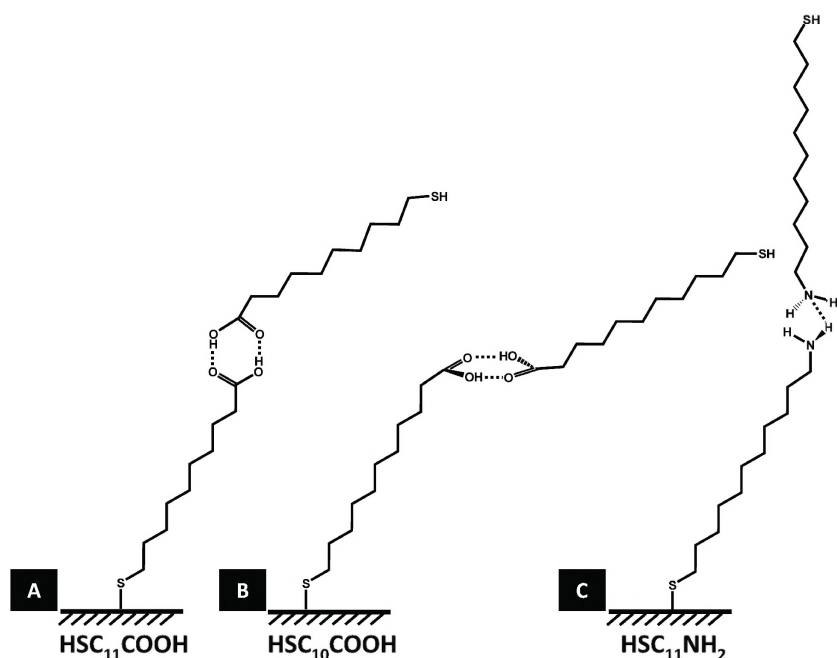


**Figure 3. Model of double layers**

Model of the formation of double layers stabilized by hydrogen bonds between the amine and carboxylic acid groups. (A) A double layer between two ‘odd’ HSC<sub>n</sub>COOH-thiols (in this case HSC<sub>11</sub>COOH), the COOH-group is out of plane. (B) A double layer between two ‘even’ HSC<sub>n</sub>COOH-thiols (in this case HSC<sub>10</sub>COOH), the COOH-group is in plane, and 90° rotated. (C) A double layer of HSC<sub>11</sub>NH<sub>2</sub> formed via a single hydrogen bond.

alkanoic acids cannot bind to gold, but they are still able to form strong hydrogen bonds with the SAM of HSC<sub>10</sub>COOH. The topographies of the resulting nanografted patches were slightly higher than those of the patches of the pure HSC<sub>10</sub>COOH thiols, and exactly matched a heterodimer bilayer of HSC<sub>10</sub>COOH⋯HOCC<sub>15</sub> and HSC<sub>10</sub>COOH⋯HOCC<sub>17</sub>, respectively, assuming the same angles as those of the homodimer bilayer (Fig. S2).

The relative height of  $2.28 \pm 0.40$  nm found for the nanografted patch of HSC<sub>11</sub>NH<sub>2</sub> (Fig. 1F) also suggests bilayer formation. In this case, fitting to our model suggests that the top layer of molecules is oriented at an angle of only  $\sim 2^\circ$  with respect to the surface normal, and  $-28^\circ$  with respect to the first layer (Fig. 3C). This different behavior in comparison to the HSC<sub>n</sub>COOH-molecules can be explained by a difference in hydrogen bonding strength and geometry. It is expected that the HSC<sub>11</sub>NH<sub>2</sub> molecules form single hydrogen bonds between their amino groups, which provides them with more degrees of freedom than the HSC<sub>n</sub>COOH-molecules and which results in an upright alignment. The weaker hydrogen bonds between the amino-functionalized thiols will probably lead to a more disordered top layer, which is directly reflected in the higher friction of the nanografted patch (Fig. 1F).

The observation that HSC<sub>11</sub>OH does not form similarly stable bilayers as the NH<sub>2</sub>- and COOH-terminated thiols is remarkable, also because O-H⋯O hydrogen bonds are generally stronger than N-H⋯N ones. This apparent inability to form interlayer hydrogen bonds might be attributed to an unfavorable competition with the formation of strong

hydrogen bonds between the HSC<sub>11</sub>OH molecules within the SAM or an unfavorable competition with the solvent for hydrogen bonding.

To investigate the mechanical stability of the second layer, the force applied by the probing AFM tip was increased. First, the response of a bilayered nanografted patch of HSC<sub>10</sub>COOH was probed over time under an *ethanol* supernatant at a load of 12 nN (Fig. 4). Within 9 scans ( $t = 12\text{--}55$  min) the top layer is lost and the resulting nanografted patch is just  $0.35 \pm 0.22$  nm high, which is in good agreement with the predicted height of a monolayer of HSC<sub>10</sub>COOH (0.39 nm) (Fig. 4A,  $t = 52$ , and Fig. 4B). After lowering the load to 3.6 nN, the bilayer structure reforms rapidly (Fig. 4B;  $t = 55\text{--}72$  min). The disappearance and reappearance of the second layer are accompanied with a decrease and increase, respectively, in lateral friction, again confirming that the SAM is more tightly packed than the bilayer.

When the same stability test of an HSC<sub>10</sub>COOH nanografted patch was carried out in *2-butanol* instead of ethanol, the second layer remained completely intact and could even resist forces up to  $\sim 30$  nN. This observation reveals the direct influence of the supernatant solvent on the bilayer stability, which is probably for an important part based on its role as competitor for the COOH $\cdots$ HOOC hydrogen bonding formation between

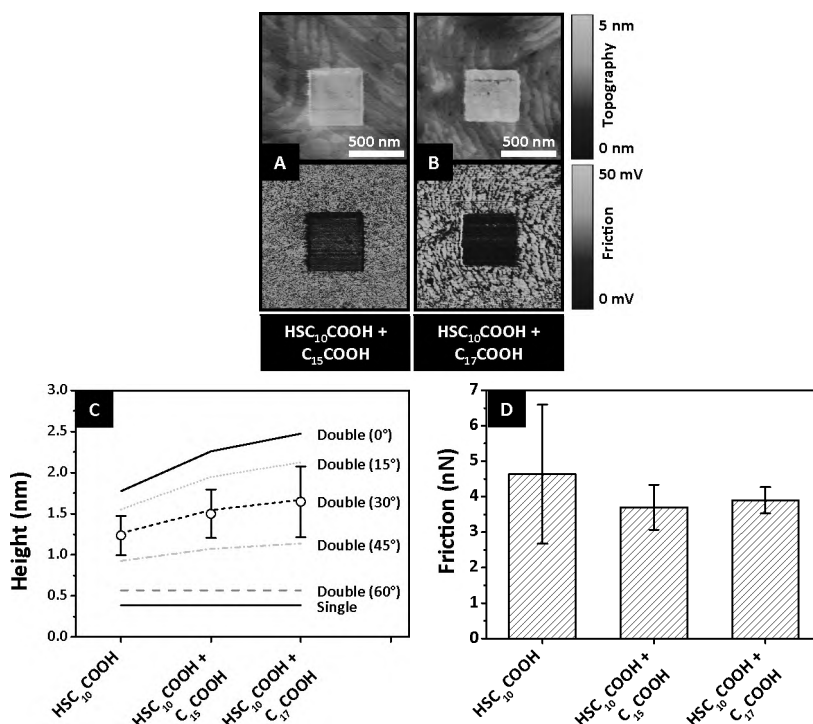


**Figure S2. Heteromeric double layers**

AFM topography (top row) and friction images (retrace, bottom row) of HSC<sub>10</sub>COOH nanografted patches grafted in the presence of 9 equivalents (A) 1-hexadecanoic acid C<sub>15</sub>COOH, and (B) 1-octadecanoic acid C<sub>17</sub>COOH. (C) Heights of the nanografted patches compared to a pure HSC<sub>10</sub>COOH–HOOC<sub>10</sub>SH nanograft and the expected heights according to a single layer or a double layer model with interlayer angles of 0°, 15°, 30°, 45° and 60°. (D) Lateral friction values of the nanografts. All data are  $\pm$  S.D. ( $N \geq 10$ ).

the thiols. The hydrogen bonding strength of the secondary alcohol 2-butanol is weaker than that of the primary alcohol ethanol. For that reason the interlayer hydrogen bonds are significantly more stable in the former solvent than in the latter, resulting in a bilayer that remains inert at high load forces. In addition, ethanol is more hygroscopic than 2-butanol, which will contribute to a further destabilization of the bilayer in the former solvent.

In a similar experiment, the stability of an  $\text{HSC}_{11}\text{NH}_2$  nanografted patch in 2-butanol was investigated (Fig. S3). Upon increasing the force load to 12 nN, a decrease in height and friction was observed and within 5 scans the second layer had completely disappeared. Upon subsequent lowering of the load, in some cases the second layer did not return (~30%). Both observations confirm our earlier hypothesis that the hydrogen bonding between  $\text{NH}_2$ -functionalized thiols in a bilayer structure is weaker than that between  $\text{COOH}$ -functionalized thiols, which reformed in all cases.

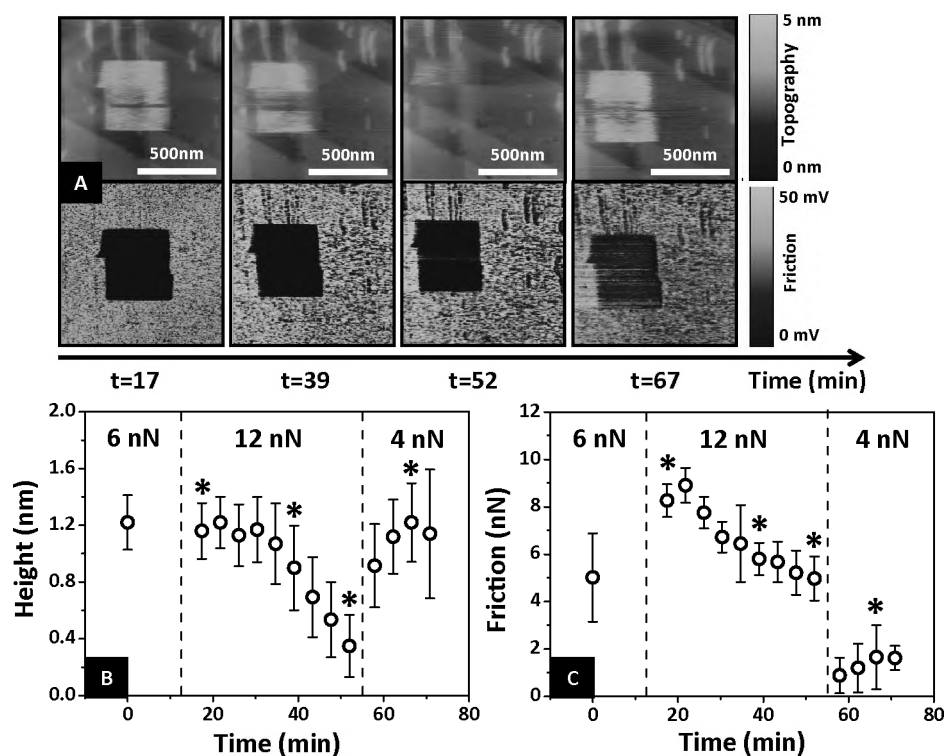


**Figure 4. Mechanical stability of a  $\text{HSC}_{10}\text{COOH}$  graft**

Mechanical stability test of a nanografted patch of  $\text{HSC}_{10}\text{COOH}$  in a  $\text{HSC}_8$  matrix performed by varying the load performed with the AFM tip. The tip scan speed is kept constant at  $6 \mu\text{m/s}$ . (A) Series of topography and friction images following an  $\text{HSC}_{10}\text{COOH}$  nanografted patch in an ethanolic supernatant solution over time. (B) Height variation of the nanografted patch over time. The nanografted patch was created and imaged at  $t=0$  at a 6 nN load, at  $t=12$  the load was increased to 12 nN, and at  $t=55$  decreased to 3.6 nN. (C) Corresponding friction values of the nanografted patch over time. The images in (A) were measured at the time points marked with an \*.

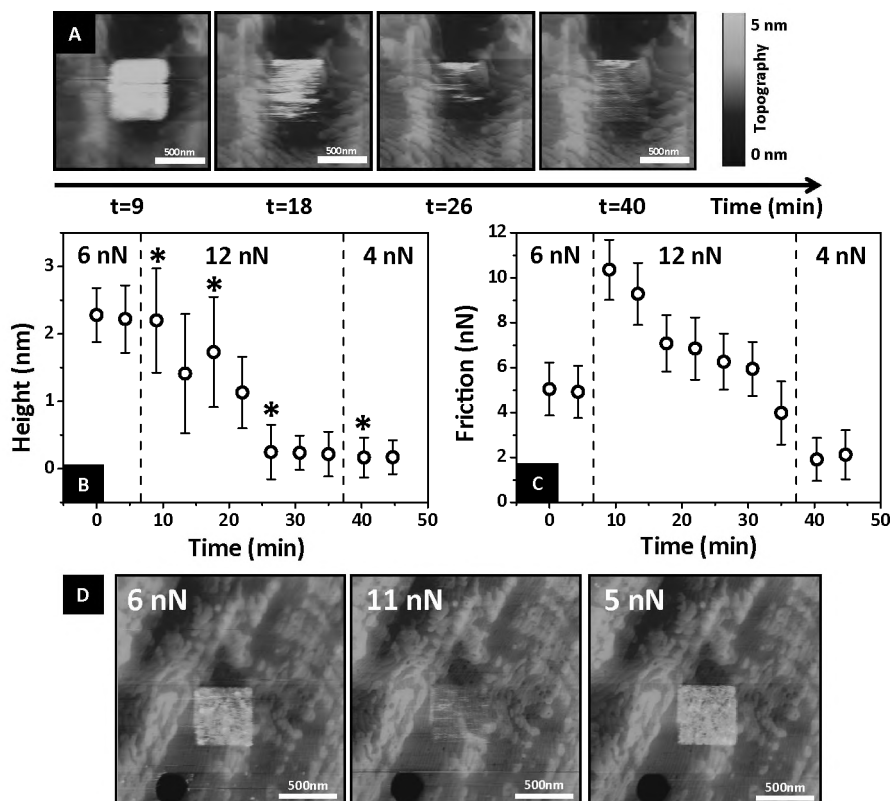


**Figure 4. Mechanical stability of a HSC<sub>11</sub>NH<sub>2</sub> graft**

Mechanical stability test of an HSC<sub>11</sub>NH<sub>2</sub> nanografted patch in a HSC<sub>8</sub> matrix performed by varying the load performed with the AFM tip. The tip scan speed is kept constant at 8 μm/s. (A) Series of topography and friction images following an HSC<sub>11</sub>NH<sub>2</sub> nanografted patch in a 2-butanol supernatant solution over time. (B) Height variation of the nanografted patch over time. The nanografted patch was created and imaged at t=0 at a 6 nN load, thereafter the load was increased to 12 nN. At t=37 the load was decreased to 3 nN, but the nanograft did not reform. (C) Corresponding friction of the nanografted patch over time. (D) Series of AFM topography images of an HSC<sub>11</sub>NH<sub>2</sub> nanografted patch imaged at successively 6 nN, 11 nN and 5 nN, showing the removal and reformation of the nanograft.

In summary, alkanethiols with –NH<sub>2</sub> and –COOH endgroups form stable bilayer structures when they are grafted in a SAM matrix from a 2-butanolic supernatant solution. The two layers are kept together by hydrogen bonds, in the form of cyclic dimers between COOH-terminated thiols or as single bonds between NH<sub>2</sub>-terminated thiols. The high friction observed for double layered nanografts is attributed to disorder in the top layer. Furthermore, in the case of ‘odd’ and ‘even’ HSC<sub>n</sub>COOH-molecules the friction slightly fluctuates due to differences in intermolecular interactions. Finally, the concentration of the molecules and the type of supernatant solution, e.g., ethanol, 2-butanol, or water, strongly influences the stability of the bilayer structures by competing with the hydrogen bond formation between the COOH- and NH<sub>2</sub>-groups of the alkanethiols.

## Acknowledgements

This study is supported by NanoNed, the Dutch nanotechnology programme of the Ministry of Economic Affairs. A.C. is supported by a VENI (916.66.028) and MEERVOUD (836.09.002) grant of The Netherlands Organization for Scientific Research (NWO). J.A.A.W.E. thanks the Council for the Chemical Sciences of The Netherlands Organization for Scientific Research (CW-NWO) for a VIDI grant (700.58.423). C.G.F. is supported by a BIO-LIGHT-TOUCH grant (FP6-2004-NEST-C-1-028781) and Immunomap grant (MRTN-CT-2006-035946) of the European Union. Arend M. van Buul is acknowledged for kindly providing us with 11-amino-1-undecanethiol.

## References

1. J. C. Love, L. A. Estroff, J. K. Kriebel, R. G. Nuzzo, G. M. Whitesides (2005). Self-assembled monolayers of thiolates on metals as a form of nanotechnology. *Chem. Rev.*, **105**, 1103-1169.
2. G. E. Poirier, E. D. Pylant (1996). The self-assembly mechanism of alkanethiols on Au(111). *Science*, **272**, 1145-1148.
3. G. E. Poirier, M. J. Tarlov (1994). The c(4x2) Superlattice of N-Alkanethiol Monolayers Self-Assembled on Au(111). *Langmuir*, **10**, 2853-2856.
4. S. Xu, G. Y. Liu (1997). Nanometer-scale fabrication by simultaneous nanoshaving and molecular self-assembly. *Langmuir*, **13**, 127-129.
5. J. E. Baio, T. Weidner, J. Brison, D. J. Graham, L. J. Gamble, D. G. Castner (2009). Amine terminated SAMs: Investigating why oxygen is present in these films. *J. Electron Spectrosc. Relat. Phenom.*, **172**, 2-8.
6. S. M. Mendoza, I. Arfaoui, S. Zanarini, F. Paolucci, P. Rudolf (2007). Improvements in the characterization of the crystalline structure of acid-terminated alkanethiol self-assembled monolayers on Au(111). *Langmuir*, **23**, 582-588.
7. H. Wang, S. F. Chen, L. Y. Li, S. Y. Jiang (2005). Improved method for the preparation of carboxylic acid and amine terminated self-assembled monolayers of alkanethiolates. *Langmuir*, **21**, 2633-2636.
8. R. Arnold, W. Azzam, A. Terfort, C. Woll (2002). Preparation, modification, and crystallinity of aliphatic and aromatic carboxylic acid terminated self-assembled monolayers. *Langmuir*, **18**, 3980-3992.
9. O. Dannenberger, K. Weiss, H. J. Himmel, B. Jager, M. Buck, C. Woll (1997). An orientation analysis of differently endgroup-functionalised alkanethiols adsorbed on Au substrates. *Thin Solid Films*, **307**, 183-191.
10. R. G. Nuzzo, L. H. Dubois, D. L. Allara (1990). Fundamental-studies of microscopic wetting on organic-surfaces .1. formation and structural characterization of a self-consistent series of polyfunctional organic monolayers. *J. Am. Chem. Soc.*, **112**, 558-569.
11. M. Bergkvist, N. Niamsiri, A. D. Strickland, C. A. Batt (2008). Substrate selective patterning on lithography defined gold on silica: Effect of end-group functionality on intermolecular layer formation. *Surf. Sci.*, **602**, 2121-2127.
12. M. Liu, N. A. Amro, G. Y. Liu (2008). Nanografting for Surface Physical Chemistry. *Annu. Rev. Phys. Chem.*, **59**, 367-386.
13. S. Xu, P. E. Laibinis, G. Y. Liu (1998). Accelerating the kinetics of thiol self-assembly on gold - A spatial confinement effect. *J. Am. Chem. Soc.*, **120**, 9356-9361.
14. J. te Riet, T. Smit, J. W. Gerritsen, A. Cambi, J. A. A. W. Elemans, C. G. Figdor, S. Speller (2010). Molecular Friction as a Tool to Identify Functionalized Alkanethiols. *Langmuir*, **26**, 6357-6366.
15. L. Shuang, P. Cao, R. Colorado, X. P. Yan, I. Wenzl, O. E. Shmakova, M. Graupe, T. R. Lee, S. S. Perry (2005). Local packing environment strongly influences the frictional properties of mixed CH<sub>3</sub>- and CF<sub>3</sub>-terminated alkanethiol SAMs on Au(111). *Langmuir*, **21**, 933-936.
16. H. I. Kim, T. Koini, T. R. Lee, S. S. Perry (1997). Systematic studies of the frictional properties of fluorinated monolayers with atomic force microscopy: Comparison of CF<sub>3</sub>- and CH<sub>3</sub>-terminated films. *Langmuir*, **13**, 7192-7196.
17. S. Cruchon-Dupeyrat, S. Porthun, G. Y. Liu (2001). Nanofabrication using computer-assisted design and automated vector-scanning probe lithography. *Appl. Surf. Sci.*, **175**, 636-642.
18. H. I. Kim, J. E. Houston (2000). Separating mechanical and chemical contributions to molecular-level friction. *J. Am. Chem. Soc.*, **122**, 12045-12046.
19. Y. H. Liu, T. Wu, D. F. Evans (1994). Lateral Force Microscopy Study on the Shear Properties of Self-Assembled Monolayers of Dialkylammonium Surfactant on Mica. *Langmuir*, **10**, 2241-2245.
20. X. D. Xiao, J. Hu, D. H. Charych, M. Salmeron (1996). Chain length dependence of the frictional properties of alkylsilane molecules self-assembled on Mica studied by atomic force microscopy. *Langmuir*, **12**, 235-237.
21. M. Hegner, P. Wagner, G. Semenza (1993). Ultralarge Atomically Flat Template-Stripped Au Surfaces for Scanning Probe Microscopy. *Surf. Sci.*, **291**, 39-46.
22. M. Castronovo, F. Bano, S. Raugei, D. Scaini, M. Dell'Angela, R. Hudej, L. Casalis, G. Scoles (2007). Mechanical stabilization effect of water on a membrane-like system. *J. Am. Chem. Soc.*, **129**, 2636-2641.
23. E. Barrena, C. Ocal, M. Salmeron (2000). Molecular packing changes of alkanethiols monolayers on Au(111) under applied pressure. *J. Chem. Phys.*, **113**, 2413-2418.
24. J. E. Sader, I. Larson, P. Mulvaney, L. R. White (1995). Method for the Calibration of Atomic-Force Microscope Cantilevers. *Rev. Sci. Instrum.*, **66**, 3789-3798.

25. **J. L. Hutter, J. Bechhoefer** (1993). Calibration of Atomic-Force Microscope Tips. *Rev. Sci. Instrum.*, **64**, 1868-1873.
26. **J. E. Sader, J. W. M. Chon, P. Mulvaney** (1999). Calibration of rectangular atomic force microscope cantilevers. *Rev. Sci. Instrum.*, **70**, 3967-3969.
27. **B. Ohler** (2007). Cantilever spring constant calibration using laser Doppler vibrometry. *Rev. Sci. Instrum.*, **78**, 0637011-0637015.
28. **R. W. Stark, T. Drobek, W. M. Heckl** (2001). Thermomechanical noise of a free v-shaped cantilever for atomic-force microscopy. *Ultramicroscopy*, **86**, 207-215.
29. **A. Noy, C. D. Frisbie, L. F. Rozsnyai, M. S. Wrighton, C. M. Lieber** (1995). Chemical Force Microscopy - Exploiting Chemically-Modified Tips to Quantify Adhesion, Friction, and Functional-Group Distributions in Molecular Assemblies. *J. Am. Chem. Soc.*, **117**, 7943-7951.
30. **J. E. Sader** (1995). Parallel Beam Approximation for V-Shaped Atomic-Force Microscope Cantilevers. *Rev. Sci. Instrum.*, **66**, 4583-4587.
31. **J. E. Sader, R. C. Sader** (2003). Susceptibility of atomic force microscope cantilevers to lateral forces: Experimental verification. *Appl. Phys. Lett.*, **83**, 3195-3197.
32. **J. L. Hazel, V. V. Tsukruk** (1999). Spring constants of composite ceramic/gold cantilevers for scanning probe microscopy. *Thin Solid Films*, **339**, 249-257.
33. **W. Alexander, J. F. Shackelford** (2001). CRC Materials Science and Engineering Handbook (p.537). *CRC Handbooks*.
34. **E. Tocha, J. Song, H. Schönherr, G. J. Vancso** (2007). Calibration of friction force signals in atomic force microscopy in liquid media. *Langmuir*, **23**, 7078-7082.
35. **D. R. Lide** (2008-2009). Handbook of Chemistry and Physics. 89th Edition.
36. **M. W. Schmidt, K. K. Baldrige, J. A. Boatz, S. T. Elbert, M. S. Gordon, J. H. Jensen, S. Koseki, N. Matsunaga, K. A. Nguyen, S. J. Su, T. L. Windus, M. Dupuis, J. A. Montgomery** (1993). General atomic and molecular electronic-structure system. *Journal of Computational Chemistry*, **14**, 1347-1363.
37. **M. D. Porter, T. B. Bright, D. L. Allara, C. E. D. Chidsey** (1987). Spontaneously Organized Molecular Assemblies .4. Structural Characterization of Normal-Alkyl Thiol Monolayers on Gold by Optical Ellipsometry, Infrared-Spectroscopy, and Electrochemistry. *J. Am. Chem. Soc.*, **109**, 3559-3568.
38. **A. Lio, D. H. Charych, M. Salmeron** (1997). Comparative atomic force microscopy study of the chain length dependence of frictional properties of alkanethiols on gold and alkylsilanes on mica. *J. Phys. Chem. B*, **101**, 3800-3805.



# CHAPTER 9

---

## General Discussion

*In science the credit goes to the man  
who convinces the world, not the  
man to whom the idea first occurs.*

*Sir Francis Darwin*



## Micro- and nanopatterns; new possibilities to study cell biological adhesion processes

The classical application of the AFM as a high resolution microscope, has proven very useful and even essential to study samples with nano- and micrometer-sized features. Because the AFM uses a sharp tip – with a radius of  $\sim 10$  nm – to probe the sample, the topography of that sample can be ‘imaged’ with sub-nanometer height and nanometer spatial accuracy. In Chapter 2 we demonstrate the added value of AFM imaging when studying cell adhesion on 3D nanopatterns. In biomaterial sciences, there is great interest to improve tissue embedding of implants.<sup>1</sup> One hypothesis to obtain this is to present nano-topographical structures to cells, thus mimicking the size of extracellular matrix (ECM) components. In the experiments described in Chapter 2, we found that fibroblasts adhere in an aligned fashion on nano-structured patterns up to a ridge width of 100 nm and a groove depth of only 35 nm.<sup>2, 3</sup> The characteristics of these patterns could be accurately determined with high-aspect ratio AFM topography imaging. The quality check of the patterns with AFM directly proved that the observed behavior of the cells can be assigned to the structures. In a similar study, we demonstrated the alignment and adhesion of osteoblasts on these structures.<sup>4</sup> These bone-forming cells deposited calcium phosphate in the grooves, an important step in the osteointegration process of implants. Another idea to stimulate implant embedment is the treatment of the implant’s surface with different coatings. We showed that a coating of calcium phosphate and/or collagen significantly improved the integration of the substrate by osteoblasts. The AFM was used here to characterize the thickness of the coating and its topography.<sup>5</sup>

In a broader cell-biological context, cells identify and sense topographical cues of the surrounding microenvironment by adhesion structures such as focal adhesions, immunological synapses, or podosomes, which consist of cytoskeleton organizing molecules, CAMs and other receptor-ligand type interactions.<sup>6</sup> To date, the exact mechanisms by which cells sense these cues or feel the mechanical stimuli remain to be determined. To address one of these questions, we studied the interaction of DCs via podosomes with different micropatterns.<sup>7</sup> Again, AFM was used to characterize the topography, and now also the elasticity and roughness of the samples. The main finding was that podosomes clearly sensed the microstructures, mainly on topographical cues. The podosomes aligned on the lower and upper ridges of the micropatterns.

In summary, AFM appeared to be a very useful and versatile instrument to study biological samples in particular in studies dealing with nanometer-sized structures, and if a resolution up to the molecular level is needed.

## Application of AFM-assisted nanografting provides direct insight into self-assembly at the molecular scale

In Chapters 7 and 8 we have shown that nanografting – in which an AFM cantilever is used to create and image nanopatterns – provides a new and powerful method for physical surface chemistry research. SAMs with various chains and endgroups were characterized by using nanografting to place unknown SAM-molecules into a matrix with known structure. Mainly due to the spatially confined self-assembly during nanografting, it was possible to directly ‘see’ – quantitatively probe by AFM – self-assembly processes at the nanoscale. Furthermore, the high sensitivity and quantitativity of height and friction measurements gave insight in the orientation and organization of the SAMs. In particular,

the quantitative friction measurements of the nanografted patches demonstrated the sensitivity of the method and the ability to better understand self-assembly processes.

Another possible application of nanografting lies in the precise nanopatterning of bio-molecules, such that they mimic the organization at the cell surface. In Chapter 6 we described an approach towards patterning of His-tagged proteins onto NTA-nanografted patches – a highly specific immobilization strategy for proteins due to a NTA-His receptor-ligand interaction. The almost single molecular control at which proteins can be immobilized by nanografting in an oriented fashion allows one to investigate biorecognition of pathogens, such as viruses, to DC-SIGN pathogen receptors. Similarly, Yu et al. exploited nanografting to bind HIV envelope proteins (gp120) to purified carbohydrate ligands.<sup>8</sup> Others studied the density and molecular conformation of DNA on surfaces,<sup>9-13</sup> as well as the orientation and packing of proteins upon immobilization on surfaces.<sup>14-19</sup> In all these studies, the strength of the nanografting method lies in the precise tailoring of receptor nanopatterns whereupon the binding of ligands can be systematically studied. A major disadvantage of nanografting is that the patterning of large areas ( $>10 \times 10 \mu\text{m}$ ) as well as nanografting complex thiolated molecules from a mixed solution seemed to be difficult (Chapter 6). In particular, the self-assembly behavior of mixed NTA- and oligo-ethylene glycol (EG)-terminated alkanethiols was more complex than that of the simple  $\text{HSC}_n\text{X}$ -alkanethiols studied in Chapters 7 & 8. In addition, the length of oligo-EG<sub>n</sub> thiols seems to be crucial to block the nonspecific absorption and Hahn et al. have reported that the critical length is around 4 EG-repeats.<sup>20</sup> However, with this length we still found substantial nonspecific absorption of our proteins. Therefore, we suggest to use even longer oligo-EG linkers in the alkanethiols to promote specific binding of His-tagged proteins onto the NTA-terminated alkanethiols.

For future research on nanopatterning proteins to mimic the cell membrane, I still suggest to use the NTA-His binding chemistry as exploited in Chapter 6 due to its high specificity, its relative simplicity, its reversibility and strength to resist physiological forces.<sup>21</sup> Other immobilization strategies, such as adding a biotin-,<sup>22, 23</sup> DNA-,<sup>24</sup> alkyne-,<sup>25</sup> or cysteine/thiol-tag<sup>26, 27</sup> to proteins of interest, could be considered. These tags facilitate that proteins can be coupled (almost) covalently on the substrate. As a potential drawback, this also means that the immobilization is virtually irreversible.<sup>22</sup> Another disadvantage of these latter tags is that proteins should be either structurally altered or chemically modified, which is, more complex than just adding a His-tag, or affects the orientation of proteins upon immobilization.<sup>22</sup> Thus, NTA-His chemistry is still one of the best options to immobilize proteins.

Taken together, to obtain the millimeter-sized nanopatterns as desired to study cell adhesion, nanografting might not be the right choice. For these purposes, I propose to explore dip-pen nanolithography (DPN),<sup>28</sup> a technique closely related to nanografting. In this technique, the tip of the AFM cantilever is used as a 'pen' to write nanopatterns on gold. An advantage of this method is that also gold-thiol chemistry can be used. However, DPN has similar limitations as nanografting on patternable area, though parallel-DPN<sup>28</sup> could make it possible to scale up the pattern size. Furthermore, whether NTA-terminated thiols really can be written with DPN is largely unknown, although patterns of biotin-terminated thiols have been described in literature.<sup>29</sup> Another option for large scale nanopatterns is to exploit preformed gold nanoislands on a substrate (e.g. glass or silicon) on which the NTA-thiols are bound and the remaining surface can be blocked.<sup>30-32</sup> A final approach would make use of the current improvements in imprint lithographic techniques, which allow stamping of the desired nanopatterns.<sup>33</sup> Recently, for example,

nano-sized patterns of up to 50 nm have been demonstrated.<sup>34, 35</sup> A major advantage of stamping is that it is fast and that glass samples or other transparent materials can be used, which is very practical when light microscopy will be exploited.

In summary, nanografting is a powerful method to study (bio)chemical processes at the nano- or even molecular-scale. The AFM can then be exploited to gain insight in the packing and orientation of (bio)molecules. However, its strength is not in patterning at large scale, which is essential when studying cells which have diameters that vary from 10 to 50 microns. For that purpose, I suggest to use alternative routes such as DPN, gold patterns, and especially stamping, to obtain nanostructures. Subsequently, nanografting might offer the possibility to investigate every single chemical step needed to immobilize the proteins, especially when complications with the binding chemistry occur.

## **AFM force spectroscopy; studying ligand-receptor interactions**

### **Probing cell dynamics at the molecular level**

As already mentioned in the General Introduction (Chapter 1), various types of CAMs all play different roles in cell adhesion depending on, for example, their mechanical characteristics. Some CAMs help to keep cells at a given location in the tissue. This, however, does not imply that no forces act on them. On the contrary, cells in tissues are always under static stress. Forces build up transiently on the individual bonds that connect cells, albeit very slowly (at rates of  $\sim 1$  pN/s) until a single bond breaks and loading forces are shifted towards other bonds.<sup>36</sup> By comparison, the other extreme is formed by immune cells flowing in the blood that suddenly need to be stopped, because, for instance they need to traverse the endothelium to reach a site of inflammation. They attach to the vascular endothelium and the CAM bonds (e.g. selectins) on this cell have to withstand forces building up at incredibly fast rates ( $\sim 10^4$ - $10^5$  pN/s).<sup>36, 37</sup> Under these conditions bonds quickly rupture, and when other bonds on the cell do not take over, the cell is released. If however, through activation of other CAMs (e.g. integrins) the immune cell gets activated, new CAM bonds are formed and the cell can get arrested and is enabled to migrate into the surrounding tissue. Thus the important mechanical property that characterizes these bonds is not static strength, but rather dynamic strength. AFM force spectroscopy (AFM-FS) is a powerful method to measure the dynamic strength of these bonds by varying the loading rates and investigation of the corresponding single bond ruptures in 'force curves'. The challenge of AFM-FS is to interpret these force curves and recognize the 'signature' of specific as well as nonspecific adhesion events, which may occur simultaneously. Subsequently, another challenge is to quantify the dynamic strength – or affinities under stress – of these receptor-ligand bonds to be able to compare the dynamic strength of different CAMs.

### **Quantification of single-molecule rupture forces by AFM-FS**

Now that AFM-FS is applied more and more in biophysical studies on different CAMs, special care has to be taken when analyzing measurements. So far, consensus exists on the application of the Bell-Evans model in analyzing force spectra. However, there is no consensus yet on how to interpret the non-linear spring behavior of PEG-spacers,<sup>38</sup> and on tethering of cells.<sup>36, 38</sup> In other words, in both cases the receptor-ligand bond is non-linearly loaded, which influences the fitting model to be used in the case of a rupture event. Tethering of cells occurs during the final phase of detachment when receptors are not connected to the cytoskeleton. Upon retraction the cell body loses contact with the substrate, but attachment is still maintained via membrane tethers (cell detachment

distances can be up to 100  $\mu\text{m}$ ).<sup>39</sup> Although these tethers influence the curve ‘signature’ drastically, the force acting on the receptor-ligand interaction at the end of the tether is unaffected. Therefore, we retrieved the loading rate just before rupture of the bond with a linear fit, such as described in Chapters 4 & 5. Besides, tethering plays a minor role in our case due to the link with the actin cytoskeleton in the case of ALCAM, or due to stiff cells with a cell wall in the case of *Candida albicans*. This way, we compensate for the higher elasticity of the cells by measuring the efficient spring constant of the full system.<sup>36</sup> Thus, the derived biophysical parameters from the Bell model are unaltered.

More importantly, to be able to compare results of different studies, such as rupture forces and Bell parameters, the measured forces should be quantified. This implies calibration of the laser light path (InvOLS = inverse optical lever sensitivity) and the spring constant of the AFM cantilever. In Chapter 3, we described the importance of spring constant calibrations and the errors that can be introduced when a poor calibration method is applied. The calibration protocol as proposed and described in Chapter 3 is in my opinion a significant step forward towards standardization of cantilever calibration methods for AFM-FS. In combination with improved deflection sensitivity measurements, in particular by calculating them (Box 1, Chapter 3), the quantification of measured forces can be standardized. Furthermore, the influence of the drag on force spectroscopy (Chapter 1), which is substantial for high rupture speeds, can be minimized by miniaturizing AFM cantilevers.<sup>40</sup> In summary, now that standard experimental procedures and data-analysis routines are getting adopted by most researchers, the comparison of biophysical parameters becomes feasible.

### Probing interactions in single molecule and single cell force spectroscopy

As already described in the General Introduction, with AFM-FS there are different possibilities to probe receptor-ligand interactions. For single molecule force spectroscopy (SMFS) the receptor as well as ligand are immobilized as isolated molecules on the cantilever and substrate, respectively. In single cell force spectroscopy (SCFS) a cell is immobilized on the cantilever and interactions are measured with a substrate of isolated molecules or another cell.

A major advantage of SMFS is the well defined probing system, because theoretically only the specific receptor-ligand interactions will be measured. At the same time, a disadvantage of this method is that isolated receptors are used, out of their biological context, and thereby potentially altering their functional state. This is of particular concern when studying integrins – consisting of a  $\alpha_n\beta_m$ -dimer – that are known to have several substrate-binding affinity states (Chapter 1). Furthermore, the degree and type of glycosylation of the ligand molecules could be different for isolated proteins compared with the native protein (Chapter 5), which in the case of (se)lectin interactions is critical for binding.<sup>41</sup> Thus, all these factors together can influence the strength (affinity) of the bond.<sup>42</sup>

In contrast to SMFS, SCFS enables single receptor-ligand interactions to be examined in their cellular environment. Using a living cell as a probe ensures that receptors are native. Several of these receptor-ligand pairs have been studied using SCFS as well as SMFS with the purified proteins. The rupture forces that are measured by SCFS and SMFS are generally in agreement, but some of them show considerable deviation.<sup>39</sup> This might indicate that the strength of receptor-ligand interactions depends on the experimental conditions. Furthermore, the manner and direction in which the bond is stressed might differ resulting in different energy barriers being crossed to break the bonds.<sup>43</sup> This might

**Table 1: SMFS versus SCFS**

Single molecules force spectroscopy (SMFS)	Single cell force spectroscopy (SCFS)
<ul style="list-style-type: none"> <li>Isolated molecules on cantilever and substrate</li> </ul>	<ul style="list-style-type: none"> <li>Cell on cantilever and isolated molecules / cell on substrate</li> </ul>
<ul style="list-style-type: none"> <li>Defined system; one ligand-receptor pair</li> </ul>	<ul style="list-style-type: none"> <li>Possibly more than one ligand-receptor pair</li> </ul>
<ul style="list-style-type: none"> <li>Specific and nonspecific interactions easily distinguishable</li> </ul>	<ul style="list-style-type: none"> <li>To distinguish specific interactions more controls needed</li> </ul>
<ul style="list-style-type: none"> <li>Not in biological context (e.g. cellular membrane)</li> </ul>	<ul style="list-style-type: none"> <li>In biological context, native conformation if endogenously expressed on cell</li> </ul>
<ul style="list-style-type: none"> <li>Unnatural loading of bond</li> </ul>	<ul style="list-style-type: none"> <li>Native loading of bond</li> </ul>
<ul style="list-style-type: none"> <li>High effective force constant</li> </ul>	<ul style="list-style-type: none"> <li>Low effective force constant</li> </ul>
<ul style="list-style-type: none"> <li>Maximum loading rate <math>\sim 100,000</math> pN/s</li> </ul>	<ul style="list-style-type: none"> <li>Maximum loading rate <math>\sim 30,000</math> pN/s</li> </ul>
<ul style="list-style-type: none"> <li>No cell handling</li> </ul>	<ul style="list-style-type: none"> <li>Facilities and skills needed to handle cells</li> </ul>
<ul style="list-style-type: none"> <li>Biological relevancy questionable</li> </ul>	<ul style="list-style-type: none"> <li>Biologically relevant</li> </ul>

also explain differences observed for different force spectroscopy methods. Next to AFM-FS, also micropipettes can be used to grasp and hold cells, detachment forces are subsequently measured using a bio-membrane force probe (BFP),<sup>44</sup> or optical tweezers.<sup>45</sup> <sup>46</sup> The ability to compare results of different force spectroscopy studies is also hampered by the fact that instead of loading rates, the uncorrected retraction rates are used to plot the dynamical behavior of an interaction, because the effective spring constant during probing is unknown.

Finally, when a cell is used in SCFS the effective force constant of the probing system is significantly lower than for isolated molecules SMFS. In other words, in addition to stretching the receptor-ligand bond when applying force, also the cell is stretched, which sometimes results in membrane tethers. This cell stretching also reduces the maximum loading rates that can be probed.<sup>39</sup> Another important consideration especially for SCFS, but also for SMFS, is the distinction of specific from nonspecific cell/tip-surface interactions. Therefore, special care must be taken to ensure that the interactions that are recorded occur predominantly, if not exclusively, between the receptor and ligand of interest. Therefore, rigorous control experiments, such as blocking with antibodies, should be performed which demonstrate the specificity of the interactions observed. Overall, the use of cells in SCFS measurements makes this method less straightforward than SMFS. However, the findings of SCFS studies are most likely more relevant in addressing cell biological questions. In summary, the differences, advantages and disadvantages of both methods (SMFS and SCFS) are given in Table 1.

## Biological interpretation of AFM-FS data

The biophysical Bell parameters derived by AFM force spectroscopy (AFM-FS) give direct insight in the affinity of a receptor-ligand interaction. Moreover, the Bell parameters make it possible to compare different receptor-ligand interactions and help to give more insight in the exact structure of the binding pocket, or the affinity regulation of a receptor. In the case of affinity regulation, we have shown that ALCAM has a different homotypic affinity (ALCAM-ALCAM) than heterotypic affinity for CD6 (ALCAM-CD6), the latter being stronger (Chapter 4). Furthermore, we concluded that affinity and avidity are two independently regulated processes in ALCAM-mediated cell adhesion. The interaction of DC-SIGN with different *Candida albicans* glycosylation mutants (Chapter 5), shows how subtle differences in the structure of the ligand influence the affinity. In both studies we compared the found Bell parameters of the CAMs with other CAMs in such called “kinetic profiles” and derive with it the mechanical properties of the receptor-ligand

bond under study. These plots help to understand the cell biological role of the CAM. To further discuss the strength of AFM-FS to gain insight into the dynamical strength of CAMs, I will discuss two examples in which AFM-FS is used. These examples will illustrate possible future directions for the application of AFM-FS in studying cell surface receptors of the immune system.

### Dynamical affinity regulation by LFA-1

The integrin LFA-1 ( $\alpha\beta_2$ ) and two of its ligands ICAM-1 and -2 were studied with AFM-FS by Wojcikiewicz et al.<sup>47-49</sup> LFA-1 binds with an at least 5-fold higher affinity to ICAM-1 than to ICAM-2 as measured by competitive binding assays and surface plasmon resonance.<sup>50, 51</sup> However, in these assays, measurements are performed without (almost) any force applied, whereas with AFM-FS the real dynamical affinity of a bond can be measured by applying pulling forces. LFA-1-ICAM-1/2 interactions play an important role on leukocytes when transmigrating across the endothelium.<sup>52-54</sup> Although both interactions have overlapping functions, ICAM-2 is mainly expressed at high levels on unstimulated endothelium.<sup>50</sup> Upon inflammation ICAM-1 expression gets upregulated and mediates a stronger adhesion of the leukocytes to the inflamed endothelium and the subsequent transmigration into the tissue (see also Chapter 1, Fig. 7).<sup>52, 55, 56</sup> Besides, LFA-1-ICAM-1 interactions play an important role in the formation of the immunological synapse between DCs and T cells (like ALCAM-CD6, Chapter 4), which is a dynamical process too. When both interactions are probed with AFM-FS it can be observed that upon loading a bond (increasing the loading rate) the rupture forces of the LFA-1-ICAM-2 interaction are lower than those of LFA-1-ICAM-1 (Fig. 1A). In addition to switching from one ligand to another to bind stronger, LFA-1 can modulate its affinity by a conformational change (see Chapter 1, Fig. 8) to become “active”. In the force spectrum (Fig. 1A) this is visible as higher rupture forces in the lower loading rate regime ( $< 7000$  pN/s). Upon increasing the avidity by clustering of LFA-1 molecules on the cell membrane, it should be noted that the affinity is similar (Fig. 1A). The overall adhesion is however in these cases much higher due to the higher availability of multiple bonds.<sup>48, 55</sup> This is similar to our observation on the avidity regulation by ALCAM (Chapter 4). The Bell parameters found for the interaction of LFA-1 with ICAM-1/2 are given in Table 2 and describe the receptor-ligand interaction as an energy diagram (see Chapter 1, Fig. 3). However, much

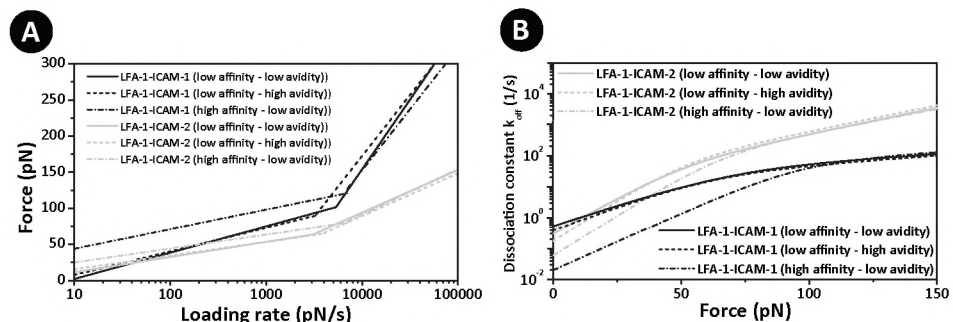


**Figure 1: Dynamical behavior of the LFA-1-ICAM-1/2 bonds**

(A) Force spectra of the LFA-1-ICAM-1 and LFA-1-ICAM-2 bonds for low and high affinity as well as avidity. (B) The corresponding kinetic profiles. A lower dissociation constant means a more stable bond. The plotted force regime is the physiological one.

better insight is obtained when plotting the dissociation rate  $k_{off}$  (1/s) of the interaction in relation to the pulling force (see also Chapter 4, Discussion). In Fig. 1B the “kinetic profiles” are given of the LFA-1-ICAM-1/2 interactions, in which a lower dissociation rate implies a more stable bond. Also, the dissociation rates become higher (more labile) upon higher forces, which is as expected because bonds under stress break more rapidly than unstressed bonds. Furthermore, it can be clearly seen that LFA-1-ICAM-1 bonds are stronger than LFA-1-ICAM-2 bonds at pulling forces >25 pN. Subsequently, by activation of LFA-1 bonds strengthen when pulling forces are lower than 100 pN (implying thermodynamically that the height of the outer barrier becomes higher in the energy diagram). Furthermore, here – like in the case of ALCAM – also avidity-affinity regulation are two separate processes that regulate cell adhesion, the dissociation rate remains unaltered. Finally, it can be seen that activated LFA-1 binds ICAM-1 approximately 3- to-5-fold better than ICAM-2 in unstressed conditions (0-10 pN) similar to the affinity differences measured by the static methods mentioned earlier. However, the added value of the AFM-FS data is that it provides detailed insight in the affinity of the bonds under stress, which much better represent the *in vivo* conditions experienced by the CAMs on cells.

### Mapping the binding pocket of $\alpha_4\beta_1$ -VCAM-1

Another nice example showing how AFM-FS can be exploited is mapping of the binding pocket of the  $\alpha_4\beta_1$ -VCAM-1 (vascular cell adhesion molecule-1) bond when binding to the integrin  $\alpha_4\beta_1$ . The binding pocket of a receptor-ligand bond consists of a complex of ionic, hydrogen, van der Waals and hydrophobic/hydrophilic bonds.<sup>59</sup> In an AFM-FS study by Zhang et al.<sup>57</sup> different binding pocket mutants are studied of the integrin  $\alpha_4\beta_1$  and its ligand VCAM-1, which also play a role in the extravasation of many leukocyte subtypes, similar to the role of the integrin LFA-1 ( $\alpha_L\beta_2$ ). In Table 2 and Fig. 2 it can be observed that the wildtype (WT)  $\alpha_4\beta_1$ -VCAM-1 bond will have a so-called ‘double barrier’ energy diagram, because it shows two different regimes in its force spectrum (Chapter 1). The constants  $x_{\beta_1}$  and  $x_{\beta_2}$  domains represent the width of the inner- and outer-barrier of the energy diagram and the  $k_1^o$  and  $k_2^o$  the height of energy barriers (Chapter 1, Fig. 3). This double barrier characteristic helps the complex to resist the

**Table 2: Bell parameters of different receptor-ligand interactions measured by AFM-FS**

System	$x_{\beta_1}$ (nm)	$k_1^o$ (s <sup>-1</sup> )	$x_{\beta_2}$ (nm)	$k_2^o$ (s <sup>-1</sup> )	Loading rate regime (pN/s)*	Reference
LFA-1-ICAM-1 (low-low) <sup>#</sup>	0.26	0.55	0.049	19	50 - 7,000 - 60,000	Wojcikiewicz et al. 2006 <sup>48</sup>
LFA-1-ICAM-1 (low-high) <sup>#</sup>	0.29	0.41	0.056	13	50 - 7,000 - 60,000	Wojcikiewicz et al. 2006 <sup>48</sup>
LFA-1-ICAM-1 (high-low) <sup>#</sup>	0.35	0.02	0.056	17	50 - 7,000 - 60,000	Wojcikiewicz et al. 2006 <sup>48</sup>
LFA-1-ICAM-2 (low-low) <sup>#</sup>	0.45	0.31	0.16	10	50 - 7,000 - 60,000	Wojcikiewicz et al. 2006 <sup>48</sup>
LFA-1-ICAM-2 (low-high) <sup>#</sup>	0.50	0.18	0.16	12	50 - 7,000 - 60,000	Wojcikiewicz et al. 2006 <sup>48</sup>
LFA-1-ICAM-2 (high-low) <sup>#</sup>	0.49	0.06	0.15	13	50 - 7,000 - 60,000	Wojcikiewicz et al. 2006 <sup>48</sup>
$\alpha_4\beta_1$ -VCAM-1 (WT)	0.59	0.13	0.10	59	50 - 20,000 - 60,000	Zhang et al. 2004 <sup>57</sup>
$\alpha_4\beta_1$ -VCAM-1 (+EDTA)	0.38	9.3	-	-	50 - 60,000	Zhang et al. 2004 <sup>57</sup>
$\alpha_4\beta_1$ -VCAM-1 ( $\Delta$ D40A)	0.59	1.2	-	-	50 - 60,000	Zhang et al. 2004 <sup>57</sup>
$\alpha_4\beta_1$ -VCAM-1 ( $\Delta$ D40E)	0.55	1.0	0.27	16	50 - 20,000 - 60,000	Zhang et al. 2004 <sup>57</sup>
$\alpha_4\beta_1$ -VCAM-1 ( $\Delta$ D143A)	0.58	0.85	0.095	72	50 - 20,000 - 60,000	Zhang et al. 2004 <sup>57</sup>
ALCAM-ALCAM	0.38	1.9	-	-	300 - 20,000	This thesis (Ch. 4) <sup>58</sup>
ALCAM-CD6	0.23	3.4	-	-	300 - 20,000	This thesis (Ch. 4) <sup>58</sup>
DC-SIGN-Candida (WT)	0.61	0.43	-	-	100 - 4,000	This thesis (Ch. 5)

\* The given values correspond to the loading rate regime probed, if three values are given the middle one corresponds to the transition loading rate. <sup>#</sup> The first low/high between brackets describes low or high affinity, the second low or high avidity.

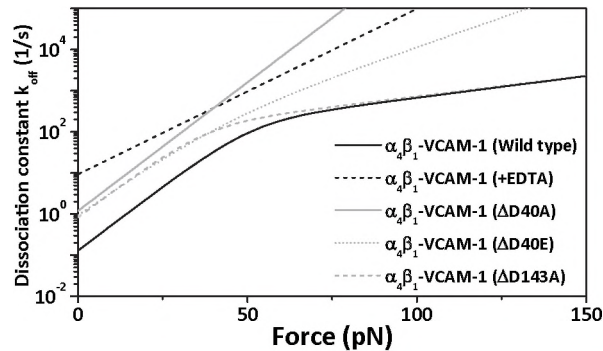


**Figure 2: The kinetic profiles of the  $\alpha_4\beta_1$ -VCAM-1 bond**

The kinetic profiles of the  $\alpha_4\beta_1$ -VCAM-1 bond show the differences between mutations at the binding pocket and the corresponding influence on the affinity.

large shear forces imposed by the bloodstream.<sup>36</sup> An important bond in the binding pocket of the  $\alpha_4\beta_1$ -VCAM-1 bond is an ionic bond of the MIDAS (metal ion-dependent adhesion site) domain in the  $\beta_1$ -subunit containing a chelated  $Mg^{2+}$  ion that bind to an Ig-domain of VCAM-1. Upon removing this ion by EDTA it can be seen that the affinity ( $k_{off}$ ) is  $\sim 70$ -fold lowered (Fig. 2). Furthermore, the bond has lost its characteristics of a double barrier and a decreased length of the binding pocket  $x_\delta$ . Probably, due to the removal of the  $Mg^{2+}$ -ion the bond is much weaker and altered, likely also due to the loss of  $Ca^{2+}$ -ion bonds.

Furthermore, a VCAM-1 deletion mutant that lacks the  $Mg^{2+}$ -ion binding aspartic acid ( $\Delta D40A$ ) has also lost its double barrier behavior but has still the same outer barrier dimension (Table 2). In Fig. 2 this alteration is visible as a line with the same slope in the 0–40 pN regime, but no overlap at higher forces. An amino acid mutant ( $\Delta D40E$ ) in which the aspartic acid (side group  $R=CH_2COOH$ ) is, however, replaced by glutamic acid ( $R=CH_2CH_2COOH$ ), still shows a double barrier behavior and fully formed binding pocket. Though, by increasing the bond length ( $\sim 0.15$  nm longer) of the amino acid side-group also the inner barrier has become  $\sim 0.17$  nm wider (see Table 2). The result is that the overall affinity of the  $\alpha_4\beta_1$ -VCAM-1 bond is much lower over the full force range. Finally, a mutation in the second domain of VCAM-1 ( $\Delta D143A$ ),<sup>60</sup> which is known to influence the adhesive behavior of the bond seems only to influence the affinity at low forces (Fig. 2) and the width of the outer barrier  $k_1^0$  (Table 2). The hypothesis is that this domain helps to stabilize the bond.<sup>57</sup> In conclusion, the aspartic acid in one domain of VCAM-1 binds via a  $Mg^{2+}$ -ion to the MIDAS site of  $\alpha_4\beta_1$  – this ionic-bond is the main bond – and another aspartic acid in a second domain of VCAM-1 helps to stabilize the total bond – this hydrogen-bond is weaker but contributes substantially to the overall affinity.

This example demonstrates the enormous potential of using AFM-FS to map binding pockets of receptor-ligand interactions by exactly measuring the influence on the dynamical response of the bond when loaded. This method will therefore be of added value in measuring the affinity of different immunologically relevant receptor-ligand interactions. For example, a similar strategy as described for  $\alpha_4\beta_1$ -VCAM-1 could be exploited to map the interaction of the CRD-domain of DC-SIGN with different carbohydrate ligands, such as those on *C. albicans* (Chapter 5).



## Future directions

Finally, I want to discuss some of the new directions for the application of the AFM in (immuno) cell-biological studies. Except for the earlier proposed strategies on nanopatterning and the application of AFM-FS to distinguish between affinity and avidity of single CAM interactions in cell, also numerous opportunities arise by linking AFM to a confocal microscope.<sup>39, 61</sup> Interesting is the possibility to use this ultrasensitive AFM/confocal microscope set-up to map the mechanical response of single living cells by AFM, while at the same time imaging and quantifying downstream cell signals by exploiting fluorescently tagged proteins. The high spatio-temporal resolution of AFM – positioning at the nanoscale with relatively high speeds (100  $\mu\text{m/s}$ ) – allows the measurement of

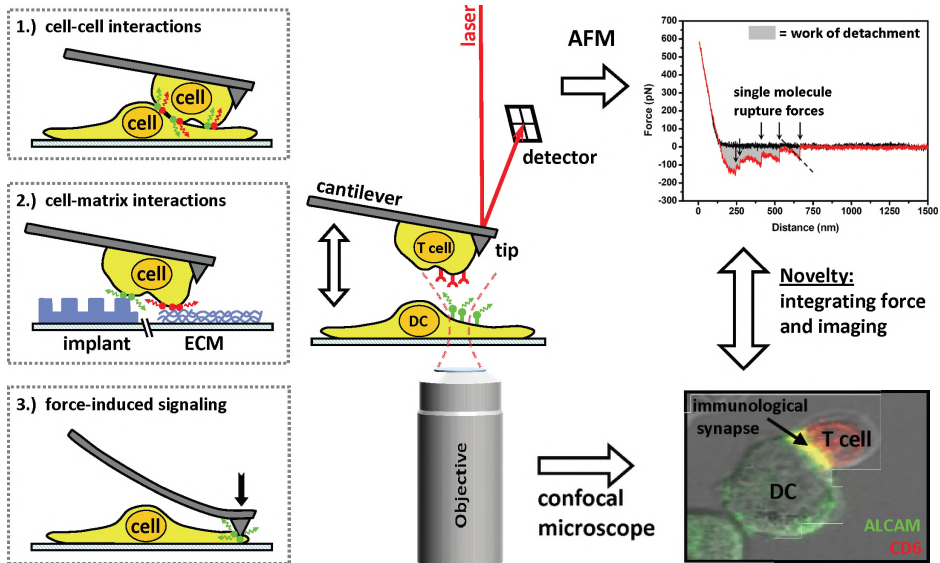


**Figure 3: Schematic representation of future experiments**

By combining AFM force spectroscopy with confocal microscopy we can probe interaction forces and visualize the interaction between two cells at the same time. The novelty of this integration of techniques is that cellular processes are imaged with high spatio-, force- and temporal information. This allows one to address the key objectives shown at the left. As example, we show the interaction of the ligand-receptor pair ALCAM-CD6 as observed in the immunological synapse of a DC and T cell. An AFM cantilever bearing a T cell is brought into contact with a DC on a substrate, imaged from below by a confocal microscope. From initial contact of the T cell and DC, the distribution of ALCAM and CD6 on the cell membrane can be imaged real-time in the forming immunological synapse. In parallel, the interaction forces are probed by the cantilever. Upon retraction of the T cell from the DC, the cells detach and single molecular ruptures can be observed by the AFM. The three main objectives are:

- (i) Cell-cell interactions. The aim is to unravel how mechanical forces between two interacting cells, either cell-pathogen or cell-cell, ultimately influence signal transduction resulting from receptor–ligand interactions.
- (ii) Cell-matrix interactions. The effect of forces exerted by the extracellular matrix (ECM) on invading cancer cells as well as forces exerted at the interface between host cells and artificial implants is the focus of this objective. Besides, the AFM will be exploited to investigate the topography of the patterned substrata.
- (iii) Force-induced signaling. AFM tips will be used to apply localized pressure forces onto cells. Furthermore, to study specific ligand-receptor pairs functionalized tips will be used. Subsequently, cellular responses to mechanical stimuli by the AFM tips, including receptor activation and signaling will be dynamically monitored.

cell-cell interactions, cell-matrix interactions, and force-induced cell signaling, with control on the timing of initial contact. The cellular responses (e.g. calcium influx, change in shape, adhesion receptor recruitment) to the contact with different topographical structures or the cantilever can be monitored simultaneously by the confocal optical microscope. In Figure 3, some possible directions are depicted to explore the highly dynamical processes of living cells. A focus point would be to use a cell-functionalized cantilever to probe interactions (i) with other cells and (ii) with different patterned or functionalized substrates. In addition, it would be very interesting to exploit the high spatio-temporal resolution of the AFM/confocal (iii) to induce forces by the cantilever on a living cell and measure the response of this cell. The feasibility of such experiments is in part demonstrated by the results described in this thesis. However, the implementation of AFM with confocal microscopy will give rise to new challenges and difficulties that should be addressed. One challenge would be, for example, to deal with the compliance of the cells especially during two cell experiments. Since cells will deform and possibly tether during the detachment stage, it will be necessary to have an AFM piezoscanner with a large z-range. However, because modern scanners can easily work over >20  $\mu\text{m}$  distances handling two cells will be feasible. Furthermore, by using adhered and stretched cells instead of rounded cells probing over long distances can be reduced. Another challenge lies in the development of new data analysis routines, which will help to better extract information on cell adhesion from force-distance curves in AFM-FS. Apart from extracting the single ligand-receptor rupture forces, from these curves the contribution could be determined from, e.g. the cytoskeleton, the composition of the cell membrane, and tethering. In other words, by improving the data analysis routines, 'signatures' of all aforementioned processes could be recognized in the force-distance curves.

In conclusion, AFM and especially single cell force spectroscopy has a high potential for life sciences, due to its versatility and the enormous variety of cell biological and medical questions to which it can be applied.

## References

1. **Z. Schwartz, E. Nasazky, B. D. Boyan** (2005). Surface microtopography regulates osteointegration: the role of implant surface microtopography in osteointegration. *Alpha Omega*, **98**, 9-19.
2. **W. A. Loesberg, J. te Riet, F. C. van Delft, P. Schon, C. G. Figdor, S. Speller, J. J. van Loon, X. F. Walboomers, J. A. Jansen** (2007). The threshold at which substrate nanogroove dimensions may influence fibroblast alignment and adhesion. *Biomaterials*, **28**, 3944-3951.
3. **F. C. M. J. van Delft, F. C. van den Heuvel, W. A. Loesberg, J. te Riet, P. Schon, C. G. Figdor, S. Speller, J. J. W. A. van Loon, X. F. Walboomers, J. A. Jansen** (2008). Manufacturing substrate nano-grooves for studying cell alignment and adhesion. *Microelectron. Eng.*, **85**, 1362-1366.
4. **E. Lamers, X. F. Walboomers, M. Domanski, J. te Riet, F. C. M. J. M. van Delft, R. Luttgé, L. Winnubst, H. J. G. E. Gardeniérs, J. A. Jansen** (2010). The influence of nanoscale grooved substrates on osteoblast behavior and extracellular matrix deposition. *Biomaterials*, **31**, 3307-3316.
5. **L. T. de Jonge, S. C. Leeuwenburgh, J. J. van den Beucken, J. te Riet, W. F. Daamen, J. G. Wolke, D. Scharnweber, J. A. Jansen** (2010). The osteogenic effect of electrosprayed nanoscale collagen/calcium phosphate coatings on titanium. *Biomaterials*, **31**, 2461-2469.
6. **B. Geiger, A. Bershadsky, R. Pankov, K. M. Yamada** (2001). Transmembrane crosstalk between the extracellular matrix-cytoskeleton crosstalk. *Nat. Rev. Mol. Cell Biol.*, **2**, 793-805.
7. **K. van den Dries, S. F. van Helden, J. te Riet, A. Cambi, C. G. Figdor** (2010). Environmental sensing through podosomes. *In preparation*.
8. **J. J. Yu, B. Nolting, Y. H. Tan, X. Li, J. Gervay-Hague, G. Y. Liu** (2006). Polyvalent interactions of HIV-gp120 protein and nanostructures of carbohydrate ligands. *NanoBioTechnology*, **1**, 201-210.
9. **M. Liu, G. Y. Liu** (2005). Hybridization with nanostructures of single-stranded DNA. *Langmuir*, **21**, 1972-1978.
10. **M. Z. Liu, N. A. Amro, C. S. Chow, G. Y. Liu** (2002). Production of nanostructures of DNA on surfaces. *Nano Lett.*, **2**, 863-867.
11. **M. Liu, N. A. Amro, G. Y. Liu** (2008). Nanografting for Surface Physical Chemistry. *Annu. Rev. Phys. Chem.*, **59**, 367-386.
12. **E. Mirmontaz, M. Castronovo, C. Grunwald, F. Bano, D. Scaini, A. A. Ensafi, G. Scoles, L. Casalis** (2008).

- Quantitative Study of the Effect of Coverage on the Hybridization Efficiency of Surface-Bound DNA Nanostructures. *Nano Lett.*, **8**, 4134-4139.
13. **M. Castronovo, S. Radovic, C. Grunwald, L. Casalis, M. Morgante, G. Scoles** (2008). Control of Steric Hindrance on Restriction Enzyme Reactions with Surface-Bound DNA Nanostructures. *Nano Lett.*, **8**, 4140-4145.
  14. **C. Staij, D. W. Wood, G. Scoles** (2008). Verification of Biochemical Activity for Proteins Nanografted on Gold Surfaces. *J. Am. Chem. Soc.*, **130**, 640-646.
  15. **D. J. Zhou, X. Z. Wang, L. Birch, T. Rayment, C. Abell** (2003). AFM study on protein immobilization on charged surfaces at the nanoscale: Toward the fabrication of three-dimensional protein nanostructures. *Langmuir*, **19**, 10557-10562.
  16. **J. R. Kenseth, J. A. Harnisch, V. W. Jones, M. D. Porter** (2001). Investigation of approaches for the fabrication of protein patterns by scanning probe lithography. *Langmuir*, **17**, 4105-4112.
  17. **K. Wadu-Mesthrige, S. Xu, N. A. Amro, G. Y. Liu** (1999). Fabrication and imaging of nanometer-sized protein patterns. *Langmuir*, **15**, 8580-8583.
  18. **Y. Hu, A. Das, M. H. Hecht, G. Scoles** (2005). Nanografting de novo proteins onto gold surfaces. *Langmuir*, **21**, 9103-9109.
  19. **G. Y. Liu, N. A. Amro** (2002). Positioning protein molecules on surfaces: A nanoengineering approach to supramolecular chemistry. *Proc. Natl. Acad. Sci. USA*, **99**, 5165-5170.
  20. **C. D. Hahn, A. Tinazli, M. Holz, C. Leitner, F. Frederix, B. Lackner, N. Muller, C. Klampfl, R. Tampe, H. J. Gruber** (2007). Pragmatic studies on protein-resistant self-assembled monolayers. *Monatshfte Für Chemie*, **138**, 245-252.
  21. **M. Conti, G. Falini, B. Samori** (2000). How Strong Is the Coordination Bond between a Histidine Tag and Ni - Nitrioltriacetate? An Experiment of Mechanochemistry on Single Molecules. *Angew. Chem., Int. Ed.*, **39**, 215-218.
  22. **P. Jonkheijm, D. Weinrich, H. Schroder, C. M. Niemeyer, H. Waldmann** (2008). Chemical strategies for generating protein biochips. *Angew. Chem., Int. Ed.*, **47**, 9618-9647.
  23. **W. Muller, H. Ringsdorf, E. Rump, G. Wildburg, X. Zhang, L. Angermaier, W. Knoll, M. Liley, J. Spinke** (1993). Attempts to mimic docking processes of the immune system: recognition-induced formation of protein multilayers. *Science*, **262**, 1706-1708.
  24. **E. M. Puchner, S. K. Kufer, M. Strackharn, S. W. Stahl, H. E. Gaub** (2008). Nanoparticle self-assembly on a DNA-scaffold written by single-molecule cut-and-paste. *Nano Lett.*, **8**, 3692-3695.
  25. **A. J. Dirks, J. J. L. M. Cornelissen, F. L. van Delft, J. C. M. van Hest, R. J. M. Nolte, A. E. Rowan, F. P. J. T. Rutjes** (2007). From (bio)molecules to biohybrid materials with the click chemistry approach. *Qsar & Combinatorial Science*, **26**, 1200-1210.
  26. **W. Lee, B. K. Oh, Y. M. Bae, S. H. Paek, W. H. Lee, J. W. Choi** (2003). Fabrication of self-assembled protein A monolayer and its application as an immunosensor. *Biosens. Bioelectron.*, **19**, 185-192.
  27. **D. S. Shah, M. B. Thomas, S. Phillips, D. A. Cisneros, A. P. Le Brun, S. A. Holt, J. H. Lakey** (2007). Self-assembling layers created by membrane proteins on gold. *Biochem. Soc. Trans.*, **35**, 522-526.
  28. **S. W. Lee, B. K. Oh, R. G. Sanedrin, K. Salaita, T. Fujigaya, C. A. Mirkin** (2006). Biologically active protein nanoarrays generated using parallel dip-pen nanolithography. *Adv. Mater.*, **18**, 1133-1136.
  29. **T. Rakickas, M. Gavutis, A. Reichel, J. Piehler, B. Liedberg, R. Valiokas** (2008). Protein-Protein Interactions in Reversibly Assembled Nanopatterns. *Nano Lett.*, **8**, 3369-3375.
  30. **H. Agheli, J. Malmstrom, E. M. Larsson, M. Textor, D. S. Sutherland** (2006). Large area protein nanopatterning for biological applications. *Nano Lett.*, **6**, 1165-1171.
  31. **D. Aydin, M. Schwieder, I. Louban, S. Knoppe, J. Ulmer, T. L. Haas, H. Walczak, J. P. Spatz** (2009). Micro-Nanostructured Protein Arrays: A Tool for Geometrically Controlled Ligand Presentation. *Small*, **5**, 1014-1018.
  32. **S. V. Graeter, J. H. Huang, N. Perschmann, M. Lopez-Garcia, H. Kessler, J. D. Ding, J. P. Spatz** (2007). Mimicking cellular environments by nanostructured soft interfaces. *Nano Lett.*, **7**, 1413-1418.
  33. **P. Maury, M. Escalante, M. Peter, D. N. Reinhoudt, V. Subramaniam, J. Huskens** (2007). Creating nanopatterns of his-tagged proteins on surfaces by nanoimprint lithography using specific NiNTA-Histidine interactions. *Small*, **3**, 1584-1592.
  34. **M. Escalante, Y. Zhao, M. Ludden, R. Vermeij, J. Olsen, E. Berenschot, C. Hunter, J. Huskens, V. Subramaniam, C. Otto** (2008). Nanometer arrays of functional light harvesting antenna complexes by nanoimprint lithography and host-guest interactions. *J. Am. Chem. Soc.*, **130**, 8892-8893.
  35. **M. Escalante, C. Blum, Y. Cesa, C. Otto, V. Subramaniam** (2009). FRET pair printing of fluorescent proteins. *Langmuir*, **25**, 7019-7024.
  36. **E. A. Evans, D. A. Calderwood** (2007). Forces and bond dynamics in cell adhesion. *Science*, **316**, 1148-1153.
  37. **D. F. Tees, R. E. Waugh, D. A. Hammer** (2001). A microcantilever device to assess the effect of force on the lifetime of selectin-carbohydrate bonds. *Biophys. J.*, **80**, 668-682.
  38. **C. Ray, J. R. Brown, B. B. Akhremitchev** (2007). Correction of systematic errors in single-molecule force spectroscopy with polymeric tethers by atomic force microscopy. *J. Phys. Chem. B*, **111**, 1963-1974.
  39. **J. Helenius, C. P. Heisenberg, H. E. Gaub, D. J. Muller** (2008). Single-cell force spectroscopy. *J. Cell Sci.*, **121**, 1785-1791.
  40. **Y. F. Dufrène** (2008). Towards nanomicrobiology using atomic force microscopy. *Nat. Rev. Microbiol.*, **6**, 674-680.
  41. **M. E. Taylor, K. Drickamer** (2007). Paradigms for glycan-binding receptors in cell adhesion. *Curr. Opin. Cell Biol.*, **19**, 572-577.
  42. **J. W. Dennis, K. S. Lau, M. Demetriou, I. R. Nabi** (2009). Adaptive regulation at the cell surface by N-glycosylation. *Traffic*, **10**, 1569-1578.
  43. **R. B. Best, E. Paci, G. Hummer, O. K. Dudko** (2008). Pulling direction as a reaction coordinate for the mechanical unfolding of single molecules. *J. Phys. Chem. B*, **112**, 5968-5976.

44. **E. Evans, K. Ritchie, R. Merkel** (1995). Sensitive force technique to probe molecular adhesion and structural linkages at biological interfaces. *Biophys. J.*, **68**, 2580-2587.
45. **M. L. Bennink, S. H. Leuba, G. H. Leno, J. Zlatanova, B. G. de Grooth, J. Greve** (2001). Unfolding individual nucleosomes by stretching single chromatin fibers with optical tweezers. *Nat. Struct. Biol.*, **8**, 606-610.
46. **I. M. Peters, Y. van Kooyk, S. J. van Vliet, B. G. de Grooth, C. G. Figdor, J. Greve** (1999). 3D single-particle tracking and optical trap measurements on adhesion proteins. *Cytometry*, **36**, 189-194.
47. **X. Zhang, E. P. Wojcikiewicz, V. T. Moy** (2002). Force spectroscopy of the leukocyte function-associated antigen-1/intercellular adhesion molecule-1 interaction. *Biophys. J.*, **83**, 2270-2279.
48. **E. P. Wojcikiewicz, M. H. Abdulreda, X. Zhang, V. T. Moy** (2006). Force spectroscopy of LFA-1 and its ligands, ICAM-1 and ICAM-2. *Biomacromolecules*, **7**, 3188-3195.
49. **E. P. Wojcikiewicz, X. Zhang, A. Chen, V. T. Moy** (2003). Contributions of molecular binding events and cellular compliance to the modulation of leukocyte adhesion. *J. Cell Sci.*, **116**, 2531-2539.
50. **H. Xu, J. K. Bickford, E. Luther, C. Carpenito, F. Takei, T. A. Springer** (1996). Characterization of murine intercellular adhesion molecule-2. *J. Immunol.*, **156**, 4909-4914.
51. **M. Shimaoka, C. Lu, R. T. Palframan, U. H. von Andrian, A. McCormack, J. Takagi, T. A. Springer** (2001). Reversibly locking a protein fold in an active conformation with a disulfide bond: integrin alphaL I domains with high affinity and antagonist activity in vivo. *Proc. Natl. Acad. Sci. USA*, **98**, 6009-6014.
52. **A. Cambi, B. Joosten, M. Koopman, F. de Lange, I. Beeren, R. Torensma, J. A. Fransen, M. Garcia-Parajo, F. N. van Leeuwen, C. G. Figdor** (2006). Organization of the Integrin LFA-1 in Nanoclusters Regulates Its Activity. *Mol. Biol. Cell*, **17**, 4270-4281.
53. **M. L. Dustin** (1998). Making a little affinity go a long way: a topological view of LFA-1 regulation. *Cell Adhes. Commun.*, **6**, 255-262.
54. **M. Kim, C. V. Carman, W. Yang, A. Salas, T. A. Springer** (2004). The primacy of affinity over clustering in regulation of adhesiveness of the integrin  $\alpha\beta_2$ . *J. Cell Biol.*, **167**, 1241-1253.
55. **Y. van Kooyk, C. G. Figdor** (2000). Avidity regulation of integrins: the driving force in leukocyte adhesion. *Curr. Opin. Cell Biol.*, **12**, 542-547.
56. **M. L. Dustin, T. A. Springer** (1988). Lymphocyte function-associated antigen-1 (LFA-1) interaction with intercellular adhesion molecule-1 (ICAM-1) is one of at least three mechanisms for lymphocyte adhesion to cultured endothelial cells. *J. Cell Biol.*, **107**, 321-331.
57. **X. Zhang, S. E. Craig, H. Kirby, M. J. Humphries, V. T. Moy** (2004). Molecular basis for the dynamic strength of the integrin  $\alpha\beta_2$ /VCAM-1 interaction. *Biophys. J.*, **87**, 3470-3478.
58. **J. te Riet, A. W. Zimmerman, A. Cambi, B. Joosten, S. Speller, R. Torensma, F. N. van Leeuwen, C. G. Figdor, F. de Lange** (2007). Distinct kinetic and mechanical properties govern ALCAM-mediated interactions as shown by single-molecule force spectroscopy. *J. Cell Sci.*, **120**, 3965-3976.
59. **H. Grubmüller, B. Heymann, P. Tavan** (1996). Ligand binding: molecular mechanics calculation of the streptavidin-biotin rupture force. *Science*, **271**, 997-999.
60. **P. Newham, S. E. Craig, G. N. Seddon, N. R. Schofield, A. Rees, R. M. Edwards, E. Y. Jones, M. J. Humphries** (1997). Alpha4 integrin binding interfaces on VCAM-1 and MAdCAM-1. Integrin binding footprints identify accessory binding sites that play a role in integrin specificity. *J. Biol. Chem.*, **272**, 19429-19440.
61. **B. J. Haupt, A. E. Pelling, M. A. Horton** (2007). Integrated confocal and scanning probe microscopy for biomedical research. *TheScientificWorldJournal*, **6**, 1609-1618.



# EPILOGUE

---

Summary  
Samenvatting  
Dankwoord  
Curriculum Vitae  
List of publications

*The most exciting phrase to hear in science, the one that heralds the most discoveries, is not “Eureka!” (I found it!) but “That’s funny...”*

*Isaac Asimov*

## Summary

Since the invention of the atomic force microscope (AFM) in 1986, the application of the instrument has shifted from a pure physicist's tool to a useful instrument for physicists, chemists and biologists. The AFM is not a classical microscope in the sense that light or electrons are used to obtain an image, it is rather a mechanical microscope. The imaging is purely based on a physical probing of the surface topography by raster scanning (zigzag movements) of a sharp tip on a cantilever across the sample. Furthermore, the AFM can probe forces with ultra-high sensitivity by moving the cantilever in the vertical direction, which is especially interesting for biological applications. The probing of forces with AFM is known as AFM force spectroscopy. These AFM measurements can be performed under physiological conditions and make it possible to study dynamical processes, such as the adhesion of a living cell to an adjacent cell or the extracellular matrix, from the single cell to single molecular level.

In the immune system diverse dynamical processes, such as the recognition of a pathogen by a dendritic cell (DC) or the transmigration of a leukocyte through the endothelium of a blood vessel, happen all the time throughout the human body. In the latter case during initial binding of these cells, bonds between different cell adhesion molecules (CAMs) are formed. These interactions have to be highly dynamic to withstand forces induced by for example the blood flow. These CAM bonds associate and dissociate at rates that change considerably under conditions of cell stress. The combination of molecular cell biology and AFM single molecule force spectroscopy provides a powerful tool to explore the complexity of these cell adhesion processes.

In this thesis, we explored the versatility of the AFM in the context of biomaterial science, nano-chemistry and cell biology. The high spatial resolution of the AFM was exploited to measure and manipulate samples at the nanoscale. Moreover, the high force sensitivity of the AFM was applied to measure adhesive properties of CAMs on cells and to address the two distinct adhesive regulation processes of a CAM: affinity and avidity.

In **Chapter 2** the high spatial resolution of the AFM was exploited to image substrates relevant for biological applications in biomaterial sciences. In particular, the adhesion behavior of fibroblasts was studied on nanopatterns. These cells adhere and align to patterns with a threshold for the patterns that are spaced at 100 nm distances and with a depth of 35 nm. The AFM's strength in probing the dimensions and structure of these patterns quantitatively illustrates the value of AFM as a tool to investigate patterns intended for biological studies addressing adhesive behavior, cell signaling, and tissue embedding.

With AFM force spectroscopy interaction forces between single molecules can be measured with piconewton accuracy. To reach this level of accuracy, a uniform and quantitative calibration method for AFM cantilevers is absolutely essential. Therefore, in **Chapter 3**, we describe an interlaboratory round robin study that was performed on 10 different AFMs in 7 different groups to obtain such a generally accepted calibration protocol. Different cantilever spring constant calibration methods were compared and we concluded that the direct Sader method was the most reliable and most accurate method to use for different types of cantilevers. In addition, the fast and improved standard protocol and practical suggestions described in this Chapter will contribute to the standardization of the AFM force spectroscopy method.

In **Chapter 4** we describe how AFM force spectroscopy is used to unravel the influence of affinity versus avidity on the homo- and heterotypic ALCAM-mediated interactions; the heterotypic ALCAM-CD6 interaction being stronger than the homotypic ALCAM-ALCAM interaction. Furthermore, by retrieving the kinetic and mechanical properties of both interactions we obtained better insight in the biological function of ALCAM. For example, expression of ALCAM on melanoma cells results in a more migratory phenotype, because ALCAM-ALCAM bonds are less stable than homotypic E-cadherin bonds that are down-regulated on these cells. In **Chapter 5** AFM force spectroscopy is used to study the interaction of the pathogen receptor DC-SIGN with the fungus *Candida albicans*. The interaction of this C-type lectin, which specifically binds to carbohydrate epitopes of the fungus, is studied at the single molecule level and compared to other receptor-carbohydrate interactions. These protein-carbohydrate interactions seem to have similar dynamical affinities, which is consistent with their physiological role in the immune system.

**Chapter 6** describes the possibilities of AFM-assisted nanografting to generate protein patterns of DC-SIGN and ALCAM to address the contribution of nano- and micro-clustering of CAMs on adhesion. We report on the immobilization strategy for His-tagged DC-SIGN and ALCAM on a self-assembled monolayer (SAM) of NTA-terminated thiols. On this platform, proteins can be specifically bound and oriented. In **Chapter 7**, we show the nanografting of patterns within a SAM by AFM. SAMs with various chains and endgroups were characterized using nanografting. We have shown that the tilt at which (functionalized) alkanethiols orient in the SAM can be accurately determined due to the subnanometer accuracy of AFM topography measurements. In particular, the formation of stable bilayered SAMs due to hydrogen binding in carboxyl- and amino-terminated alkanethiols could be studied in great detail and is described in **Chapter 8**. Subsequently, by the systematic investigation of mechanical friction properties of SAMs with different endgroups ( $-\text{CH}_3$ ,  $-\text{CF}_3$ ,  $-\text{OH}$ ,  $-\text{SH}$ ,  $-\text{COOH}$  and  $-\text{NH}_2$ ) we found specific friction 'signatures' for the different chemical endgroups. In particular, we were able to measure odd-even effects in methyl-terminated (**Chapter 7**) and carboxyl-terminated alkanethiols (**Chapter 8**). These observations were only possible because of the higher order of self-assembly in nanografted patches. Moreover, the spatially confined self-assembly during nanografting allows for quantitative measurements of self-assembly processes at the nanoscale, which demonstrates the new possibilities for surface physical chemistry.

Finally, in **Chapter 9** a general discussion and future prospective on the topics presented in this thesis are given.



## Samenvatting

In 1590 ontdekten twee Nederlandse lenzenmakers, Zaccharias Jansen en zijn vader Hans, al experimenterend met het plaatsen van meerdere lenzen in één buis, dat objecten dichtbij sterk vergroot waren. Enige decennia later gebruikte Antoni van Leeuwenhoek deze kennis om de eerste microscoop te bouwen voor zijn studies en werd bekend als de uitvinder van de microscoop. Deze eerste microscopen maakten gebruik van lenzen om het licht te bundelen en daardoor het onderzochte voorwerp te vergroten. Sindsdien hebben vele verbeteringen, voornamelijk in de 20<sup>ste</sup> eeuw, ervoor gezorgd dat lichtmicroscopie tegenwoordig veel wordt gebruikt om bijvoorbeeld cellen, weefsels en materialen te bestuderen. Echter de resolutie van de traditionele lichtmicroscopie is begrensd door de diffractielimiet van licht; dat wil zeggen dat details kleiner dan de golflengte van het zichtbare licht (tussen 380 en 780 nanometer – een miljardste meter) niet onderscheiden kunnen worden. In 1931 bouwde Ernst Ruska een ander type microscoop gebaseerd op het gebruik van elektronen, die een veel kleinere golflengte hebben dan zichtbaar licht. Met deze elektronenmicroscoop kon men details waarnemen die zo klein zijn als enkele atomen. Begin jaren '80 ontwikkelde men bij IBM in Zwitserland nog een ander type microscoop. Dit type microscoop maakt gebruik van een naaldje ('probe') om een oppervlak lijn voor lijn af te tasten ('scannen') en vervolgens af te beelden. De behaalde resolutie is daarbij zo hoog, dat atomen en moleculen kunnen worden afgebeeld. De naam voor dit type microscopie is scanning probe microscopie (SPM) en het type microscoop waarvan ik in dit proefschrift veelvuldig gebruik heb gemaakt, de atomic force microscoop (AFM – atoomkrachtmicroscoop), maakt hier deel van uit.

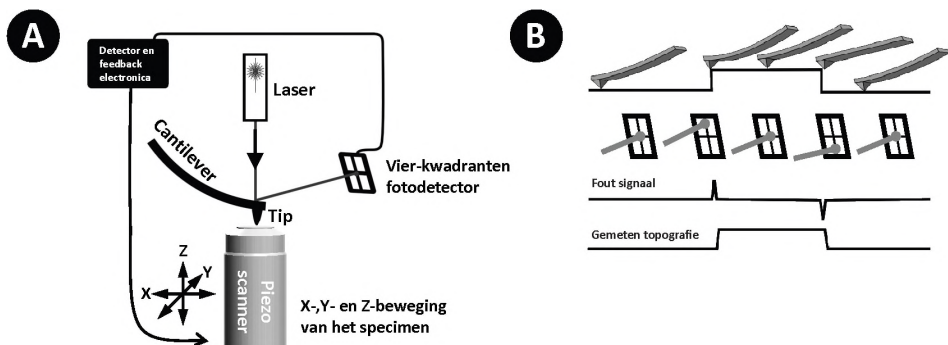
De eerste jaren na de uitvinding van de AFM in 1986 werd deze vooral gebruikt door fysici, sinds de laatste vijftien jaar wordt deze echter ook steeds meer gebruikt door chemici en biologen. De AFM is niet een klassiek type microscoop, hij maakt namelijk geen gebruik van licht of elektronen om een afbeelding te maken. Het is een mechanische microscoop. Dit houdt in dat een afbeelding gemaakt wordt door een oppervlak fysiek af te tasten door middel van zigzag scannen met een super scherp naaldje op een hefboompje – de *cantilever* (Figuur 1). Verder kan men met de AFM supergevoelig krachten meten door de cantilever in de verticale richting (z-richting) te bewegen. Dit is met name interessant voor biologische toepassingen, waarbij de techniek van krachten meten met de AFM ook bekend staat als AFM krachtspectroscopie. De krachtmetingen kunnen gedaan worden onder omstandigheden die vergelijkbaar zijn met die in het menselijk lichaam, waardoor dynamische processen bestudeerd kunnen worden zoals de adhesie (hechting) van een levende cel aan een andere cel of aan het bindweefsel. Deze metingen zijn mogelijk op enkele cellen en zelfs op enkele moleculen.

In ons immuunsysteem vinden elk moment verscheidene dynamische processen plaats, zoals het herkennen van een binnengedrongen ziekteverwekker door een dendritische cel (DC) – de belangrijkste bewaker cel – of het migreren van een witte bloedcel van het bloed naar de onderliggende weefsels, waarbij de cel de wand van een bloedvat moet passeren. Om de bloedvatwand te kunnen passeren zullen de witte bloedcellen eerst moeten binden aan de cellen van het bloedvat; dit doen ze door het vormen van moleculaire bindingen tussen verscheidene cel adhesie moleculen (CAM's) op het celmembraan. De gevormde bindingen moeten erg dynamisch en sterk zijn om krachten te kunnen verduren die op de cel inwerken, zoals die van het stromende bloed. Hierbij gaan deze CAM moleculen bindingen aan en verbreken deze continu, maar

wanneer de spanningen en dus krachten toenemen, zal de balans verschuiven tussen het aangaan van bindingen en het verbreken ervan. Door moleculaire celbiologische kennis over deze processen te combineren met AFM krachtspectroscopie kunnen we met ongekend detail deze complexe cel adhesie processen bestuderen.

In dit proefschrift hebben we de veelzijdigheid van de AFM als kracht- en afbeeldmicroscopie gebruikt om onderzoek te doen naar biomaterialen, nanochemie en celbiologie. De hoge resolutie van de AFM is gebruikt om oppervlakken nauwkeurig af te beelden en om oppervlakken te manipuleren op de nanoschaal. Daarnaast is de hoge krachtgevoeligheid van de AFM gebruikt om de sterkte eigenschappen van verschillende CAM's te meten op cellen en om twee verschillende adhesie regelmechanismen te onderscheiden, genaamd affiniteit – de sterkte van de individuele binding – en aviditeit – de mate van samenwerking tussen moleculen.

In **Hoofdstuk 2** beschrijf ik hoe de hoge resolutie van de AFM gebruikt kan worden bij het afbeelden van substraten die gebruikt worden als biomaterialen voor implantaten. In het bijzonder bestudeerden we het adhesiegedrag van fibroblasten – cellen die de weefselstructuur van het lichaam vormen – op nanopatronen. We vonden dat deze cellen zich hechten en uitlijnen aan de nano-lijnstructuren tot een afstand van 100 nm tussen de lijnen en een groefdiepte van 35 nm. De krachtige resolutie van de AFM werd hierbij gebruikt om de precieze dimensies en structuur van de patronen te meten. Bovendien laat dit de toegevoegde waarde van de AFM zien als instrument om patronen te bestuderen die gebruikt worden voor biologische studies naar hechtingsgedrag van cellen, cel signaaloverdracht en het ingroeien van implantaten in lichaamsweefsels.



**Figuur 1: Atoomkrachtmicroscopie (AFM)**

(A) Met een piezo scanner kan een specimen afgetast worden door deze te bewegen in de x-, y- en z-richting. Met behulp van de de scherpe tip (een 'naaldje') aan het uiteinde van een flexibel hefboompje ('cantilever') kunnen we vervolgens de topografie van het specimen afbeelden. Door middel van een laserstraal die gereflecteerd wordt van het uiteinde van de cantilever en een vier-kwadranten detector kan de doorbuiging van deze cantilever gemeten worden. (B) Bij het meten van de topografie van een specimen, hier aangeven als de lijn met een verhoging in het midden, kan je zien dat hoogte verschillen gemeten worden als verschuiving omhoog en omlaag van de laser op de fotodetector door de doorbuiging van de cantilever (bovenste lijn van plaatjes). Normaal gesproken zal in de zogenaamde contact modus deze doorbuiging gecompenseerd worden door het specimen zo in de z-richting te bewegen dat de laser weer in het midden van de detector valt (zie tweede regel van plaatjes). Het signaal van de echte laser positie wordt geïnterpreteerd als het 'fout signaal' (zie derde lijn) en de beweging van de z-scanner als de werkelijke topografie (onderste lijn).

Met AFM krachtspectroscopie kunnen interactiekrachten gemeten worden tussen enkele moleculen met picoNewton nauwkeurigheid. Om deze mate van nauwkeurigheid te halen is een algemeen geaccepteerd en nauwkeurig calibratie protocol voor cantilevers noodzakelijk. Daarom beschrijven we in **Hoofdstuk 3** een “round robin” studie, inhoudende dat dezelfde set van cantilevers gecalibreerd is op 10 verschillende AFM’s, die in 7 verschillende onderzoeksgroepen staan. Hiermee hebben we getracht een algemeen geaccepteerd calibratie protocol te beschrijven. Inhoudelijk hebben we een aantal calibratie methoden vergeleken en geconcludeerd dat de Sader methode de meest betrouwbare en nauwkeurigste methode is voor verschillende types cantilevers. Bovendien zal het snel uit te voeren en verbeterde protocol en de praktische suggesties die we beschrijven in dit hoofdstuk bijdragen aan de standaardisatie van de AFM krachtspectroscopie methode.

In **Hoofdstuk 4** beschrijven we hoe AFM krachtspectroscopie gebruikt kan worden om de rol te ontrafelen die affiniteit en aviditeit hebben op homotypische – tussen dezelfde moleculen – en heterotypische – tussen twee verschillende typen – ALCAM interacties. Hierbij is de ALCAM-CD6 binding (heterotypisch) sterker dan de homotypische ALCAM-ALCAM binding. Daarnaast hebben we door het bepalen van de kinetische en mechanische eigenschappen van beide bindingen een beter inzicht gekregen in de biologische functie van ALCAM. Bijvoorbeeld, een verhoogde expressie van ALCAM is gerelateerd aan een sterker migrerend fenotype van melanoom kanker cellen, onze metingen laten zien dat dit kan komen doordat ALCAM-ALCAM bindingen minder stabiel zijn dan homotypische E-cadherine bindingen die de kanker cel verloren heeft. In **Hoofdstuk 5** beschrijven we hoe AFM krachtspectroscopie gebruikt kan worden om de interactie tussen de receptor van ziekteverwekkers op een dendritische cel (DC) genaamd DC-SIGN en de schimmel *Candida albicans* te onderzoeken. De interactie van deze C-type lectine, die specifiek bind aan carbohydraat (suiker) structuren op de schimmel, is bestudeerd tot op het niveau van enkele moleculen en vergeleken met resultaten van andere receptor-suiker bindingen. Er blijkt overeenstemming te zijn tussen de dynamische affiniteiten van al deze bindingen, wat op zijn beurt weer overeenstemt met de rol die dit type bindingen spelen in het immuunsysteem.

Een beschrijving van de mogelijkheden om met de AFM nanopatronen te maken van eiwitten vindt men in **Hoofdstuk 6**. We gebruiken de nanografeer methode (*nanografting*) om patronen te maken van DC-SIGN en ALCAM om hun bijdrage aan adhesie van cellen te vinden door middel van nano- en microclusters. Wij doen verslag over de strategie waarop eiwitten, zoals DC-SIGN en ALCAM, gekoppeld kunnen worden aan een oppervlak door middel van een histidine label en moleculen met een NTA-groep. De moleculen met een NTA-groep zijn zogenaamde alkaanthiol-moleculen die een netjes gestructureerde monolaag vormen op goud, de zogenoemde zelf-geassembleerde monolaag (SAM; een uit zichzelf vormende laag met een dikte van één molecuul). Doordat de histidine-NTA binding erg specifiek en uniek is kunnen eiwitten netjes geordend op een oppervlak worden gepositioneerd. In **Hoofdstuk 7** laten we zien hoe patronen in een SAM-laag geschreven kunnen worden met behulp van de AFM. Door middel van het nanograferen van verscheidene alkaanthiol-moleculen met verschillende alkaan lengtes en verschillende chemische eindgroepen konden monolagen van deze moleculen gekarakteriseerd worden. We laten onder andere zien dat de hoek waaronder de moleculen zich oriënteren nauwkeurig bepaald kan worden door de subnanometer nauwkeurigheid van AFM topografie metingen. Een bijzondere vinding was dat een stabiele dubbele laag van SAM structuren gevormd wordt wanneer de alkaanthiol

moleculen aan het uiteinde een zuur- of amine-groep hebben. In veel detail hebben we kunnen zien, dat deze moleculen een dubbele laag vormen vanwege waterstofbruggen. Dit beschrijven we in **Hoofdstuk 8**. Verder hebben we door het systematisch bestuderen van de mechanische frictie van SAM-lagen met verschillende chemische eindgroepen ( $-\text{CH}_3$ ,  $-\text{CF}_3$ ,  $-\text{OH}$ ,  $-\text{SH}$ ,  $-\text{COOH}$ , en  $-\text{NH}_2$ ) gevonden dat deze frictie specifiek is voor elk type chemische eindgroep en gebruikt kan worden als een soort 'vingerafdruk'. Andere bevindingen waren dat we met onze methode even-oneven effecten konden waarnemen voor methyl-alkaanthiolen (**Hoofdstuk 7**) en alkaanthiolzuren (**Hoofdstuk 8**). Dat we dit konden waarnemen was alleen mogelijk doordat de organisatie van de moleculen in de gegraveerde SAM-laag erg goed was. Verder maakt het geobserveerde proces – ruimtelijk begrensde molecuul ordening – het mogelijk om kwantitatieve metingen te doen van zelf-organisatie op de nanoschaal. Dit biedt verscheidene nieuwe mogelijkheden voor het veld van de "fysische oppervlakte chemie".

Ten slotte bediscussieer en beschrijf ik de belangrijkste bevindingen van mijn onderzoek in **Hoofdstuk 9** en geef ik mogelijkheden aan voor vervolgonderzoek op de diverse studies.

## Dankwoord

**Z**o, het laatste stukje van het proefschrift. Na bijna 5 jaar als junior onderzoeker is het zover, ik kan de laatste hand leggen aan een boekje dat behalve een wetenschappelijke proeve, ook vooral de periode afsluit die een persoonlijke proeve is áls wetenschapper. Ik kijk op deze periode sowieso terug als mooie jaren, waarin ik me goed heb kunnen ontwikkelen vooral door de prettige samenwerking met ontzettend veel aardige mensen die ik hierbij wil danken.

Ten eerste mijn twee promotoren Sylvia en Carl bij wie ik de gelegenheid heb gekregen in mei 2005 te mogen beginnen met mijn promotieonderzoek. Een samenwerking tussen de SPM groep, of toen nog eigenlijk EVSF2, en het TIL. Een samenwerking tussen fysici en biologen, twee verschillende werelden, maar voor mij nu één wereld.

Beste Sylvia, ik kan me nog herinneren hoe ik 5 jaar geleden kwam solliciteren bij jou in de oude beta-faculteit. Een presentatie, rondleiding en een gesprek en het bleek ik was aangenomen. Hoewel dat mij lange tijd onbekend bleef door een mailtje naar mijn 'Hotmeil' adres! Verder zou ik je zeer willen bedanken voor de vrijheid die je me hebt gegeven in mijn promotietraject om mijn onderzoek mijn eigen richting op te sturen. Je hebt er voor gezorgd dat het junior onderzoeker/AIO/OIO zijn echt een 'in opleiding' traject is geweest, waarin ik zeer veel geleerd heb. Danke vielmals!

Beste Carl, jij ook superbedankt natuurlijk, maar 'ladies first'. De geschiedenis gaat iets verder terug naar het voorjaar van 2003 in Enschede. Als doctoraal student Technische Natuurkunde wilde ik graag afstuderen bij jouw bijzondere leerstoel Celbiofysica en dan het liefst in Nijmegen. In oktober 2003, mocht ik dan ook starten met afstuderen en leerde ik hoe interessant het is om als natuurkundige met biologische vraagstukken bezig te zijn. Ik was dan ook erg blij, dat ik in 2005 mocht beginnen als promovendus om nog veel meer te leren over immunologie. In de afgelopen jaren heb ik, behalve dat, nog veel meer van je geleerd. Wetenschap is meer dan alleen het doen van experimenten, het is ook managen, enthousiasmeren, samenwerken, netwerken en bovenal kritisch en creatief nadenken. Door jouw vertrouwen en sturing had dit boekje er niet zo goed uitgezien. Ontzettend bedankt!

Naast twee promotoren heb ik jou, Alessandra, als co-promotor. Ook van jou heb ik super veel geleerd de laatste jaren, toen je mijn dagelijks begeleider werd na het vertrek van mijn eerste twee. Zonder jouw doortastende en motiverende begeleiding was dit boekje niet tot stand gekomen in zijn huidige vorm. Bovendien heeft jouw kritische en praktische blik op de wetenschap ervoor gezorgd dat zaken net wat sneller en beter geregeld of op papier werden gezet. Verder heeft jouw persoonlijke positieve kritiek er mede aan bijgedragen dat ik, in ieder geval voorlopig, verder ga in de wetenschap. Ik ben dan ook trots dat ik de eerste promovendus van jou zal zijn als co-promotor.

Zoals ik net al noemde, mijn eerste twee begeleiders Frank de Lange en Peter Schön, degenen die mijn promotieproject schreven en gehonoreerd kregen bij NanoNed. Echter beiden vertrokken jullie voortijdig. Frank, jij was degene die me ertoe bewogen heeft om te gaan promoveren. Toen ik namelijk als jouw student begon in 2003, had ik er nog nauwelijks over gedacht om te gaan promoveren, echter gedurende mijn afstudeerperiode begon ik te beseffen hoe leuk het was om onderzoek te doen en dat ik best wel doctor zou willen worden. Ook gaf je me het voorbeeld dat een fysicus zich thuis kan voelen in een biologische setting en dat de brug tussen natuurkunde en biologie goed te slaan valt. Jammer genoeg bleek echter al gauw dat je gekozen had om

klinisch fysicus te worden, toen ik begon als promovendus. Een keus die ik goed kan begrijpen en waarvan je geloof ik geen moment spijt hebt gekregen. Hartelijk dank voor je begeleiding van het eerste uur!

Peter, ich möchte auch dir gerne danken für deine freundliche Begleitung und für deinen Enthusiasmus jedesmal, wenn ich mit dir Resultate besprach. Wie Frank, wähltest du auch etwas Neues, eine Stelle bei Veeco in Münster, in der Nähe von deiner Freundin. Obwohl auch das nicht lange dauerte, und du nun schon wieder seit einiger Weile an der Universität Twente beschäftigt bist. Resümierend: Es war schön, Dr. Schön, mit dir gearbeitet zu haben!

Beste Hans, vooral het laatste jaar heb jij ook bijgedragen aan mijn werk. Met jouw hulp heb ik ook de chemische component van mijn onderzoek onder de knie gekregen. Ook mede door jouw betrokkenheid in met name de nanografting hoofdstukken is daar toch ook een mooi stukje werk uitgekomen. Heel erg bedankt voor alle hulp en nuttig commentaar.

Tim, ofwel TimSmiT het palindroom ;-), wat een topstudent ben jij geweest, jouw experimenten hebben heel wat bijgedragen aan dit boekje! Het was erg leuk om met jou anderhalf jaar lang samen te werken met de AFM in het NanoLab. Een gezellige tijd. Gesprekken over films, Lost en Tenacious D en niet te vergeten prachtige schema's op het whiteboard. Het ga je goed in Hollywood!

Verder, wil ik nog een paar oud-collega's en anderen met wie ik heb samengewerkt bij het tot stand komen van dit proefschrift bedanken. Aukje, dankjewel voor al je ALCAM kennis, en de round robin partners voor de hulp met calibreren. Verder de collega's in Twente en Barcelona waarmee we elke twee maanden lekker discussiëren via de SMART. Daarnaast wil ik ook Walter, Edwin, Lise, Ljupcho, Timothy, Huanan en Frank W. van Biomaterialen bedanken voor het vertrouwen die jullie in mij hebben bij het meten van jullie samples met AFM.

Furthermore, I like to thank my manuscript committee for reading my thesis and for giving some useful comments. Furthermore, I like to especially thank Peter Hinterdorfer for hosting me twice in his lab. It was a nice experience!

Dan mijn twee paranimfen, Duncan en Ben. Duncan, ik vind het leuk dat je mijn paranimf wilt zijn. Beiden begonnen we ongeveer tegelijkertijd met promoveren bij EVSF2/SPM en hebben heel wat gekletst over werk, maar meer nog over vakanties, boeken en toekomstplannen. Onder andere het wekelijkse fitness-uurtje en de Ameland cursus waren erg gezellig. Verder vind ik het leuk dat je nu toch ook gekozen hebt om post-doc te worden. Nog een tijdje en dan kan je ook je boekje verdedigen.

Mijn andere paranimf, Ben, relaxte gast!, de keus was snel gemaakt. Feestjes ben je altijd voor in, ik vind het dan ook super leuk dat we al jaren samen in de outdoorborrel commissie zitten, nu samen met Jori, maar daarvoor met Suzanne. Verder nog gezellige snowboard tripjes gemaakt, gemountainbiked en lunchen in de kantine. Altijd in voor een gesprek, soms over werk voor praktische tips, maar net zo vaak over vakanties, voetbal, feestjes etc. De gezelligheidsfactor zit met jou altijd snor!

Voor de gezellige en prettige tijd die ik de laatste jaren heb gehad, moet ik natuurlijk nog veel meer collega's bedanken. Ik wil beginnen mijn mede-AIOs van SPM te bedanken: Michiel – natuurwetenschapper superdeluxe, Jelena – altijd in voor gezelligheid, Duncan, Joris, Minko, Thomas, Arend en Fieke (beide een klein beetje SPM, toch?). Jullie hebben heel wat gezelligheid gebracht in het NanoLab en op ettelijke borrels en feestjes.

Daarnaast zullen de vele discussies over het wel en wee in het lab en daarbuiten me zeker bijblijven. Verder allen nog veel succes met de laatste loodjes (of laatste jaren) van jullie promotieonderzoek – dat jullie ook snel een boekje geschreven hebben!

Verder al de andere collega's van SPM en SSI, ook jullie wil ik bedanken voor jullie hulp en gezelligheid. Ten eerste, de technici Jan G. – heel wat discussies over AFM's! – Jan H., Pieter, Tonnie en Albert voor hulp bij vragen. De secretaresses, Marie-Louise, Riki en Marilou voor het geduld bij het beantwoorden van al mijn 'hoe-regel-je-dit' vragen. De andere SPMers en oud-SPMers: Bas, Oleg, Serhiy, Moniek, Fresia, Lucian, Melissa, Koen, Martijn, Roy ook bedankt voor de fijne tijd. Verder ook alle SSlers dankjewel voor de gezellige gezamenlijk activiteiten; Theo, Chris, beide Johans, Daniel, Dmitry, Venci, Fred, Sasha, Jing & Bas, Kadir.

Dan de collega's van de overkant, de TILLers, of zijn de SPMers nu de overkant? Ik heb me bij jullie net zo thuis gevoeld als aan de overkant en is het nu mijn nieuwe plekje als postdoc. Het is fijn om nu één plekkie te hebben, waar ik helemaal thuis ben. Ook hier een prettige werksfeer, alleen een tikje anders dan bij de natuurkundigen aan de overkant. Ik moet zeggen dat ik me tussen de biologen steeds beter ben thuis gaan voelen en hopelijk vinden jullie een natuurkundige ondertussen niet meer zo eng ;-)) Ik wil jullie allen bedanken voor die jaren gezelligheid. Toch wil ik een aantal mensen speciaal noemen. Allereerst mijn U-genootjes door de jaren heen: Inge – altijd opgewekt – Sandra – fijn nog een natuurkundige – Agnieszka – bedankt voor de orchideeëntips – Machteld – stoere hockeyster. En natuurlijk Jan en Yvet van Celbiologie, bedankt voor de leuke tijd op de 6<sup>e</sup>! Daarnaast de Utje-buren Koen, Marjolein, Ben en voorheen ook Suzanne. Met jullie is het altijd gezellig buurten en discussiëren over serieuze maar zeker net zo vaak niet zo serieuze onderwerpen. Daarnaast is het altijd relaxt lunchen met jullie, Martijn, Jori en Stefan. Hopelijk houden we het nog een tijdje gezellig!

Verder wil ik de rest van de staf bedanken – Ruurd, Gosse, Jolanda en Theo – voor het gezamenlijk met Carl en Alessandra organiseren en draaiende houden van een succesvol lab waar het met plezier werken is. Hierbij is de ondersteuning van Louise, Jeanette en Sandy ook onontbeerlijk voor het helpen bij de dagelijkse organisatie.

Behalve werk was er ook gelukkig nog tijd voor ontspanning. Zo waren er de mountainbike tochtjes samen met Martijn, Ben, Hans en Daniel; heerlijk door de bossen crossen en natuurlijk het beklimmen van El Diablo! Het wordt weer tijd om weer snel te gaan fietsen. Borrelen met de outdoorcommissie, Ben, Jori en Suzanne, het was super om gezamenlijk iets leuks voor de hele groep te organiseren en keer op keer geslaagd. Dat we nog een tijdje mogen doorgaan! Hierbij wil ik Jurjen, Nina, Anna, Wendy, Marleen, Saartje, Christina, Luis Javier en de rest van de TILLers bedanken voor de jaren gezelligheid. Net zoals de mensen van Celbiologie op de 6<sup>e</sup> waar ik ook jaren met veel plezier heb gezeten.

Verder wil ik mijn vrienden bedanken voor alle gezelligheid en het helpen relativeren van mijn promotiewerk. Gelukkig is er meer dan werk alleen.

Natuurlijk wil ik ook mijn ouders en de rest van de familie bedanken voor alle steun en interesse in het promoveren. Ik weet dat het soms voor jullie moeilijk voor te stellen is wat ik doe en wat er nu zoveel tijd kost dat ik er jaren mee bezig ben geweest!

Lieve Barbara, jij bent het mooiste wat me de laatste 5 jaar is overkomen. Zo maar via een NCMLS cursus kwam ik jou tegen! Wat hebben we samen de laatste jaren hard gewerkt om nu bijna tegelijkertijd doctor te worden en over 3 maanden zullen we ook nog man en vrouw zijn. Samen kunnen we alles aan!

## *Curriculum Vitae*

**J**oost te Riet werd op 7 juli 1980 geboren te Losser. In 1998 haalde hij zijn VWO diploma op het Twents Carmel Lyceum te Oldenzaal. Aansluitend volgde hij de studie Technische Natuurkunde aan de Universiteit Twente te Enschede met de afstudeerrichting Biofysische Technieken. Tijdens deze studie liep hij 4 maanden stage op de afdeling Toegepaste Biologie aan de Universiteit van Linköping in Zweden onder begeleiding van prof. dr. Carl-Fredrik Mandenius. Dit onderzoek richtte zich op de toepassing van een nieuw type commercieel verkrijgbare (Surface Plasmon Resonance) sensor voor de detectie van eiwitten. Zijn afstudeerstage van 12 maanden werd gedaan aan de Radboud Universiteit Nijmegen op de afdeling Tumor Immunologie onder leiding van dr. Frank de Lange en prof. dr. Carl G. Figdor. Tijdens deze stage deed hij onderzoek naar de toepassing van AFM krachtspectroscopie om de precieze regulatie van cel adhesie door het eiwit ALCAM te bestuderen. Gedurende zijn studie heeft hij verscheidene nevenactiviteiten gehad, waaronder secretaris van de studiereiscommissie Aztec, inhoudende dat hij voor de studievereniging Arago een 3 weekse studiereis naar Californië en Mexico heeft georganiseerd. Daarnaast is hij jarenlang redacteur voor het studieverenigingsblad Focus geweest.

Na het behalen van zijn ingenieurstitel begon hij als junior onderzoeker op de afdelingen Scanning Probe Microscopie (voorheen Experimentele Vaste Stof Fysica 2) van de Radboud Universiteit en Tumor Immunologie van het UMC St. Radboud. Onder begeleiding van dr. Alessandra Cambi, prof. dr. Sylvia Speller en prof. dr. Carl G. Figdor werd het promotieonderzoek uitgevoerd wat in dit proefschrift beschreven is. Gedurende het promotie traject bracht hij een kort werkbezoek aan het lab van prof. dr. Peter Hinterdorfer op de Universiteit van Linz (Oostenrijk).

Thans is hij werkzaam als postdoc op de afdeling Tumor Immunologie van het UMC St. Radboud onder begeleiding van prof. dr. Carl G. Figdor en dr. Alessandra Cambi. Door de honorering van een gezamenlijk aangevraagde NWO-middelgroot subsidie zal hij betrokken zijn bij de aanschaf en ingebruikname van een gecombineerde AFM-confocaal microscoop. Vervolgens zal hij met dit systeem verder immunologisch onderzoek doen naar o.a. de interactie van dendritische cellen met pathogenen en T cellen.



## List of publications

**Joost te Riet**, Aukje W. Zimmerman, Alessandra Cambi, Ben Joosten, Sylvia Speller, Ruurd Torensma, Frank N. van Leeuwen, Carl G. Figdor, Frank de Lange.

***Distinct kinetic and mechanical properties govern ALCAM-mediated interactions as shown by single molecule force spectroscopy.***

Journal of Cell Science, 2007; 120: 3965-3976

Walter A. Loesberg, **Joost te Riet**, Falco C.M.J.M. van Delft, Peter Schön, Carl G. Figdor, Sylvia Speller, Jack J.W.A. van Loon, X. Frank Walboomers, John A. Jansen.

***The threshold at which substrate nanogroove dimensions may influence fibroblast alignment and adhesion.***

Biomaterials, 2007; 28: 3944-3951

Falco C.M.J. van Delft, Eric C. van den Heuvel, Walter A. Loesberg, **Joost te Riet**, Peter Schön, Carl G. Figdor, Sylvia Speller, Jack J.W.A. van Loon, X. Frank Walboomers, John A. Jansen.

***Manufacturing substrate nano-grooves for studying cell alignment and adhesion.***

Microelectronics Engineering, 2008; 85: 1362-1366

Lise T. de Jonge, Sander C.G. Leeuwenburgh, Jeroen J.J.P. van den Beucken, **Joost te Riet**, Willeke F. Daamen, Joop G.C. Wolke, Dieter Scharnweber, John A. Jansen.

***The osteogenic effect of electrosprayed nanoscale collagen/calcium phosphate coatings on titanium.***

Biomaterials, 2010; 31: 2461-2469

Edwin Lamers, X. Frank Walboomers, Maciej Domanski, **Joost te Riet**, Falco C.M.J.M. van Delft, Regina Luttmge, Louis A.J.A. Winnubst, Han J.G.E. Gardeniers, John A. Jansen.

***Nanogrooved substrates influence osteoblast-like cell behavior and extracellular matrix deposition.***

Biomaterials, 2010; 31: 3307-3316

**Joost te Riet**, Tim Smit, Jan W. Gerritsen, Alessandra Cambi, Johannes A.A.W. Elemans, Carl G. Figdor, Sylvia Speller.

***Molecular friction as a tool to identify functionalized alkanethiols.***

Langmuir, 2010; 26: 6357-6366

**Joost te Riet**, Tim Smit, Michiel J.J. Coenen, Jan W. Gerritsen, Alessandra Cambi, Johannes A.A.W. Elemans, Sylvia Speller, Carl G. Figdor.

***AFM topography and friction studies of hydrogen-bonded bilayers of functionalized alkanethiols.***

Submitted for publication

**Joost te Riet**, Allard J. Katan, Christian Rankl, Stefan W. Stahl, Arend M. van Buul, In Yee Phang, Alberto Gomez-Casado, Jan W. Gerritsen, Alessandra Cambi, Alan E. Rowan, G. Julius Vancso, Pascal Jonkheijm, Jurriaan Huskens, Tjerk H. Oosterkamp, Hermann Gaub, Peter Hinterdorfer, Carl G. Figdor, Sylvia Speller.

***Interlaboratory round robin on cantilever calibration for AFM force spectroscopy.***

Submitted for publication

Ljupcho Prodanov, **Joost te Riet**, Edwin Lamers, Maciej Domanski, Regina Luttmge, Jack J.W.A. van Loon, John A. Jansen, X. Frank Walboomers.

***Interaction between nano-textured surface and mechanical loading influences osteoblast-like cells behavior.***

Submitted for publication